LIBRARY
TECHNICAL REPORT SECTION
NAVAL POSTGRADUATE SCHOOL
MONTEREY, CALIFORNIA 93940

NPS 63-81-001

NAVAL POSTGRADUATE SCHOOL

Monterey, California

FINAL TECHNICAL REPORT OF NSF
GRANT ATM 77-14821

"DYNAMICS OF TROPICAL WAVES AND MONSOONS"

by

Chih-Pei Chang and Roger T. Williams

April 1981

Final Report
for Period September 1977 - October 1980

Approved for public release; distribution unlimited.

Prepared for: National Science Foundation
Washington, D.C. 20550

NAVAL POSTGRADUATE SCHOOL
Monterey, California 93940

Rear Admiral J. J. Ekelund
Superintendent

D. A. Schrady
Acting Provost

The work reported herein was supported by the National Science Foundation, Atmospheric Research Section, under Grant ATM 77-14821.

This report was prepared by:

SECURITY CLASSIFICATION OF THIS PAGE (When Data Entered)

REPORT DOCUMENTATION PAGE

READ INSTRUCTIONS BEFORE COMPLETING FORM

1. REPORT NUMBER: NPS 63-81-001	2. GOVT ACCESSION NO.
3. RECIPIENT'S CATALOG NUMBER	
4. TITLE (and Subtitle): Final Technical Report of NSF Grant ATM 7714821. "Dynamics of Tropical Waves and Monsoons"	5. TYPE OF REPORT & PERIOD COVERED: Final Report for Sept 1977 - Oct 1980
	6. PERFORMING ORG. REPORT NUMBER
7. AUTHOR(s): C.-P. Chang and R. T. Williams	8. CONTRACT OR GRANT NUMBER(s): NSF ATM 77-14821
9. PERFORMING ORGANIZATION NAME AND ADDRESS: Naval Postgraduate School Monterey, California 93940	10. PROGRAM ELEMENT, PROJECT, TASK AREA & WORK UNIT NUMBERS
11. CONTROLLING OFFICE NAME AND ADDRESS: National Science Foundation Washington, D.C. 20550	12. REPORT DATE: April 1981
	13. NUMBER OF PAGES: 169
14. MONITORING AGENCY NAME & ADDRESS (if different from Controlling Office)	15. SECURITY CLASS. (of this report): UNCLASSIFIED
	15a. DECLASSIFICATION/DOWNGRADING SCHEDULE

16. DISTRIBUTION STATEMENT (of this Report)

Approved for public release; distribution unlimited.

17. DISTRIBUTION STATEMENT (of the abstract entered in Block 20, if different from Report)

18. SUPPLEMENTARY NOTES

19. KEY WORDS (Continue on reverse side if necessary and identify by block number)

Tropical Meteorology
Monsoon
MONEX
Tropical Waves
Barotropic Instability

20. ABSTRACT (Continue on reverse side if necessary and identify by block number)

The Asian monsoons represent a substantial portion of the energy of the global atmospheric circulation. The objective of this research is to study the large scale motions of the monsoons, in terms of their structure, development, maintenance and the interrelationships between them. The research consisted of five parts:

DD FORM 1 JAN 73 1473 EDITION OF 1 NOV 65 IS OBSOLETE
S/N 0102-014-6601

UNCLASSIFIED
SECURITY CLASSIFICATION OF THIS PAGE (When Data Entered)

(1) Synoptic scale diagnostic studies of the winter monsoon - The main results suggest the importance of cold surge-forced low level convergence in the enhancement of organized convecti in synoptic disturbances.

(2) Planetary scale diagnostic studies of the winter monsoon Results suggest a coherent variation of the local Hadley and Walker circulations, and East and West Asia jet streak during cold surges.

(3) Linear theoretical studies of waves in a variable mean fl - Results show the importance of barotropical growth of linear waves downstream from the most unstable part of the summer monsoon easterly jet.

(4) East Asia monsoon trough (Mei-Yu) during early summer - Structure and dynamic differences are diagnosed between different segments (more tropical vs. more mid-latitude) of this subtropical system.

(5) Simple modeling studies of monsoon variations - Domain-averaged, atmosphere-ocean coupled model simulation demonstrat the strong interplay that influences the active and break cycles of the monsoons.

TABLE OF CONTENTS

1. DESCRIPTION OF RESEARCH AND RESULTS

The objective of this research is to study the large scale motions of the monsoons and associated tropical wave disturbances, in terms of their structure, development, maintenance and the interrelationship between them. The research consisted of the following five parts:

a) Synoptic scale diagnostic studies of the winter monsoon

As a pre-MONEX pilot study, we carried out a detailed synopt analysis of the surface/850 mb level for the period 1-13 December 1974 over the Winter MONEX (W-MONEX) area using radiosonde, pibal, surface ship and satellite data. The purpose was to examine the possible interactions between the northeasterly cold surges off the Asian continent and the convective disturbances in the near-equatorial region. During this period two surges occurred in the area which appear to interact with two near-equatorial disturbances in the South China Sea. Based on this case study the following preliminary conclusions were made:

1) Following a cold surge, freshening of low-level northeasterlies spreads rapidly (in 12-24 h) from the Taiwan and Luzon Straits southwestward to near 16^{o} N, and then down to the near equatorial latitudes with almost no time lag, provided there is no disturbance in the South China Sea to prevent it from doing so.

2) The southward incursion of cold temperatures is concentrated in the western part of the South China Sea along the Vietnam coast, and progresses at a slower pace compared to that of the widely-spread freshening of the winds over the entire South China Sea. In the eastern and central parts of the South China Sea

the fast-streaming northeasterlies are modified rapidly by air-sea interaction. The longitudinal difference in air-sea interaction is probably due to the difference in sea-surface temperature.

3) As a result of 1) and 2), the near-equatorial latitudes of the South China Sea will experience widely-spread increased northeasterly monsoon winds prior to the cold temperatures.

4) Pre-existing low-latitude synoptic-scale cyclones, whether semi-stationary equatorial trough disturbances which developed over the northern coast of Borneo, or westward propagating waves from the western Pacific, may respond to the surges in the following way:

i. While the surface temperature is still warm, the organized deep cumulus convection intensifies in relation to the freshening of low-level northeasterlies probably because of enhanced low-level convergence. It dissipates in relation to the slackening of northeasterlies.

ii. After the intensification due to the freshened monsoon flow, the convection weakens in relation to the later-arrived surface cold air incursion in the western South China Sea, which is probably due to the stabilizing effect.

These results were reported in Chang, Erickson and Lau (1979).

During 1978-79 we participated in the field phase of W-MONEX with Professor Chang and Dr. Webster serving as members of a U.S. scientific team at the International MONEX Operation

Centre in Kuala Lumpur, Malaysia. We have collected a set of Phase I W-MONEX data including radiosonde, pibal, ship, aircraft and satellite data. These data are being used to produce a subjective analysis for the surface/gradient, 850 mb, 700 mb and 500 mb levels. The analysis is in cooperation with scientists at Malaysian Meteorological Service, and National Taiwan University, and will be published in March 1981 (Chang et al, 1981). Our analysis is concentrated in a region (95^{o} E - 140^{o} E, 5^{o} S - 25^{o} N) where near-equatorial synoptic to subsynoptic scale disturbances were active during Phase I of W-MONEX. The preliminary results showing the life cycles of some of these disturbances at various pressure levels were reported at the 6th Planning Meeting for MONEX.

b) Planetary scale diagnostic studies of the winter monsoon

As a companion study to a), we used the 200 mb objective analyses of wind and temperature produced by the Fleet Numerical Weather Central to study the planetary scale circulations during December 1974. The emphasis was on the possible interrelationships between the fluctuations of several major components of the planetary scale winter monsoon, especially those in relation to the cold surges and synoptic scale convective disturbances in the equatorial South China Sea. During the one month period a total of four surges occurred in the South China Sea (the first two were included in the synoptic study). The kinematic and thermal structures suggest a picture of coherent variations of several circulation features which may be described by the following sequence of events:

1) Prior to the occurrence of a cold surge on the South China coast, the cooling due to cold advection over northern China increases which strengthens the East Asia local Hadley circulation through increased sinking motion.

2) Almost simultaneous with the strengthening of the heat sink in northern China, the East Asia jet stream centered near Japan intensifies as a result of the upstream acceleration which is due to increased upper level ageostrophic flow associated with the enhanced local Hadley circulation.

3) The variation of the West Asia jet stream centered over Afghanistan and Pakistan is out of phase with that of East Asia jet stream, with the minimum of the latter lagging slightly the maximum of the former. The apparent inverse relationship may be due to the Coriolis deceleration by the upper-level equatorward meridional wind which is found upstream of the jet prior to and during the surge. This meridional wind also implies the possible occurrence of a reversed local Hadley-type circulation.

4) The rapid eastward movement of an upper level trough which deepened over northern Japan appears to be a precursor to the outbreak of northeasterly cold air along the South China coast.

5) Immediately after a cold surge, the convection associated with pre-existing synoptic-scale disturbances in the equatorial South China Sea will intensity thereby sustaining or increasing the already enhanced local Hadley circulation.

6) However, the strengthening of the local Hadley cell does not continue too long (beyond one day) after the surge, as the upper tropospheric outflow from the South China Sea region also

accelerates along the equator toward both the central Pacific and the east coast of Africa thereby strengthening the east and west Walker cells. This indicates that while the near-equatorial convection is affected by fluctuations in the cold air outbreak from the northern midlatitudes, their influence does not necessarily feedback significantly into the northern extratropical circulations. Thus the cold surge appears to be a largely northern mid-latitude controlled phenomenon which extends its effects deeply into a wide equatorial belt.

These results were reported in Chang and Lau (1980) and are viewed as preliminary because of the short data period. They will be re-examined in the renewed project which will study the W-MONEX period as well as a larger data base of several winter seasons.

c) Theoretical studies of waves in a variable mean flow

The purpose of this part is to examine the dynamic behavior of the basic monsoon flows which are characterized by zonal asymmetries as well as time variations. The stability properties of parallel flows have been studied thoroughly before, but very little is known regarding the effects of the spatial and temporal variations of the monsoon flow on synoptic and shorter scale motions. In consideration of this, we adopted the approach of using simple numerical models to isolate the various effects of the variable mean flow. The first step was to experiment with a linear model in which the barotropic stability properties of a steady easterly Bickley jet with "slow" east-west variation were examined. The Bickley jet, which resembled the upper tropospheric

easterly jet over South Asia during the summer monsoon, was maintained by specified forcing terms. The results of this study, which were reported in Tupaz, Williams and Chang (1978), indicate that in several aspects the structure and growth rate of the waves propagating in the mean flow are grossly similar to that expected from the parallel flow theory of barotropic instability. However, in the unstable region the resultant structure of the waves causes a spatial growth rate greater than that predicted by the local growth rates computed within a parallel flow model. In the stable region, the structure leads to a strong dynamic damping. When a uniform advective velocity is added to a variable mean flow, the difference between the magnitude of the growth rate of the computed waves and that implied by the parallel flow theory is somewhat reduced. However, in this case, a stronger zonal asymmetry in the spatial growth rate curve with respect to the jet maximum occurs as a result of slower adjustment of the wave structure to the local stability conditions.

The foregoing linear model results were obtained using open inflow, outflow boundary conditions. When a cyclic east-west boundary condition was used, the wave behavior was more irregular than the open boundary case. However, when the wave structure was time averaged, the results compared very well with those obtained in the open-boundary case. The cyclic boundary experiments were reported in an M.S. thesis by Nagle (1978).

At the time of writing this report, we have developed a nonlinear model to study the barotropic dynamics of interacting short waves and externally forced long waves (variable mean flow).

A forcing function is included in the barotropic vorticity equation which makes the zonally varying basic flow a steady state solution of the equation. The basic flow, which is similar to the one treated by Tupaz, Williams and Chang (1978), contains a jet that is locally unstable in the middle of the region. When waves are introduced into this forced flow, they will grow and modify the mean flow until a statistically steady state is achieved. The difference between the new mean flow and the original one is a result of nonlinear interaction with the short waves. Additionally, the structure of the short waves can be compared with structures obtained from linearized models. The preliminary results will be reported in Williams, Chang and Lim (1981).

d) East Asia monsoon trough during early summer

During the pre- and early summer period of mid-May to mid-June, a rainy phenomenon dominates the weather over the coastal regions of East Asia including Japan and southeastern China. This period represents the local rainfall maximum each year except for the maximum in the summer typhoon season which usually begins after mid-July. The rainfall during this period is called "Mei-Yu" (plum rain) in China and "Baiu" in Japan. It may be continuous or intermittent for several days to a few weeks and includes frequent rainshowers and thunderstorms. Synoptically this rainfall is associated with the repeated occurrence of a front which develops in the mid-latitudes and slowly moves southeastward to establish its quasi-stationary position extending from southern Japan to southern China. The front position coincides with the early summer monsoon trough in East Asia and its existence may be viewed as a

manifestation of the trough. The beginning of the rain season also signifies the onset of the northern summer monsoon in this part of the world.

In order to improve our understanding of the Mei-Yu trough, we decided to study it with both an observational approach and numerical modeling. An observational study (Chen and Chang, 1980) for the period of 10-15 June 1975 was carried out for the purpose of determining the structure and vorticity budget of the trough. Analyzed grid-point data based on the dense upper-air station network over southeastern China and Japan are used to construct the cross-sectional structure of the trough along three sections. The trough is manifested at the 850 mb by a quasi-stationary front which moves slowly southward in the western section near the southern China coast, remains nearly stagnant in the central section over the East China Sea between Taiwan and Japan, and fluctuates back and forth in the northwest-southeast direction within a narrow zone over southern Japan. The period of study is separated into two stages, each with six 12-hourly time intervals, which represent the mature and decay stages of the trough. Within each stage all data in the three sections are time-composited with respect to the trough axis. The main results are as follows:

1) The central and eastern sections of the Mei-Yu trough have a structure resembling a typical mid-latitude baroclinic front with a strong north and northwestward tilt in the vertical towards a middle tropospheric cold core. The horizontal temperature gradient across the trough is strong throughout the

troposphere. Significant cumulus convection prevails immediately south or southeast of the 850 mb trough and apparently contributes substantially to the heating of the middle troposphere which, in addition to the normal mid-latitude baroclinic processes, is important in maintaining a thermally direct secondary circulation normal to the trough. However, the low-level vorticity and convergence distribution suggests that CISK plays a smaller role compared to the differential vorticity advection.

2) The western section, which is in the lower latitudes and subject to a stronger influence of the moist southwest monsoon flow, exhibits several features that are less common in mid-latitude fronts while more typical in tropical systems such as an ITCZ. The trough is confined to a shallow layer in the lower troposphere with almost no vertical tilt, and is capped by a middle tropospheric warm core resembling an equivalent barotropic system. The horizontal temperature gradient is much weaker than the eastern section but during the mature stage the horizontal wind shear across the trough is stronger. It is also associated with intense cumulus convection and a thermally direct secondary circulation, but both appear to be induced by a CISK process.

3) The generation of cyclonic vorticity by horizontal convergence in both eastern and western sections is offset by strong damping processes. In the eastern section the damping appears to be due to vertical cumulus scale transports which tend to balance the forcing by cumulus heating. In the western section the Mei-Yu trough is situated over the mountainous region of southern China coast in the mature stage and the friction at 850 mb due to topography provides the main damping mechanism.

In the decaying stage the low-level trough moves southward offshore and weakens as a result of the decreasing baroclinic field, indicating that CISK cannot maintain the trough without the forcing by the large-scale frontogenesis processes.

From the foregoing results the Mei-Yu trough appears to be a mixed mid-latitude-tropical system. This trough is established when East Asia polar fronts repeatedly move southward into southeastern China and southern Japan during the pre- and early summer. The strong modification of the western segment of the front is in distinct contrast to the eastern segment, although cumulus convection and intense precipitation are important in the entire trough region.

Parallel to the observational study, which will be continued to include more cases, we plan to carry out numerical modeling of the Mei-Yu trough. We have investigated the possibility of using a two-dimensional frontal model with the incorporation of boundary layer and cumulus parameterizations to study the mean structure of the trough at various segments (Williams, Chou, Cornelius and Glevy, 1981). This frontal model is a modified version of the numerical model that was developed by Williams (1974). The frontogenesis is forced by a nondivergent basic wind field that contains stretching deformation, and has an Ekman layer structure in the boundary layer. Vertical and horizontal diffusions of heat and momentum are represented. The new model predicts specific humidity and includes condensation heating and moist convective adjustment. The study shows that condensation heating has little effect on the surface front, but it is

important at upper levels. It is reasonable to expect that this model can be used to simulate changes in the structure of the East Asia Mei-Yu trough as a function of location, moisture supply and other parameters.

e) Simple modeling studies for monsoon variations

A number of experiments aimed at identifying basic processes in the variations of monsoon systems using a simple atmosphere-ocean coupled model (Webster and Lau, 1977) have been undertaken. In particular the role of hydrology in maintaining the mean structure of a monsoon system has been studied. It was found that the mean seasonal structure is determined by an interplay between the basic drive of the monsoon system (differential heating between the land and ocean regions) and the hydrologic cycle. Furthermore it was found that subseasonal variations depended strongly upon a similar interplay. The study of the transient nature of the model monsoon has allowed some insight into the "break" and "active" cycle on the monsoon system. These results were reported in Webster and Chou (1980), Webster and Stephens Another study, based on a different version of the model, aiming at the role of the interactions between the ocean and atmosphere in affecting the large-scale tropical circulation was reported by Lau (1978).

2. COOPERATION WITH SCIENTISTS OF NATIONAL TAIWAN UNIVERSITY UNDER THE U.S.-TAIWAN COOPERATIVE SCIENCE PROGRAM

Besides the international cooperative efforts with Mr. B. K. Cheang, Malaysian Meteorological Service, Dr. H. Lim, Meteorological Service Singapore and Dr. P. J. Webster, CSIRO, Australia mentioned

elsewhere in this report, the principal investigator was supported by the U.S.-Taiwan Cooperative Science Program under NSF Grant INT-7814557 which provided supplemental travel funds for the principal investigator to travel to Taiwan. In these trips to Taiwan we have accomplished the following:

1) In cooperation with Professors C. Y. Tsay and G. T. Chen of the National Taiwan University in setting up enhanced MONEX observational stations at Dongshadao (116.8° E, 20.7° N) and Nanshadao (114.8° E, 10.3° N). The former is a radiosonde station and the latter a pibal station. Both stations were operated by Chinese military services from Taiwan. During W-MONEX operations at both stations were enhanced such that special observations were taken to insure a minimum of twice-daily observations and four times daily during all intensive periods. Data collected from these enhanced observations are invaluable for many W-MONEX studies.

2) Cooperative research with Professors Tsay and Chen in the analysis of W-MONEX data which resulted in the streamline/isotach atlas being published by Chang et al (1981) as mentioned in Section 1 part a. Plans are now being made to digitize this data set in order to carry out a study of the synoptic disturbances in the South China Sea.

3) Cooperative research with Professor Chen in the study of Mei Yu with the results published by Chen and Chang (1980), as mentioned in Section 1 part d.

3. LIST OF PUBLICATIONS

Chang, C.-P., J. E. Erickson and K. M. Lau, 1979: Northeasterly cold surges and near-equatorial disturbances over the Winter MONEX area during December 1974. Part I: Synoptic aspects. Mon. Wea. Rev., 107, 812-829.

Chang, C.-P., D. M. Delaney and E. Maas, 1979: Possible influences of sea-surface temperatures on the easterly waves over the equatorial Pacific. Papers Meteor. Res., 2, 1-13.

Chang, C.-P. and K. M. Lau, 1980: Northeasterly cold surges and near-equatorial disturbances over the Winter MONEX area during December 1974. Part II: Planetary scale aspects. Mon. Wea. Rev., 108, 298-312.

Chang, C.-P., B. K. Cheang, G. T. Chen and C. Y. Tsay, et al, 1981: Regional synoptic analysis during Phase I of Winter MONEX. Naval Postgraduate School Tech. Rept., 285 pp (in press).

Chen, G. T. and C.-P. Chang, 1980: The structure and vorticity budget of early summer monsoon trough (Mei-Yu) over southeastern China and Japan. Mon. Wea. Rev., 108, 942-953.

Lau, K. M., 1979: A numerical study of tropical large-scale air-sea interaction. J. Atmos. Sci., 36, 1467-1489.

Tupaz, J. B., R. T. Williams and C.-P. Chang, 1978: A numerical study of baroclinic instability in a zonally varying easterly jet. J. Atmos. Sci., 35, 1265-1280.

Webster, P. J. and L. C. Chou, 1980: Seasonal structure of a simple monsoon system. J. Atmos. Sci., 37, 354-382.

Webster, P. J. and G. Stephens, 1980: Low-frequency transitions of a simple monsoon system. J. Atmos. Sci., 37, 1521-1541.

Williams, R. T., L. C. Chou, C. Cornelius and D. Glevy, 1980: Effects of condensation and surface motion on the structure of steady-state fronts. J. Atmos. Sci., 38, (in press).

Williams, R. T., C.-P. Chang and H. Lim, 1980: Non-linear barotropic interactions between synoptic scale waves and a zonally varying mean flow (in preparation).

4. THESES

Maas, E., Jr.: Composite analysis of easterly waves in the tropical Pacific during two contrasting periods of sea-surface temperature anomalies, M.S., 1977.

Delaney, D. M.: A composite satellite study of the 1972-73 easterly waves in the tropical western Pacific, M.S., 1977.

Nagle, B. M.: A numerical study of barotropic instability of a zonally varying jet with cyclic boundary conditions. M.S., 1978.

Erickson, J. E.: A synoptic study of the northeast monsoon over the South China Sea and its vicinity during December 1974. M.S., 1979.

5. SCIENTIFIC COLLABORATORS

G. T. Chen, Professor, National Taiwan University

B. K. Cheang, Malaysian Meteorological Service

L. C. Chou, Graduate Research Associate

D. M. Delaney, Graduate Student

J. E. Erickson, Graduate Student

H. Lim, Visiting Scientist from Meteorological Service Singapore

C. Y. Tsay, Professor, National Taiwan University

P. J. Webster, Visiting Scientist from CSIRO

6. COMMENTS

This research is being continued under NSF Grant ATM 80-13153.

Reprinted from MONTHLY WEATHER REVIEW, Vol. 107, No. 7, July 1979
American Meteorological Society
Printed in U. S. A.

Northeasterly Cold Surges and Near-Equatorial Disturbances over the Winter MONEX Area during December 1974. Part I: Synoptic Aspects

C.-P. CHANG, J. E. ERICKSON AND K. M. LAU

Northeasterly Cold Surges and Near-Equatorial Disturbances over the Winter MONEX Area during December 1974. Part I: Synoptic Aspects

C.-P. CHANG, J. E. ERICKSON[1] AND K. M. LAU

Department of Meteorology, Naval Postgraduate School, Monterey, CA 93940

(Manuscript received 20 November 1978, in final form 7 February 1979)

ABSTRACT

This is a pre-Winter Monsoon Experiment (Winter MONEX) pilot study to examine the possible interactions between the northeasterly cold surges off the Asia continent and the convective disturbances in the near equatorial region. Based on surface and 850 mb wind and temperature analyses, satellite data, and synoptic weather charts of the Hong Kong Royal Observatory, a sequence of synoptic events associated with two cold air surges and near-equatorial disturbances over the Winter MONEX area of South China Sea and its vicinity during December 1974 is discussed. The results lead to the tentative conclusions that due to the varying degree of air–sea interactions between cold air originating from the southeastern China coast, Taiwan and Luzon Straits, and that originating from the South China coast, the near-equatorial latitudes of the South China Sea will experience a freshening of the low-level northeasterly monsoon winds prior to a decrease in surface temperature which, if it occurs, is confined to the Western portion of the South China Sea. This allows a near-equatorial disturbance (which may have originated from the semi-stationary near-equatorial trough over the coast of North Borneo or from a westward propagating wave in the western Pacific) to be intensified at an early state of the surge by enhanced low-level convergence and organized deep cumulus convection. Afterward it may be weakened by either the cold air incursion along the Vietnam coast or a slackening of the northeasterlies.

1. Introduction

The northern winter monsoon is one of the most energetic and convective systems of the atmosphere. During its development the major convective area of the planetary scale is shifted from the normal summer position near India to the vicinity of the equatorial "maritime continent" (Ramage, 1971) region of Malaysia, Indonesia and the South China Sea. Although the thermally direct overturning is basically similar to that of the summer monsoon (Krishnamurti *et al.*, 1973), the winter monsoon exhibits a distinct character which differs considerably from a simple mirror image of its summer counterpart. Its heavy convective precipitation and associated latent heat release in the near-equatorial latitudes is situated immediately south of the very cold Asia land mass, thus producing a strong north–south heating gradient which serves as not just the dominant heat source for the global circulation at this time of the year, but also as the largest heat source among all systems in the atmosphere.

In a simple sense the planetary-scale winter monsoon circulation may be viewed as the East Asian local Hadley cell. The lower tropospheric branch is represented by the equatorward northeasterly flow which is intermittently reinforced by the cold air surges from the Siberian High, and its ascending branch is associated with the strong convection in the vicinity of the maritime continent which normally is the location of the equatorial troughs. The intensity of this local Hadley cell makes it the single most important contributor to the zonally averaged meridional transports during winter. Somewhat similar to the alternating active and break conditions of the summer monsoon, the intense heat source of this circulation is also subject to considerable fluctuations which may be manifested by the variation in the intensity of the semi-stationary equatorial troughs in the maritime continent and/or the development and decay of propagating synoptic-scale disturbances in the South China Sea. Due to the poor data coverage, very little is known about the structure and characteristics of either the stationary troughs or the synoptic disturbances. However, there are some indications that some of the temporary intensifications of these near-equatorial convective systems are correlated with the sporadic cold surges off the China coast (Ramage, 1971; Cheang, 1977), although it is not clear how the cold surges, which are usually confined to the lowest

[1] Present affiliation: Detachment 1, Air Force Global Weather Central, Pentagon, Virginia 20330.

levels of the atmosphere, enhance the convection. Since the convective systems contribute substantially to the gigantic heat engine that drives the planetary-scale circulation during winter, the understanding of their behavior and possible interaction with the cold surges from the north becomes an important problem of tropical and monsoon meteorology. This is also one of the primary scientific objectives of the winter phase of the Monsoon Experiment (Winter MONEX which is to be implemented during the Global Weather Experiment of 1978–79. The purpose of the present work is to carry out a pre-MONEX pilot study of this problem using the existing surface, upper-air and satellite data during the first half of December 1974, in order to identify certain features and questions pertinent to the possible relationship between the cold surges and the near-equatorial convective systems. Results of this work may be useful as a guide for MONEX planning and post-MONEX studies. In this paper (Part I) we will present a detailed synoptic analysis of a sequence of cold surges and near-equatorial disturbances in the South China Sea based on surface, 850 mb and satellite data, the results of which suggest a plausible effect of the surges on the disturbances. In a subsequent paper (Chang and Lau, 1979, Part II) changes of the corresponding planetary-scale features, such as the Hadley and Walker circulations, in relation to the synoptic events will be discussed.

2. Data and analysis

The region of the synoptic study is centered in the South China Sea which is surrounded by the South China coast to the north, Taiwan to the northeast, Philippines to the east, Borneo to the south, Malaysia and Sumatra to the southwest and the Indochina Peninsula to the west. The data used are conventional and satellite.

a. Conventional data

These include all surface and upper air station data available from the National Climatic Center in Ashville, the Royal Observatory in Hong Kong (ROHK) and the National Taiwan University in Taipei. In addition, surface ship reports were provided by the Fleet Numerical Weather Central in Monterey. The ROHK also provided us their operational surface and upper air weather charts which are of excellent quality for the area north of approximate 20°N. South of 20°N, especially over the South China Sea, the data coverage was quite sparse. Considering all the available data we decided to carry out detailed streamline and isotach analyses for a combined "level" of 850 mb and surface only, because the surface coverage often was enhanced by the additional ship reports and the 850 mb level contained some semi-regular pibal winds. (Satellite nephanalysis was also used at this level whenever appropriate.) During the analysis process we attempted to make the resultant maps more representative of the 850 mb conditions rather than those of the surface, so they may be viewed as "gradient-level" analyses. In addition, the surface ship wind speeds were relied upon more heavily than the island station reports based on Riehl and Somervell's (1967) observation that the island reports in the South China Sea are often an underestimate compared to ship reports. This was also confirmed by Adler *et al.* (1970) who compared sustained winds at Xishadao (17°N, 112°E), Dongshadao (21°N, 116°E) (see Fig. 14) and ships in their vicinity, and found that the ship wind speeds average about 1.4 times the land station winds. Among the ship winds, those observed by ships heading into the wind were by and large more reliable than those heading downwind.

Surface temperature analyses also were performed although they were believed to be less reliable than the wind analyses, mainly due to the difficulty of removing the diurnal effects over land stations, and the variation in the quality of ship temperature reports. However, they may be useful in giving some indications of temperature tendencies in the South China Sea. Both the wind and temperature analyses were done at 6 h intervals and included ship reports within 3 h of the synoptic time.

Since pressure variations are usually small in the tropical regions, it is difficult to improve ROHK's analyses even with some additional data. We therefore relied on the ROHK weather charts for the surface pressure field. We also used the ROHK charts when upper level synoptic situations, most north of 20°N, were needed for discussion.

b. Satellite data

These include the Defense Meteorological Satellite Program (DMSP) high-resolution visible and infrared imageries, and the National Environmental Satellite Service tropical mercator mosaics composited from the NOAA-3 satellite data. The former proved to be very useful for nephanalyses and the latter were used mainly to identify broad-scale features. The once-daily NOAA mosaics were near 0800 GMT in the central longitudes of the South China Sea which corresponds to local afternoon. The DMSP visible data were available between local morning (0000 GMT) and afternoon, while the infrared data are usually available near local midnight (1700 GMT). Unless specifically mentioned as infrared, the satellite data used in the subsequent discussions were all visible.

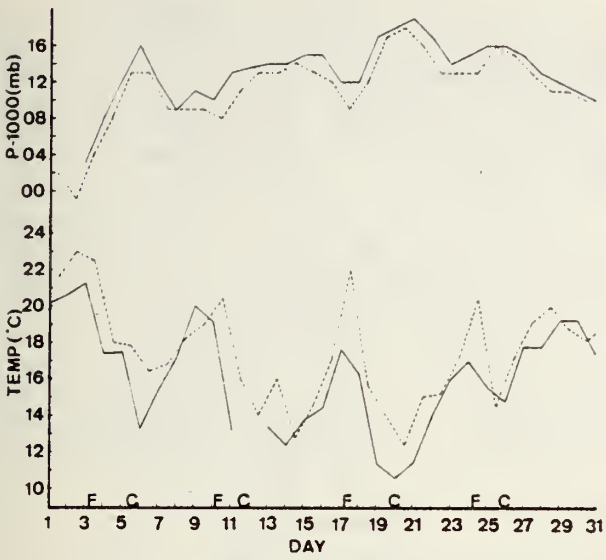

FIG. 1. Surface temperature and pressure as a function of time at Hong Kong. Solid lines connect 0000 GMT values and dashed lines 1200 GMT values. Dates of minimum temperature and of frontal passage are marked by C and F, respectively.

3. Sequence of synoptic events during 3–12 December 1974

The definition of a cold surge for local weather forecasters in Southeast Asia may be either a sharp drop in surface temperature, an occurrence of a minimum temperature substantially below the seasonal average, a sudden freshening of the northerly or northeasterly monsoon winds, or a combination of these events. If we define a cold surge as one in which the surface temperature in Hong Kong drops by at least 6°C within 24 or 48 h, then four surges during December 1974 may be identified in Fig. 1, which shows the 12 h Hong Kong surface temperature and pressure as a function of time. Each of the cold surges was preceded by a frontal passage which occurred 2–3 days before the minimum temperature was reached. The last two surges coincided with the passage of typhoons in the South China Sea, which was rather unusual for this time of the year. As a result of the typhoon passages, organized deep convection outside of the typhoons were suppressed by the widespread subsidence and it was difficult to assess the influence of the cold surges on the near-equatorial atmosphere. Thus we will focus only on the period 3–12 December 1974, which included the first two surge events, one between 4–6 December 1974 and the other between 10–11 December 1974. In the following we will summarize the highlights of the events during this period. For details of the map and satellite series the readers are referred to Chang *et al.* (1979).

Hereafter the designator hhZdd will be used to denote the time and date, where hh is the hour (GMT) and dd is the day in December 1974, e.g., 12Z06 means 1200 GMT 6 December 1974. The abbreviation SCS will be used to denote the South China Sea.

a. Conditions prior to the first cold surge

At 00Z03 the ROHK surface analysis (not shown) indicated high pressure dominating the China mainland, with a well-defined cold front extending from northern Taiwan west-southwestward to just north of Hong Kong and progressing slowly but steadily southward across South China. A large pressure difference of 12.9 mb between 30°N, 115°E and Hong Kong was observed, which exceeded the surge forecast criterion set by Riehl (1968) who proposed that if this difference is >10 mb a cold surge will begin in 48 h. (A pressure difference of 9.8 mb at 12Z02 provided an earlier indication of a possible impending surge.)

The surface cold front passed Hong Kong at 06Z03, which is shown in the 850 mb/surface analysis (Fig. 2). At this time the northeasterly monsoon in the northern SCS was broken by a ridge axis extending from an anticyclonic center east of the Luzon Strait southwestward through one just east of Hainan (hereafter referred to as A1) to another in southeastern Thailand. The near-equatorial trough was oriented west-southwest to east-northeast, connecting a major cyclonic center northwest of Borneo at 4°N, 112°E (hereafter referred to as C1) and another southeast of the Philippines near 70°N, 137°E (hereafter referred to as C2) which is outside of Fig. 2. Both of these cyclonic centers will be followed closely in this synoptic series as their development and evolution will be very important for our discussion.[2] The wind over the entire SCS was generally light (5–10 kt).

The cold frontal passage at Hong Kong showed up in the NOAA satellite mosaic of 08Z03 (Fig. 3) as the southern edge of the overcast which covered most of eastern and central China. Fine weather prevailed over most of the SCS except for an area of convective activity in the Sula Sea (5–10°N, 120°E) associated with a dissipating front which had pushed equatorward to about 8°N. Near the equatorial trough two groups of convective clouds were identified. Associated with C1 was a bandlike pattern which extended northeast–southwest along the northern edge of Borneo, but the convection was quite weak and scattered lacking any definite vortical structure. Associated with C2 was a much more intense and organized cloud cluster. These two groups of convective cloudiness will hereafter be referred to as CB1 and CB2, respectively. In addition, significant convective activities were located off the coast of Sumatra.

[2] Their tracks and intensity changes are summarized in Fig. 14, which may be used as an aid in following the discussion of the synoptic sequence.

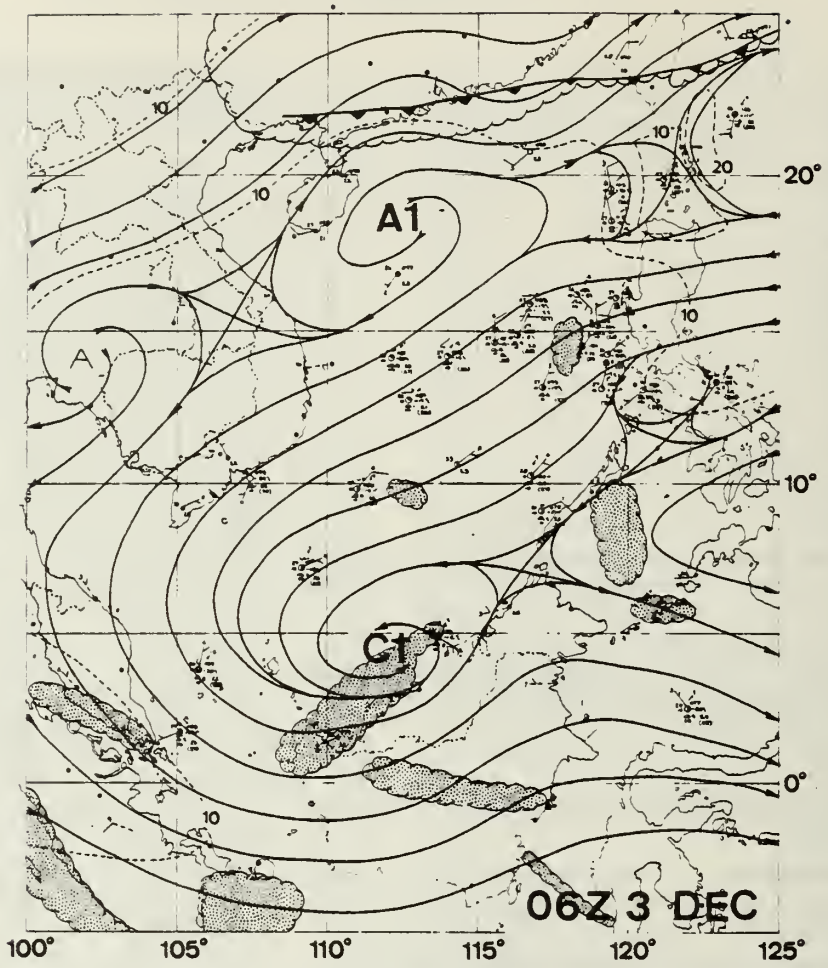

FIG. 2. The 850 mb/surface streamline and isotach analysis of 0600 GMT 3 December 1974. Solid wind vectors are surface reports and dashed vectors 850 mb reports. Nephanalysis of major cloudiness is also included.

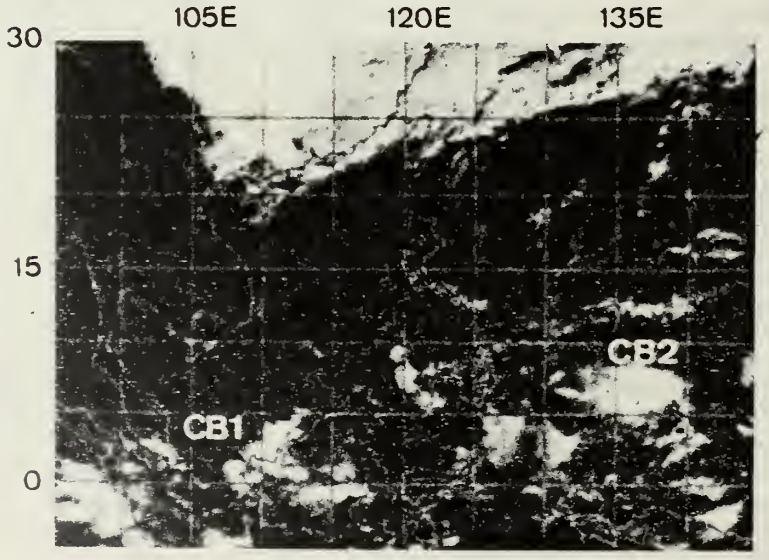

FIG. 3. NOAA-3 mosaic for 3 December 1974, centered near 0800 GMT.

22

Through 18Z03 (analyses not shown) the low-level winds over SCS remained light and a strong surface temperature gradient was observed immediately off the South China coast although the front had passed. Riehl and Somervell (1967) have pointed out that because of the supply of heat and moisture from the water plus heating by subsidence, a strong gradient of temperature and dew point remains stationary off the coast during northeast winds, but these gradients do not necessarily indicate the presence of any fronts. Thus the stationary temperature gradient cannot be taken as an indicator that the front has stalled. A DMSP infrared imagery of 17Z03 (not shown) still showed that only isolated deep convection existed in CB1, while CB2 remained strong.

b. The first cold surge

At 00Z04 a sharp increase in the 850 mb/surface wind (not shown) from 5–10 to 20–30 kt occurred in the cold air behind the front, which had pushed southward to the southern tip of Hainan. A cold tongue of air associated with the cold surge entered the northern part of the SCS and marked the first instance of cold air intrusion into the SCS (not shown). Equatorward of the front the wind speed had increased to ~15 kt. With the northward shift of the anticyclonic center A1, the entire SCS was dominated by the northeasterly monsoon flow. The satellite pictures (DMSP at 00Z04 and NOAA mosaic near 08Z04, not shown) all show that the overcast over southern China had extended over the water by ~150 km. The convection CB1 remained a widely isolated system of thunderstorm activities while CB2, maintaining its organized and somewhat vortical cluster appearance, had moved westward to the south of the Philippines. The westward speed of about 8° longitude per day indicated that CB2 (and C2) may be a synoptic-scale easterly wave in the western Pacific (Chang, 1970).

The ROHK uses an objective surge-forecasting technique based on the 500 mb analysis (Bell, personal communication). In this technique a surge can be expected to occur within 24–48 h when the 500 mb winds over Lake Baikal are northwesterly (usually indicating a trough passage in the westerlies) and the 500 mb temperature is below −30°C at 40°N in the longitude of Hong Kong. According to the 500 mb analysis of ROHK, these requirements were met at 12Z04. Although by our present definition the surge had already started, Fig. 1 shows that the sharp decrease in surface temperature was halted at 00Z04 for 36 h. The ROHK technique therefore apparently was useful in forecasting the continued sharp temperature drop which was resumed near 12Z05.

By 06Z05 the western edge of the front may be located near 13°N or so off the Vietnam coast. A possible indication of this was the rapidly southward progressing convective activities which had developed over the past 12 h and reached 12°N along the coastal lowlands (NOAA mosaic near 08Z05, not shown). To the local forecasters this is a well-known phenomenon associated with frontal surges in the SCS, and is apparently caused by the low-level onshore winds. Widely spread freshening of the north-easterlies, averaging ~20 kt, continued over the entire SCS.

During the next 18 h the anticyclonic center A1 moved northward inland and by 12Z05 the 850 mb wind (not shown) at Hong Kong had switched to an almost completely northerly direction. This was indicative of a cold surge occurring over southern China. Between 12Z05 and 00Z06 Hong Kong recorded the lowest surface temperature (Fig. 1). This event was reflected clearly by the NOAA mosaic near 08Z06 (Fig. 4), which showed a large area of clearing behind the bandlike stratus cloudiness indicating very intense and deep subsidence of the cold air. Ahead of the stratus deck the DMSP picture of 02Z06 (not shown) revealed extensive open cellular-type convective cells over the northern half of the SCS. This shallow convective cloudiness indicated the strong air-sea interaction due to the cold air advection near the surface, and the strong turbulent mixing and upward transports of the sensible and latent heat across the sea surface as the average surface wind increased to ~25 kt (not shown). An increase in the cloudiness banking along the Vietnam coast was also noticed and was likely an indication of the increased northeasterly onshore flow. The surface temperature analysis at 00Z06 (Fig. 5) revealed that the temperature gradient was still strong in the northern SCS, but the cold air tongue had reached the southern tip of the Vietnam coast.

Near the equatorial trough, the convective cloudiness between Vietnam and Borneo had coincided with C1 which had moved to the northwest of Borneo. This cloudiness was quite organized and a vortical pattern was evident from the satellite pictures (not shown) surrounding the center of C1. Compared to CB1 two days earlier, this new CB1 was much more intense. It also connected CB2 to the southeast of the Philippines (where it had stalled somewhat), and the extensive cloudiness northeast of the Malaysia Peninsula to form a well-defined Intertropical Convergence Zone (ITCZ) cloud band on the NOAA mosaic. The NOAA picture also showed scattered clouds along a northeast–southwest direction in the central SCS which provided a clue for the location of the southwestern segment of the front. Based on this, the cold front was analyzed down to 8°N in the 06Z06 850 mb/surface chart (Fig. 6). The very strong surface

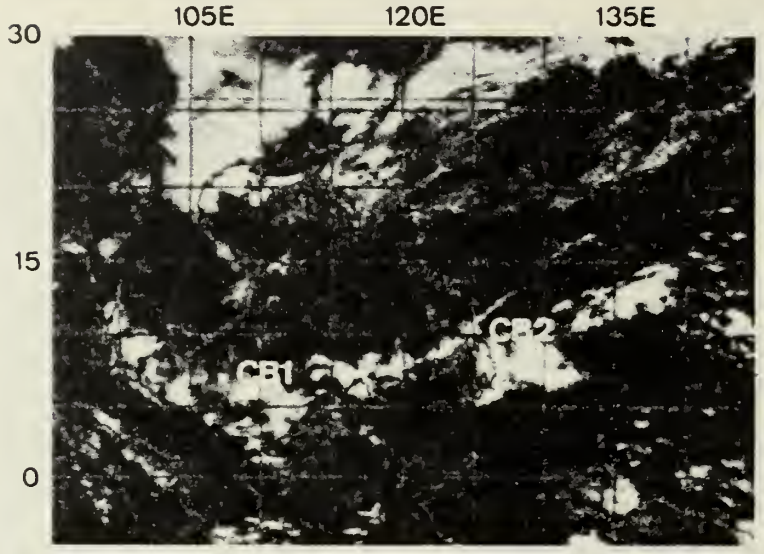

FIG. 4. NOAA-3 mosaic for 6 December 1974, centered near 0800 GMT.

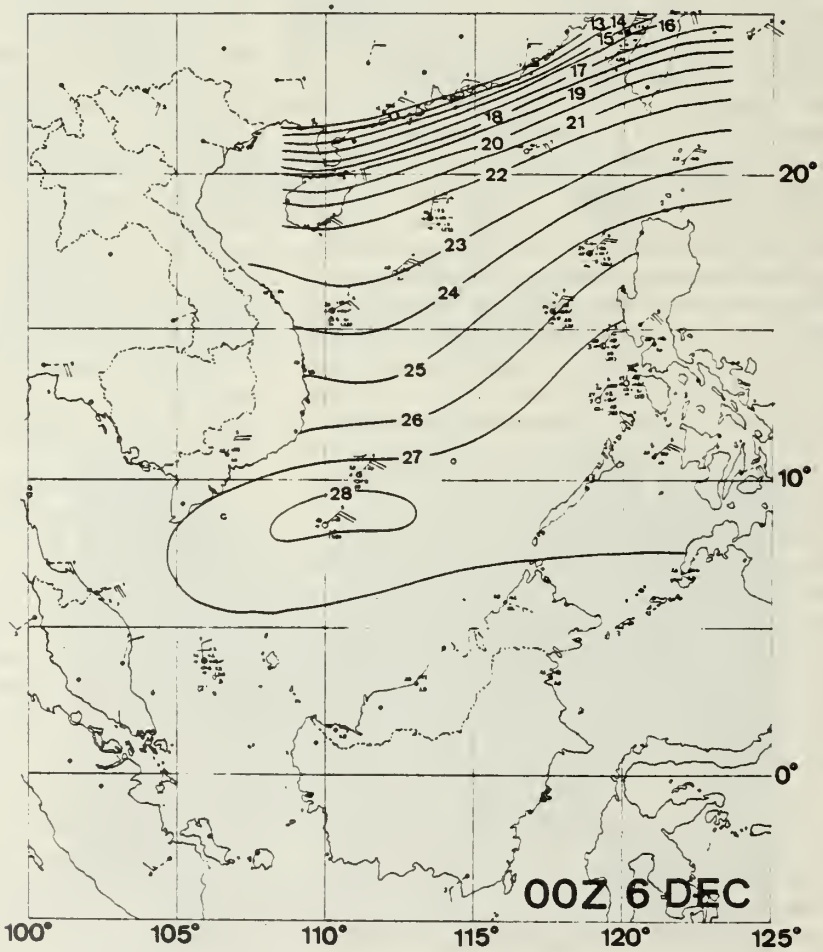

FIG. 5. Surface temperature analysis for 0000 GMT 6 December 1974.

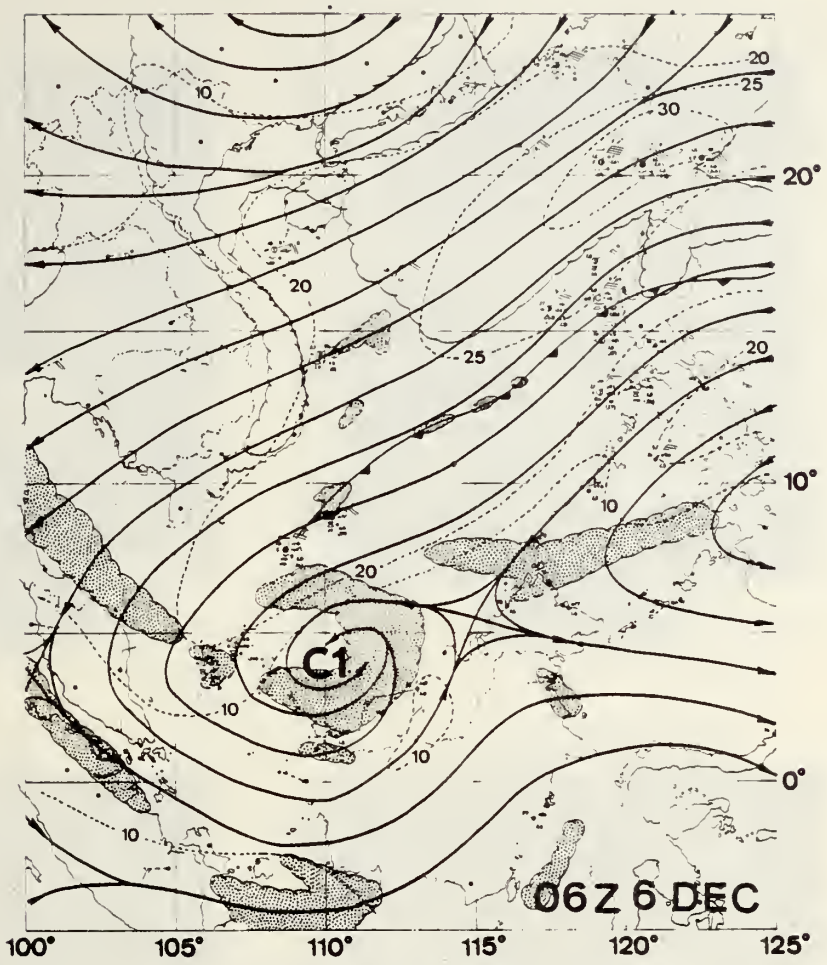

FIG. 6. As in Fig. 2 except for 0600 GMT 6 December 1974.

northeasterlies (35–40 kt) in the Taiwan and Luzon Straits also served as a strong indication that the cold front had pushed southward very rapidly.

By 00Z07, drastic changes in the equatorial trough region had occurred. While the surface northeasterlies slackened in the northern SCS, those in the south continued to pick up speed and converged into C1 which had become elongated in the east-west direction with a strong cyclonic shear. The most striking development, as indicated in the DMSP picture of 01Z07 (Fig. 7a), was the rapidly intensifying CB1 which became a highly organized, round-looking cloud cluster with cirrus streaming outward indicating strong outflow at the upper levels. A decrease of thunderstorm activities also was observed along the Vietnam coast, apparently due to the diminish of the northeasterly on-shore flow in the northwestern SCS.

c. After the first cold surge

The intense convection of CB1 was sustained through 18Z07, based on the DMSP infrared pictures (not shown). The strong low-level convergence also remained with C1, which had moved further northward away from the Borneo coast. This together with the anticyclonic and divergent flow at 200 and 300 mb over the same general area, as indicated by the ROHK upper level analyses (not shown), pointed to a warm core vortex maintained by deep convection. However, a turn of events occurred by 04Z08. At that time the DMSP picture (Fig. 7b) indicated that the convective activities in CB1 had been somewhat diffused, and was spread mainly in the northwestern quadrant of C1 according to the 850 mb/surface analysis of 06Z08 (not shown). Examination of the surface temperature analysis of 00Z08 (Fig. 8) showed that the cold air tongue had swept past the southern tip of Vietnam to the coast of Malaysia, suggesting a possible stabilization effect of CB1 due to the advent of cold air. Meanwhile, the major center of convection seemed to have shifted to CB2, which had moved by about 3° latitude northward during the past 12 h to a position immediately east of the Philippines.

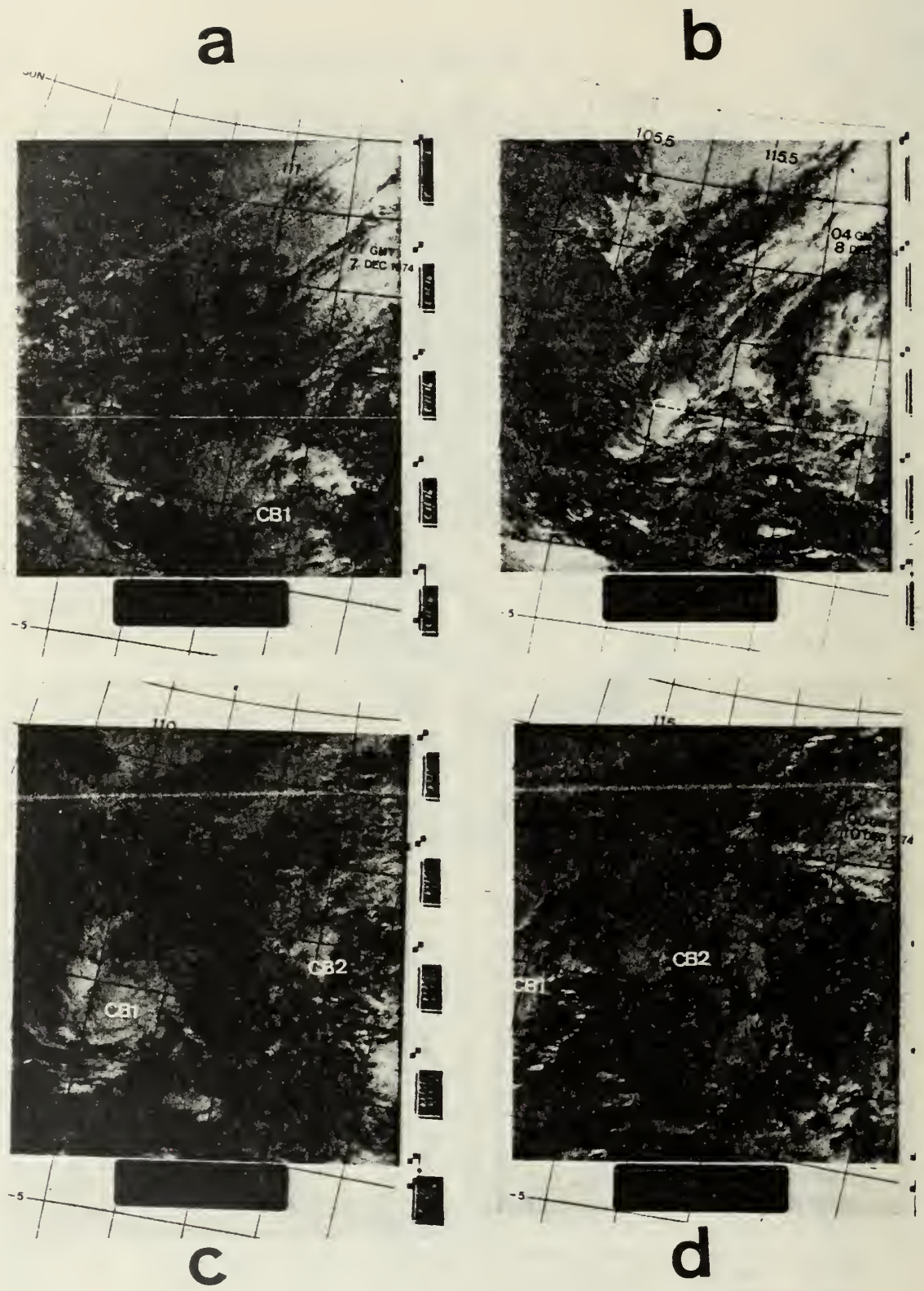

FIG. 7. DMSP visible picture for (a) 0100 GMT 7 December 1974, (b) 0400 GMT 8 December 1974, (c) 0400 GMT 9 December 1974, and (d) 0000 GMT 10 December 1974.

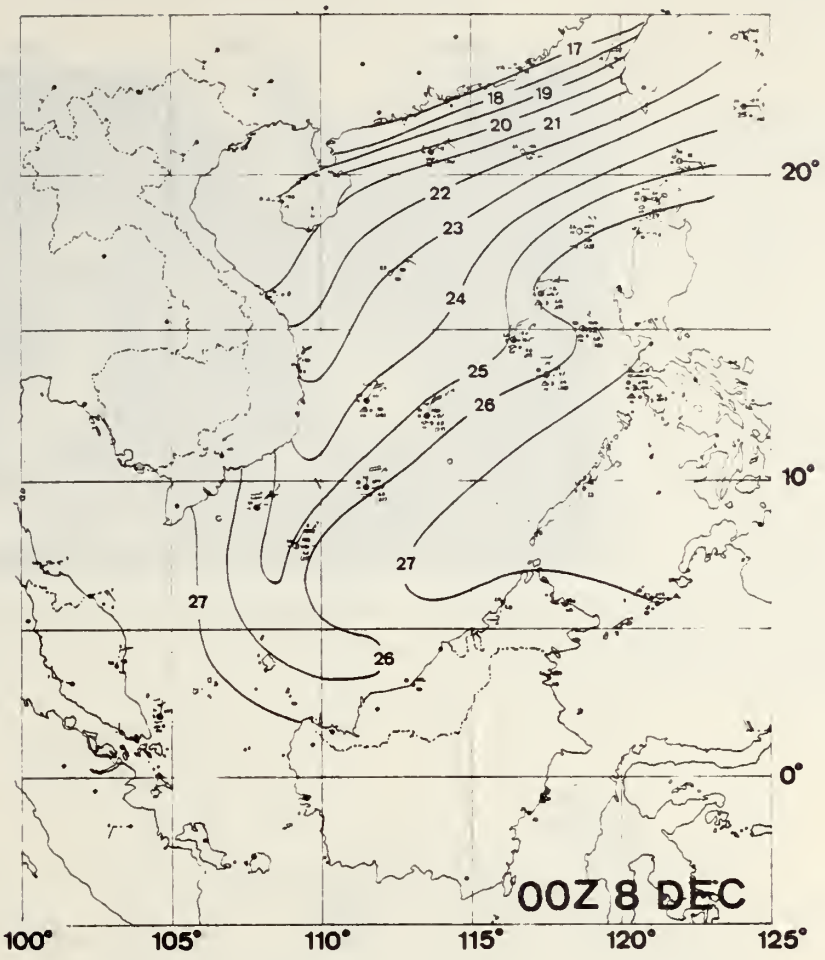

FIG. 8. Surface temperature analysis for 0000 GMT 8 December 1974.

This decrease in the intensity of CB1 since 00Z08, however, turned out to be short-lived and the convection began to reintensify again near 17Z08, when the DMSP infrared picture (not shown) revealed that CB1 had resumed its intensity of 24 h earlier. The ROHK upper level analyses at 00Z09 (not shown) indicated that the cyclonic circulation of C1 could be determined up to 500 mb. At the same time, the 00Z09 surface temperature analysis (not shown) indicated that the cold air in SCS had receded except for a narrow region immediately adjacent to the Vietnam coast line.

d. Conditions prior to the second cold surge

Throughout the period of intensification, temporary weakening and re-intensification of CB1, the low-level northeasterly monsoon flow remained strong (~20 kt) in the central SCS. This situation continued as CB1 intensified. The 04Z09 DMSP picture (Fig. 7c) showed that CB1 had become a semi-symmetric, highly vortical cloud cluster with convective cloud bands spiraling around the center mass, in sharp contrast to its appearance 24 h earlier (Fig. 7b. While CB1 was intensifying, CB2 weakened considerably as it hit the central Philippine islands. the NOAA mosaic near 08Z09 (Fig. 9) clearly depicted this "out-of-phase" change of CB1 and CB2, and the dominance of the former over the entire SCS. The intensification of C1 could also be seen from the 850 mb/surface analysis at 12Z09 (Fig. 10), where a surface wind of 35 kt was reported for the first time south of C1 on the northern coast of Borneo.

In Fig. 10 a cold front had moved into the South China coastal region from the north. The 00Z10 DMSP picture (Fig. 7d) showed the strong convection of CB1 which had begun to drift slowly westward, and the first appearance of a clearly defined low-level vortex associated with C1. The vortex was defined by thin cumuliform lines which spiral cyclonically into a center at 7.5°N, 111.5°E. Maximum convective activity was confined to the northern and northwestern quadrants where low-level convergence was concentrated. Strong convective activity also began to develop in CB2,

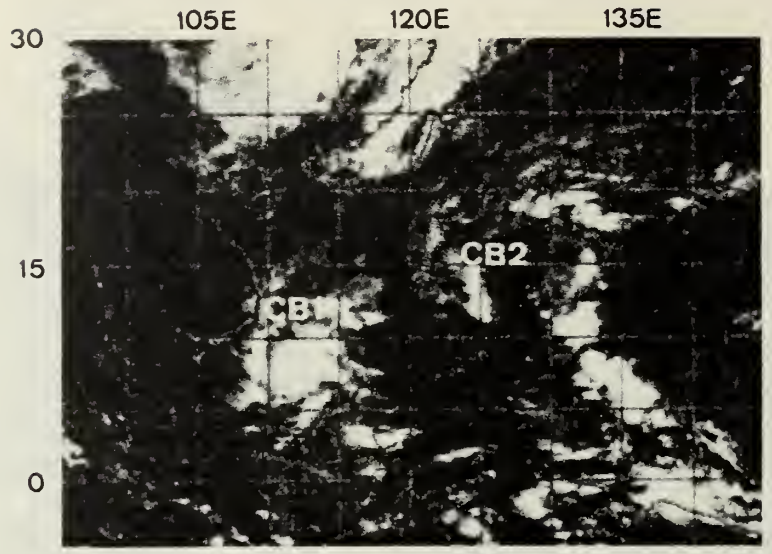

FIG. 9. NOAA-3 mosaic for 9 December 1974, centered near 0800 GMT.

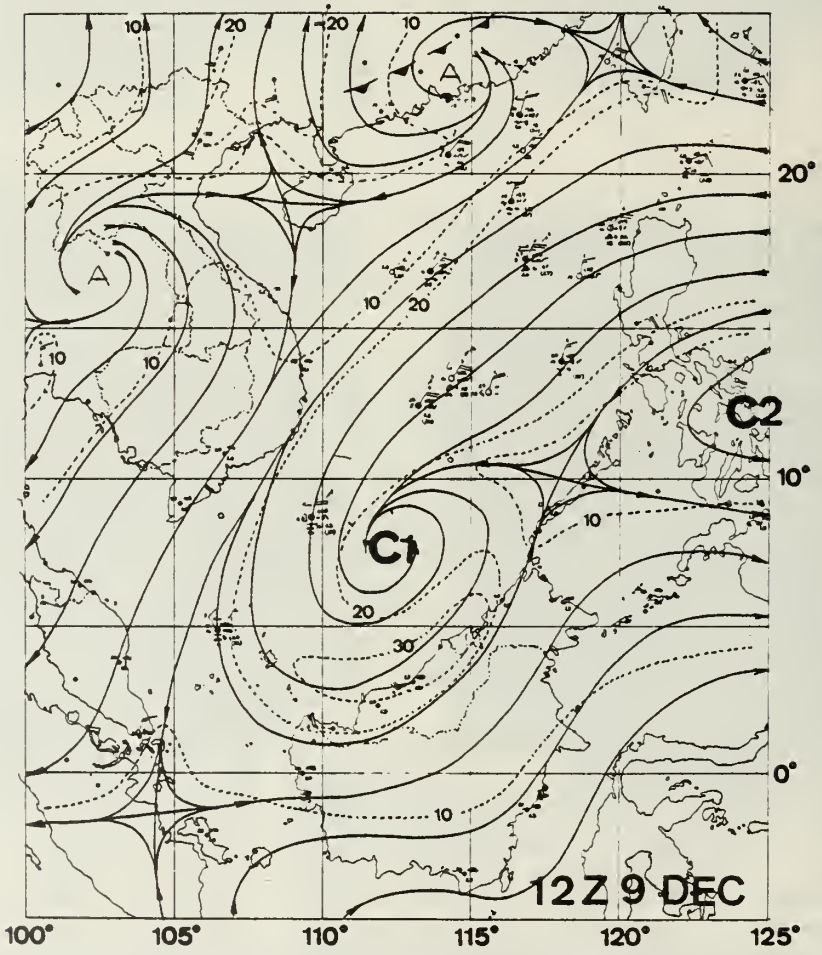

FIG. 10. As in Fig. 2 except for 1200 GMT 8 December 1974. No satellite data available for nephanalysis.

which had migrated with C2 westward into the eastern SCS. Meanwhile, a third cyclonic circulation center (C3) appeared northeast of the Philippines near 18°N, 125°E, (Fig. 11), causing the trough line to orient northeast-southwest parallel to the ridge line extending from the Gulf of Tonkin to Thailand. Between the ridge and trough lines the strong pressure gradient (~7.5 mb between Hong Kong and Saigon based on ROHK surface analysis) apparently caused an increase of low-level northeasterlies in the SCS to 25 kt from the Taiwan Strait to the northern quadrant of C1.

e. The second cold surge

The ROHK objective surge forecast criterion mentioned earlier was satisfied again at 00Z09. Approximately 30–36 h later, the cold front passed Hong Kong between 06Z10 and 12Z10. Following the frontal passage Hong Kong registered a temperature drop of 7°C in the next 12 h (Fig. 1) and a shift in wind direction from northwesterly to northeasterly. Almost simultaneously the ≥25 kt surface wind regime penetrated into the southern part of SCS south of 10°N (Fig. 11 shows the low-level condition at 12Z10). A point worth noting here is that, while C1 remained quasi-stationary, C2 had resumed its rapid westward movement, as it had moved ~4° longitude between 00Z10 and 12Z10. The cyclonic center C3 also had a similar movement.

At 00Z11 the surface cold front had swept into the northern SCS where it met C3 and the northwestern periphery of C2 as both cyclonic centers moved rapidly westward. Strong northeasterly winds in excess of 30 kt were reported west of the northeast-southwest trough line which connected C1, C2 and C3. In this area surface ship reports also indicated a large area of increased cloudiness and rainshowers with ceilings as low as 200 m. By this time it was clear that both C2 and C3 had moved out of the near-equatorial trough which appeared to reestablish itself between 5–10°N with the forma-

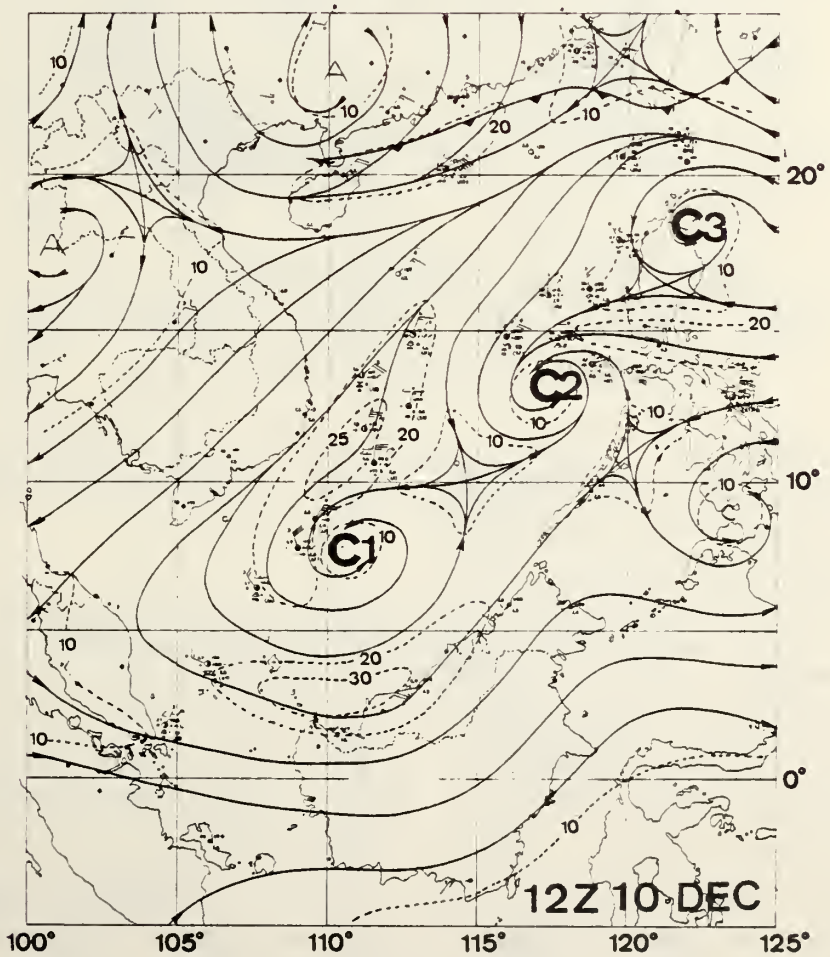

FIG. 11. As in Fig. 2 except for 1200 GMT 10 December 1974. No satellite data available for nephanalysis.

tion of another cyclonic center to the west of Mindanao in the Sula Sea. Six hours later C3 had disappeared from the 850 mb/surface analysis (not shown).

Between 02Z11 and 08Z11 a wide cloud band associated with the cold front ahead of the clearing zone was found on the DMSP and NOAA pictures (not shown) along the South China coast. This cloud band extended southwestward over the northern SCS and merged with the convection CB2, which had continued to intensity. A substantial weakening of CB1 was noted with the maximum cloudiness continuing to be confined to the northern and western quadrants of C1. The 00Z11 surface temperature analysis (Fig. 12) shows cooler monsoon air was being funneled rapidly southward between the Vietnam coastline and C2 into the northwestern vicinity of C1. Thus the influx of cold air from the north again appeared to have influenced the rapid decay of CB1. Along the northern Vietnam coast cloudiness due to strong onshore flow had reappeared since the frontal surge over Hong Kong near 06Z10.

The weakening of CB1 progressed almost as dramatically as its reintensification 3–4 days earlier. By 01Z10 the DMSP picture (not shown) revealed that CB1 had lost most of its organization and shrunk to a narrow northeast–southwest cloud band between Vietnam and Borneo. The strong contrast to this was the development of CB2 which had intensified to become the dominant convective system in the SCS. As CB2 touched the Vietnam coast it also appeared to split into an "inverted V" to the northeast and a well-organized vortical cloud cluster to the southwest (NOAA mosaic at 08Z12, not shown). About one day later, the DMSP picture at 01Z13 (not shown) provided the evidence that the separation of CB2 had been completed some time ago.

The satellite data proved invaluable in analyzing the separation of C2 on the 850 mb/surface charts at 00Z12 (Fig. 13) which showed clearly that the strong northeasterly monsoon wind was almost absent in the central SCS due to the westward traverse of C2 across the sea. This will be an important point in the discussion of the relation-

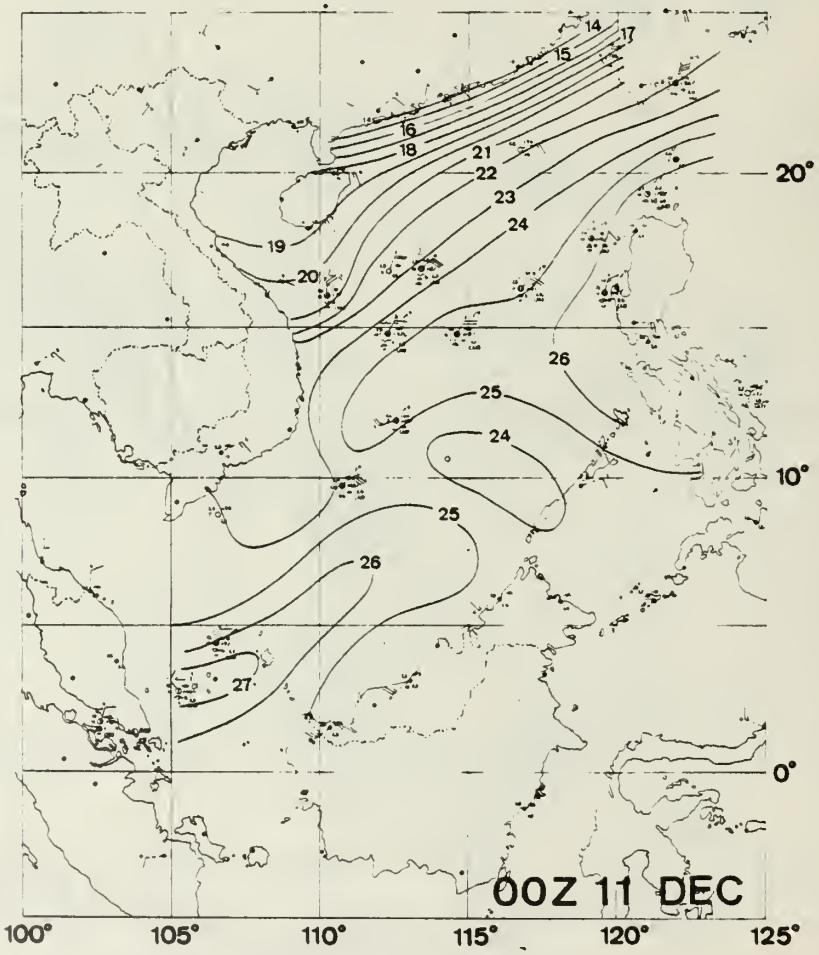

FIG. 12. Surface temperature analysis for 0000 GMT 11 December 1974.

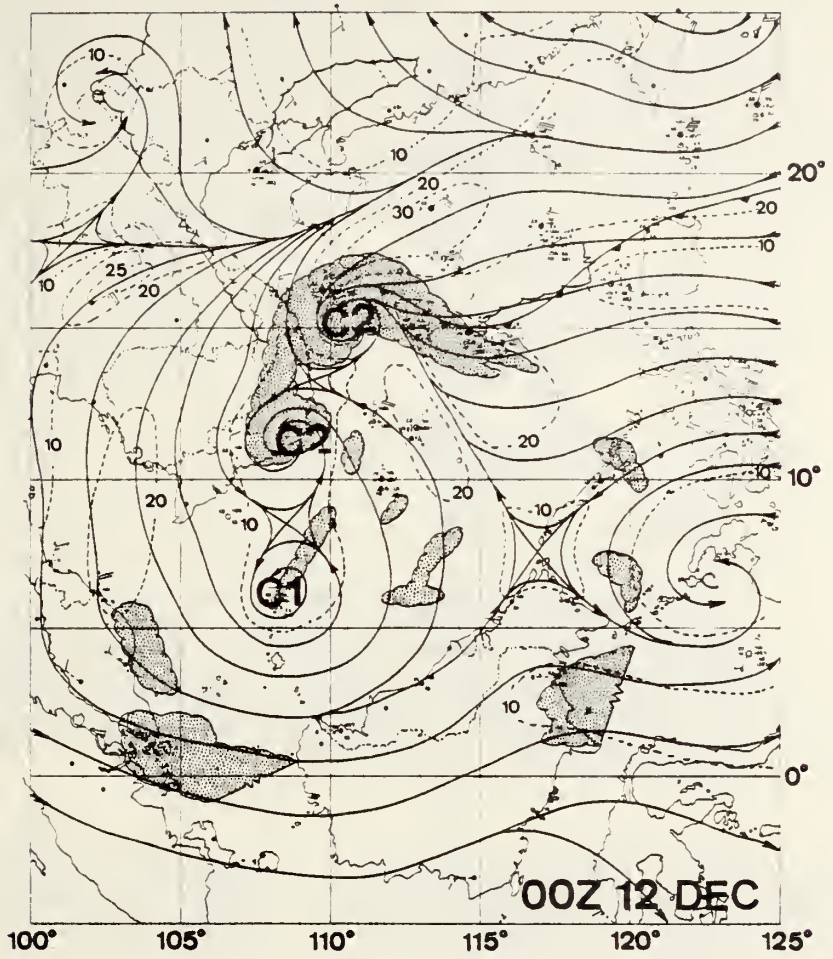

FIG. 13. As in Fig. 2 except for 0000 GMT 12 December 1974.

ship between the cold surges and the near-equatorial convective disturbances in the next section.

4. Discussion

Several previous investigators (e.g., Navy Weather Research Facility, 1969) have constructed time cross sections along northeast-southwest trajectories in the SCS to study the sequence of events following a cold surge. Fig. 14 shows such a straight-line trajectory from the Taiwan Strait to the southern tip of the Malaysia Peninsula. A surface air temperature cross section along this line is shown in Fig. 15. Here it can be seen that the occurrence of the first cold surge in the Taiwan Strait, similar to that in Hong Kong, took place in two segments. The first segment was associated with the frontal passage near 12Z03 which was followed by the second segment beginning 12Z05. In the northern SCS the cross section seems to suggest that the cold air intruded very rapidly to reach about 18°N and then propagated at a somewhat slower speed equatorward. The second surge which began at 12Z10 appeared to develop nearly simultaneous temperature drops all the way down to 12°N. However, an inspection of the time series of the surface temperature and pressure at several stations in the northern SCS (Figs. 1 and 16) reveals that the situation is not so straightforward. In these figures it is clear that the stations in Taiwan and the Taiwan Strait (Taipei, Makung, Dongkong), as well as those immediately off the South China coast (Hong Kong and Haikow) all show significant temperature drops and pressure rises following the cold surges. Moderate temperature drops for both surges and a pressure rise for the first surge also are evident at the western SCS station of Xishadao. However, at the northeastern SCS station of Donshadao, which is about 300 km off the South China coast and 400 km downstream from the Taiwan Strait, there is very little evidence of significant temperature or pressure changes due to the surges. Thus it appears that the cold air streaming down the Taiwan Strait and off the southeastern China coast east of the Nanling Range was modified in the northeastern SCS rather

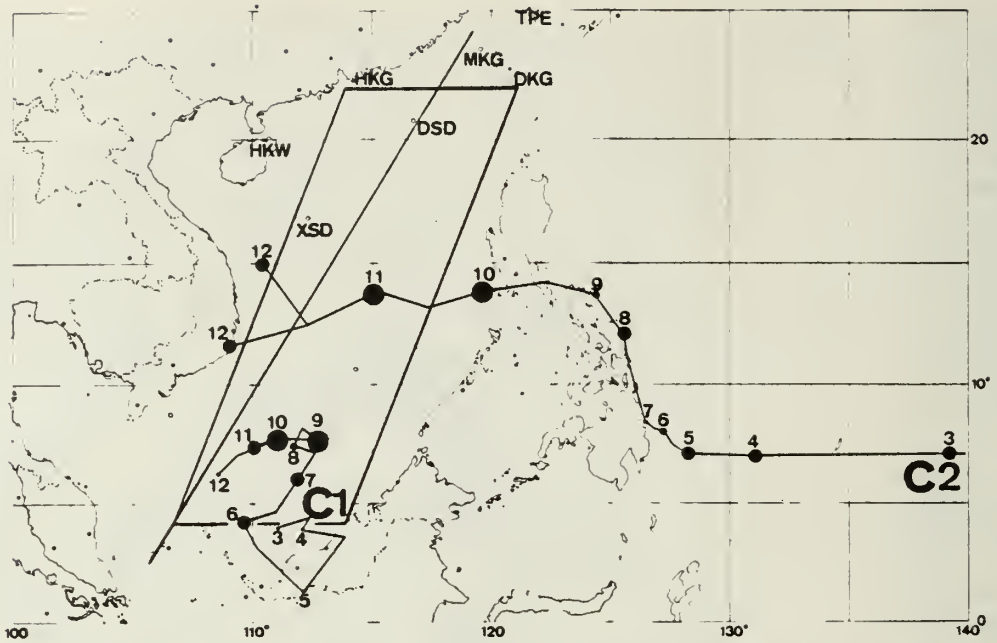

FIG. 14. Map showing the northeast-southwest line where time cross section of surface temperature is constructed in Fig. 15, and the northeast-southwest band where time-cross section of longitudinally averaged 850 mb/surface wind speed is constructed in Fig. 17. Also indicated are the following stations where temperature and pressure time series are shown elsewhere in this paper: Hong Kong (HKG, Fig. 1), Taipei (TPE, Fig. 16a), Makung (MKG, Fig. 16b), Dongkong (DKG, Fig. 16c), Haikow (HKW, Fig. 16d), Dongshadao (DSD, Fig. 16e) and Xishadao (XSD, Fig. 16f). The tracks of cyclonic centers C1 and C2 are also plotted with the size of the circles indicating schematically the intensity of associated organized convection at 0000 GMT.

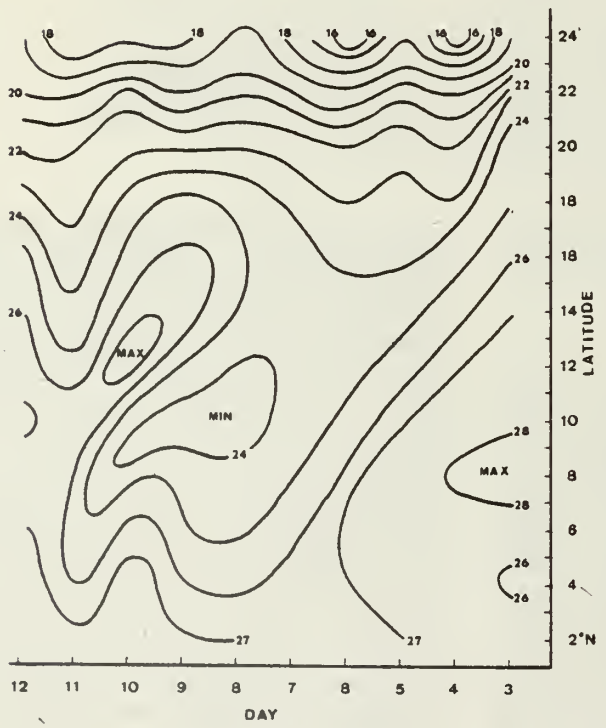

FIG. 15. Time-latitude cross section of analyzed surface temperature (°C) along the northeast-southwest line shown in Fig. 14.

rapidly by the marine influence, while in the western part of the SCS cold air originating from the South China coast west of the Nanling Range had remained over land somewhat longer thereby stayed colder. This air was channeled southward along the Vietnam coast and penetrated deeply into the near-equatorial latitudes. This longitudinal variation of the surface temperature change also is confirmed by examination of the surface temperature analyses. Sadler and Harris (1970), in a climatological study of the Southeast Asia, noted that the December-mean surface temperature map shows a relatively cold region immediately off the Vietnam coast, which, in addition to the effect of the cold surges, may also be due to the cooler coastal water compared to other parts of the SCS. Apparently different degree of air-sea interaction occurred between the western and eastern parts of the surges during the northeasterly monsoon, and when the surge air originating from the South China coast west of the Nanling Range reaches the southwestern SCS the surface temperature becomes even lower than the climatological mean.

A northeast-southwest cross section of the low-level winds, on the other hand, is more representative of the time sequence of events, because the freshening of the northeasterlies during surges usually occur over the entire SCS. Fig. 17 is such a

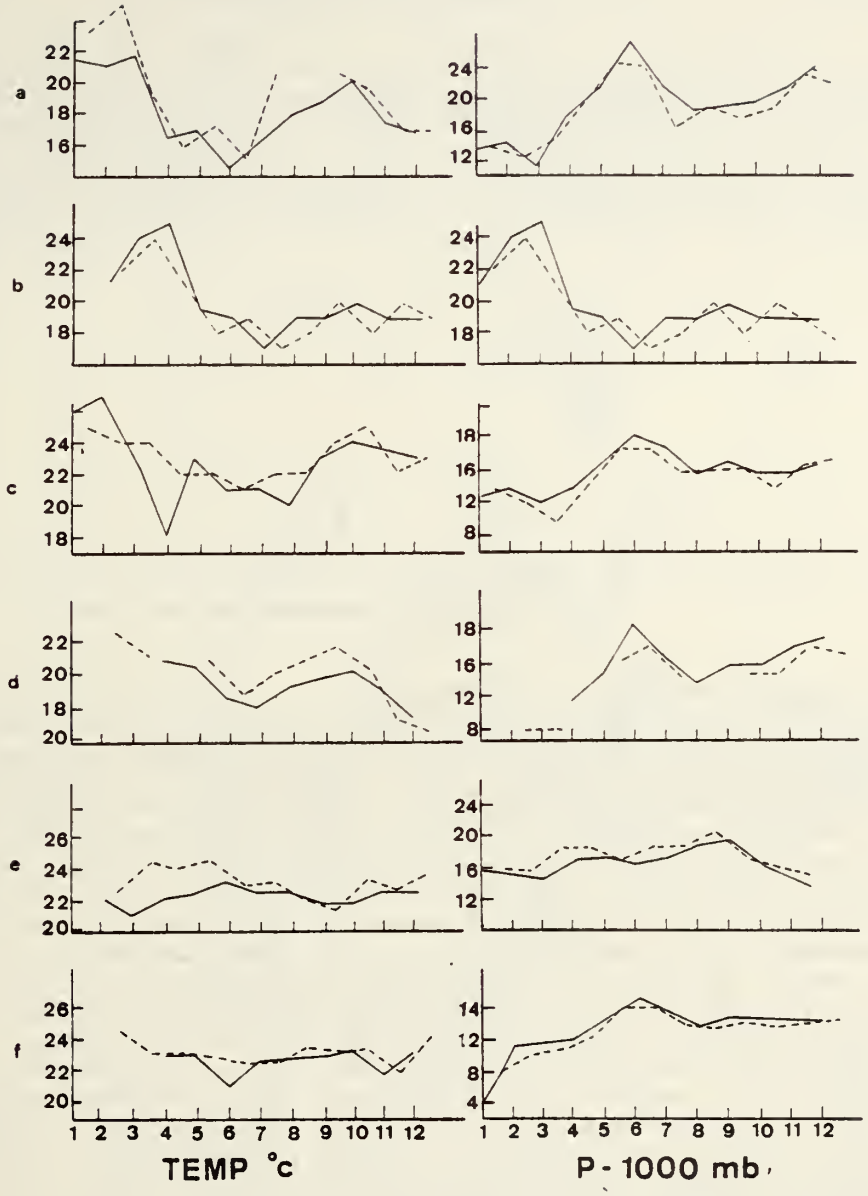

FIG. 16. As in Fig. 1 except for (a) Taipei, (b) Makung, (c) Dongkong, (d) Haikow, (e) Dongshadao, and (f) Xishadao where the 1000 mb temperature is shown instead of the surface temperature. (The surface temperature is missing for most of the period.)

cross section but it is based on longitudinally averaged wind speeds over a northeast-southwest band which is indicated in Fig. 14. The reason that a band, instead of a straight-line trajectory, is used is because the considerable movement and changes in the intensity of the cyclonic centers C1 and C2 (which also are shown in Fig. 14) would make a cross section along a straight line somewhat misleading in the latitudes of the two cyclonic centers. In Fig. 17 the two cold surges may be followed by the 20 and 25 kt isotachs. They first appeared in the Taiwan Strait at 00Z04 and 00Z05, respectively, for the first surge, and around 12Z10 for the second surge. In both cases a southward propagation of the freshening of the winds may be traced to about 16°N within 12–24 h. From there this increase in the northeasterlies spread almost simultaneously down to the southern SCS near 7°N in the first surge. In the second surge it was stopped near 15°N because of the westward movement of C2 across the central SCS. The strong winds between 9–11°N centered at 00Z11 are obviously due to the presence of C1 and C2.

From the movement tracks and intensity changes

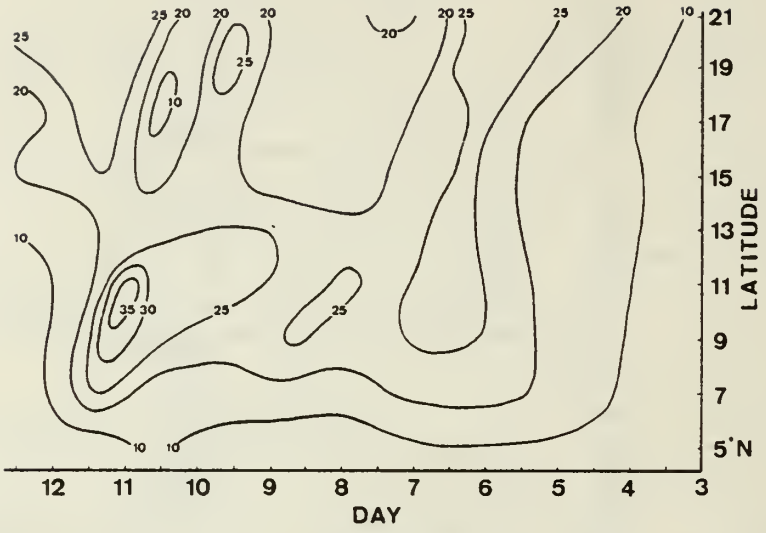

FIG. 17. Time-latitude cross section of longitudinally averaged low-level wind speed (kt) along the northeast-southwest band shown in Fig. 14.

of C1 and C2 shown in Fig. 14, it appears that the organized convection associated with cyclonic disturbances in the near-equatorial latitudes was influenced directly by the monsoon surges. Prior to the first cold surge when the low-level wind in the SCS was very light ($\lesssim$10 kt), C1 was a semi-permanent, semi-stationary feature in the equatorial trough over the northern coast of Borneo. It was associated with only widely scattered convection. Immediately after the first surge, C1 developed very intense, organized convection resembling an impressive tropical cyclone on the satellite pictures. Except for a temporary weakening around 8 December 1974, it maintained its strength as the northeasterlies in the central SCS remained strong ~20 kt). The second surge coincided with the westward movement of C2 which moved into the central SCS as a propagating wave disturbance in the ITCZ, after being temporarily stalled and deflected northward when it reached the Philippines (perhaps due to the strong vortex advection effect of C1 at that time). Since C2 was north of C1 during the second surge, it apparently intercepted the northeasterly surge and became intensified (and subsequently split) itself. Hence the southward penetration of the monsoon winds was blocked and the intense convection of C1 dissipated in 24 h.

The correlation between the low-level northeasterlies and the convective activities in the cyclonic disturbances probably is due to the changes in the low-level convergence which apparently is modulated by the northeasterly winds. This possibility is supported by the usual concentration of cloudiness in the northwestern or northern quadrants of the cyclonic center. Such a situation also was reported previously by Harris *et al.* (1971).

The southward incursion of cold temperatures along the Vietnam coast also appeared to impact the convective activities of the near-equatorial disturbances. The first weakening of C1 around 8 December 1974 coincided with the cold air incursion after the first surge. This cold incursion was a slower process than the freshening of the northeasterlies because it had to go around the western side of the SCS. The weakening of C1 was not severe probably because the northeasterlies remained strong, and when the cooling trend in the vicinity of C1 reversed, so did the weakening of its convection. When C2 blocked off the northeasterlies after the second surge, it also funneled cold air southward cyclonically along the Vietnam coast, resulting in a much faster cooling in the southwestern SCS compared to the first surge and apparently helped the collapse of convection associated with C1.

5. Concluding remarks

From the foregoing analyses and discussion, we would like to make the following tentative conclusions which should be reexamined after Winter MONEX data are available:

1) Following a cold surge, the freshening of low-level northeasterlies spreads rapidly (12–24 h) from the Taiwan and Luzon Straits southwestward to near 16°N, and then down to the near-equatorial latitudes with almost no time lag, if there is no disturbance in the SCS to prevent it from doing so.

2) The southward incursion of cold temperatures is concentrated in the western part of the SCS along the Vietnam coast, and progresses at a slower pace compared to that of the widely spread freshen-

ing of the winds over the entire SCS. In the eastern and central parts of the SCS the fast-streaming northeasterlies are modified extensively by air-sea interaction. The longitudinal difference in air-sea interaction probably is due to the differences both in the distance of air trajectories over water and in the sea-surface temperature.

3) As a result of the first two developments, the near-equatorial latitudes of SCS will experience widely spread increased northeasterly monsoon winds prior to the cold temperatures.

4) Pre-existing, low-latitude synoptic-scale cyclones, whether semistationary equatorial trough disturbances which developed over the northern

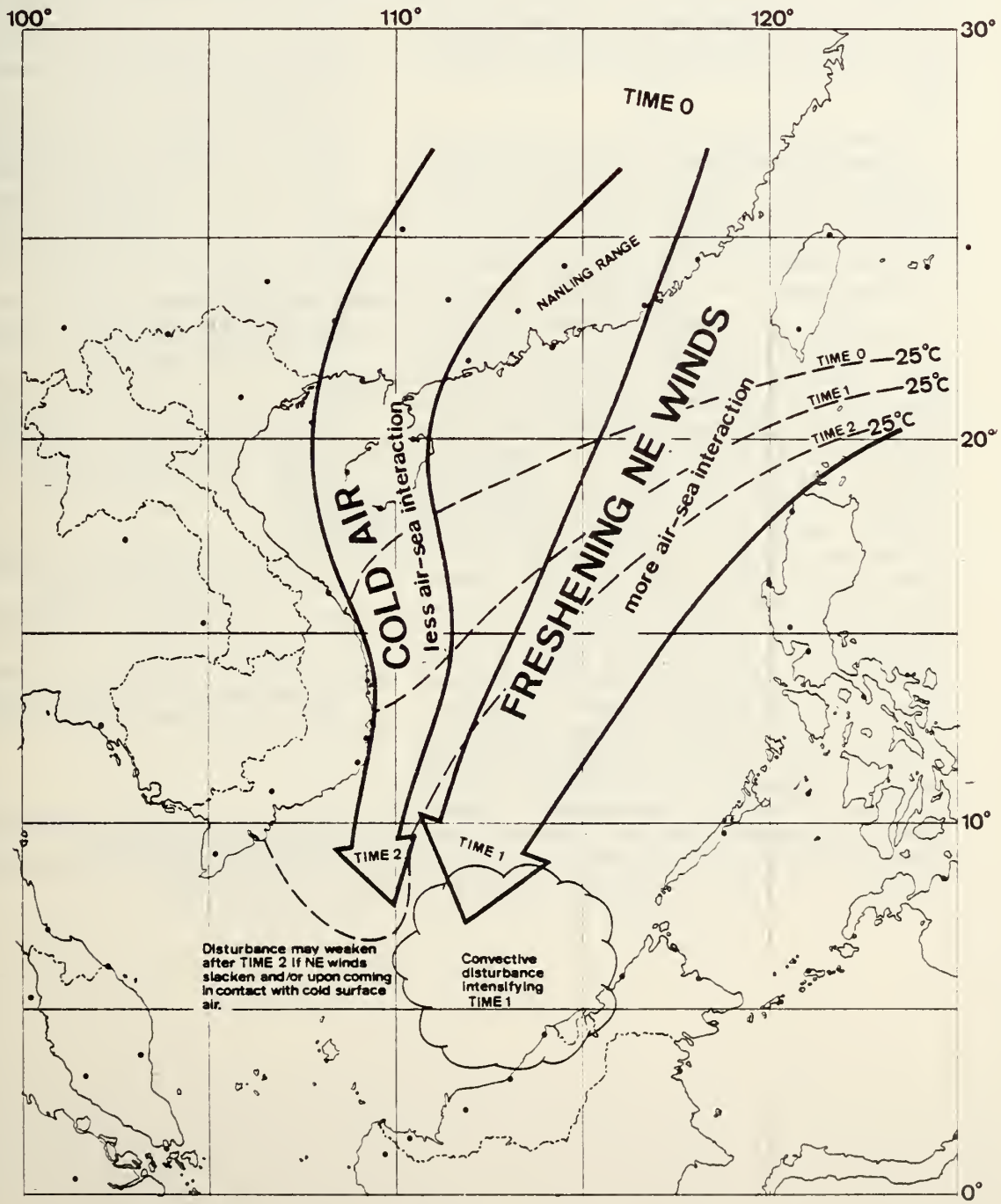

FIG. 18. Schematic model depicting the time sequence of a cold surge and the position of the 24°C surface air isotherm. Here times 1 and 2 are approximately 12–24 and 24–48 h after time 0, respectively. See text for details.

coast of Borneo, or westward propagating waves from the western Pacific, may respond to the surges in the following way:

(i) Intensification of organized deep cumulus convection in relation to the freshening of low-level northeasterlies while the surface temperature is still warm, probably because of enhanced low-level convergence; and the dissipation of organized convection in relation to the slackening of northeasterlies.

(ii) After the intensification due to the freshened monsoon flow, a weakening of the convection in relation to the later-arrived surface cold air incursion in the western SCS, probably due to the stabilizing effect.

The above sequence of events is summarized in the schematic model shown in Fig. 18. Here time 0 represents the time when the cold surge occurs in southern China, time 1 represents the time when the freshening of northeasterlies reaches southwestern SCS approximately 12–24 h after time 0, and time 2 is approximately 24–48 h after time 0.

Acknowledgments. We wish to thank Prof. J. C. Sadler of the University of Hawaii and Prof. G. T. J. Chen of National Taiwan University for valuable suggestions, Mr. Gordon Bell, Dr. P. C. Chin and Dr. K. S. Tsui of the Hong Kong Royal Observatory and Mr. B. K. Cheang and Mr. L. C. Quah of the Malaysia Meteorological Service for discussion, and Mr. S. K. Rinard for assistance in data processing. Data used in this study were made available by National Climatic Center, National Environmental Satellite Service, Fleet Numerical Weather Central, Naval Environmental Prediction Research Facility, Hong Kong Royal Observatory and National Taiwan University. One of us (CPC) wishes to thank the U.S. MONEX Project Office, National Center for Atmospheric Research, for co-sponsoring his visits to Kuala Lumpur, Hong Kong and Taipei for discussion and data collection. This work was supported by the National Science Foundation, Division of Atmospheric Sciences, Global Atmospheric Research Program, under Grant ATM77-14821 and Division of International Programs, U.S.-R.O.C. Cooperative Science Program, under Grant INT78-14557; and by the National Environmental Satellite Service/NOAA, under Contract 7-11030.

REFERENCES

Adler, R. R., L. R. Brody and W. L. Somervell, 1970: A preliminary survey of Southeast Asia fall transformation season weather. Navy Weather Research Facility Tech. Paper No. 10–70, 74 pp.*

Chang, C.-P., 1970: Westward propagating cloud patterns in the tropical Pacific as seen from time-composite satellite photographs. *J. Atmos. Sci.*, 27, 133–138.

——, and K. M. Lau, 1979: Northeasterly cold surges and near-equatorial disturbances over the Winter MONEX area during December 1974. Part II: Planetary-scale aspects. To be submitted to *Mon. Wea. Rev.*

——, J. E. Erickson and K. M. Lau, 1979: Synoptic events of northeasterly cold surges and near-equatorial disturbances over the Winter MONEX area during 3–13 December 1974. Tech. Rep. NPS63-79-001, 85 pp. [Available from Dept. of Meteorology, Naval Postgraduate School].

Cheang, B. K., 1977: Synoptic features and structures of some equatorial vortices over the South China Sea in the Malaysia region during the winter monsoon, December 1973. *Pure Appl. Geophys.*, **115**, 1303–1334.

Harris, B. E., J. C. Sadler, G. Ing, F. Ho and W. R. Brett, 1971: Synoptic regimes which affect the Indochina Peninsula during the winter monsoon. Tech. Rep. UHMET-71-1, University of Hawaii, 31 pp.**

Krishnamurti, T. N., N. Kanamitsu, W. J. Koss and J. D. Lee, 1973: Tropical east-west circulations during the northern winter. *J. Atmos. Sci.*, **30**, 780–787.

Navy Weather Research Facility, 1969: The diagnosis and prediction of Southeast Asia northeast monsoon weather. Tech. Rep. NWRF 12-0669-144, 73 pp.*

Ramage, C. S., 1971: *Monsoon Meteorology*. Academic Press, 296 pp.

Riehl, H., 1968: Surface winds over the South China Sea during the northeast monsoon season. Navy Weather Research Facility Tech. Pap. No. 22-68, 24 pp.*

——, and W. J. Somervell, 1967: Weather sequences during the northeast monsoon. Navy Weather Research Facility Tech. Pap. No. 7-67, 78 pp.*

Sadler, J. C., and B. E. Harris, 1970: The mean tropospheric circulation and cloudiness over Southeast Asia and neighboring areas. Univ. of Hawaii Tech. Report HIG-70-26, 38 pp.**

* Available from the Naval Environmental Prediction Research Facility, Monterey CA 93940.

** Available from the Department of Meteorology, University of Hawaii, Honolulu 96822.

Reprinted from PAPERS IN METEOROLOGICAL RESEARCH,
Vol. 2, No. 1, April 1979, pp. 1-13
A Journal of the Meteorological Society of the Republic of China

Possible Influences of Sea-Surface Temperature on the Easterly Waves over the Equatorial Pacific

C. – P. Chang, D. M. Delaney and E. Maas, Jr

Department of Meteorology
Naval Postgraduate School
Monterey, California 93940

Possible Influences of Sea-Surface Temperature on the Easterly Waves over the Equatorial Pacific

C. – P. Chang, D. M. Delaney and E. Maas, Jr

Department of Meteorology
Naval Postgraduate School
Monterey, California 93940

(Manuscript received 4 February 1979, in final form 12 March 1979)

ABSTRACT

The sea-surface temperature (SST) in the equatorial Pacific exhibited considerable variations between the latter halves of 1972 and 1973. A previous spectral study (Chang and Miller, 1977) has revealed that the structure of the easterly waves in the western and central equatorial Pacific during these two periods also varied significantly, and some of the variations may be attributed to the SST variations. In this study the composite technique is used to analyze the subjectively-digitized satellite data together with the meridional wind, temperature and relative humidity data for the same area and periods, in order to obtain further insight into the possible relationship between the variations of SST and easterly waves. The results lead to the following interpretations:

1) For a given season the spatial variation of the convective activity *organized by the easterly waves* may be influenced by the local, including up to about 10° longitude upstream, SST.
2) On the other hand, the spatial variation of the *seasonal-mean* convective cloudiness in a given season seems to be related to the larger-scale gradient of the SST anomalies and the associated Walker circulation, rather than to the local SST.
3) There is some indication that the interannual variation of the seasonal-mean convective cloudiness may depend somewhat on the interannual variation of the local SST.
4) The vertical structure of the easterly waves is probably a function of the vertical shear of the basic-state zonal wind, as was reported by previous studies; but contrary to previous belief it appears to be unrelated to the degree of convective activity associated with the waves.
5) The waves are probably generated by non-thermal energy sources in the east-central Pacific (or propagating into this region from further east), where the SST-influenced wave convective activity may determine the wave amplitude which remains nearly constant in the western Pacific due to a balance between cumulus heating and damping.

1. Introduction

The sea-surface temperature (SST) in the equatorial Pacific exhibited considerable variations during the latter halves of 1972 and 1973. Fig. 1, which is based on the data archived at the Pacific Environmental Group, National Marine Fisheries Service, Monterey, shows the seasonal-averaged SST as well as the departures from a five-year (1972-1976) mean. In 1972 the

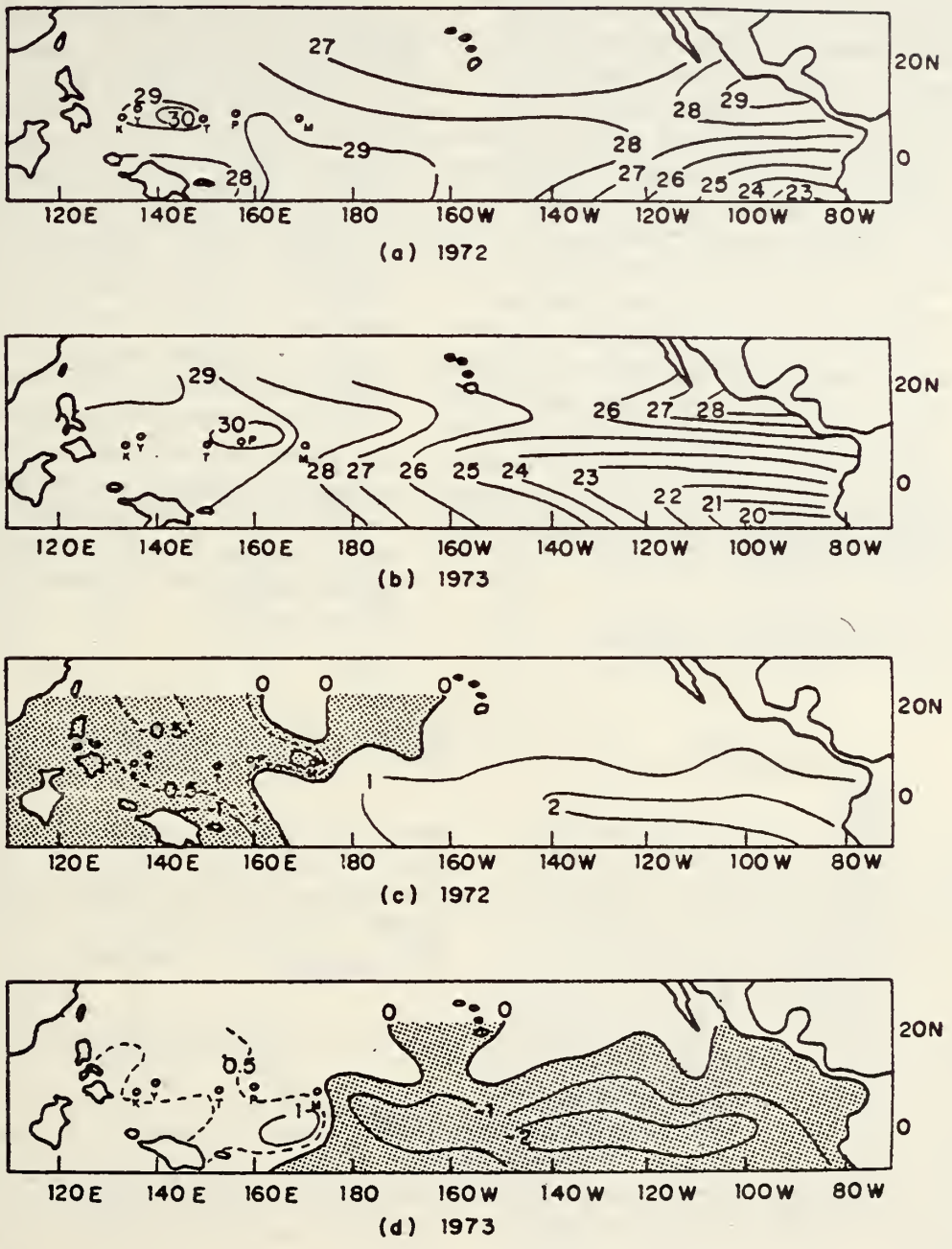

Fig. 1. July-December mean sea-surface temperature (°C) for 1972 (a) and 1973 (b), and the anomalies from the 1972-1976 five-year mean for 1972 (c) and 1973 (d).

SST was anomalously warm (~2°C above normal) in the eastern Pacific, and, to a much lesser degree, appeared to be anomalously cold in the western Pacific. In 1973 the reverse was true. As a result the normal zonal SST gradient was almost completely removed in 1972, while it was sharpened in 1973 especially in the central Pacific. A previous study by Chang and Miller (1977) revealed that spatial and temporal variations existed in the structure of the synoptic-

scale, 4-5 day easterly waves in the western and central equatorial Pacific during May-December and some of the variations may be attributed to the SST variations. However, their findings are mainly limited to the wind field due to the use of spectrum analysis which could not isolate significant cross-spectral signals involving thermal and moisture parameters. The interpretation of the results was also constrained by the SST data as only the eastern Pacific SST in Fig. 1 was available to them. The purpose of this study is to use the compositing technique to analyze the subjectively-digitized satellite cloud data together with the temperature and relative humidity data for the same area during the latter halves of these two years, in order to obtain further insight into the possible relationship between the interannual and spatial variations of SST and easterly waves.

2. Data and analysis procedure

Digitized satellite data are not available from the National Environmental Satellite Service (NESS) for 1972-1973. The satellite data used in this study are the visible (for 1972 and 1973) and infrared (1973 only) tropical mercator mosaics obtained from NESS. For the last six months of each year, these data are subjectively digitized by the procedure described below which basically follows that used by Payne and McGarry (1977). The mosaics are first divided into 1° squares in the area of interest. Within each square a visual determination is made as to whether deep convective clouds (bright in the visible mosaic and cold cloud top in the infrared mosaic) are present. The visible data are also examined closely in bright areas for signs of cumulus towers. The percentage of deep convective 1°-squares within a 5°-square centered on each of the five radiosonde stations, Majuro, Ponape, Truk, Yap and Koror (Fig. 2) are then calculated.

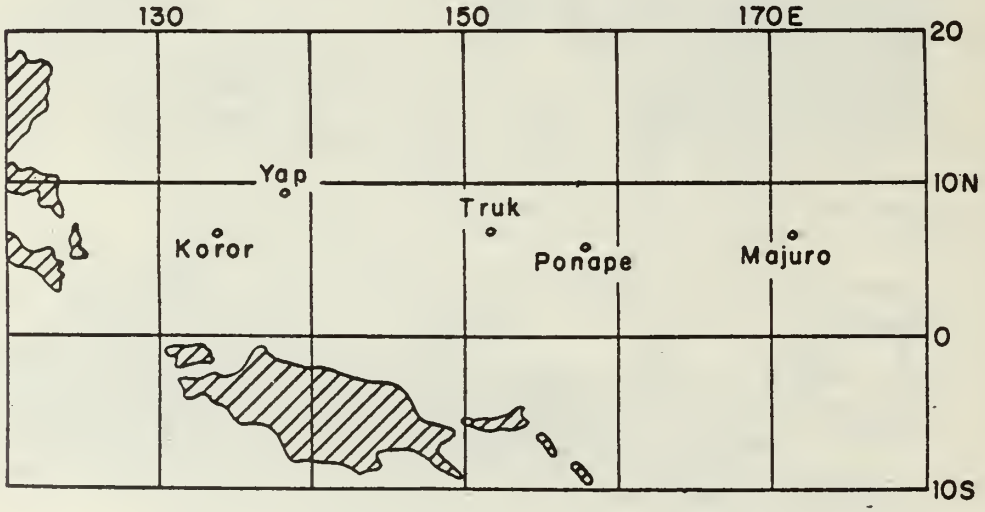

Fig. 2. Stations used in this study.

The times for eight phases of the wave passage (ridge, maximum northerly wind, trough, maximum southerly wind and the in-between categories) at each of the five stations are determined by the time series of the lower-tropospheric vertically-averaged (1000 mb to 500 mb) meridional wind components. These time series have been filtered to retain only fluctuations within the 2-10 day periodicity range. The satellite data corresponding to these times

are used to obtain the percentage convective cloud cover at each station during the various stages of wave passage for each year.

Since only once-daily satellite data are available for the 1972 season, for those reports of wave phase category falling between the daily reports, data 12 hours before and after are averaged to reach a percentage convective cloud estimate. For the 1973 season, the nighttime infrared data are used together with the visible data to provide a 12-hr interval coverage.

The convective cloud cover, as well as wind components, temperature and relative humidity obtained from radiosonde reports (Chang and Miller, 1977) during the latter halves of 1972 and 1973 are composited according to the wave phase categories with a method similar to that used by Reed *et al.* (1976). The total number of "waves" passing by each station and the averaged period and wavelength deduced for the two seasons are listed in Table 1.

These results are substantially similar to those obtained by Chang and Miller's (1977) spectral analysis.

Table 1. Number of "Waves" passing by each station and the averaged period and wavelength.

Season	Koror	Yap	Truk	Ponape	Majuro	Averaged Period	Averaged Wavelength
1972	31	31	35	36	34	4.6 days	3000 km
1973	34	34	38	37	34	4.3 days	2900 km

3. Results

Due to their proximity and the similarities in the composited distribution of every parameter studied, the results for Koror and Yap (KY) and for Truk and Ponape (TP) are respectively averaged to provide a simpler basis for discussion.

3.1 Meridional velocity

Figs. 3–4 show the composited wave structure at each station as represented by the meridional velocity fluctuations. The results are generally consistent with the spectral results of Chang and Miller (1977) in that 1) the lower tropospheric amplitudes are greater in 1972 than in 1973, 2) there is very little vertical phase tilt for the 1972 waves except for a ~180° phase reversal near 300 mb, and 3) vertical tilt is significant in 1973, with a general eastward tilt with height at Majuro and TP and westward tilt at KY.

3.2 Percentage convective cloud cover

The composited convective cloudiness at each station are shown in Fig. 5. With the exception of Majuro 1973, all the stations show a maximum in the trough region which indicates an enhancement of convective activity in the wave troughs. For Majuro 1973, the curve suggests that a substantial portion of the convective cloudiness is not organized by the waves. Seasonal means of convective cloudiness at each station are also shown in Fig. 5. In 1972 the mean values decrease steadily westward from Majuro to Koror, while in 1973 they are nearly uniform across the five stations with very slight variations. The result is substantially more mean cloudiness in 1973 than in 1972 at the western-most stations of KY.

The departures of cloudiness from the mean in the vicinity of the wave trough, which may be viewed as a measure of the amplitude of the wave-modulated convection fluctuations, behave differently compared to the mean cloudiness. In 1972 the departures generally increase toward the west. In 1973 there is a dramatic increase

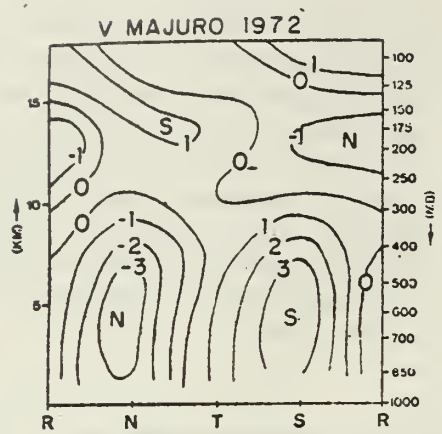

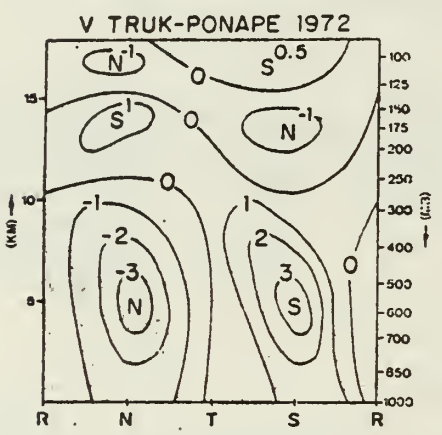

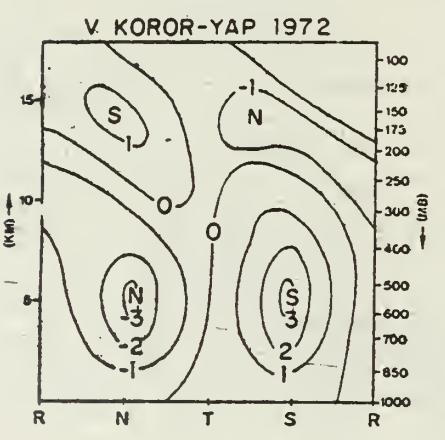

Fig. 3. Composited wave structure of the meridional wind fluctuations during 1972 for the indicated stations. Unit: ms $^{-1}$. (Data missing for 1000 mb Majuro.) The abscissa indicates ridge (R), maximum northerly (N), trough (T), maximum southerly (S) positions.

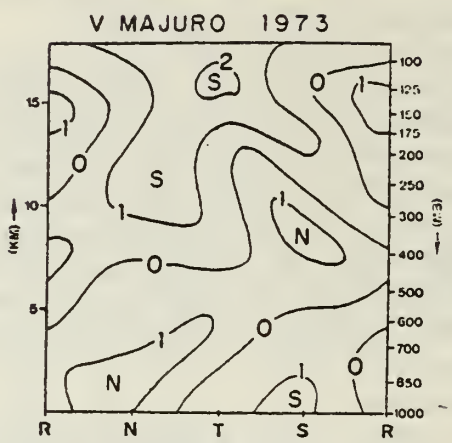

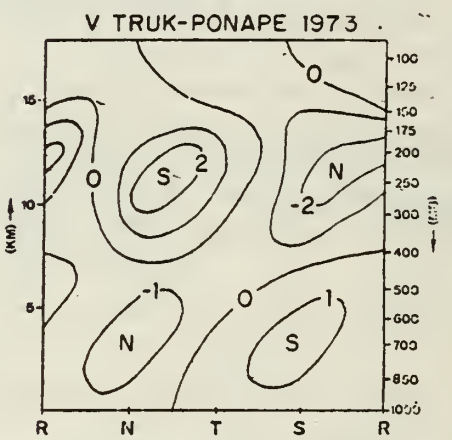

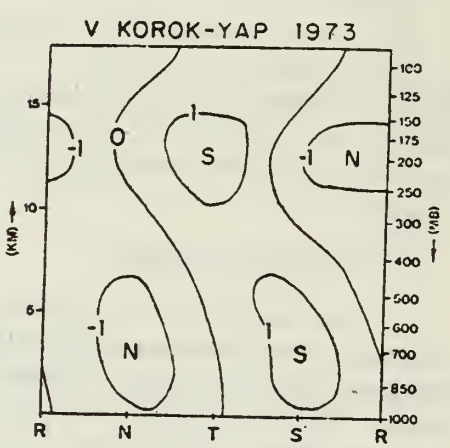

Fig. 4. As Fig. 3 except for 1973.

from Majuro to TP, followed by a decrease from TP to KY.

The extent of the representation of wave structure by the time-series data at an individual

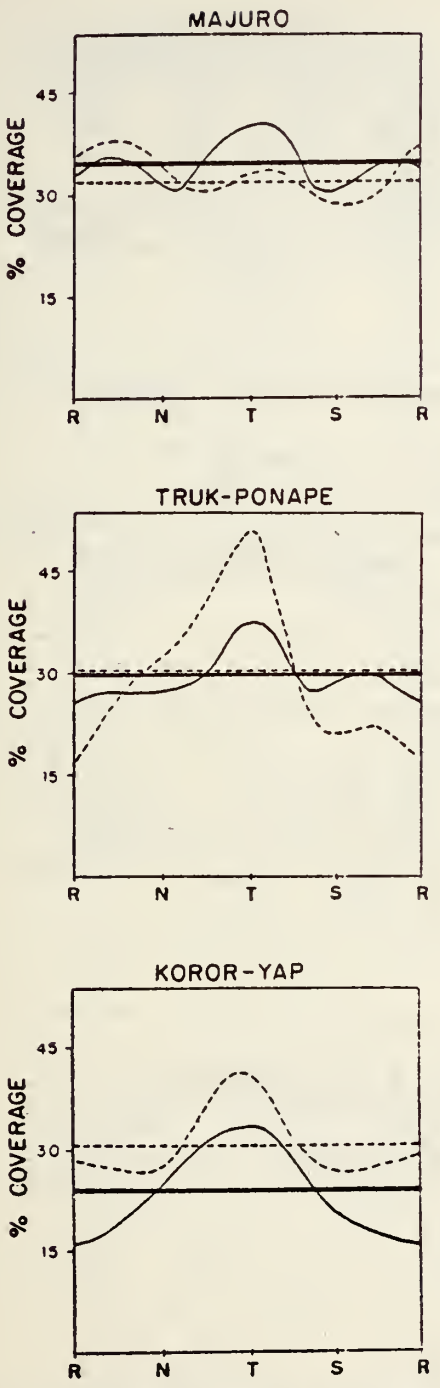

Fig. 5. Composited distribution of convective cloudiness within a wave for the indicated stations. Solid lines are for 1972 and dashed lines for 1973. Seasonal means indicated by horizontal straight lines.

station may be evaluated by constructing composites of the spatial distribution of cloudiness during passage of the trough axes. Since the westernmost stations, Koror, Yap, Truk and Ponape, exhibit quite similar patterns in the distribution of convective activity and only Majuro deviated from the collective pattern, Truk and Majuro are chosen to construct the composited horizontal distributions of convective cloudiness during passage of the wave troughs. These distributions are shown in Fig. 6 and are based on data from the original 1°-squares with a five-point smoothing to make them comparable to the 5°-square data used in individual time series composites. Comparing Figs. 5 and 6, it is evident that the spatial distribution composites of the enhancement and suppression of the convective activity are quite similar to the patterns deduced from individual station time series. The distinct maximum in the trough occurs in all cases except Majuro 1973. This indicates that the patterns deduced from individual time series indeed represent propagating waves rather than just stationary fluctuations at local stations.

3.3 Temperature

The composites of the temperature structures are given in Figs. 7 - 8. All stations show a warm core in the middle-upper troposphere except Majuro. An upper-level cold core is sometimes indicated above the warm core levels. For TP 1973 this upper-level cold core is most intense apparently reflecting stronger convective activity in the troughs. At Majuro in 1972 the troughs appear to be very slightly cold core near 300 mb where the upward motion is usually maximum. The 1973 troughs at Majuro indicate a well-defined cold core. Since in the tropics errors of temperature observations are probably comparable to the actual fluctuations, the well-defined pattern of Majuro 1973 should indicate a more definite cold core than that of Majuro 1972.

3.4 Relative Humidity

The relative humidity composites are

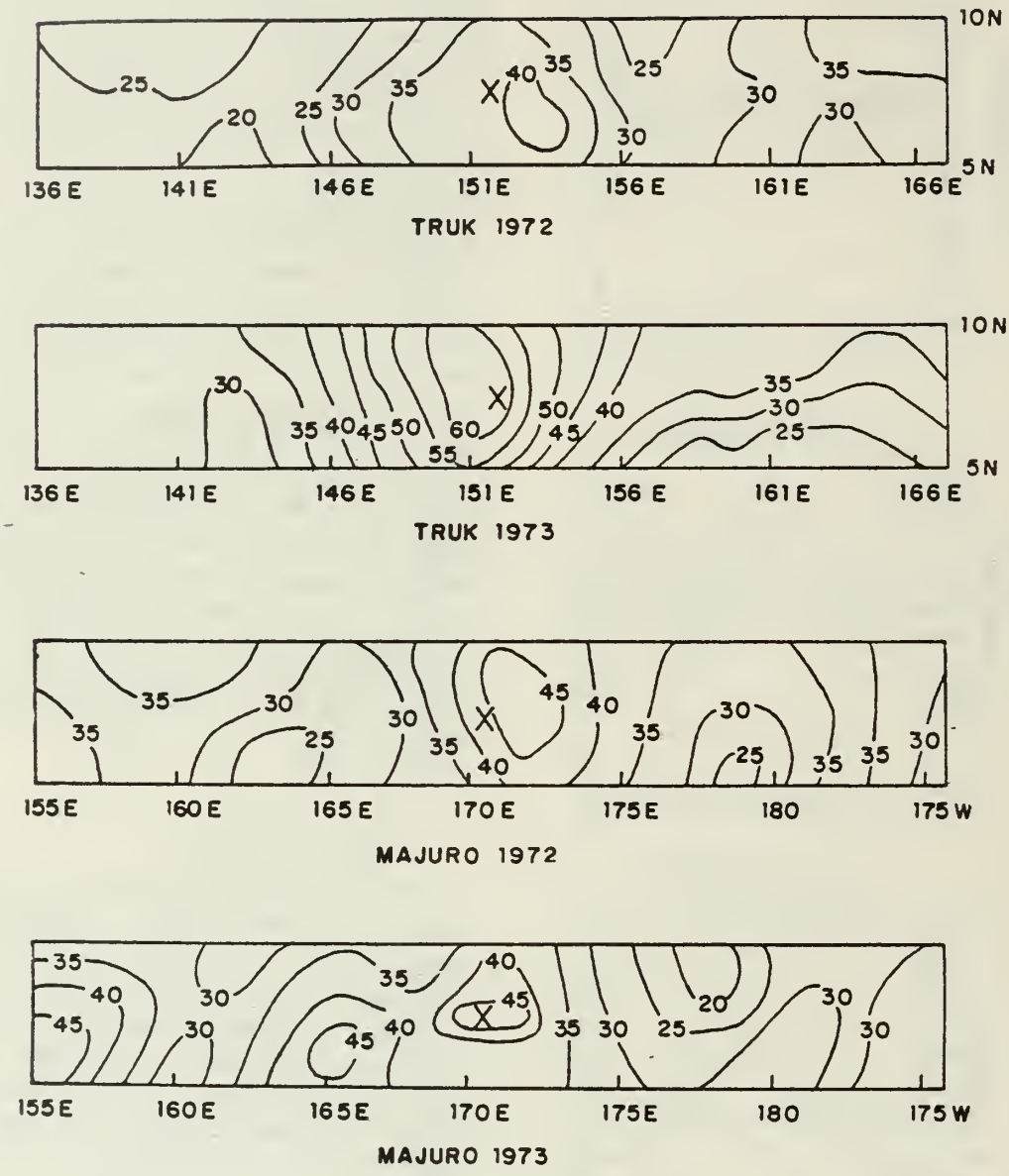

Fig. 6. Composited spatial distribution of convective cloudiness centered at Truk for 1972 (a) and 1973 (b), and at Majuro for 1972 (c) and 1973 (d). The cross indicates position of station.

given in Figs. 9-10. With the exception of Majuro 1973, all stations in both years have large, well-defined moist centers in the vicinity of the trough. Majuro 1973 has a moist region expanding over half of a wavelength ahead of the trough with a maximum in the vicinity of the northerly wind component. In general, moisture maxima during 1972 are found at a higher level than in 1973. The vertical structure of the moisture fields also agrees roughly with the vertical

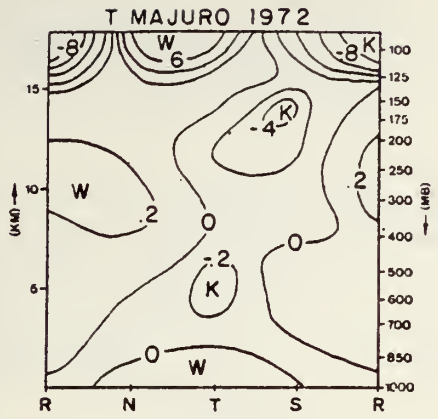

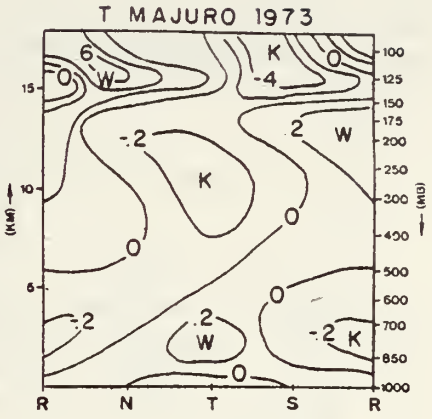

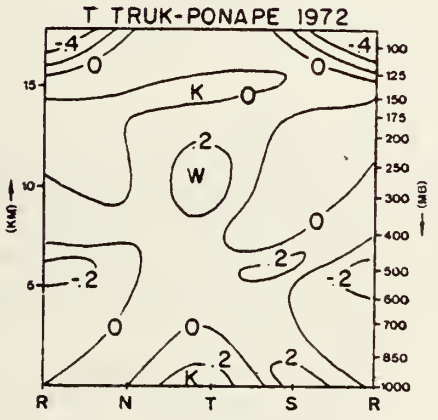

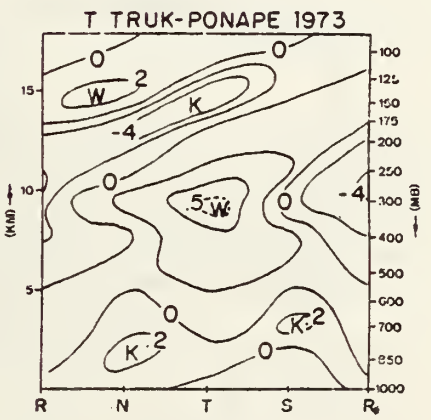

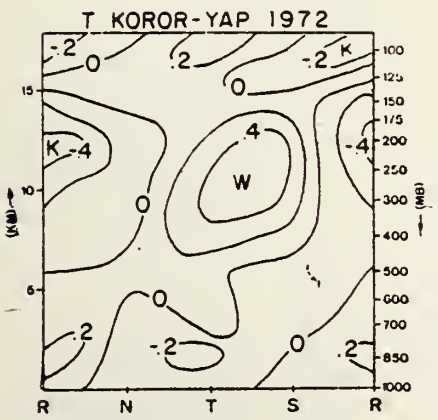

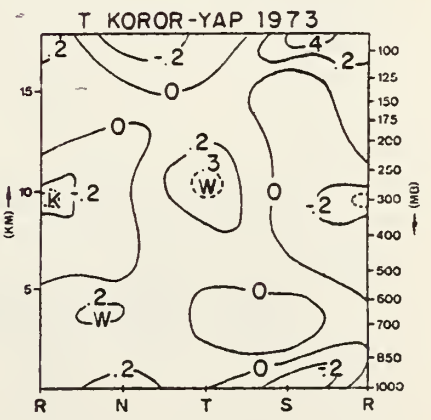

Fig. 7. As Fig. 3 except for temperature fluctuations. Unit: °C.

Fig. 8. As Fig. 7 except for 1973.

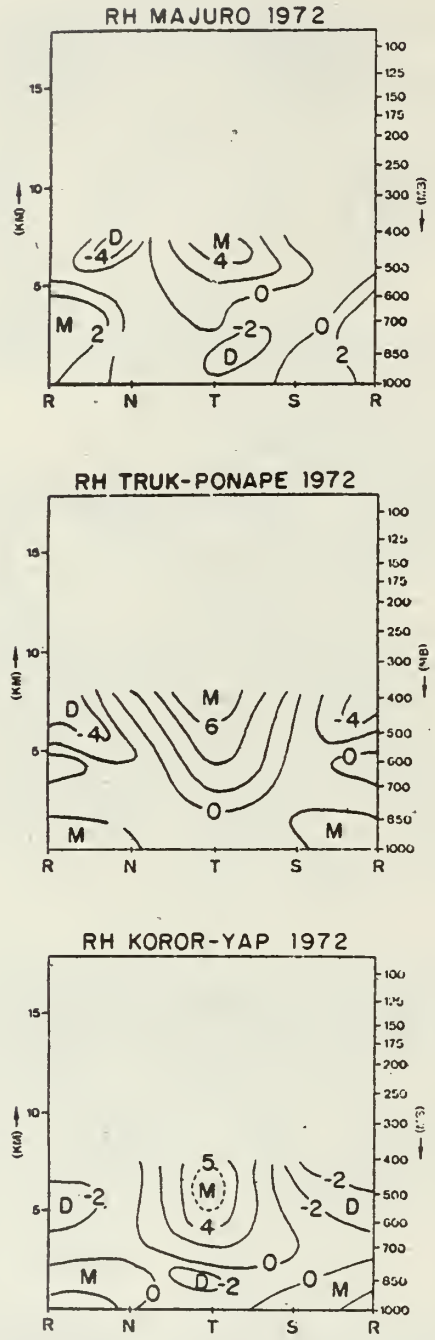

Fig 9. As Fig. 3 except for relative humidity fluctuations. Unit: % (Data above 400 mb missing.)

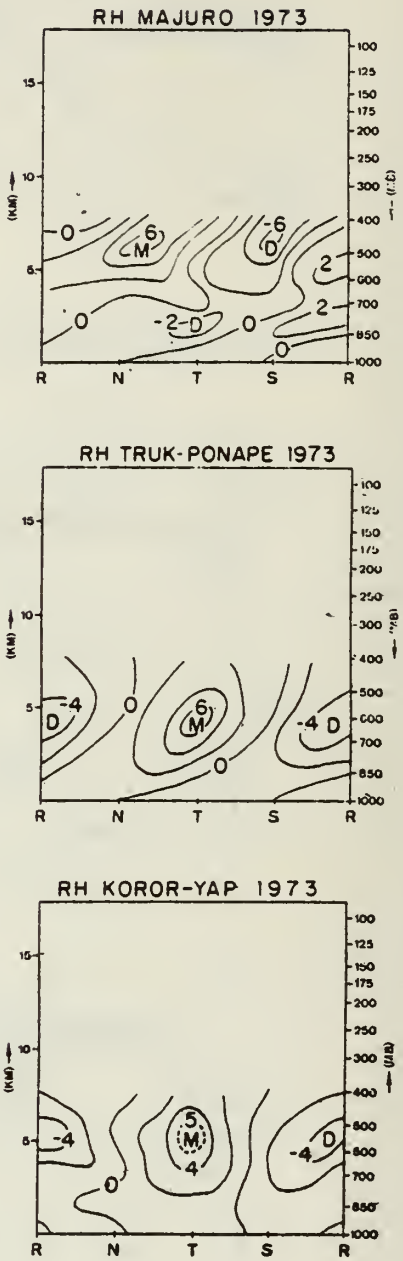

Fig. 10. As Fig. 9 except for 1973.

tilt of the meridional structure of the waves, with every little tilt at all stations in 1972 and a strong eastward tilt in the lower troposphere for stations east of Yap in 1973.

4. Discussion

The results shown in Fig. 5 suggest that the convective cloudiness is least organized by the wave passages at Majuro compared to the stations further west. This is consistent with the thermal structure in the wave troughs. To see this, the seasonal mean convective cloudiness, as well as the departure at the troughs from the means, are summarized in Table 2. The departure values may be viewed as a measure of the degree

Table 2. Seasonal mean percentage convective cloudiness for the indicated stations in 1972 and 1973 and the departures from the seasonal means

		Koror-Yap	Truk-Ponape	Majuro
Seasonal Mean	1972	24	30	35
	1973	31	31	33
Departure From Mean	1972	10	8	6
	1973	11	21	1

of modulation of convection by the waves. Comparing this with the results shown in Figs. 7–8, it is seen that during 1972 the waves at Majuro show a weak cold core in the trough near 500 mb, when the trough cloudiness is 6.3% above the mean. For 1973 the cold core in the trough is more definitive between 200 mb and 400 mb and the trough cloudiness is only 1% above the mean. Since these thermal structures imply a kinetic energy sink, they suggest that one or more energy sources other than the latent heat release in the waves operating near or upstream of Majuro. The difference between the cold core structures at Majuro for the two years is also consistent with the relative humidity distribution (Figs. 9–10), if we consider that maximum humidity occurring in the trough indicates the best organization of the moisture field by the waves. For 1972 the moisture field is already organized with a maximum in the trough between 400–700 mb when the waves reach Majuro, compared to 1973 when it is less organized until the waves pass Majuro. Examining the SST distributions in Fig. 1, it appears that these differences in the cloudiness, temperature, and moisture fields between the two years may be explained by the difference in the SST's upstream of Majuro in the following way. In 1972 the warm eastern and central Pacific SST anomalies should be more favorable for convection compared to the cold anomalies in 1973. This is likely to give rise to better-organized cloudiness and moisture fields in 1972 which, in turn, cause those waves reaching Majuro to have a weaker and ill-defined cold core compared to 1973.

As the waves continue to propagate westward past Majuro, Table 2 and Fig. 5 suggest that the influences of the SST may be relevant for explaining consistently the convective activity associated with the waves. During 1972 it can be seen from Table 2 that there exists a small but steady westward increase in the modulation of the convection due to the passage of the wave troughs, which is continuous for at least 40° of longitude (4000 km) from Majuro to Koror. Since the waves propagate from east to west, and the wave structure may retain some memory from its immediate past history, to examine the possible "local" influence of SST at each station we will consider the SST in an area about 10° longitude upstream from the station. Using this definition, the "local" SST rises by ~0.5°C from Majuro to TP and ~0.5°C from TP to KY for 1972 (Fig. 1). During the same period the seasonal-mean cloudiness actually decreases substantially from Majuro westward to Koror. From the mean zonal wind deduced by Chang and Miller (1977), it seems that this decrease in the mean cloud cover is closely related to the

noted eastward migration of the upward branch of the Walker circulation, 60° from its normal position near the Philippine Islands to the vicinity of the dateline, during the period of anomalously warm SST in the east-central Pacific. The present results thus suggest that the slight westward increase in the local SST tends to enhance the wave-organized cumulus convection, while time-mean cloudiness apears to be related to the Walker circulation which is probably influenced by the larger (several thousand km)-scale gradient of the SST anomalies.

During 1973, the results shown in Table 2 indicate a dramatic increase in the modulation of convective cloudiness by the waves from Majuro to TP, coinciding with a sharp rise in the SST of ~2°C between the stations (Fig. 1). As the waves propagate further westward towards KY, a reduction in the positive deviation in the troughs from the mean cloudiness can be seen, apparently responding to a reversal in the SST gradient. The magnitude of this gradient (~0.7°C) is significantly less than the upstream one, and the reduction in the trough cloudiness deviation is also much smaller (by a factor of two) compared to the increase (by a factor of ten) from Majuro to TP. The time-mean cloudiness for the 1973 season indicates no substantial variation between the stations, again suggesting that only the convective field organized by the waves may be influenced by the local SST. However, at KY the higher seasonal-mean cloudiness in 1973 compared to 1972 also suggests that the interannual variation of mean cloudiness could be influenced by the interannual variation of the local SST, since the local SST in 1973 is ~0.5°C higher than 1972.

The temperature and moisture (relative humidity) composites shown in Figs. 7-10 also provide some support to the foregoing interpretation of the longitudinal distribution of the wave-modulated convective cloudiness. As mentioned earlier, the temperature composites indicate warm core structures at all stations with the exception of Majuro. The magnitudes of these warm cores are consistent with the pattern of convective modulation indicated in Table 2. The 1972 results show a slight increase in the magnitude of the warm cores with westward propagation, in agreement with the increased deviations of trough cloudiness. During 1973, the thermal structure changes from a well-defined cold core at Majuro to a well-defined warm core at TP, followed by a slight decrease in the magnitude of the warm core at KY. This is again consistent with the dramatic increase in convective modulation from Majuro to TP, followed by a decrease from TP to KY. Although it is recognized that some of these changes are well within the observational error ranges, the consistent pattern nevertheless suggests a good probability that the latent heat release by the deep convection causes the thermal structure to change accordingly. The relative humidity composites at all stations are remarkably similar to the convective cloudiness distribution, adding credibility to the subjective method of digitizing the satellite imagery.

The results of the vertical tilt of the meridional wind fluctuations agree with those of Chang and Miller (1977), who hypothesized that the difference in the vertical structure stem from the seasonal variations in the vertical shear of the mean zonal wind. This vertical mean wind shear is influenced by the intensity and position of the Walker circulation which appears to be related to the larger (several thousand kilometers)-scale gradient of the SST anomalies through the latter's influence on the seasonal-mean convection. As was shown by earlier studies (Krueger and Winston, 1974; Ramage, 1977; Chang and Miller, 1977), the magnitude of the near-equatorial zonal overturnings during the 1972 season is quite weak. On the other hand, a strong Walker circulation occurred in 1973, indicating markedly greater vertical shear outside the upward branch for that season. A point worth noting here is that the large vertical tilt at TP in 1973 occurs when the wave-modulated convection is very strong. Thus there appears to be no direct relationship between the degree of vertical tilt and that of the convection of a wave. This result is contrary to the previous belief that strong convective activities will cause a smaller vertical tilt (Reed *et al.* 1977; Chang and Miller, 1977).

Although the thermal and convective fields of the waves are influenced by the variations of

the local SST, as discussed earlier, there is no indication of a similar effect on the amplitude of the meridional wind fluctuations. Within each season, no changes in the wave amplitude can be discerned among the five stations. The lower tropospheric amplitudes in 1972 are all ~3ms^{-1}, and in 1973 they are ~1.5 ms^{-1}. Based on the present data, the only explanation for the seasonal difference in the wave amplitudes that is apparent to us is the upstream influence of the SST in the eastern and central Pacific. If one assumes that during both years there was an equal amount of non-thermal energy sources which generate waves in this region, then in 1973 the better-defined cold cores over the cold eastern and central Pacific Ocean would act as a stronger kinetic energy drain, damping the amplitude of the generated waves as they propagate westward away from the source region. A similar effect will occur if the waves propagate into the eastern-central Pacific from further east. On the other hand, the effect of this energy sink in 1972 is lessened as the warmer SST, through more organized convection, reduce the intensity of the cold cores and thereby enable the waves reaching Majuro to have larger amplitudes than 1973. Westward of Majuro the convective latent heating takes over to become the primary energy source as evidenced by the warm cores. If the waves have reached an equilibrium intensity prior to reaching Majuro, the increased latent heating could be balanced by increased damping due to cumulus-scale transports resulting in nearly constant wave amplitudes west of Majuro.

5. Concluding remarks

The foregoing discussion may be summarized as follows:

1) For a given season the spatial variation of the convective activity *organized by the easterly waves* may be influenced by the local, including the immediate upstream, SST.

2) On the other hand, the spatial variation of the *seasonal-mean* convective cloudiness in a given season seems to be related to the larger-scale gradient of the SST anomalies and the associated Walker circulation, rather than to the local SST.

3) There is some indication that the interannual variation of the seasonal-mean convective cloudiness may depend somewhat on the interannual variation of the local SST.

4) The vertical structure of the easterly waves is probably a function of the vertical shear of the basic-state zonal wind, as was reported by Chang and Miller (1977); but contrary to previous belief it appears to be unrelated to the degree of convective activity associated with the waves.

5) The waves are probably generated by non-thermal energy sources in the east-central Pacific (or propagating into this region from further east), where the SST-influenced wave convective activity may determine the wave amplitude which remains nearly constant in the western Pacific due to a balance between cumulus heating and damping.

Recently, Ramage (1977) has suggested that a correlation of SST and local precipitation on a seasonal scale does not exist because, although near Canton Island a positive correlation is usually observed, in the other parts of the tropical ocean negative or low correlations frequently occur. However, the present results indicate that, while seasonal mean cloudiness associated with the large scale SST gradients may have different types of correlations with the SST anomalies, the local SST effect does seem to be important in the organization of deep convection by synoptic scale disturbances.

ACKNOWLEDGEMENTS

We wish to thank Dr. D. McCline of the Pacific Environmental Group, National Marine Fisheries Service, NOAA and Mr. D. Bepristis for providing the sea-surface temperature data, and to Professor R. L. Haney for reading the manuscript. This work was supported by the National Environmental Satellite Service, NOAA, under contract 7-11030, and by the National Science Foundation, Climate Dynamics Research Section, under Grant ATM 77-14821. Parts of the material in this paper were presented at the RMS/AMS/DMG/RS Conference on Meteorology over the Tropical Oceans, August 1978, London, UK.

REFERENCES

Chang, C.-P., and C. R. Miller, III, 1977: Comparison of easterly waves in the tropical Pacific during two periods of contrasting sea-surface temperature anomalies. *J. Atmos. Sci.*, **34**, 615–628.

Krueger, A. F., and J. S. Winston, 1974: A comparison of flow over the tropics during two contrasting circulation regimes. *J. Atmos. Sci.*, **31**, 385–370.

Payne, S. W. and M. McGarry, 1977: The relationship of satellite-inferred convective activity to easterly waves over West Africa and the adjacent ocean. *Mon. Wea. Rev.*, **105**, 413–420.

Ramage, C. S., 1977: Sea-surface temperature and local weather. *Mon. Wea. Rev.*, **105**, 540–544.

Reed, R. J., D. C. Norquist, and E. E. Recker, 1976: The structure and properties of African wave disturbances as observed during Phase III of GATE. *Mon. Wea. Rev.*, **104**, 317–333.

赤道太平洋海面溫度對東風波之可能影響

張 智 北 D. M. Delaney E. Maas, Jr.

美 國 海 軍 研 究 學 院 氣 象 系

1972 和 1973 的兩個下半年的赤道太平洋的海面溫度有很大的變化。以前的一個波譜分析（張智北和Miller, 1977）曾發現在這兩個期間赤道太平洋西及中部的東風波結構也有顯著的變化。本文乃係以合成方法來分析這兩個期間及地區的人造衛星資料（經過主觀數值化）以及經向風、氣溫和相對濕度，以期進一步探討海面溫和東風波變化間的可能關係。分析之結果導致以下的解釋：

1) 在同一季節內由東風波組織的對流活動的空間變化可能受到當地（包括上游經度10度）海面溫的影響。

2) 另方面，季平均的對流雲量似與海面溫距平的大範圍梯度及與其關連的 Walker 環流有關，而與當地海面溫無關。

3) 若干跡象顯示年與年間季平均對流雲量的變化可能與年與年間當地海面溫之變化有些關係。

4) 東風波的垂直結構可能是基本緯向風的垂直風切的函數。此點和以前其他研究之結果相同。但是與以前所認爲相反的是，此結構似與東風波的對流活動程度無關。

5) 東風波可能係由東、中太平洋地區非熱性的能源所引起，（或是由更東地區進行至該地區。）在該地區受海面溫影响的東風波對流活動可能決定波幅之大小。但由於積雲對流的熱源和消弱作用趨於平衡，此波幅至西太平洋仍保持大致不變。

Reprinted from MONTHLY WEATHER REVIEW, Vol. 108, No. 3, March 1980
American Meteorological Society
Printed in U. S. A.

Northeasterly Cold Surges and Near-Equatorial Disturbances over the Winter MONEX Area During December 1974. Part II: Planetary-Scale Aspects

C.-P. CHANG AND K. M. W. LAU

Northeasterly Cold Surges and Near-Equatorial Disturbances over the Winter MONEX Area During December 1974. Part II: Planetary-Scale Aspects

C.-P. CHANG AND K. M. W. LAU

Department of Meteorology, Naval Postgraduate School, Monterey, CA 93940

(Manuscript received 11 June 1979, in final form 7 December 1979)

ABSTRACT

In Part I of this pre-winter MONEX study a synoptic analysis on the interaction between cold air surges off the East Asian continent and the synoptic-scale disturbances, especially their associated convection, in the equatorial South China Sea during December 1974 was carried out. In this paper we investigate some kinematic characteristics of the planetary-scale circulation changes during the same period in the midlatitudes and tropics in relation to the cold surges and the synoptic-scale disturbances.

The main findings suggest a picture of coherent variations of several planetary-scale circulation features which may be described by the following sequence of events:

1) The East Asia local Hadley circulation strengthens as the cooling due to cold air advection over northern China increases prior to a cold surge on the South China coast. This is accompanied by an intensified jet stream maximum centered over Japan, which is apparently a result of the upstream acceleration by the upper level poleward flow.

2) The jet stream maximum over Afghanistan–Pakistan varies inversely with the eastern jet maximum and appears to be related to a West Asia meridional circulation which becomes thermally indirect prior to the surge.

3) Immediately after a cold surge the convection associated with preexisting synoptic-scale disturbances in the equatorial South China Sea intensifies which causes the East Asia local Hadley circulation to reach its maximum intensity and also strengthens two east–west (Walker) cells along the equator.

4) Shortly ($\leq$1 day) after the surge the increased large-scale ascending motion over the equatorial South China Sea due to the continued strong convective activity associated with the synoptic disturbances contributes mainly to a further increase in the intensity of the two Walker cells.

The foregoing events suggest that the winter monsoon cold surge is basically a phenomenon controlled by the northern midlatitudes and its influences penetrate significantly equatorward into the tropics. The feedback into the Northern Hemisphere extratropics appears to be relatively unimportant.

1. Introduction

The importance of the northern winter monsoon as one of the most energetic heat engines in driving the earth's atmosphere has attracted ever-increasing attention from tropical meteorologists. Based on 200 mb winds at Saigon and Singapore, Ramage (1971) noted an increase in the strength of the local Hadley circulation when heavy rain spells occurred in peninsular Malaysia and Sarawak during the cold surge periods in the South China Sea. Bjerknes (1969) and Krishnamurti *et al.* (1973) showed the existence of strong east–west circulations in the equatorial latitudes in addition to the Hadley-type circulations. The strongest of these circulations has rising motions over the maritime continents of Indonesia and Borneo, connected meridionally by sinking motions over Siberia and South Australia and longitudinally by subsidence over the equatorial central Pacific and eastern Africa. In a compositing study Murakami and Unninayar (1977) observed that during periods of maximum eddy kinetic energy at 200 mb, which seems to correspond to monsoonal cold surges, the large-scale circulations are characterized by a strong jet stream over Japan and a deep 200 mb trough over the central North Pacific and an enhanced local Hadley cell over central China.

The winter phase of the Monsoon Experiment (Winter MONEX) during 1978–79 is designed to study several important questions of the winter monsoon. Among them are 1) northeasterly cold surges off the Asian continent and the convective disturbances in the near-equatorial South China Sea and vicinity, and 2) the manifestations and consequences of these interactions on the planetary-scale circulation over the entire monsoon region.

In Part I of this pre-MONEX study (Chang *et al.*, 1979; hereafter referred to as I) a detailed 850 mb/surface synoptic analysis of a sequence of cold

surges and near-equatorial disturbances over the Winter MONEX area of the South China Sea and vicinity during December 1974 was carried out. The results suggest that 1) extensive freshening of low-level northeasterlies associated with a surge penetrates rapidly into the equatorial South China Sea ahead of the more slowly progressing decrease in surface air temperature; 2) this decrease in surface temperature is generally confined to a narrow region in the western portion of the South China Sea just off the east coast of Vietnam, apparently due to the varying degree of air-sea interactions between the eastern and western portions of the surge air; and 3) the near-equatorial synoptic disturbances and their associated cumulus convection may be intensified or weakened depending on the degree of enhancement of the low-level convergence due to the northeasterly surges and/or the stabilizing effect due to the surface cold air incursion.

The purpose of this portion (Part II) of the study is to investigate the changes in the planetary-scale features, such as the Hadley-type or Walker-type circulations in relation to the synoptic events associated with the cold surges during December 1974. As in I, we will focus on the sequential change of events, except that the analysis will be based on the twice-daily upper troposphere data (200 mb wind and 300 mb temperature). This is in contrast to most previous studies of the planetary-scale winter monsoon which have been mostly limited to time-mean conditions (Krishnamurti *et al.*, 1973; Sadler, 1975) or compositing over selected periods of several days (Murakami and Unninayar, 1977; Murakami, 1977).

During December 1974 a total of four cold surges (see I) occurred in the South China Sea. The first two surges occurred within the period 3–13 December 1974 and were free from the influence of any typhoons. The last two surges occurred in the latter half of the month and coincided with the unusual (during winter) passage of typhoons in the South China Sea. In I we only analyzed the period of the first two surges because the widespread subsidence outside of the typhoons interferes with other convective systems and makes it very difficult to delineate the effects of the cold surges on the near-equatorial atmosphere. In this part we again concentrate on the large-scale features of the first period but since many large-scale features, especially those in midlatitudes, are less affected by the typhoons, our analyses are extended into the rest of the month whenever it is judged to be useful.

Although one December provides only a very limited sample for studying the general behavior of the planetary-scale circulation changes of the winter monsoon, the available detailed synoptic analysis at the surface/gradient level during the first half of this period (I) makes it possible to discuss the planetary-scale events in relation to the synoptic disturbances in the equatorial South China Sea. Furthermore, the interactions between the two scales of motion sometimes seem to be quite complex and variable. This is perhaps due to the often irregular behavior of the monsoonal surges and the synoptic disturbances in the South China Sea, as well as to the availability and quality of data in the region which themselves vary from time to time. We hope that through this detailed study of the December 1974 cases we can better delineate the possible relationships between the various circulation events thus providing some useful guidance for future statistical studies using a larger data sample over a longer period.

2. Data

The data set used in this study is based on the upper tropospheric wind data from the Fleet Numerical Weather Central global band objective analysis where wind analyses at 200 mb and temperature analyses at 300 mb from 1–31 December 1974 are available twice daily on a 49 × 144 mercator grid between 40°S and 60°N around the tropical belt. Analyzed data are also available at several other levels but the above levels are chosen due to the richness of commercial aircraft and satellite data. They are used along with radiation measurements from scanning radiometers aboard NOAA polar orbiting satellites. These satellite measurements are used by the National Environmental Satellite Service to produce twice-daily or daily coverage of outgoing longwave, available and absorbed solar radiation, from which the net radiation and the albedo can be computed.

The twice-daily zonal (u) and meridional (v) wind components at 200 mb are divided into a rotational part and a divergent part, i.e.,

$$\mathbf{V} = -\nabla\chi + \mathbf{k} \times \nabla\psi, \tag{1}$$

where the streamfunction ψ and the velocity potential χ are obtained by solution of the Poisson equations

$$\nabla^2\psi = \zeta = \left(\frac{\partial v}{\partial x} - \frac{\partial u \cos\phi}{\cos\phi \partial y}\right) \sec\phi, \tag{2}$$

$$\nabla^2\chi = -\delta = -\left(\frac{\partial u}{\partial x} + \frac{\partial v \cos\phi}{\cos\phi \partial y}\right) \sec\phi. \tag{3}$$

Here ζ and δ are the vorticity and divergence, respectively; and the horizontal coordinates in the mercator projection are taken as

$$x = a\lambda, \quad y = a \ln\left(\frac{1 + \sin\phi}{\cos\phi}\right), \tag{4}$$

where a is the radius of the earth, and λ and ϕ are longitude and latitude, respectively.

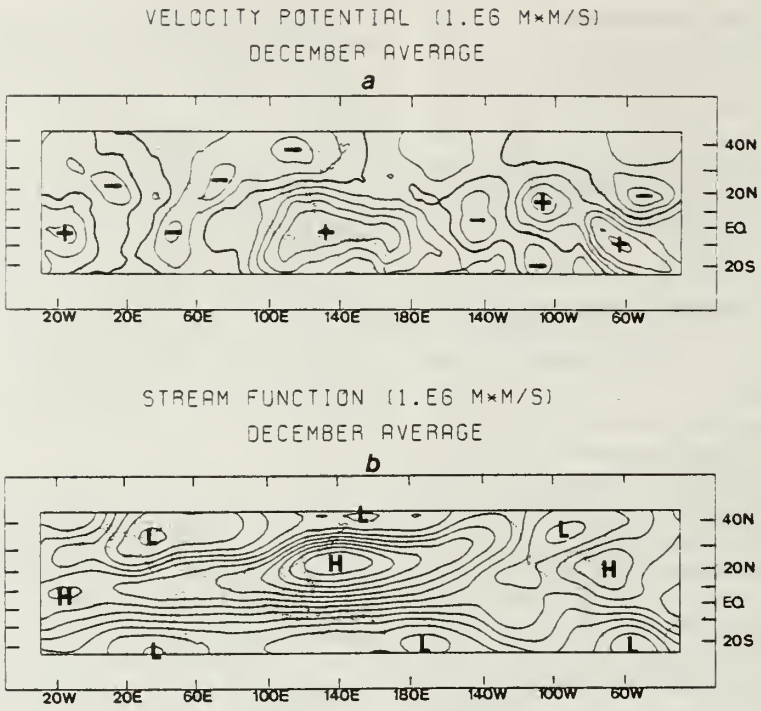

FIG. 1. Latitude-longitude sections of the monthly mean (December 1974) (a) 200 mb velocity potential in units of 10^6 m^2 s^{-1} at intervals of 2 units and (b) 200 mb streamfunction in units of 10^6 m^2 s^{-1} at intervals of 10 units. In (a) the positive and negative areas are separated by heavy lines.

As boundary conditions for (2) we assume $\chi = 0$ at 40°S and 60°N and the values for ψ at the northern and southern boundaries are obtained from the computed field using a method similar to that of Hawkins and Rosenthal (1965).

Since only 200 mb winds are analyzed, vertical motion is not explicitly calculated. However, it is reasonable to assume that large-scale overturnings in the troposphere have a deep vertical scale comparable to the tropospheric depth. Thus the 200 mb divergence distributions may be used to infer the horizontal distribution of the large-scale vertical motion. Furthermore, it will be assumed that for large-scale flow $\delta \propto \chi$. This assumption, although obviously involving error in the case where the flow pattern is not a single harmonic in x and y, seems acceptable in view of Krishnamurti *et al.*'s (1973) study.

3. Brief summary of the synoptic events

For convenience of later discussion the synoptic events in the South China Sea detailed in I during the first period of December 1974 are summarized here. Cold surges occurred in Hong Kong on 6 and 10 December, preceded by the passage of a cold front on 3 and 9 December, respectively. Within 12–24 h after both surges, a rapidly southward propagating freshening of the low-level northeasterly winds was traced to ~16°N. The convection associated with a relatively stationary cyclonic disturbance center (labeled C1 in I) off the northwest of Borneo was intensified by the increased northeasterlies within 24 h of the first surge (6–7 December), but later on weakened temporarily (8 December) by cold surface air incursion along the coast of Vietnam before being reintensified by the sustained northeasterlies when surface air temperature warmed up again (9–10 December). The second surge occurred at the same time as a new cyclonic center (C2) originating from the ITCZ of the western Pacific traversed westward across the central South China Sea north of C1. During 11–12 December C2 intercepted the northeasterly surge and became intensified while blocking off the southward penetration of the northeasterly winds. This plus the cyclonic funneling of surface cold air near the Vietnam coast by C2 apparently weakened the convection of C1 resulting in the rapid dissipation of the latter. At the end of the period (1200 GMT 12 December) C2 touched land on the Vietnam coast and split into two smaller vortices which dissipated within 24–48 h.

4. Results and discussion

a. Monthly mean conditions

Most of our discussion will focus on the tropical band between 40°E–140°W and 25°S–48°N, which

covers all major areas that are most likely to come under the influence of the winter monsoon of East Asia. However, for the sake of completeness the χ and ψ fields for the entire tropical belt between 15°S and 48°N will be displayed.

The monthly mean χ field for December 1974 (Fig. 1a) shows a broad region of 200 mb divergence over the maritime continent of Indonesia and Borneo with a small secondary maximum further to the east near 160°E). Another area of significant positive χ centers is found west of Mexico and the northern part of South America extending into the equatorial Atlantic. According to the assumptions described in Section 2, these centers indicate deep rising motion in the troposphere which is most likely due to the presence of strong heat sources. The location of this rising motion is consistent with the previous observation by Ramage (1968). Streamlines of divergent winds emanating from positive χ centers show that both north-south and east-west components are important in the overturning motions. Parts of the divergent flow originating from the South China Sea and maritime continent subside over a broad area over Asia with the maximum 200 mb convergence centered in North China, constituting a strong local Hadley cell which occupies a longitudinal span from East Asia to the western Pacific. Other parts of this divergent flow stretch along the equator in both directions to form two east-west, or Walker-type cells. The eastern Walker cell encompasses the equatorial western Pacific with a descending branch in the equatorial central Pacific. The western Walker cell extends across the Indian Ocean and Arabian Sea with a descending branch over the east coast of Africa.

In the monthly mean ψ field (Fig. 1b) the most outstanding feature is the presence of a prominent anticyclone to the northeast of the South China Sea in the western Pacific south of Japan. It takes up a somewhat west-southwest to east-northeast orientation and extends eastward into the north-central Pacific and westward to eastern Africa. North of this anticyclone is a cyclonic center over northern Japan which is separated from the anticyclonic center by a westerly jet stream extending from northwestern Tibet to the north central Pacific. South of this anticyclonic center is another anticyclonic center (Southern Hemisphere, ψ minimum) to the east of Australia with an easterly zonal flow over the maritime continent separating the two centers. Similar north-south distributions of cyclonic and anticyclonic centers, although less prominent, are found over the continents of North and South America, and Europe and Africa.

The westerly jet stream is strongest off the northeast coast of China. Blackmon *et al.* (1977) have shown that the upstream acceleration of the seasonal-mean jet core must be attributed to the strong mean poleward ageostrophic flow at the upper levels in the upstream longitudes where the convergence of eddy flux of westerly momentum is absent. The strong divergent flow of the local Hadley cell over East Asia shown in Fig. 1a is consistent with this argument. It is also interesting to note that the pairs of anticyclones straddling the equator are in accordance with the analyses of Matsuno (1966) who showed that such a distribution is a result of the geostrophic adjustment of the equatorial flow responding to a symmetric heat source.

b. Day-to-day variations of χ and ψ

Throughout the first half of December 1974 the 200 mb positive χ centers over the heat source regions of Sumatra, Indonesia and Borneo as well as those over northern South America stand out as semi-permanent features. However, large day-to-day variations exist within each region. The χ and ψ fields at 1200 GMT for 5–8 December are shown in Figs. 2 and 3. Prior to the cold surge on 6 December, the upward branch of the East Asia local Hadley cell indicated by the positive χ center is somewhat concentrated near the equator east of 140°E. At 1200 GMT 6 December, ~12 h after the cold surge is recorded in Hong Kong, a convergence area which indicates enhanced subsidence first appears over the northern East China Sea, reflecting a strengthening of cold air advection. Throughout the next 36 h, the convection associated with the near-equatorial cyclonic disturbance C1 (see I) continues to build up. This coincides with the time of the penetration of the northeasterly surface flow to the near-equatorial latitudes of the South China Sea. At this time (1200 GMT 7 December) the positive χ center over the equatorial western Pacific is seen to diminish substantially, and the upward branch of the local Hadley cell shifts westward to the southern South China Sea with an extensive downdraft region over central China. This agrees with the observed roughly 180° out-of-phase relationship between the synoptic-scale organized convection in the southern South China Sea and the equatorial western Pacific during the first half of the month (see I) and is likely a result of the suppressed convection by the widespread subsidence in adjacent regions outside the active convection centers. Meanwhile, two negative χ areas also appear in the equatorial region, one to the east centered near 160°W in the central Pacific, and another to the west centered near 50°E over the western Arabian Sea and the East African coast. This distribution implies the development of zonally oriented, Walker-type circulations on both sides of the vast heat source in the equatorial South China Sea. The 300 mb temperatures for zonal wavenumbers 1 and 2 (Fig. 4) indicate that these

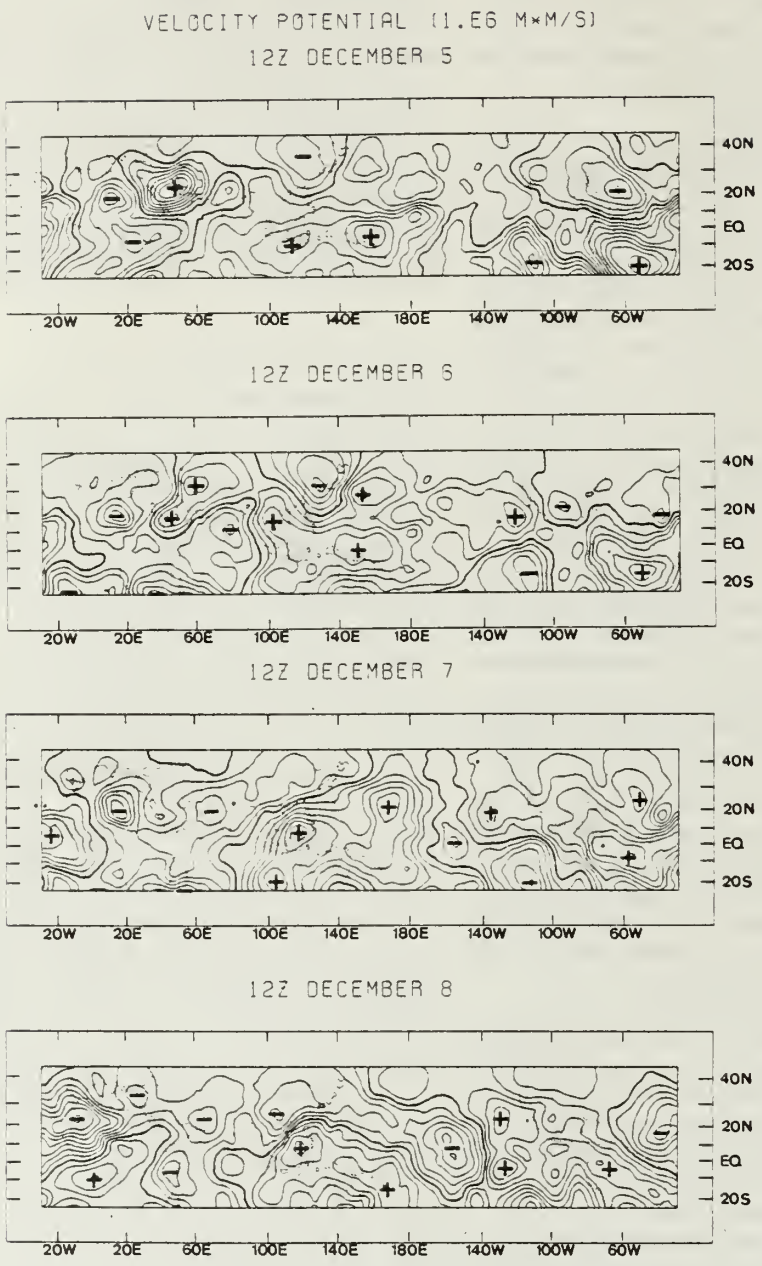

FIG. 2. As in Fig. 1a except for the velocity potential at 1200 GMT for the period 5–8 December 1974.

are thermally direct circulations. Judging from the gradient of the χ isopleths, the strength (~ 8 m s^{-1}) of these east-west circulations is comparable to that of the north-south circulations.

By 0000 GMT 8 December, the surface temperature analysis in I shows that a cold air tongue has penetrated southward along the Vietnam coast and apparently leads to a temporary weakening of the convection associated with the disturbance C1. The weakening is also reflected in the 200 mb χ field of 1200 GMT 8 December, where the χ maximum in the South China Sea shrinks noticeably from 12 h earlier. This χ maximum reintensifies again shortly after through 1200 GMT 9 December (not shown) together with the reintensification of C1 at that time. After 0000 GMT 10 December C1 begins to dissipate while another cyclonic disturbance (C2) propagates into the South China Sea from the western Pacific. The subsequent changes in position and intensity of the convection associated with C1 and C2 as described in I and Section 3 are reflected fairly closely by the changes in the positive χ

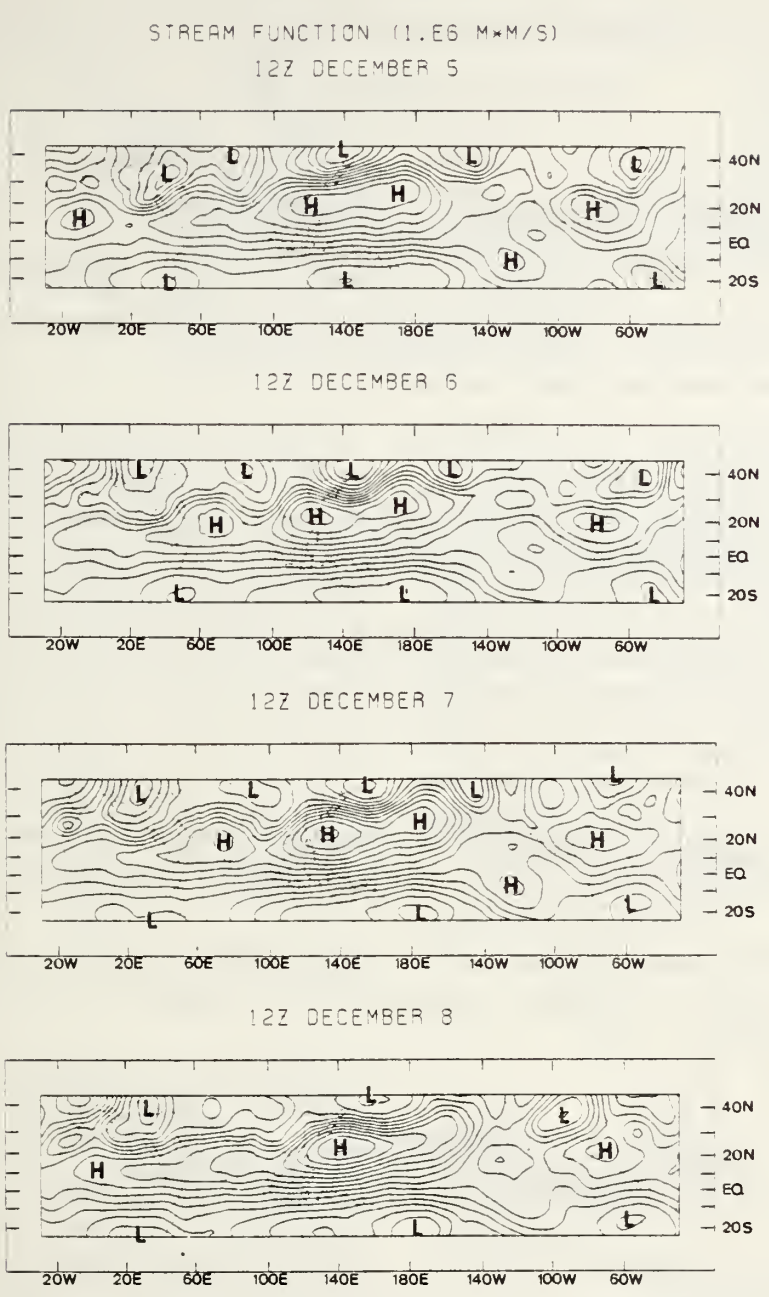

FIG. 3. As in Fig. 1b except for the streamfunction of 1200 GMT for the period 5–8 December 1974.

center over the South China Sea (not shown). This suggests that the upper tropospheric outflow responds sensitively and immediately to the synoptic-scale convection.

The ψ field of the first half of December 1974 shows that the anticyclonic center which fluctuates between the northern South China Sea and the western Pacific remains strong throughout the period. A slowly eastward moving upper-level trough near northern Japan is noted beginning 3 December (not shown), when a surface cold front passes Hong Kong. The trough is relatively shallow at this time but it causes the basically east-west ψ isopleths off the northeast coast of China to pack closely indicating an increase in the zonal flow over this area. This increase in the jet strength is apparently related to the local increase in baroclinicity of the middle troposphere. Danielson and Ho (1969) found that the outbreak of the Siberian cold air is usually accompanied by the rapid eastward movement of an upper level low east of Lake Baikal in Siberia. This increased baroclinicity is

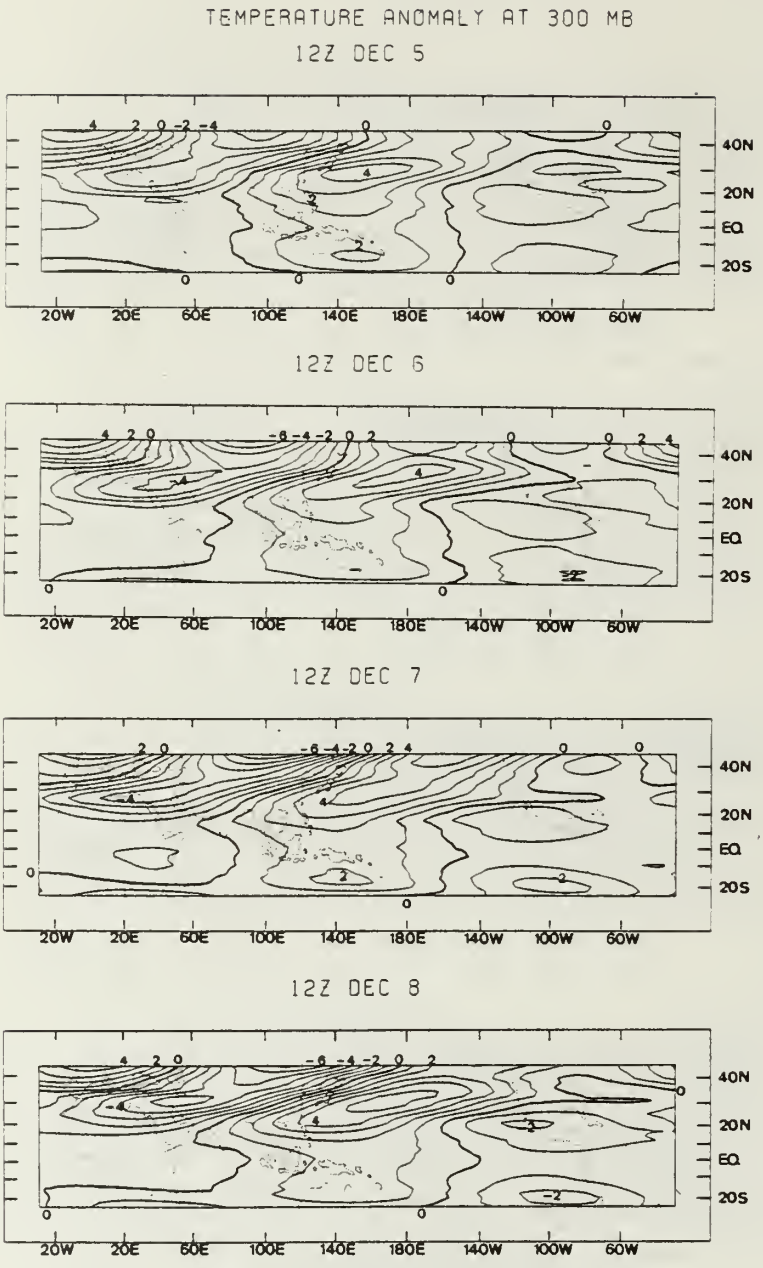

FIG. 4. As in Fig. 2 except for the temperature at 300 mb.

consistent with the observation that cyclonic activity picks up as an upper level trough migrates eastward over this region. According to Murakami (1977), these cyclones interact with an approaching upper level trough and develop into mature extratropical cyclones as they move eastward away from land with strong low-level northerly winds bursting out from the heart of the continent.

At the time of the first cold surge (1200 GMT 6 December), the upper level trough digs deeply southward giving a wavy appearance to the subtropical jet stream, which later (7–8 December) resumes a more zonal pattern. An upper level trough also appears on 10 December and intensifies on 12 December (not shown) over northern Japan, but its development is further to the north and not well shown in our domain.

c. Time series

To examine the causality of events, time series of several 200 mb large-scale circulation parameters averaged over selected regions for the entire month of December 1974 are constructed. These regions

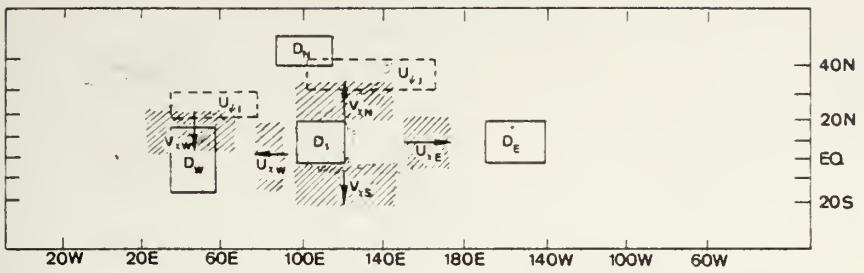

FIG. 5. Map showing different areas over which the parameters indicated are averaged. See text for the explanations of symbols.

are chosen to include those maxima of divergence, convergence, and χ and ψ gradients that appear to be connected with the cold surges and convective activities in the South China Sea as seen in the monthly mean charts of χ and ψ. The selected regions and parameters are shown in Fig. 5. Here in regions D_1, D_N, D_E and D_W the parameter is divergence, in regions $U_{\psi I}$ and $U_{\psi J}$ the parameter is the zonal component of the rotational part of the wind $(-\partial\psi/\partial y)$, in regions $U_{\chi W}$ and $U_{\chi E}$ the parameter is the zonal component of the divergent part of the wind $(-\partial\chi/\partial x)$, and in regions $V_{\chi N}$, $V_{\chi S}$ and $V_{\chi W}$ the parameter is the meridional component of the divergent part of the wind $(-\partial\chi/\partial y)$. In the time series diagrams the dates of the frontal passage and recorded minimum surface temperature in Hong Kong are denoted by F and C, respectively, on the time axis.

1) 200 MB DIVERGENCE OVER SOUTH CHINA SEA AND BORNEO

The upper part of Fig. 6 shows the time series of D_1 which is the area-averaged 200 mb divergence over the equatorial South China Sea and Borneo. In this figure a smoothed curve (heavy line) is drawn based on the unsmoothed time series (thin line). It may be seen that the former has five maxima, the first four of which are labeled M1–4 in the diagram. For the first two surge cases D_1 starts to increase almost at the same time as the cold fronts preceding the surges pass Hong Kong, i.e., a time *before* the cold air reaches the South China Sea, and then appears to be further enhanced reaching a maximum ~1–2 days after the cold surge in Hong Kong. The correlation between D_1 and the deep convective activities in the South China Sea is quite obvious, with the unsmoothed curve showing a variation during M1 that corresponds well to the intensification (on 7 December), temporary weakening (on 8 December) and re-intensification of the cyclonic disturbance C1. In addition, the strong peak of M2 on 11 December clearly indicates the enhanced upward motion associated with the disturbance C2 as it moves eastward across the South China Sea when the second surge in Hong Kong occurs. These correspondences are also confirmed in the radiation measurements from the NOAA satellites averaged over region D_1 (Fig. 7). The predominant maxima in the albedo and minima in the outgoing longwave radiation on 7 and 11 December points to a large increase in high cloudiness. [According to Winston and Krueger (1977) a value < 250 W m^{-2} in the outgoing radiation would indicate, in tropical latitudes, a large amount of cloudiness reaching to high tropospheric levels whereas an albedo > 0.3 is likely to mean the presence of highly reflected clouds associated with cumulonimbus activities from organized deep convection.]

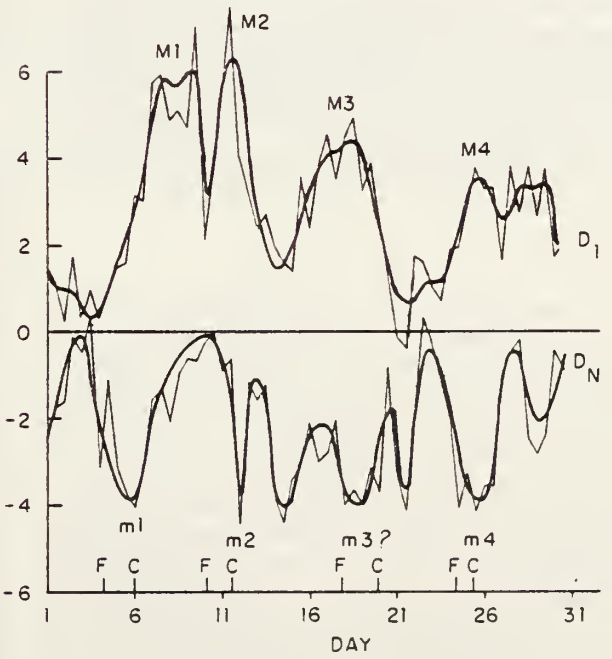

FIG. 6. Area-averaged divergence over regions D_1 and D_N in units of 10^{-6} s^{-1}. Twice daily values are indicated by thin lines and the best fitting curves by heavy lines. The symbols M1–4 and m1–4 denote respectively the maxima and minima in D_1 and D_N corresponding to the major cold surges of the month. On the horizontal axis, the letters F and C denote dates of frontal passage and recorded minimum surface temperature in Hong Kong.

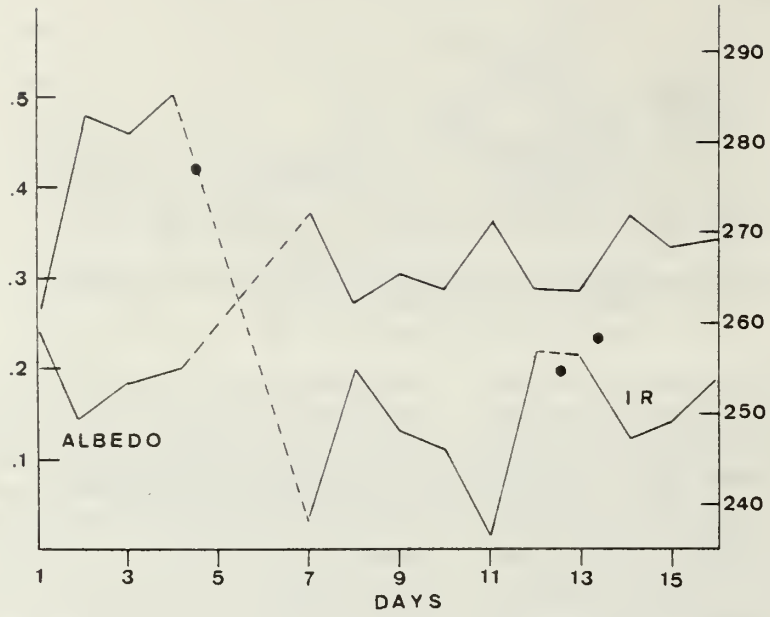

FIG. 7. Day IR radiation (W m^{-2}) and albedo over region D_1 during the period 1–15 December 1974. Dotted lines indicate interpolations for missing data, and the black dots indicate night IR radiation.

During the second half of the month, M3 precedes a cold surge in Hong Kong by ~1 day and M4 occurs almost simultaneously with a surge in Hong Kong. This is a period when the South China Sea is under the influence of typhoons and the phase of D_1 with respect to the cold surges is obviously interfered by the typhoons.

For easy comparison the D_1 curve will be included in the diagram of several other time series.

2) HADLEY-TYPE CIRCULATIONS

The parameter D_N is shown in the lower part of Fig. 6 which represents the 200 mb divergence over northern China. Here it is predominantly negative reflecting the descending branch of the local Hadley cell over the cold land surface in East Asia. For all four surge cases, a decrease of the 200 mb convergence is seen a few days prior to each frontal passage in Hong Kong, with a rapid increase in convergence occurring slightly before the frontal passage except for the second surge when the two events are approximately simultaneous. In Fig. 6, four minima of D_N are labeled by m1–4. (The choice of m3 is less certain than others.) Only those which appeared to correspond to the four cold surges in the South China Sea are labeled. The other minima may be related to other events not discussed here, e.g., the convergence that may be associated with an eastward moving front at the latitude of D_N. Comparing the D_N to D_1 curves, we notice the following for the first two surges:

(i) Before each surge occurs in Hong Kong, both the divergence over the South China Sea (D_1) and the convergence over northern China ($-D_N$) increase almost simultaneously indicating the strengthening of the northern local Hadley cell.

(ii) For the first surge case D_1 continues to increase after the surge in Hong Kong. This is apparently due to the intensification of the convective activities associated with the cyclonic disturbance C1, but this increase of the upward motion over the South China Sea apparently does not feed back into the downward branch of the local Hadley cell since $-D_N$ begins to fill immediately as the surge passes Hong Kong.

(iii) For the second surge case both the increase prior to and decrease after the surge in D_1 and $-D_N$ are very rapid. The whole event takes place within ~2–3 days, and apparently responds to the intensification and collapse of the cyclonic disturbance C2 as it traverses across the South China Sea. The convergence over northern China continues its increase ~12 h after the cold surge in Hong Kong, but it is difficult to determine whether this reflects a local Hadley cell feedback from the South China Sea divergence because of the short time span of the whole event.

The roughly 180° out-of-phase relationship for major fluctuations between D_1 and D_N is still evident around the fourth surge case even though typhoon activities affect the second half of the month. This relationship manifests the vacillations in the northern

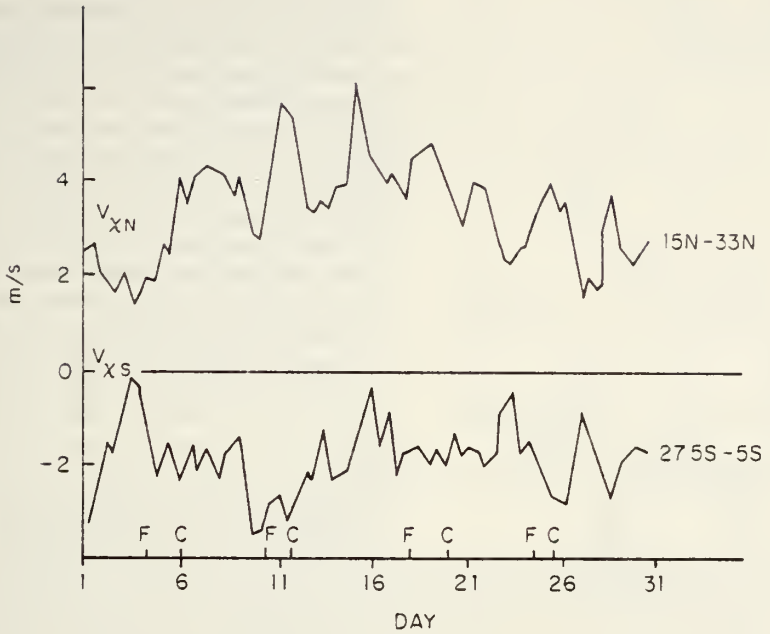

FIG. 8. Time-series of the meridional component of the divergent part of the wind ($-\partial\chi/\partial y$) averaged over the area indicated by $V_{\chi N}$ and $V_{\chi S}$ in Fig. 5.

local Hadley circulation in relation to the cold surges. Another view of these vacillations may be obtained by examining the zonally averaged (100–160°E) divergent component of the 200 mb meridional wind, $V_{\chi N}$ (for 15°N–33°N) and $V_{\chi S}$ (for 5°S–27.5°S). Fig. 8 shows both time series. Comparing to D_1, it is obvious that for surges 1, 2 and 4 the increases in the divergence over the South China Sea are correlated to an increase of ~2–3 m s^{-1} in the northward divergent velocity. There are also some indications of increased southward divergent velocity especially for surges 2 and 4, but these increases appear to be less significant compared to those of the northward divergent velocity. The facts that D_1 starts to increase almost simultaneously with $V_{\chi N}$ (and $-D_N$) prior to the intensification of convection associated with the near-equatorial disturbances in the South China Sea, and that the increase of the northward divergent winds occurs with little time lag between different latitude bands between the equator and 33°N (not shown), suggest that the initial increase in the divergence over the equatorial South China Sea may be directly related to the increased cooling and its associated subsidence in the north via the local Hadley circulation. This near-simultaneous development across a large span of latitudes is consistent with the observation by Ramage (1971, pp. 159–160) in the surge case of 16 January 1967. The enhanced convection in the South China Sea due to the cold surges, however, contributes significantly in a later stage to further increase or sustain the local Hadley circulation.

3) WALKER-TYPE CIRCULATIONS

As described earlier, the monthly-mean and daily 200 mb velocity potential fields clearly depict the existence and variations of Walker-type east-west overturning motions. Figs. 9 and 10 show that the 200 mb divergence over the equatorial central

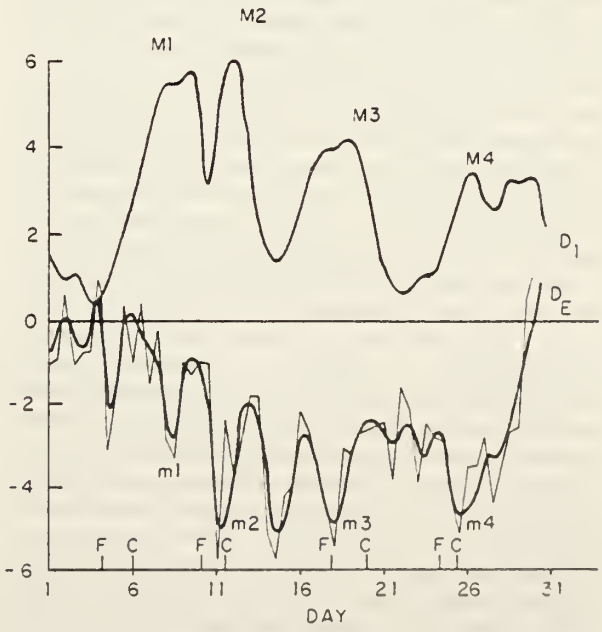

FIG. 9. As in Fig. 6 except for the area-averaged divergence over D_E. The curve for D_1 is included for comparison.

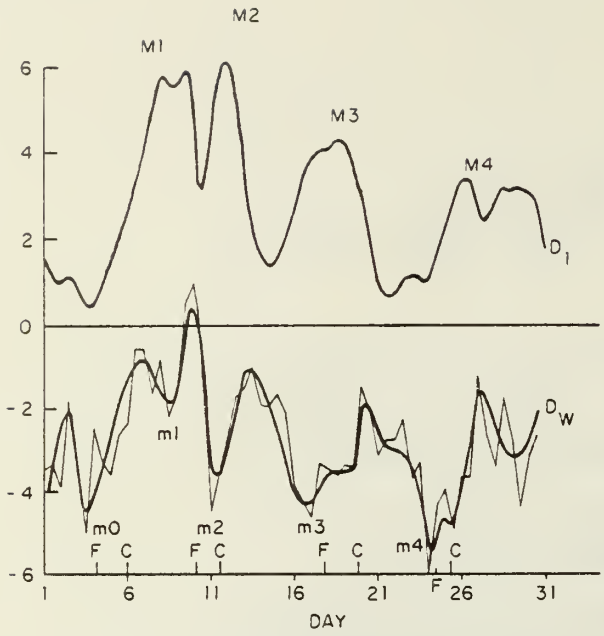

FIG. 10. As in Fig. 9 except for the area-averaged divergence over D_W.

Pacific, D_E, and that over the western Arabian Sea and East African coast, D_W, are both predominantly negative indicating sinking motion of the Walker cells. In addition, both time series show a negative correlation with that of D_1, although the correlation is higher for D_W than for D_E. In the D_W series approximately five minima stand out conspicuously. The last four minima may be identified with the four surge events. (The first one is labeled m0 and will be discussed later). On the other hand, the fluctuation in the D_E series is of higher frequencies and the four minima identified with the surges represent only about half of the fluctuations. Thus the South China Sea convective appears to influence the western Arabian Sea-East Africa area more than the central Pacific. During the first surge case the increase of convergence over both regions ($-D_E$ and $-D_W$) begins after the surge in Hong Kong, when D_1 has already increased about halfway. In the discussion of the local Hadley circulation we have pointed out that $-D_N$ increases with D_1 prior to the first surge in Hong Kong. Thus it appears that the local Hadley circulation is enhanced first by the increased cold advection over northern China, which almost simultaneously causes the upper level divergence over the equatorial South China Sea to increase and reach its maximum one day after the surge in Hong Kong. Most of this increased outflow then diverges out both eastward and westward resulting in the subsequent enhancement of the eastern and western Walker cells with sinking motions in the central Pacific and the western Arabian Sea-East Africa area, respectively.

The increase and subsequent decrease of $-D_E$ and $-D_W$ around the second surge in Hong Kong are, similar to those of D_1 and $-D_N$, quite abrupt and remarkable. Hence in this surge case the increase of cooling over northern China leads immediately to an intensification of the South China Sea convection and the strengthening of both the local Hadley and the eastern and western Walker cells. The lack of a time lag in the enhancement of the Walker cells is probably due to the immediate response of the convection associated with the westward propagating disturbance C2 (see I), which is in the path of the penetrating northeasterlies at the time of the second surge. The rapid collapse of this convection as C2 touches land on the Vietnam coast results in an immediate weakening of the Walker cells.

Throughout the remaining period of the month, the correspondence between D_1 and $-D_E$, $-D_W$ are still quite good despite the typhoon activities. This is probably indicative of stronger influence by the South China Sea convection and upward motion on the downward branches of the equatorial Walker cells compared to that of the local Hadley cell which is in midlatitudes.

Fig. 11 shows the divergent zone velocities $U_{\chi E}$ and $U_{\chi W}$ both averaged in a maximum zonal χ-gradient area on the east and west sides of D_1, respec-

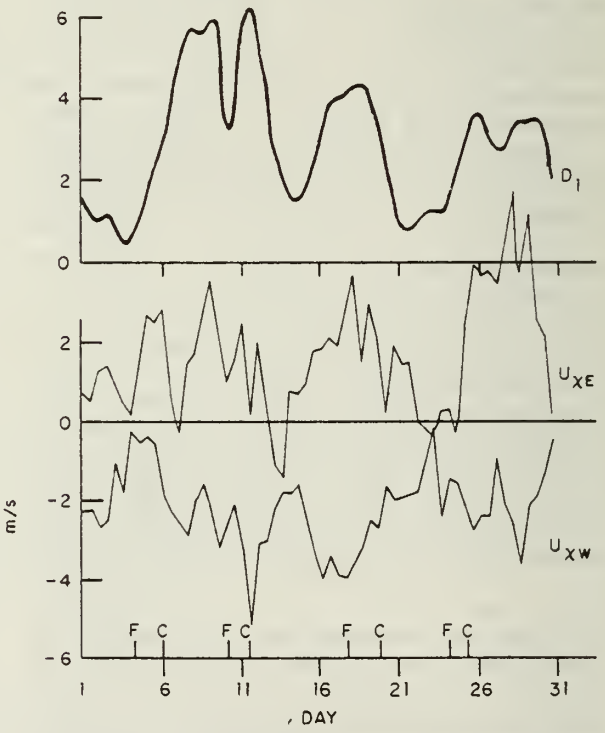

FIG. 11. Time series of zonal component of the divergent part of the wind ($-\partial\chi/\partial x$) averaged over areas $U_{\chi E}$ and $U_{\chi W}$ indicated in Fig. 5.

6.2

tively. The general in-phase relationship between D_I and $U_{\chi E}$ and the 180° out-of-phase relationship between D_I and $U_{\chi W}$ throughout the month are clearly evident in this figure, and a closer examination reveals the slight time lag of the strengthening of the U_χ's compared to the increase of D_I in the first surge case. In the second surge case the abrupt development shows up by an increase of ~1.5 m s^{-1} for the outflow toward the east and ~4 m s^{-1} toward the west, which are comparable to the increase of the corresponding local Hadley cell. The magnitudes of these outflows again indicate that the influence via the Walker cells by the South China Sea convection on the western Arabian Sea-East African regions is stronger than on the central Pacific region.

4) JET STREAMS

Fig. 12a shows the time series of the area-averaged zonal component of the rotational part of the velocity, $U_{\psi J}$ and $U_{\psi I}$, and Fig. 12b, the area-averaged total zonal wind U_J and U_I. The index J, I denotes, respectively, the areas from eastern China to the western North Pacific centered in Japan, and from Saudi Arabia to northwestern India. Although the strength of the jet streams over these regions are likely to be represented more accurately by the total zone wind, comparison of Fig. 12a with Fig. 12b shows that while the magnitudes of the rotational wind components $U_{\psi J}$, $U_{\psi I}$ are only ~60–70% of the total wind U_J, U_I, the major maxima (labeled by M1–4) and minima (labeled by m1–4) of the corresponding time series occur at almost the same time. Therefore the rotational part of the wind in this

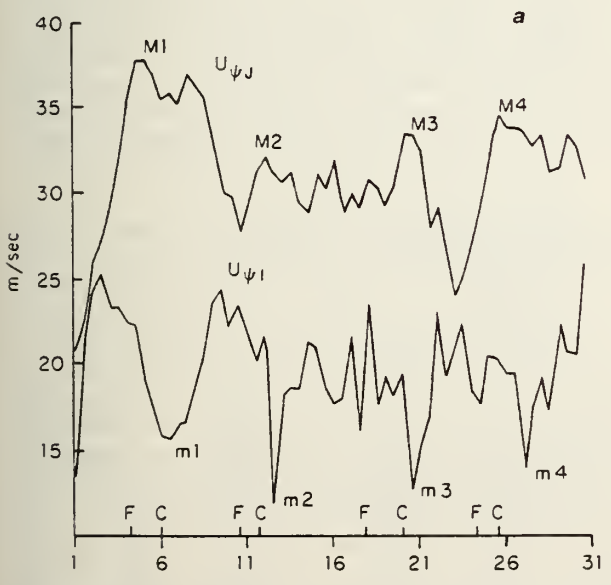

FIG. 12a. As in Fig. 11 except for the zonal component of the rotational part of the wind ($-\partial\psi/\partial y$) averaged over the area $U_{\psi J}$ and $U_{\psi I}$ indicated in Fig. 5.

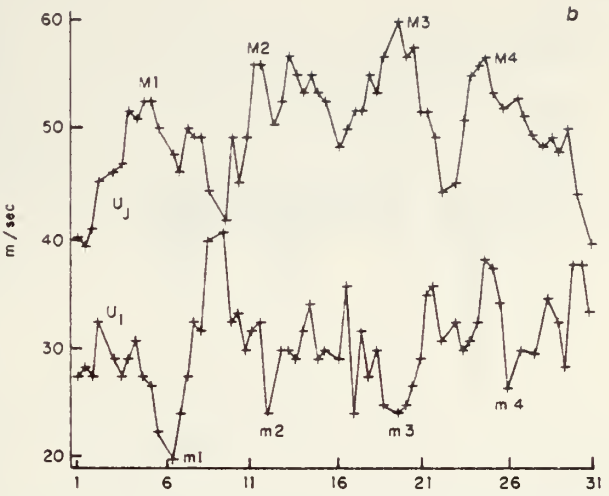

FIG. 12b. Same as Fig. 11 except for the total zonal component of the wind U_J, U_I.

case is a fairly good indication of the variation of the jet streams over the above regions. In the following we have used the U_ψ series as the basis of our discussion.

From Fig. 12a it is readily seen that $U_{\psi J}$ and $U_{\psi I}$ are negatively correlated with a slight time lag. The East Asia jet stream increases in every one of the four cases before a surge occurs in Hong Kong and reaches maximum near the time of the surge in Hong Kong. In each case $U_{\psi I}$ starts to decrease ~12 h after $U_{\psi J}$ starts to increase, and reaches minimum just slightly ($\lesssim$1 day) after the surge in Hong Kong.

The increase of $U_{\psi J}$ preceding the surges has been observed by Murakami and Unninayar (1977) and is indicative of the increase in the baroclinicity over East Asia. The local Hadley cell connecting regions D_I and D_N is situated upstream of $U_{\psi J}$. According to Blackmon *et al.* (1977), the upstream acceleration of the seasonal mean jet stream can only be explained by the upper level poleward flow associated with the meridional circulation. If we transform this argument into the time variation of the jet maxima, the increase of $U_{\psi J}$ prior to each surge case coincides with the strengthening of the local Hadley cell and is therefore likely a result of the latter event.

In the $U_{\psi I}$ time series, four distinct minima are evident within 1–2 days after each surge. The possible explanation of the behavior of this time series is less obvious since a conspicuous local Hadley cell is not identified in the monthly-mean χ field. In the absence of other evidence, the most direct explanation would depend on the decelerating mechanism of an anomalous local meridional circulation in the reversed Hadley sense. To examine this possibility further, we construct the time series of $V_{\chi W}$ (Fig. 13) which is the area-averaged 200 mb divergent meridional velocity between equator–25°N and 30–60°E

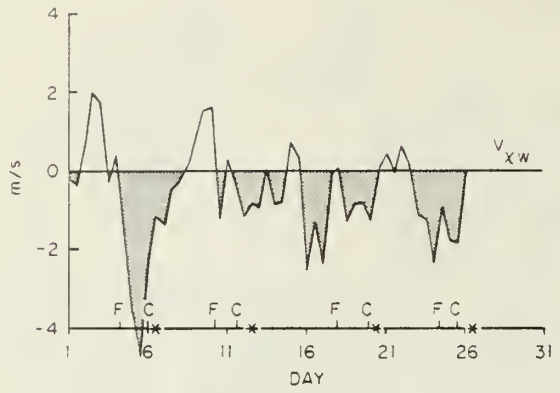

FIG. 13. As in Fig. 8 except for the area $V_{\chi W}$ indicated in Fig. 5. The asterisk on the abscissa denotes the time of occurrence of minimum of $U_{\psi I}$.

in the upstream region of $U_{\psi I}$. Here it is seen that prior to the occurrence of each minimum of $U_{\psi I}$, $V_{\chi W}$ is usually negative for a few days with the first decrease of $V_{\chi W}$ being most remarkable and apparently causing the minimum m0 in the western Arabian Sea-East Africa divergence D_W (Fig. 10). Hence it seems reasonable to attribute, at least partially, the deceleration of $U_{\psi I}$ prior to the surge to the appearance of a reversed local Hadley cell upstream.

There is, however, still no explanation for the highly negative correlation between $U_{\psi I}$ and $U_{\psi J}$. Since the reversed local Hadley circulation is upstream of the $U_{\psi I}$ maximum in the spatial accelerating region, it requires an energy source such as a convergence of eddy momentum fluxes at the upper level or a strong eddy heat flux at the lower level. At this state we can only surmise that one or both of these eddy processes occur in the $V_{\chi W}$ region which is somehow influenced by the events in East Asia. More work, especially on the calculation of eddy fluxes as a function of time, is needed in order to answer this question. Nevertheless, we may infer from the occurrence of the anomalous reversed local cell that an east-west, probably thermally direct, circulation may appear in the midlatitudes during the East Asia cold surges with rising motion over West Asia and sinking motion over northern China. However, because the tropopause is lower and the cold air over northern China is confined to the lowest levels of the troposphere, this midlatitude east-west circulation would be much shallower than the equatorial Walker cells.

5) THERMAL STRUCTURE OF OVERTURNING CIRCULATIONS

As mentioned in Section 4b, when the day-to-day variations of the χ field are compared with the zonal wavenumbers 1 and 2 temperature at 300 mb, we can identify the east-west Walker cells to be thermally direct circulations. In order to assess the variation of the strength of these direct circulations, the covariance of $\overline{T'\chi'}$ at 15°N, equator and 15°S for wavenumbers 1 and 2 at 0000 GMT during 3–12 December 1974 are shown in Table 1. Here T is the 300 mb temperature, the overbar indicates a zonal average, and the prime indicates the departure from this average. Since we assume χ is positively correlated with the upper level divergence and therefore the vertical motion in the troposphere, it is clear that throughout the period the planetary-scale east-west overturnings are thermally direct in the entire equatorial belt. (The only exception is 3 December at 15°N.) The intensity of this circulation reaches maximum at the equator and 15°S on 7 December which is 1 day after the first surge in Hong Kong, and the primary contribution comes from wavenumber 2. It reaches maximum again on 11 December at all three latitudes coinciding with the second surge in Hong Kong, and with wavenumber 1 dominating the energy conversion this time. We may recall that the South China Sea cyclonic disturbance C1, which is intensified as a consequence of the first surge, is located near 7°N

TABLE 1. Daily variation of $\overline{T'\chi'}$ for wavenumbers 1 and 2 during 3–12 December 1974. Units are in 10^6 °C m² s⁻¹.

Date (December 1974)	Latitude 15°N $\overline{T'_1\chi'_1}$	15°N $\overline{T'_2\chi'_2}$	15°N Σ 1, 2	0° $\overline{T'_1\chi'_1}$	0° $\overline{T'_2\chi'_2}$	0° Σ 1, 2	15°S $\overline{T'_1\chi'_1}$	15°S $\overline{T'_2\chi'_2}$	15°S Σ 1, 2
3	−3.2	1.4	−1.8	−0.7	1.6	0.9	−0.3	0.7	0.4
4	0.6	1.2	1.8	−0.2	1.3	1.1	−1.2	1.4	0.2
5	1.4	0.1	1.5	0.6	1.6	2.2	0.1	1.9	2.0
6	0.7	0.4	1.1	0.3	1.1	1.4	0.5	0.7	1.2
7	−0.9	1.7	0.8	0.5	2.7	3.2	1.0	2.5	3.5
8	1.9	−0.7	1.2	0.4	0.2	0.6	0	1.3	1.3
9	1.4	−1.0	0.4	0.3	0.1	0.4	−0.1	1.2	1.1
10	0.9	−0.5	0.5	0.6	0.5	1.1	−0.2	0.8	0.6
11	2.3	0.3	2.0	2.2	0.5	2.7	2.3	1.2	3.5
12	0.5	1.5	2.0	1.6	0.1	1.7	2.1	0.9	3.0

while the disturbance C2, which is intensified by the second surge, propagates along ~14°N. This position difference probably accounts for the difference in the covariance of $\overline{T'\chi'}$ at 15°N between the two events. The development of the synoptic disturbances cannot be readily used to explain why in both cases comparable enhancement of thermal energy conversion occurs in the southern latitudes. Apparently the activity of the upward motion branch of the Walker cells covers a broad area over the South China Sea and the maritime continents and is not limited to just the center of the synoptic disturbances.

The postulated midlatitude east-west circulation cannot be examined by $\overline{T'\chi'}$ because such a circulation, if it exists, is most probably confined entirely to levels below 300 mb.

A similar covariance between the 300 mb temperature and 200 mb χ may be calculated for the local Hadley circulations. This is shown in Table 2, which includes $[T^*\chi^*]$ at six longitudes: 40°E, 80°E, 120°E, 160°E, 160°W and 120°W during 3–12 December 1974. Here the bracket indicates a north-south average between the belt 25°S–48°N, and the stars indicate the departure from this average. It is apparent that throughout the period this covariance is positive between 80 and 160°E, with maximum values every day occurring at 120°E along the East China coast. In addition, the magnitude at this longitude increases from 3 December until its first maximum on 7 December, which is one day after the first surge in Hong Kong. It then decreases somewhat through 10 December followed by a sudden increase to the next maximum on 11 December, corresponding to the second surge in the South China Sea. These variations of the thermally direct energy coversion for the East Asian local Hadley cell are consistent with the evolution of the circulation as inferred from D_1, D_N and $V_{\chi N}$.

Along 40°E, which is upstream of the West Asia jet, the $[T^*\chi^*]$ covariance is mostly negative. Compared to Fig. 13, it is seen that the equatorward acceleration of $V_{\chi W}$ between 3–5 December and between 10–11 December do correspond to periods of indirect thermal energy coversion. The magnitude of $[T^*\chi^*]$, however, is smaller compared to that along 120°E and the variations appear to be more irregular.

In general the magnitude of the covariance for the local Hadley cell is larger than those of the Walker cells. This is expected because the north-south temperature gradients in the subtropics and midlatitudes are much larger than the east-west gradients along the equator.

5. Concluding remarks

In order to study the planetary-scale circulation changes in relation to the winter monsoon cold surges, we have investigated the December 1974 upper tropospheric data with an emphasis on temporal variations of the kinematic characteristics of the motions. A total of four cold surges occurred in the South China Sea during this period, although only the first two were free from any typhoon influences. The following summary of time sequence of events is mostly based on all four surge cases, except that pertaining to the post-surge East Asia local Hadley cell which is based only on the first two surge cases:

1) Prior to the occurrence of a cold surge on the South China coast, the cooling due to cold advection over northern China increases; this strengthens the East Asia local Hadley circulation through increased sinking motion.

2) Almost simultaneous with the strengthening of the heat sink in northern China, the East Asia jet stream centered near Japan intensifies as a result of the upstream acceleration which is due to increased upper level ageostrophic flow associated with the enhanced local Hadley circulation.

3) The variation of the West Asia jet stream centered over Afghanistan and Pakistan is out of phase with that of East Asia jet stream, with the minimum of the latter lagging slightly the maximum of the former. The apparent inverse relationship may be due to the Coriolis deceleration by the upper level equatorward meridional wind which is found upstream of the jet prior to and during the surge. This meridional wind also implies the possible occurrence of a reversed local Hadley-type circulation.

4) The rapid eastward movement of an upper level trough which deepened over northern Japan appears to be a precursor to the outbreak of north-easterly cold air along the South China coast.

5) Immediately after a cold surge, the convection associated with pre-existing synoptic-scale disturbances in the equatorial South China Sea will intensify thereby sustaining or increasing the already enhanced local Hadley circulation.

TABLE 2. Daily variation of $[T^*\chi^*]$ at different longitudes during 3–12 December 1974. Units are in 10^6 °C m^2 s^{-1}.

Date (December 1974)	Longitude					
	40°E	80°E	120°E	160°E	160°W	120°W
3	−8	18	20	14	0	12
4	−20	21	25	20	−8	−2
5	−1	17	38	10	−8	−10
6	16	2	40	10	0	−5
7	−4	17	52	23	2	−8
8	2	20	43	18	−10	4
9	16	18	38	14	−8	2
10	−18	26	33	10	−20	0
11	−20	30	64	30	−15	−19
12	−4	21	35	15	5	−1

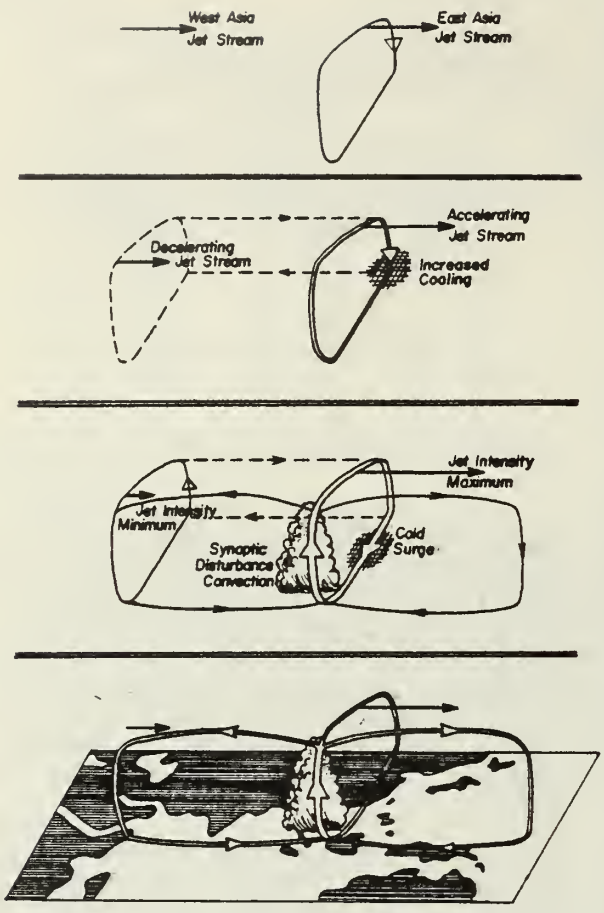

FIG. 14. Schematic diagram showing the sequence of events before and after the cold surge in the South China Sea. See text for details.

6) However, the strengthening of the local Hadley cell does not continue too long (beyond one day) after the surge, as the upper tropospheric outflow from the South China Sea region also accelerates along the equator toward both the central Pacific and the east coast of Africa thereby strengthening the east and west Walker cells. This indicates that while the near-equatorial convection is affected by fluctuations in the cold air outbreak from the northern midlatitudes, their influence does not necessarily feed back significantly into the northern extratropical circulations. Thus the cold surge appears to be a largely northern midlatitude controlled phenomenon which extends its effects deeply into a wide equatorial belt.

The above series of events is also summarized in a schematic diagram shown in Fig. 14. Here the four panels indicate the time sequence of events which may repeat itself in the case of periodic surges. The intensities of the jet streams are represented by their relative length and the intensities of the overturning circulations are represented by their relative width. Since Blackmon *et al.* (1977) reported the requirement of a thermally indirect circulation downstream of the seasonal mean jet maxima over the oceanic regions in order to account for the deceleration of the jet stream, it is possible that such circulations do exist and vacillate along with those shown in Fig. 14.

It should be emphasized that because of the constraint by the requirement of comparing the planetary- and synoptic-scale events, the present study is limited to one December only. The results obtained can only be viewed as suggestive. In order to clarify some of the less certain aspects an investigation based on compositing a much larger sample of data is currently being planned.

Acknowledgments. We wish to thank Fleet Numerical Weather Central and National Environmental Satellite Service/NOAA for providing the data used in this study, and Mr. S. K. Rinard for his help in data processing. This research was supported by National Science Foundation, Global Atmospheric Research Program, under Grant ATM77-14821, and by National Oceanic and Atmospheric Administration under Contracts 7-11030 and NA-79AAG03158.

REFERENCES

Bjerknes. J., 1969: Atmospheric teleconnections from the equatorial Pacific. *Mon. Wea. Rev.*, **97**, 163–172.

Blackmon, M. L., M. J. Wallace, N.-C. Lau and S. L. Mullen, 1977: An observational study of the Northern Hemisphere wintertime circulation. *J. Atmos. Sci.*, **34**, 1040–1053.

Chang, C.-P., J. E. Erickson and K. M. Lau, 1979: Northeasterly cold surges and near-equatorial disturbances over the Winter MONEX area during December 1974. Part I: Synoptic Aspects. *Mon. Wea. Rev.*, **107**, 812–829.

Danielson, E. F., and F. P. Ho, 1969: An isentropic trajectory study of a strong northeast monsoon surge. Sci. Rep. No. 2, AFCRL-69-0036, Hawaii Institute of Geophysics, 13 pp. [Available from Dept. of Meteorology, University of Hawaii, Honolulu.]

Hawkins, H. F., and S. L. Rosenthal, 1965: On the computation of streamfunction from the wind field. *Mon. Wea. Rev.*, **93**, 245–252.

Krishnamurti, T. N., N. Kanamitsu, W. J. Koss and J. D. Lee, 1973: Tropical east-west circulations during the northern winter. *J. Atmos.Sci.*, **30**, 780–787.

Matsuno, T., 1966: Quasi-geostrophic motions in the equatorial area. *J. Meteor. Soc. Japan*, **44**, 25–41.

Murakami, T., 1977: Changes in regional energetics over the North Pacific. South China and the Indonesian Sea during winter. *Mon. Wea. Rev.*, **105**, 1508–1520.

——, and M. S. Unninayar, 1977: Atmospheric circulation during December 1970 through February 1971. *Mon. Wea. Rev.*, **105**, 1024–1038.

Ramage, C. S., 1968: Role of a maritime continent on the atmospheric circulation. *Mon. Wea. Rev.*, **96**, 365–370.

——, 1971: *Monsoon Meteorology*. Academic Press, 296 pp.

Sadler, J., 1975: The upper tropospheric circulation over the global tropics. Tech. Rep. 75-05, Dept. of Meteorology, University of Hawaii, 35 pp.

Winston, J. S., and A. F. Krueger, 1977: Diagnosis of the satellite-observed radiative heating in relation to the summer monsoon. *Pure Appl. Geophys*, **115**, 1131–1144.

Reprinted from Monthly Weather Review, Vol. 108, No. 7, July 1980
American Meteorological Society
Printed in U. S. A.

The Structure and Vorticity Budget of an Early Summer Monsoon Trough (Mei-Yu) over Southeastern China and Japan

Tai-Jen George Chen[1] and Chih-Pei Chang

Department of Meteorology, Naval Postgraduate School, Monterey, CA 93940

(Manuscript received 5 July 1979, in final form 28 February 1980)

ABSTRACT

One of the most persistant rain-making events over East Asia is the development of an early summer monsoon trough (Mei-Yu) which extends from southeastern China to southern Japan. This work studies the structure and vorticity budget of a Mei-Yu system for the period 10–15 June 1975.

Subjectively analyzed grid-point data are time composited with respect to the trough axis along three cross sections over southeastern China (western section), southern East China Sea (central section) and southern Japan (eastern section), respectively, during the mature and decaying stages of the trough. The results indicate that the structure of the eastern and central sections resembles a typical midlatitude baroclinic front with strong vertical tilt toward an upper level cold core and a strong horizontal temperature gradient. On the other hand, the western section resembles a semitropical disturbance with an equivalent barotropic, warm core structure, a weak horizontal temperature gradient, and a rather strong horizontal wind shear in the lower troposphere.

Cumulus convection activity south of the 850 mb trough is significant in all three sections and contributes substantially to the thermally direct secondary circulation, but the large-scale organizing mechanism differs from one section to another. In the eastern and central sections it is mainly due to differential vorticity advection while in the western section it is due to Ekman pumping (CISK). The generation of cyclonic vorticity is counteracted by cumulus damping in the eastern section and by boundary layer friction in the mountainous western section.

1. Introduction

During the pre- and early summer period of mid-May to mid-June, a rain-producing phenomenon dominates the weather over the coastal regions of East Asia including Japan and southeastern China. This period represents the local rainfall maximum each year outside of the summer typhoon season. The rainfall during this period is called "Mei-Yu" (plum rain) in China and "Baiu" in Japan. It may be continuous or intermittent for several days to a few weeks and includes frequent rainshowers and thunderstorms, with rainfall rate of up to a few hundred millimeters per day. Synoptically this rainfall is associated with the repeated occurrence of a front which develops in the midlatitudes and slowly moves southeastward to establish a quasi-stationary position extending from southern Japan to southern China. The front's position coincides with the early summer monsoon trough in East Asia and its existence may be viewed as a manifestation of the trough. The beginning of the rainy season also signifies the onset of the northern summer monsoon in this part of the world.

The Severe Rainstorms Research Project of the Japan Meteorological Agency has carried out several experiments in the Kyusku district and its adjacent oceanic areas during the Baiu seasons of 1968–72 to study the heavy rainfall. One of the main findings from the experiments is that the front is characterized by a smaller horizontal temperature gradient than that in a typical polar front but is accompanied by an ageostrophic low-level jet stream (e.g., Matsumoto *et al.*, 1971). The heavy rainfall was found to be associated with this jet which is presumably due to the downward transport of horizontal momentum by cumulus convection (Matsumoto, 1972; Akiyama, 1973). Mesoscale convective systems were observed to be imbedded in the intermediate-scale cyclones or weak depressions in the Baiu front and were responsible for the intense rainfalls (Ninomiya and Akiyama, 1971, 1972; Akiyama, 1974).

There is relatively little work reported in the open literature pertaining to the study of the Mei-Yu front over southeastern China and its vicinity. Recently Chen and Tsay (1977, 1978) carried out a detailed synoptic analysis of a Mei-Yu system during 10–15 June 1975 and provided, for the first time, a data base of relatively high resolution for a Mei-Yu system. Since the eastern part of the Mei-Yu front is over

[1] Permanent affiliation: Department of Atmospheric Sciences, National Taiwan University, Taipei 107 Taiwan, R.O.C.

0027-0644/80/070942-12$07.00

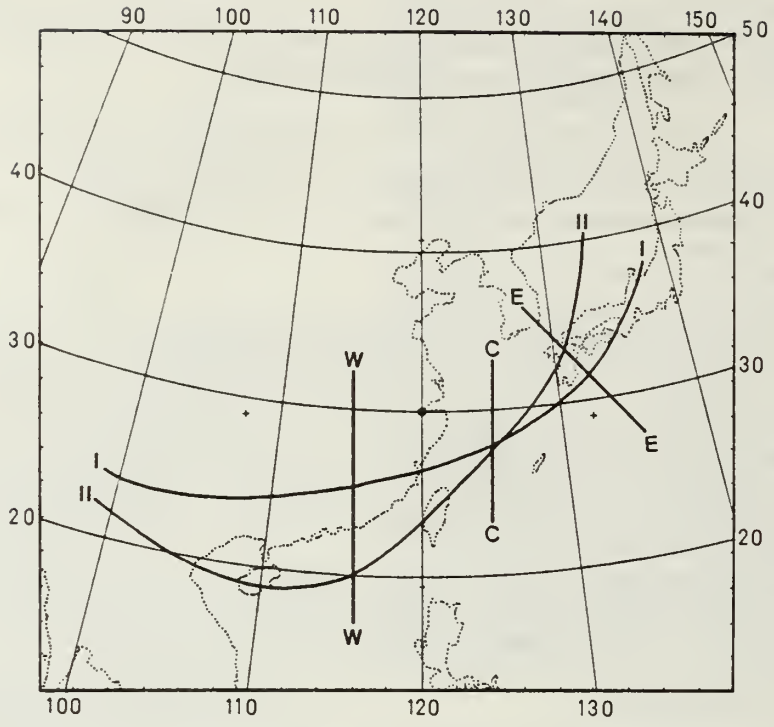

FIG. 1. Mean positions of 850 mb Mei-Yu trough during stages I and II and the cross sections W, C and E.

central and southern Japan and extends as far north as ~40°N, while the western part of the front penetrates to the northern part of the South China Sea south of 20°N, the front may be viewed as a combined midlatitude and tropical system. This property is especially interesting in view of the role of the Mei-Yu systems in the northern summer monsoon of East Asia. The purpose of this paper is to compare the eastern, western and central segments of a Mei-Yu front in terms of the cross-sectional structure and vorticity budgets using Chen and Tsay's (1977) data set. Although the cross-section analysis does not allow an explicit accounting of the mesoscale disturbances imbedded in the front, we hope that the present study will be a first step toward revealing the basic characteristics of the mean states of the different segments and that it will provide a basis for understanding the similarities and differences between the different segments which form the combined midlatitude-tropical system.

2. Data and method of analysis

The subjective analysis of the 10–15 June 1975 case by Chen and Tsay (1977) was done twice daily at all mandatory levels over the area between 10–55°N and 85–150°E. The data were tabulated at 240 km grid intervals after a 25-point smoothing (Bosart, 1970). They also computed the kinematic vertical velocity and vorticity budget terms at the individual times using centered finite differences for all space and time derivatives. The kinematic vertical velocity was adjusted according to the smoothed-terrain Ekman pumping value at 850 mb and adiabatic value at 100 mb. The vorticity equation used was

$$\frac{\partial \eta}{\partial t} = -\mathbf{V}\cdot\nabla\eta - \eta\cdot\nabla\mathbf{V} - \omega\frac{\partial \eta}{\partial p} - \mathbf{k}\cdot\nabla\omega\times\frac{\partial \mathbf{V}}{\partial p} + F,$$

where all the notations are conventional. Each term was computed directly, except the friction term (F) which was the residual necessary for balancing the equation.

In addition to Chen and Tsay's data, high-resolution Defense Meteorological Satellite Program imageries are used to subjectively estimate the total and the cumulonimbus (Cb) cloud covers within each 1° longitude-latitude square. These estimates are then averaged over each 2° × 2° grid. The Cb clouds are determined by the brightness and degree of organization in the visible imageries and by the whiteness (indicating cold cloud top) in the infrared imageries.

Three cross sections (W, C and E) are chosen to depict the structure in the western, central and eastern segments, respectively, of the Mei-Yu system (Fig. 1). Section W is oriented north-south

over southeastern China and is approximately perpendicular to the 850 mb Mei-Yu trough (defined by the minimum geopotential line on the isobaric surface). The trough in this area moves slowly southward for the entire period of study. Section C, also oriented north-south, lies over the East China Sea and intersects the nearly stationary part of the 850 mb trough at a 60° angle. Section E, which is oriented northwest-southeast across Korea and southern Japan, is similar to section W, roughly perpendicular to the 850 mb trough. This trough moves back and forth in a northwest-southeast direction over this area during the period of study.

In order to reduce the amount of data for easy discussion, the 12 h data are composited within each of two stages which are defined by the intensity of the cyclonic vorticity associated with the 850 mb Mei-Yu trough over southeastern China (Section W). Fig. 2a shows the time cross section of relative vorticity and the trough position (dashed line) at 850 mb for section W. Based on this figure, the entire period is divided into stages I and II, which cover the periods 0000 GMT 10 June to 1200 GMT 12 June and 0000 GMT 13 June to 1200 GMT 15 June, respectively. Each stage contains data of six synoptic times at 12 h intervals. Stage I represents the mature stage during which the maximum cyclonic vorticity associated with the trough in Section W is approximately conserved. Stage II represents the decaying stage within which the averaged maximum cyclonic vorticity in section W decreases more than 50% from that of stage I. Figs. 2b and 2c show the relative vorticity and trough position for sections C and E, respectively. Notice that the two stages defined above do not necessarily imply similar intensity changes as that in section W. In section E the averaged maximum vorticity decreases by ~20% from stages I to II, but in section C it increases by more than 30%. It will be shown later, however, that stage II in general represents a decaying stage for all three sections as far as the intensities of the height-trough, temperature gradient and convective activity are concerned.

The compositing is done by time-averaging data, within each stage, that are categorized with respect to the 850 mb trough for all mandatory levels between 850 and 400 mb for all three sections. No surface data are used as the height of terrain varies between sea level and 1.1 km.

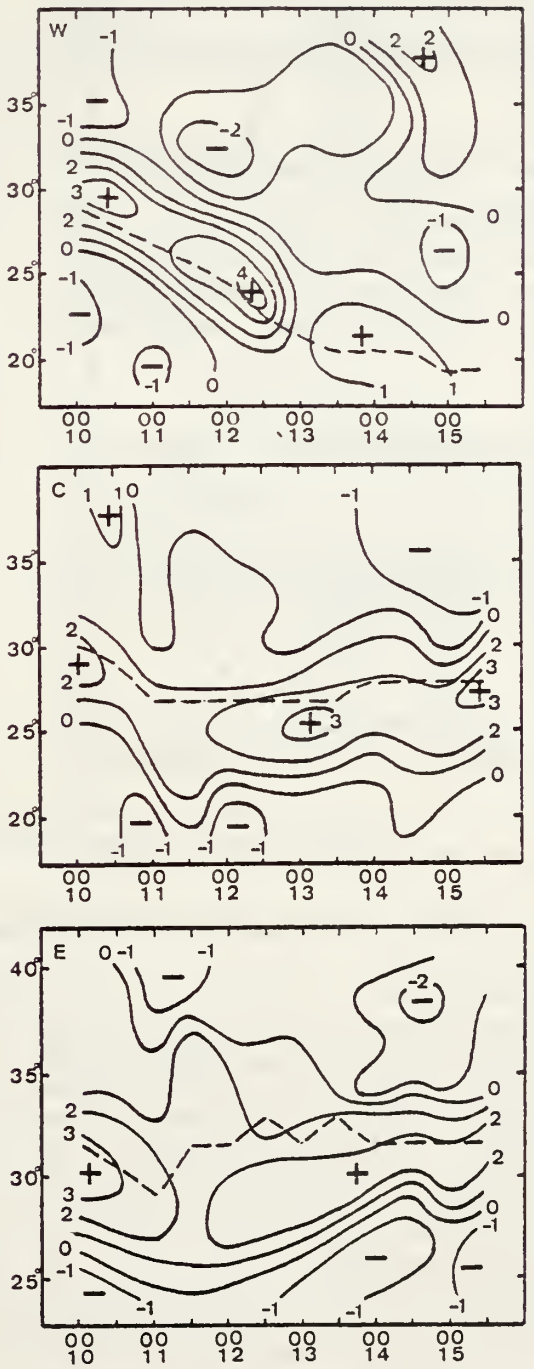

FIG. 2. Time-latitude cross sections of relative vorticity (10^{-5} s^{-1}) at 850 mb in (a) section W, (b) section C and (c) section E.

3. Sectional structure of the Mei-Yu trough

a. Mean position and movements of the 850 mb trough

As shown in Fig. 1, the 850 trough moves in somewhat different manners in the three sections. In section W the trough moves southward at an averaged speed of 9 km h^{-1} during stage I and slows down to 6 km h^{-1} during stage II. The mean positions of the trough are located near 26 and 20°N in stages I and II, respectively. In section C the trough is nearly stagnant at about 28°N. In section E it migrates between 28–35°N with a mean position shifting from 38°N northwestward to 32°N from stages I to II.

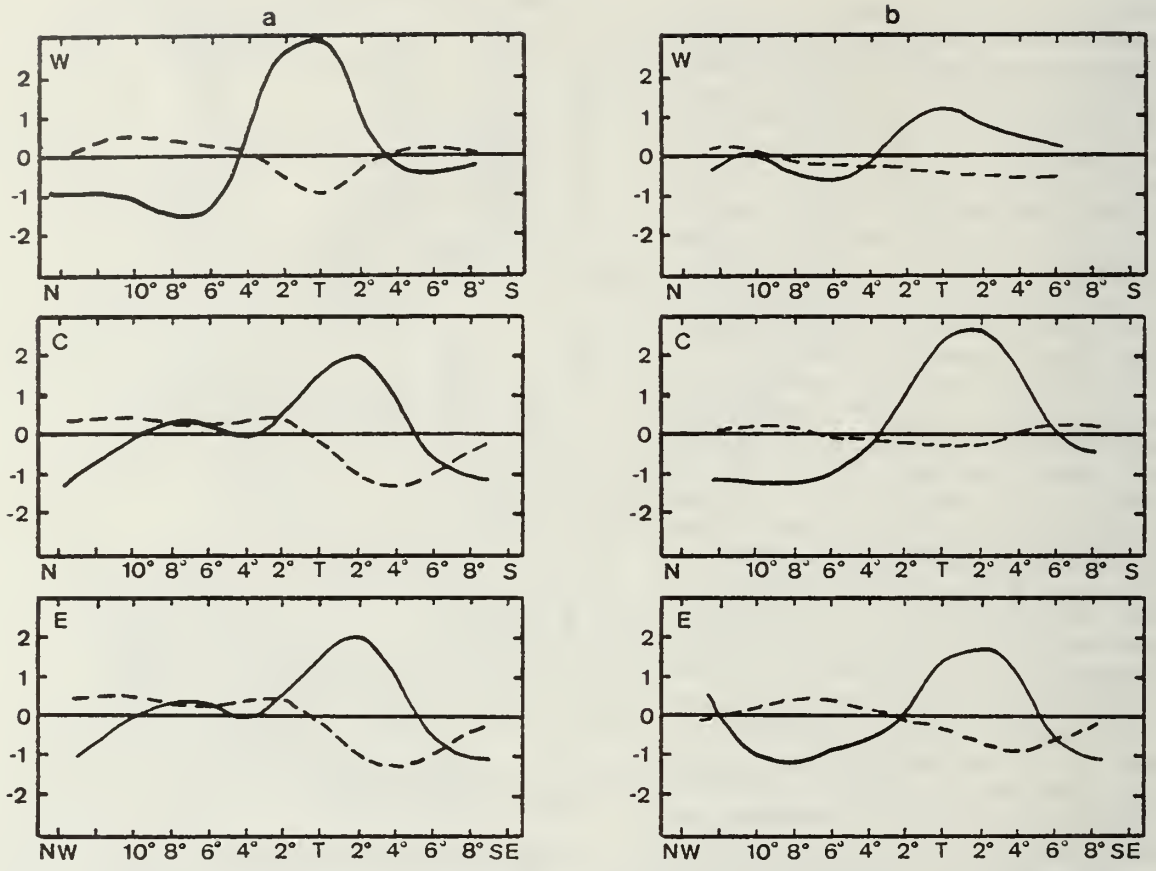

FIG. 3. Distribution of relative vorticity (solid) and divergence (dashed) at 850 mb in sections W, C and E during (a) stage I and (b) stage II. Units are 10^{-5} s^{-1}. The abscissa indicates distance in degrees latitude from the trough (T).

b. Geopotential height

The distribution of geopotential height in the three sections is described here but their diagrams are not shown explicitly. Instead, the vertical trough lines are shown in the diagrams of all other cross sections. In section W the trough is quite shallow, being well defined only at 850 and 700 mb in stage I with essentially no vertical tilt. It becomes ill defined at these two levels in stage II. Above 700 mb it is totally indiscernible in both stages.

The trough in section C, on the other hand, is well defined at all levels up to 400 mb (the highest level analyzed) and tilts significantly northward in stage I. The geopotential gradient weakens only slightly in stage II.

Similar to section C, the trough in section E during stage I is also well defined and tilted at all levels up to 400 mb except that the tilt is somewhat smaller. It weakens slightly in stage II with no change in the tilt. The moderate tilt resembles that of a typical frontal cyclone in its occluded stage.

c. Relative vorticity

Time cross sections of relative vorticity and trough position at 850 mb (Fig. 2) indicate that the Mei-Yu trough is within a zone of cyclonic vorticity. The maximum of this vorticity coincides with the trough in section W and is to the immediate south or southeast of the trough in sections C and E. It is clear that from stages I to II the width of the cyclonic vorticity zone broadens in section W, remains nearly unchanged in section C and narrows in section E.

The 850 mb relative vorticity in both stages in all three sections is shown in Fig. 3. Although the relative position of the vorticity maximum varies between the three sections, their magnitudes during stage I are comparable, all of the order of 2–3 $\times$ 10^{-5} s^{-1}. From stages I to II this magnitude decreases by 60% in section W, 20% in section E and increases by 30% in section C, as may be inferred from Fig. 2.

At 700 mb (not shown) the vorticity maximum is situated 2° latitude north of the 850 mb trough in section W and directly over the 850 mb trough in sections C and E during both stages. The magnitude in stage I is comparable to that at 850 mb in sections C and E but is smaller in section W. From Stages I to II this magnitude is reduced by 70, 30 and 20% in sections W, C and E, respectively.

In all three sections the cyclonic vorticity is

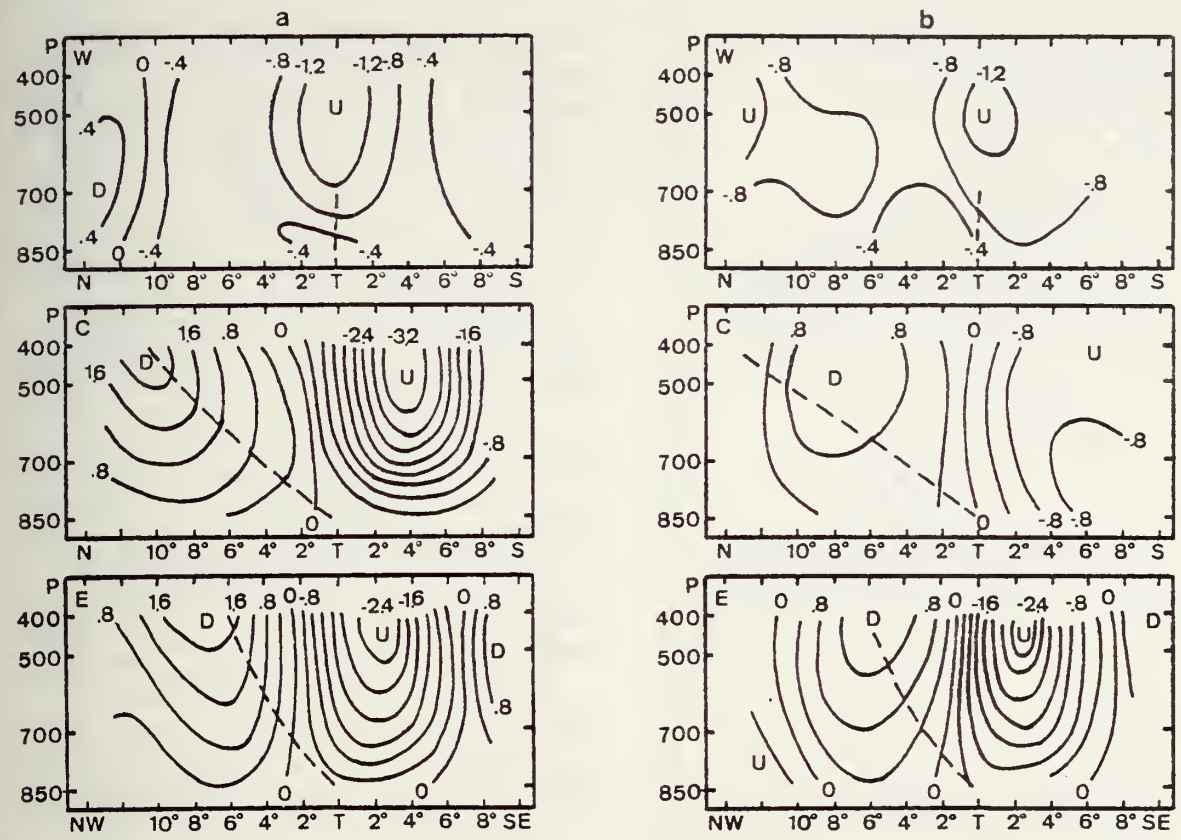

FIG. 4. Vertical cross sections of pressure velocity (μb s^{-1}) in sections W, C and E during (a) stage I and (b) stage II. Dashed lines indicate the trough axes. The abscissa is distance in degrees latitude.

mainly due to the shear, across the Mei-Yu trough, of the wind component parallel to the trough. In stage I this shear at 850 mb is about twice as large in section W as in sections C and E. In stage II it decreases remarkably in section W by 80% at 850 mb and 95% at 700 mb. However, it decreases by only 25% at 850 mb and 55% at 700 mb in section C and remains practically unchanged at both levels in section E.

d. Horizontal divergence

Horizontal divergence at 850 mb during both stages is also shown in Fig. 3. The error of composited divergence is estimated to be $<10^{-6}$ s^{-1}. The convergence maximum coincides with the vorticity maximum and the 850 mb trough in section W. However, the vorticity maximum is found to lie between the trough and the convergence maximum in sections C and E. The magnitude of convergence is comparable among the three sections during stage I. In stage II it is reduced substantially in sections W and C but only slightly in section E. At 700 mb (not shown), the distribution is very similar to that at 850 mb except the magnitude is slightly smaller.

e. Vertical velocity

Vertical cross sections of the pressure velocity (ω) in both stages are shown in Fig. 4. In stage I the upward motion reaches maximum at 500 mb in all three sections. It is located over the 850 mb trough in section W, 4° latitude south of the trough in section C and 3° latitude southeast of the trough in section E. On the north side of the trough downward motion prevails with a maximum at 400 mb in sections C and E, and at 700 mb in section W. This well-organized vertical velocity couplet is indicative of the existence of a well-developed secondary circulation normal to the trough. In stage II the circulation becomes substantially less vigorous in sections W and C, but it maintains its intensity in section E.

f. Temperature

Fig. 5 shows the vertical cross sections of the deviation of temperature (T') from the cross-sectional mean at each level. Here the mean value is the average over a distance of 2500 km from 1000 km south of the trough to 1500 km north of it. This distance is the approximate length scale, along the

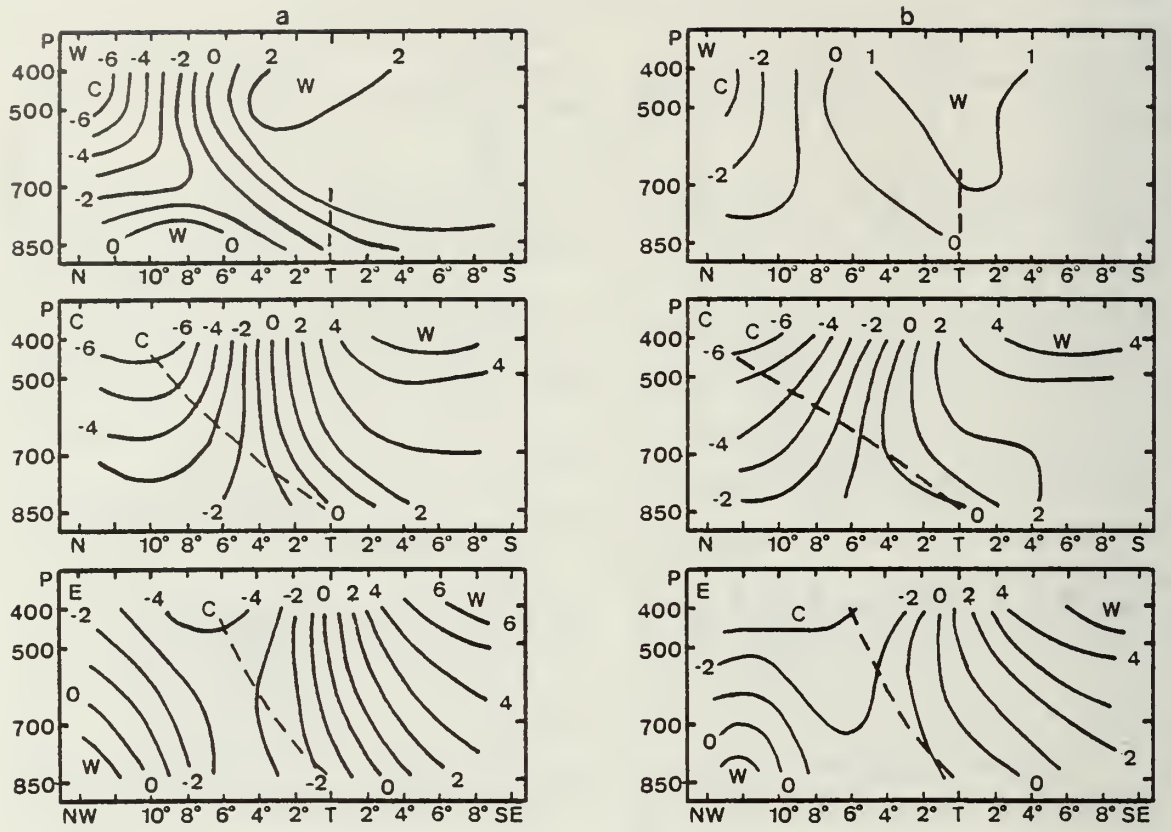

FIG. 5. As in Fig. 4 except for T' (°C).

normal direction of the Mei-Yu system, of the lower tropospheric relative vorticity.

The maximum T' for all cases are found in the upper-middle troposphere near 400 mb. In section W the warmest air is found in the middle troposphere right above the 850 mb trough. This is hydrostatically consistent with the shallowness of the trough in this section. On the other hand, the mid-tropospheric warm air is south of the 850 mb trough in sections C and E. Compared to the vertical velocity distribution (Fig. 4), it is evident that the secondary circulation is thermally direct with warm air rising and cold air sinking. This implies a baroclinic energy conversion which appears to decrease significantly from stages I to II in sectioins W and C where the horizontal gradients of both ω and T' weaken markedly. This conversion remains about the same, however, during the two stages in section E.

g. Mixing ratio

Vertical cross sections of the deviation of mixing ratio (q') in both stages I and II are quite similar. Only those for stage I are shown in Fig. 6. It is seen that the moist air in sections W and C domes upward in the immediate vicinity to the south of the trough and has a northward extension in the mid-troposphere. In section W, the maximum positive q' at all levels coincides with the 850 mb trough except at 850 mb where it is 2° latitude south of the trough. In sections C and E, however, it is located 2–5° latitude south and 4–7° latitude southeast of the trough, respectively.

The upward extension of the moist center into the mid-troposphere correlates positively with the upward vetical velocity and temperature. This may indicate the importance of the vertical moisture transport and the possibility that the warm center in the middle-upper troposphere is largely due to warming by cumulus convection. These points will be reaffirmed by examining the distribution of the satellite cloud data in the next subsection.

h. Satellite cloud cover

The maximum total cloud cover is confined to a rather narrow, elongated band nearly parallel to the 850 mb trough in the warm side (not shown). Fig. 7 shows the distribution in the three cross sections. The maximum cloud band is ~2° latitude from the trough in section W and 4–6° from the trough in sections C and E. During stage I more than half of the total cloud cover within this band is due to Cb activity, which decreases rapidly away from the band

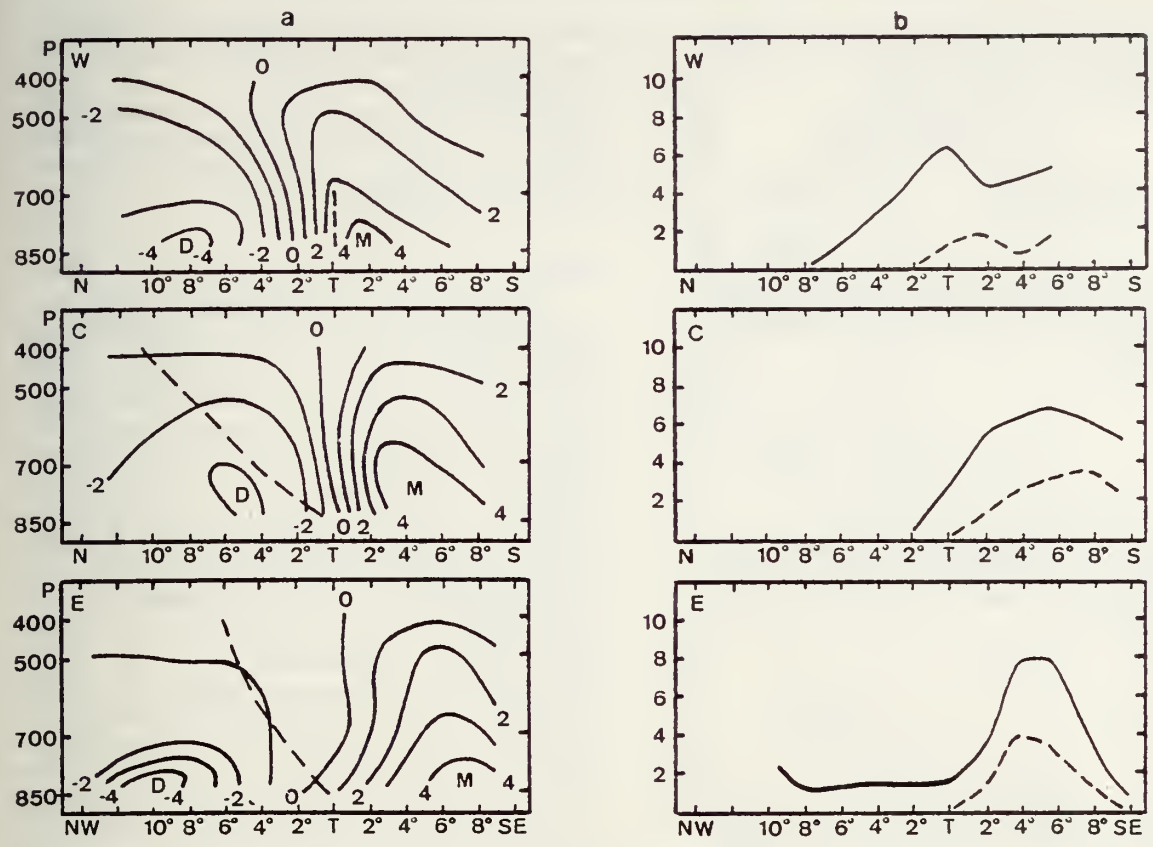

FIG. 6. As in Fig. 4 except for q' (g kg^{-1}).

so that practically no Cb activity is observed in the trough itself. This well-organized band of convection is consistent with the large-scale convergence below 500 mb and the associated upward motion and is indicative of the importance of synoptic-scale control of the convection.

Over and to the north of the 850 mb trough the cloud cover tends to decrease eastward from sections W to E. This is consistent with an examination of the velocity field (not shown) which reveals that during both stages the low-level southwesterly warm and moist flow reaches and even penetrates the trough in section W while it stops short of the trough in the other sections. However, from stages I to II the Cb activity decreases most drastically in section W (by ~70%) whereas it decreases only moderately (by ~20–30%) in sections C and E.

4. Vorticity budgets

Section C is excluded from the composite budget study because it extends over a mainly oceanic area where the data network is not adequate for vorticity budget calculations. Figs. 8 and 9 show the horizontal advection, divergence generation and residual terms for both stages, respectively. All other terms are about one order smaller than the last two terms. The smallness of the local tendency term justifies the compositing of data within each stage. The composited values for all terms represent the individual time values fairly well.

a. Western section

Negative horizontal vorticity advection is found on both sides of the trough at 850 and 700 mb in stage I and reaches a maximum 2–3° latitude south and 4–5° latitude north of the trough. Thus this term does not significantly induce any north-south movement of the trough. In stage II somewhat smaller negative advection remains south of the trough while slightly positive advection is found to the north of the 850 mb trough, suggesting that vorticity advection tends to push the trough northward. The fact that the trough moves southward through both stages implies that the horizontal advection is being overcome by other processes.

Cyclonic vorticity generation due to horizontal convergence prevails in the vicinity of the trough in the lower troposphere and reaches a maximum at 850 mb in stage I. During stage II the generation becomes smaller and is confined ~850 mb in and to

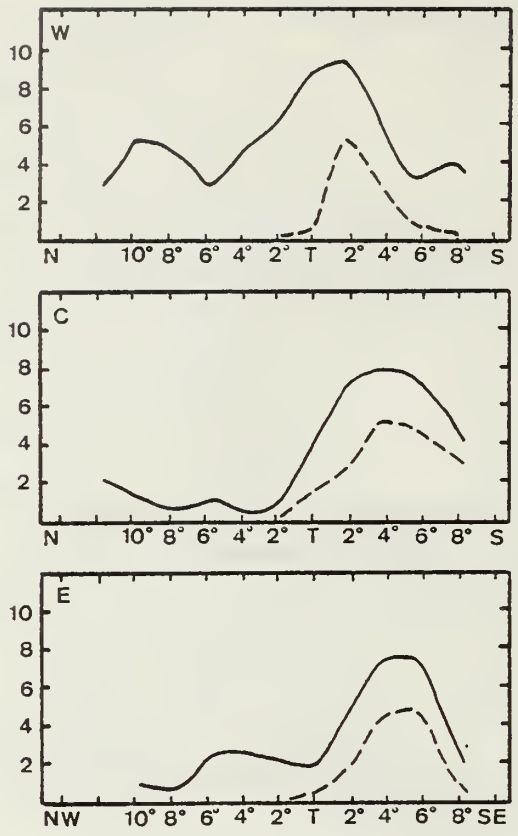

FIG. 7. As in Fig. 3 except for total (solid) and cumulonimbus (dashed) cloud covers. Units are tenths.

the south of the trough, but it is the only positive term in the trough. Thus it is the only process that maintains the intensity of the Mei-Yu trough.

In stage I the residual and divergence terms are comparable in magnitude but with different patterns. The former is negative in and to the north of the trough and positive south of the trough, whereas the latter is positive across the trough. It is seen that the magnitude of the residual term is maximum at 850 mb. In stage II, the negative residual decreases in magnitude but spreads to the south of the trough at 850 mb.

b. Eastern section

Positive vorticity advection over the 850 mb trough increases from 850 to 500 mb during both stages. A negative center of the horizontal advection term in the lower troposphere is found ~4–6° latitude to the warm side of the trough, preventing the trough from moving southeastward.

The generation of cyclonic vorticity by horizontal convergence prevails over and to the southeast of the trough at all levels and reaches a maximum 2–4° latitude to the southeast of the trough in the lower troposphere during both stages. The maximum generation term is found to coincide with cyclonic vorticity maximum at 850 mb.

Negative residual term prevails over and to the southeast of the trough and becomes maximum in the lower troposphere 2–4° latitude to the southeast of the trough in both stages.

5. Discussion

The most apparent difference between the western and eastern sections of the Mei-Yu trough is in the vertical structure. In the western section the trough has practically no vertical tilt and is confined to a shallow layer in the lower troposphere, capped hydrostatically by a warm core in the mid-troposphere. This structure resembles that of many equivalent barotropic, warm-core tropical disturbances (Wallace, 1971). On the other hand, the trough in the central and eastern sections tilt strongly north and northwestward into a cold center near 400 mb, indicating a deep, cold-core baroclinic system which is typical of midlatitudes.

The horizontal temperature gradient near the surface across the Mei-Yu front (Fig. 5) is much weaker in the western section than in the central and eastern sections. (This remains true if the virtual temperature gradient is considered.) However, during the mature stage the cross-trough shear of the wind component parallel to the front is stronger in the western section. This again indicates that the western section is somewhat similar to tropical disturbances in contrast to the midlatitude, strongly baroclinic nature of the other sections. In fact, the weak temperature gradient and strong horizontal wind shear during the mature stage plus the equivalent barotropic vertical structure make the western section look more like an Intertropical Convergence Zone than a typical midlatitude front.

In all three sections the secondary circulation normal to the trough is thermally direct so that available potential energy is converted into kinetic energy locally. The temperature, moisture and cumulus convection distributions correlate very well, indicating that this available potential energy may be generated by latent heat release in the Cb convection area in addition to the normal mid-latitude baroclinic process. Moreover, the change of the degree of convective activity from the mature stage to the decay stage agrees quite well with the change of the intensity of the secondary circulation in each section. Both weaken substantially in the western section, moderately in the central section and remain almost steady in the eastern section.

Although significant cumulus convection is present in all three sections, the roles of large-scale mechanisms responsible for organizing the convection appear to vary. In the western section the low-

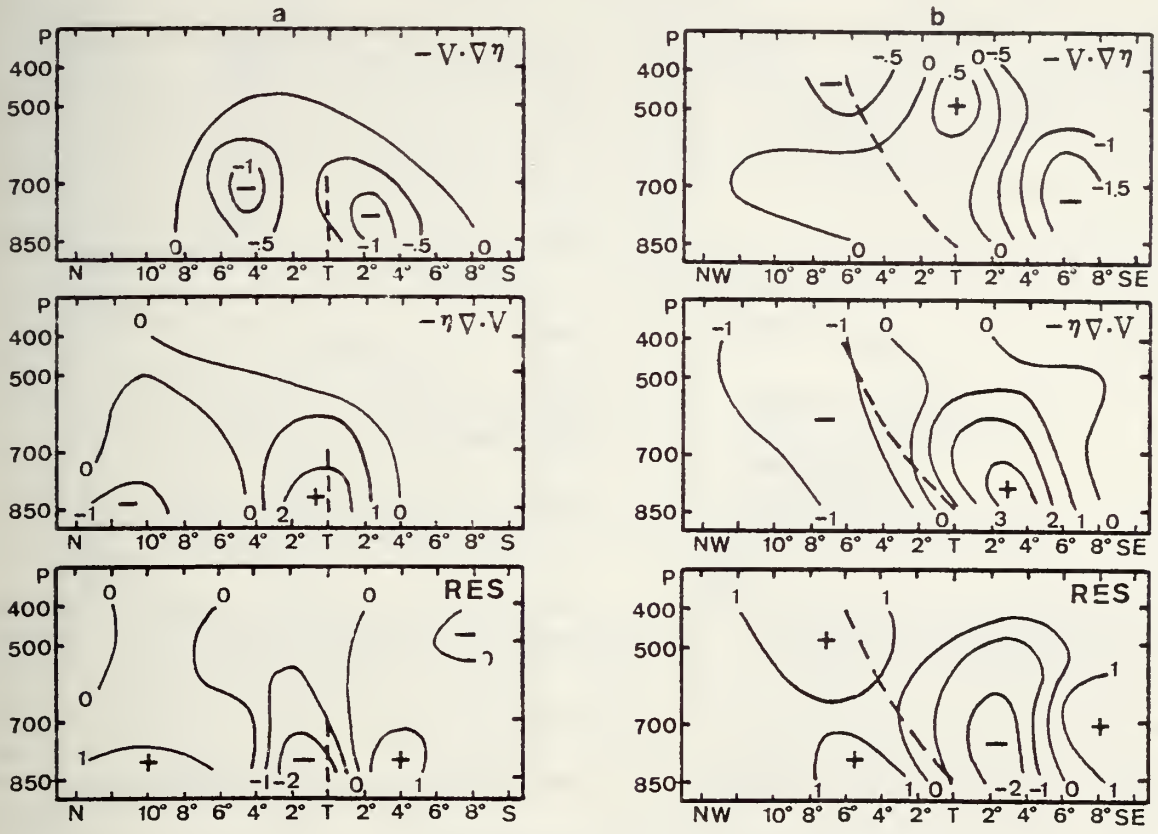

FIG. 8. Vertical cross sections of horizontal vorticity advection, divergence and residual terms during stage I in (a) section W and (b) section E. Units are 10^{-5} s^{-1} $(12\ h)^{-1}$. Dashed lines indicate the trough axes. The abscissa is distance in degree latitude.

level vorticity maximum approximately coincides with the low-level convergence center. This suggests that the vertical motion and therefore the cumulus convection may be largely due to Ekman pumping, thus resembling the conditional instability of the second kind (CISK) process. On the other hand, a significant phase difference between the low-level vorticity and convergence is found in the central and eastern sections, indicating that the vertical motion is mostly produced by differential vorticity advection. CISK may still play some role as the vorticity and convergence are slightly positively correlated.

The generation of cyclonic vorticity by horizontal convergence is of primary importance at lower levels. The generation reaches a maximum in or on the warm side of the trough and, even though being partially offset by the residual term, it tends to counteract the retrogression effect of the horizontal advection thereby keeping the trough quasi-stationary.

The residual term in general is negatively correlated with the generation term and represents the damping of vorticity. Several processes may be responsible for this damping. Comparison of the Cb cloud distribution (Fig. 7) and the residual term (Figs. 8, 9) indicates that in the eastern section the maximum damping of the cyclonic vorticity is almost in phase with the area of maximum convection. It therefore seems reasonable to identify the vertical transport by cumulus convection as the damping mechanism in this region. This is similar to the result found by Chen and Bosart (1979) for a composite extratropical cyclone and by numerous others for tropical disturbances (e.g., Reed and Johnson, 1974). However, in the western section the maximum damping of cyclonic vorticity is north of the trough in the cloud-free area where the cyclonic vorticity is also maximum. South of the trough the residual term is positive and acts to dissipate the anticyclonic vorticity at 850 mb. In contrast to the eastern section where the magnitude of the damping term is substantial throughout the lower and middle troposphere, in the western section it is confined to a shallow layer adjacent to the 850 mb.

Fig. 10 shows the smoothed topography in these sections. From this figure and the observed Ekman relationship of the residual term counteracting the divergence term at 850 mb, it is obvious that the mountainous region in southern China, extending to the 850 mb level, exerts a boundary-layer friction effect on the lower tropospheric flow. Thus the damping in the western section ap-

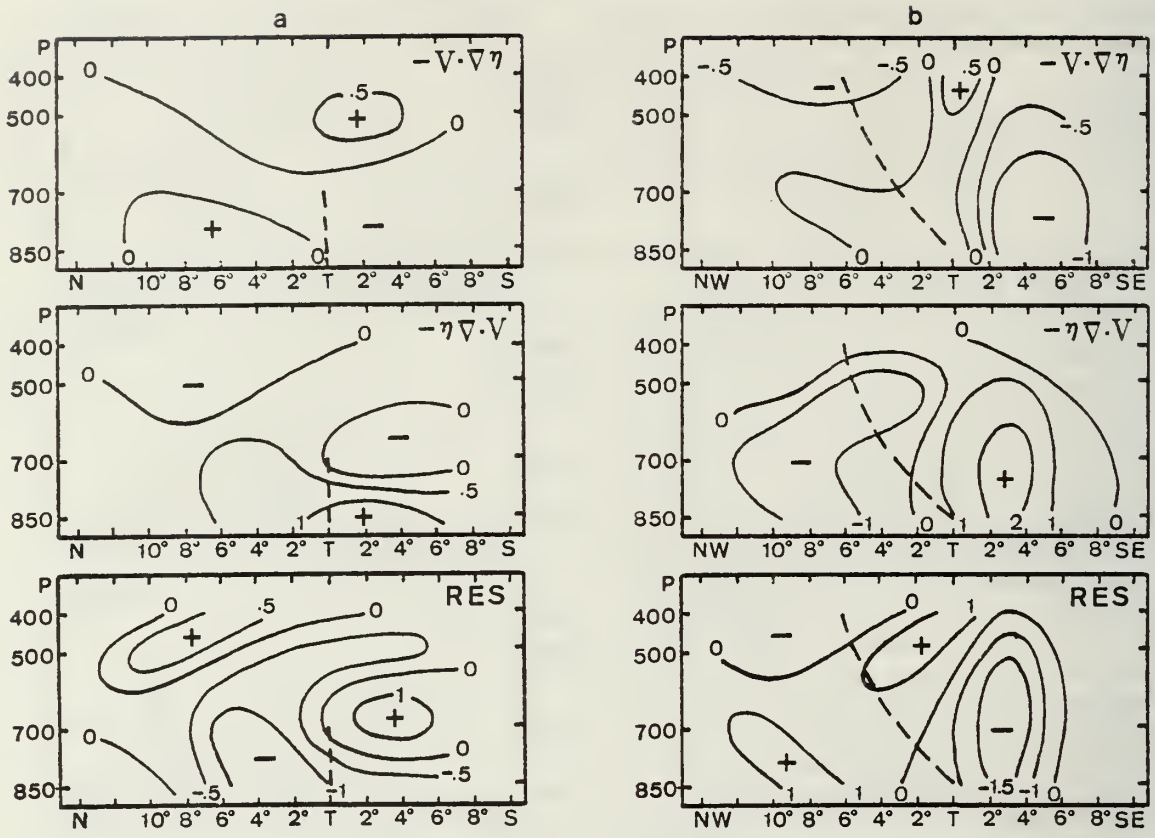

FIG. 9. As in Fig. 8 except for stage II.

parently is more due to the topography than the cumulus convection. The importance of CISK during the mature stage in the western section is consistent with the relative importance of surface friction.

From stages I–II the western section of the low-level trough moves southward off the southern China coast and over the northern part of the South China Sea. The weak horizontal temperature gradient is further reduced throughout the troposphere indicating a decrease in the local baroclinicity. Apparently, this represents a change in the large-scale environment which is sufficient to weaken the trough. This means that the existence of the CISK process depends on the large-scale forcing (frontogenesis) and cannot by itself maintain the trough. The eastern section of the trough moves back and forth over approximately the same area in the two stages and does not experience a significant change in the large-scale flow condition. The cumulus damping and latent heat forcing are proportional to each other resulting in no significant net dissipation of the trough intensity.

6. Summary

This paper studies the structure and vorticity budget of the early summer monsoon trough (Mei-Yu) over subtropical East Asia for the period 10–15 June 1975. Analyzed grid-point data based on the dense upper air station network over southeastern China and Japan are used to construct the cross-sectional structure of the trough along three sections. The trough is manifested at the 850 mb by a quasi-stationary front which moves slowly southward in the western section near the southern China coast, remains nearly stagnant in the central section over the East China Sea between Taiwan and Japan, and fluctuates back and forth in the northwest-southeast direction within a narrow distance over southern Japan. The period of study is separated into two stages, each with six 12 h time intervals, which represent the mature and decay stages of the trough. Within each stage all data in the three sections are time-composited with respect to the trough axis. The main results are as follows:

1) The central and eastern sections of the Mei-Yu trough have a structure resembling a typical mid-latitude baroclinic front with a strong north and northwestward tilt in the vertical toward a middle tropospheric cold core. The horizontal temperature gradient across the trough is strong throughout the troposphere. Significant cumulus convection prevails immediately south or southeast of the 850 mb

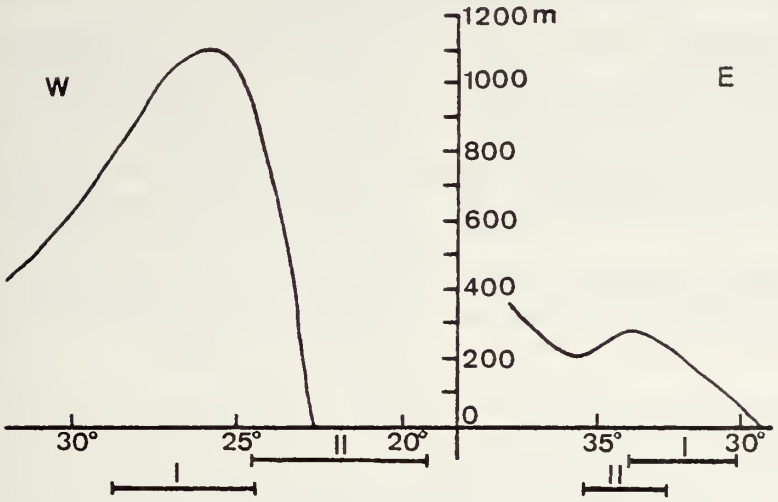

FIG. 10. Smoothed topography in the western and eastern sections. The abscissa is latitude in degrees. The ranges of movement of the 850 mb trough in stages I and II are shown.

trough and apparently contributes substantially to the heating of the middle troposphere which, in addition to the normal midlatitude baroclinic processes, is important in maintaining a thermally direct secondary circulation normal to the trough. However, the low-level vorticity and convergence distribution suggests that CISK plays a small role compared to differential vorticity advection.

2) The western section, which is in lower latitudes and subject to a stronger influence of the moist southwest monsoon flow, exhibits several features that are less common in midlatitude fronts while more typical in tropical systems such as the ITCZ. The trough is confined to a shallow layer in the lower troposphere with almost no vertical tilt and it is capped by a mid-tropospheric warm core resembling an equivalent barotropic system. The horizontal temperature gradient is much weaker than in the eastern section but during the mature stage the horizontal wind shear across the trough is stronger. There is also intense cumulus convection and a thermally direct secondary circulation and both appear to be induced by a CISK process.

3) The generation of cyclonic vorticity by horizontal convergence in both eastern and western sections is offset by strong damping processes. In the eastern section the damping appears to be due to vertical cumulus scale transports which tend to balance the forcing by cumulus heating. In the western section of friction at 850 mb due to the mountainous region of the southern China coast provides the main damping mechanism in the mature stage. In the decaying stage the low-level trough moves southward offshore and weakens as a result of the decreasing baroclinic field, indicating that CISK cannot maintain the trough without the large-scale baroclinic forcing.

From the foregoing results the Mei-Yu trough appears to be a mixed midlatitude-tropical system. This trough is established when East Asian polar fronts repeatedly move southward into southeastern China and southern Japan during the pre- and early summer. The strong modification of the western segment of the front is in distinct contrast to the eastern segment, although cumulus convection and intense precipitation are important in the entire trough region. The present study is limited to one case only and is limited to the mature and decaying stages of the trough after the quasi-stationary position has already been established. Plans are now being made to study more cases and to include the developing stage which hopefully will shed more light on the development and physical mechanisms of the early summer monsoon trough in East Asia.

Acknowledgments. This work was supported by the National Science Foundation, Global Atmospheric Research Program, under Grant ATM77-14821 and U.S.-R.O.C. Cooperative Science Program, under Grant INT78-14557, and by the Naval Environmental Prediction Research Facility. We wish to thank Prof. R. T. Williams for discussions and Prof. R. L. Haney for reading the manuscript. One of us (TJC) wishes to thank the R.O.C. National Science Council for sponsoring in part his sabbatical leave from National Taiwan University.

REFERENCES

Akiyama, T., 1973: Ageostrophic low-level jet stream in the Baiu season associated with heavy rainfalls over the sea area. *J. Meteor. Soc. Japan*, 51, 205–208.

——, 1974: mesoscale organization of cumulus convection in the large-scale rainband in the Baiu season. *J. Meteor. Soc. Japan*, 52, 448–451.

Bosart, L. F., 1970: Mid-tropospheric frontogenesis. *Quart. J. Roy. Meteor. Soc.*, **96**, 442–471.

Chen, G. T. J., and L. F. Bosart, 1979: A quasi-Lagrangian vorticity budget of composite cyclone-anticyclone couplets accompanying North American polar air outbreaks. *J. Atmos. Sci.*, **36**, 185–194.

——, and C. Y. Tsay, 1977: A detailed analysis of a case of Mei-Yu system in the vicinity of Taiwan. Tech. Rep. Mei-Yu-001, Dept. Atmos. Sci., National Taiwan University, 249 pp.

——, and ——, 1978: A synoptic case study of Mei-Yu near Taiwan. *Pap. Meteor. Res.*, **1**, 25–36.

Matsumoto, S., 1972: Unbalanced low-level jet and solenoidal circulation associated with heavy rainfalls. *J. Meteor. Soc. Japan*, **50**, 194–203.

——, K. Ninomiya and S. Yoshizumi, 1971: Characteristic features of "Baiu" front associated with heavy rainfall. *J. Meteor. Soc. Japan*, **49**, 267–281.

Ninomiya, K., and T. Akiyama, 1971: The development of the medium-scale disturbances in the Baiu front. *J. Meteor. Soc. Japan*, **49**, 663–677.

——, and ——, 1972: Medium-scale echo clusters in the Baiu front as revealed by multi-radar composite echo maps. (Part I). *J. Meteor. Soc. Japan*, **50**, 558–569.

Reed, R. J., and R. H. Johnson, 1974: The vorticity budget of synoptic-scale wave disturbances in the tropical western Pacific. *J. Atmos. Sci.*, **31**, 1784–1790.

Wallace, J. M., 1971: Spectral studies of tropospheric wave disturbances in the tropical western Pacific. *Rev. Geophys. Space Phys.*, **9**, 557–612.

Reprinted from JOURNAL OF THE ATMOSPHERIC SCIENCES, Vol. 36, No. 8, August 1979
American Meteorological Society
Printed in U. S. A.

A Numerical Study of Tropical Large-Scale Air-Sea Interaction

KA MING W. LAU

Department of Meteorology, Naval Postgraduate School, Monterey, CA 93940

(Manuscript received 28 November 1978, in final form 5 April 1979)

ABSTRACT

In a series of numerical experiments using a simplified, domain-averaged, coupled air-sea model, some aspects of the low-latitude large-scale interaction between the atmosphere and the ocean are investigated. Experiments are designed with a view toward elucidating basic mechanisms involved in the coupled processes. In this paper, we focus on the response of coupled system to 1) steady forcing, 2) seasonal variations and 3) large perturbations and continuous short-period random forcings.

Results indicated that the sea surface temperature (SST) distribution, which is strongly controlled by the oceanic upwelling, is the primary factor in determining the location and transition of the tropical rainbelt. The strongest convective activities in the ITCZ, however, depend mainly on the moisture supply from horizontal convergence and the static stability of lower atmosphere, and do not necessarily coincide with the occurrence of maximum SST. It is also demonstrated that the positive feedback processes between latent heat release in the ITCZ convection and the Hadley cell are opposed by oceanic upwelling and the concomitant cooling of the mixed layer through a stabilization of the lower atmosphere and a decrease of moisture supply from the tropical oceans. Further, results of the forced oscillation experiment suggest that the statistical effect of a large number of short-term atmospheric disturbances is capable of generating large-scale low-frequency variabilities in the coupled system. The separation in time scale is possibly the manifestation of a red-shifted spectral response in a multi-time-scale coupled climate system.

1. Introduction

The mean position of the ITCZ, as seen from satellite maps, is delineated by a narrow band of bright cloudiness, stretching almost continuously around the globe at low latitudes. In the central and eastern Pacific, the ITCZ cloud band is located north of the geographic equator throughout the year. Immediately to the south lies an arid zone, marked by clear skies, having a latitudinal extent of about 30° in the eastern Pacific but tapering off rapidly toward the central Pacific. In the western Pacific, the ITCZ is not as continuous and stationary as in eastern Pacific, being interrupted by transient waves with intermittent less cloudy skies. During the Northern Hemisphere summer, the ITCZ of the western Pacific advances further north into monsoon Asia, and in the winter migrates south of the equator into the maritime continents of Southeast Asia. The often quite abrupt boundary separating the wet and dry zone along the equator, and the strong interannual variability in their extents have been known from long series of atmospheric and ocean records at Canton Island (Wyrtki, 1977). Detailed features of the ITCZ, including its seasonal displacement, are most obvious in the weekly and monthly maps of satellite-derived rainfall rates over the entire Pacific Ocean compiled by Rao *et al.*, (1976) (Fig. 1). The very dissimilar behavior of the ITCZ in different parts of the Pacific has been related to the extent of the upwelling in the underlying ocean, which is closely coupled to the atmosphere through fluxes of heat and momentum.

There is an abundance of literature on the correlations between various components of the tropical atmospheric and oceanic circulation. From observational studies Kraus (1959) established the existence of oscillations in the recipitation-evaporation cycles of the trades. Positive correlations between SST and the strength of the ITCZ in the central Pacific were first suggested by Bjerknes (1966, 1969, 1972). A recent study by Ramage (1977), however, indicated that such a direct relationship does not exist in the extreme eastern Pacific. Barnett (1977) in his empirical orthogonal function analysis suggested strong coupling between the trade winds and the underlying ocean. The positive feedback between the ITCZ, the trade winds and SST was confirmed in recent studies (Rieter, 1978a,b) which further indicated that the feedback is only part of a global atmosphere-ocean interaction, among many other controlling factors. Within the oceans, studies of the predictabilities of SST (Davis, 1976) have led to the suggestion that the observed variabilities of SST in the North Pacific is largely a result of the atmosphere driving the ocean. More recently the low-frequency

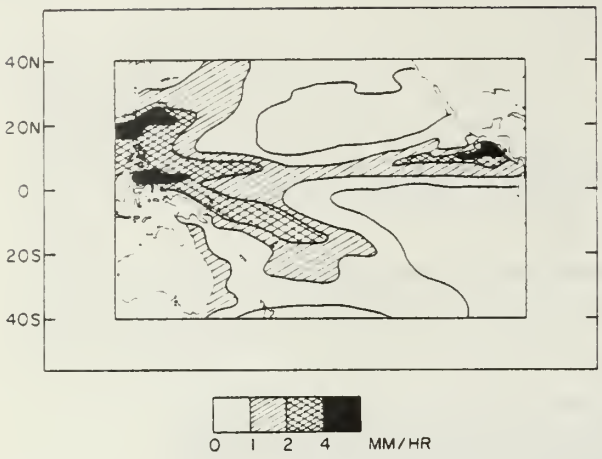

FIG. 1. Satellite-derived annually averaged precipitation rates compiled from Rao *et al.* (1976).

variabilities in the seasonal thermocline have been explained in terms of stochastic forcings by short-period atmospheric disturbances (Frankignoul and Hasselmann, 1977).

Theoretical studies of the tropics (e.g., Pike, 1971; Manabe *et al.*, 1974) further confirmed that the ITCZ development is closely tied to the SST distribution, although others (Charney, 1966; Bates, 1970) had earlier stated that the CISK mechanism could account for the ITCZ growth. The general circulation experiments of Manabe *et al.* (1974) demonstrated that the tropical rain-belt comprising many centers of intense precipitation, tends to settle over the warmest SST. However, they did not consider the interactive role of the ocean. Joint atmosphere-ocean general circulation models (e.g., Manabe *et al.*, 1975) undoubtedly still provide the most important tool for comprehensive studies of the coupled system. Yet extended simulations with these models over time scale of years are greatly limited by the large amount of resources and complexities involved. While Pike's coupled model is very much simpler than the general circulation models, it is still too complex for extended integrations beyond the annual time scale. Nevertheless, large variabilities are observed in the tropical atmosphere and ocean in the interannual time scales and well beyond, e.g., the El Niño and its related anomalous atmospheric circulations. The long time scale involved in the interaction calls for the development of simple coupled models that can accommodate the complex dynamics of the atmosphere-ocean system, while at the same time be economically feasible for carrying out extended numerical experiments.

McWilliams and Gent (1978), using a highly parameterized air-sea coupled model, recently showed that damped oscillations of several year periods can occur in an equatorial atmosphere-ocean system. At a slightly more sophisticated level using a domain-average representation, a dynamical climate model was developed by Webster and Lau (1977) and Lau (1977) [hereafter referred to as WL and LAU, respectively] to study the coupled processes in the atmosphere-ocean system. In a study using the coupled model (Webster *et al.*, 1977) a possible link was suggested between the evolution of the planetary-scale monsoons and the SST. The model has also been used successfully to establish the important role of an interactive ocean on the global energy balance (Lau, 1978).

In a series of numerical experiments we aim at studying the basic mechanisms involved in the large-scale tropical atmosphere-ocean interaction using the coupled model (WL). In this study we only concentrate on experiments with a single domain-averaged component of the tropical air-sea coupling in order to test the model performance and sensitivity under various circumstances. The present study will serve as a means to interpret results of a more comprehensive study which the author is now undertaking using the fully interactive model (i.e., including zonal interaction between the different domains). Specifically in this paper we focus on the following:

1) The maintenance and seasonal transition of the ITCZ and its interaction with SST and oceanic upwelling in the oceanic domains corresponding to the western, central and eastern Pacific, respectively.

2) The feedback mechanisms involved in the interaction between the ITCZ, the Hadley circulation and oceanic upwelling.

3) Excitation of transients or low-frequency oscillations in the model atmosphere-ocean system.

2. Model description

The model formulations are detailed in WL and LAU; only a brief description will be given here. In this model the three-dimensional structure of ocean-atmosphere-land system is divided into longitudinal domains which represent regions of similar physics or boundary conditions. The governing primitive equations of the atmosphere are then averaged in longitude over these fixed domains generally of differing zonal extent. This produces a system of equations which are functions of time, height and latitudes for each domain and with each domain interacting with adjacent domains through fluxes of heat, momentum and pressure work. In the oceans, similar averaging is applied to different oceanic domains. The governing equations within each oceanic domain are prognostic equations for the mixed-layer temperature and depth which include advective terms due to wind-driven and

thermally-driven circulations. Equatorial upwelling dynamics are included in the open ocean domains, and coastal upwelling and boundary current transports are included in domains adjacent to the continents. Over land regions, the surface temperature is computed from heat balance at the ground surface. The model has been developed aiming at the interactions between the various components of the earth–atmosphere–ocean system with time scales extending from seasonal to interannual.

In this paper, we only deal with part of the system, emphasizing the meridional controls. The effect of continentality is not considered, except where it produces a coastal upwelling effect on the ocean domains bordering a continent.

a. The atmosphere model

The governing equations for the atmosphere are the "domain-averaged" set used in WL and LAU:

$$\left.\begin{aligned}
\bar{u}_t &= f\bar{v} - \bar{M}(\bar{v}) + \bar{D}(u') + \bar{I}^u + \bar{F}^u \\
\bar{v}_t &= -f\bar{u} - \bar{M}(\bar{v}) + \bar{D}(v') + \bar{I}^v + \bar{F}^v - \frac{1}{a}\bar{\psi}_\phi \\
\bar{T}_t &= -\bar{M}(\bar{T}) + \bar{D}(T') + \bar{I}^T + \bar{F}^T + \bar{Q} \\
\bar{q}_t &= -\bar{M}(\bar{q}) + \bar{D}(q') + \bar{I}^q + \bar{F}^q + \bar{S} \\
\bar{\omega}_p &= -\frac{1}{a\cos\phi}(\bar{V}\cos\phi)_\phi + \bar{I}^\omega \\
\bar{\psi}_p &= -R\bar{T}/p
\end{aligned}\right\}, \tag{1}$$

where the overbars represent averages over a longitudinal domain (see WL for details), subscripts denote partial derivatives, and λ, ϕ, p denote longitude, latitude and pressure, respectively. $\bar{F}$ represents vertical and subgrid-scale processes, $\bar{Q}$ the non-adiabatic heating rate and $\bar{S}$ the source or sink of moisture. $\bar{M}(\bar{X})$, $\bar{D}(X')$ represent the meridional and vertical fluxes by the mean motion and by large-scale eddies, respectively. Two important modifications are noted in (1) as compared with those used in LAU. First, the domain interaction terms $\bar{I}$ are all set to zero. This has the effect of decoupling the various atmospheric domains in longitude, leaving only the zonally symmetric part of the motion within each domain. Physically, this means the atmosphere within each domain is driven entirely by meridional and vertical fluxes of heat and momentum in addition to insolation and latent heat release. Second, the water vapor cycle together with a scheme of cumulus parameterization are now included, as described in the next section.

b. The hydrology cycle and cumulus parameterization

As the tropical atmosphere is largely driven by cumulus heating, the inclusion of moist processes into the dry version of the atmosphere model in LAU is an essential part of the present study. Here, we divide the latent heat release into two kinds: (i) that released when the predicted mixing ratio exceeds its saturation values regardless of the static stability and (ii) that released under conditionally unstable stratification and when the total horizontal convergence exceeds a certain critical value. When the former occurs, the rate of condensation is given by

$$S_L = (|q - q_{\text{sat}}| + q - q_{\text{sat}})/2\Delta t, \tag{2}$$

where q_{sat} is the saturation mixing ratio. The heating rate due to large-scale condensation is

$$Q_L = \frac{L}{c_p} S_L, \tag{3}$$

where L is the heat of condensation and c_p the specific heat of air at constant pressure.

In the cumulus parameterization we follow an approach similar to Ooyama (1964, 1969) and Anthes (1977). We assume that when the atmosphere is conditionally unstable (i.e., $\partial\theta_e/\partial p > 0$) and the vertical moisture flux is upward, only a fraction $(1 - b)$ of the total upward water vapor flux into a column denoted by

$$\bar{S}_c = -\eta(p)(1 - b)\langle\omega q\rangle/\Delta p \tag{4}$$

is condensed and precipitated out of the column, while the remaining fraction b is used to increase the moisture content of the column. Here η is a non-dimensional parameter which is a measure of the rate of entrainment in the convective updraft. In Eq. (4)

$$\langle\ \rangle = \frac{1}{p_0}\int_{p_0}^{0}(\ )dp \tag{5}$$

denotes vertical average through the depth of the atmospheric column. Within each layer, the heating

rate due to convection is therefore

$$\bar{Q}_c(p) = \begin{cases} -\eta(p)(1-b)\dfrac{L}{c_p \Delta p}\langle\tilde{\omega}\tilde{q}\rangle, & \langle\tilde{\omega}\tilde{q}\rangle < 0 \\ 0, & \langle\tilde{\omega}\tilde{q}\rangle > 0. \end{cases} \tag{6}$$

Using a one-dimensional cloud model Anthes (1977) has derived an expression for $\eta(p)$ in terms of cloud-scale variables. For a two-layer model, which is used here, and in the absence of detail cloud processes, we adopt a slightly different approach. By considering the conservation of moist static energy for a parcel in a convective updraft, Ooyama (1971) showed that the entrainment parameter is the same in the two layers and is approximately given by

$$\eta = -\frac{\theta_e^1 - \theta_e^0}{\theta_e^2 - \theta_e^1}, \tag{7}$$

where θ_e^0, θ_e^1, θ_e^2 are the equivalent potential temperatures representative of the boundary layer, the lower layer and the upper layer of a two-layer model. When there is convection ($\tilde{\omega}\tilde{q} < 0$), the parameter η determines the magnitude of the stabilizing effect. If the environment is very unstable (large positive η) moist convection rapidly develops with 1) an equal amount of heating in the two layers and 2) a large vertical transport of moisture [by Eq. (4)]. Both effects will decrease η and therefore stabilize the atmosphere by limiting excessive heating. The fraction b is estimated following Anthes (1977) by

$$b = \begin{cases} \left(\dfrac{1 - \langle \mathrm{RH}\rangle}{1 - \mathrm{RH}_c}\right)^n, & \langle \mathrm{RH}\rangle \geq \mathrm{RH}_c \\ 1, & \langle \mathrm{RH}\rangle < \mathrm{RH}_c \end{cases} \tag{8}$$

where n is a positive exponent of order 1. It can be seen from (8) that the fraction $(1 - b)$ of upward moisture flux that is precipitated decreases from near 1 in a saturated column to zero as the mean relative humidity $\langle \mathrm{RH}\rangle$ approaches some critical value RH_c. The total diabatic heating and the moisture sink is given by

$$\left.\begin{aligned} \bar{Q} &= \bar{Q}_c + \bar{Q}_L \\ \bar{S} &= \bar{S}_c + \bar{S}_L \end{aligned}\right\}. \tag{9}$$

To complete the hydrology cycle, we have to specify the sources of moisture. Over tropical oceans, evaporation contributes a significant amount of moisture into the lower atmosphere. The evaporation rate over the ocean is estimated by

$$E_v = \rho_S C_D |\mathbf{V}_S|(q_s - q_0), \tag{10}$$

where $\mathbf{V}_S$ is the surface wind, C_D the drag coefficient and ρ_S the density of air at the surface. Subscripts s and 0 denotes values at the surface and in the boundary layer (anemometer level), respectively. Other sources of moisture from subgrid-scale processes and transport by large-scale eddies are calculated in the same way as for other conservative quantities (see WL for details). In the experiments described in this paper, we used an empirical relation between the surface drag coefficient C_D and the surface wind speed (Garratt, 1977) given by

$$C_D = 0.51|\mathbf{V}_S|^{0.46} \times 10^{-3}, \tag{11}$$

which gives close approximation to observed neutral drag coefficients in the range $4 < |\mathbf{V}_S| < 20$ m s^{-1}.

c. The ocean model

The ocean is represented by an advective mixed layer where horizontal transport is effected through a wind-driven and a thermally-driven circulation. Coastal and equatorial upwellings are included in a simple manner making use of the steady-state balance between the surface wind stress and the local ocean circulation. The governing equations for the ocean mixed-layer temperature (T_s, taken to be the same as SST and mixed-layer depth (h, abbreviated by MLD) are the same as in LAU, i.e.,

$$\left.\begin{aligned} (T_s)_t + \mathbf{V}_s\cdot\nabla T_s &= \frac{2}{h^2}[-(G - D - W_{-h}K^*) + hJ(-h)] \\ (h)_t + \mathbf{V}_s\cdot\nabla h + W_{-h} &= 2[(G - D) + I(-h) - 2h\bar{J}(-h)][\Lambda h(T_s - T_{-h}) + 2K^*]^{-1} \\ (T_{-h})_t &= -W^*_{-h}\Gamma + (R_{-h})_z \\ W^*_{-h} &= (h)_t + \mathbf{V}_s\cdot\nabla h + W_{-h} \end{aligned}\right\}, \tag{12}$$

where $G - D$ represents the net energy input from the wind less dissipation within the layer. $I(z)$, $J(z)$, $R(z)$ are heating functions, Γ the lapse rate of temperature below the thermocline, K^* the kinetic energy storage within the layer, W_{-h} the grid-scale upwelling, and $\mathbf{V}_s$ the horizontal current vector in the mixed layer (see LAU for details). Here, as in the atmospheric model, horizontal advection is allowed only in the meridional direction. The sign of the vertical turbulent heat transfer at the thermocline interface is controlled by the discrete Heaviside stepfunction ($\Lambda = 0$ when $W^*_{-h} < 0$ and $\Lambda = 1$ when $W^*_{-h} > 0$).

8 v

The grid-scale upwelling is made up of three components

$$W_{-h} = W_0 + W_e + W_B, \tag{13}$$

where W_0 is the upwelling due to large-scale thermally-driven circulation, W_e the upwelling in the open ocean due to Ekman and geostrophic divergence, and W_B the local sidewall upwelling at the coast and at the equator. Parameterizations of the above quantities are given in detail in LAU where it is shown that along a eastern shoreline, the magnitude of vertical velocity in the coastal upwelling is given by

$$W_B = -(\tau^\lambda \pm \tau^\phi)(2E_H|\sin\phi|)^{-1/2}(2\Omega a)^{-1} \tag{14}$$

and at the equator by

$$W_B = -\tau^\lambda E_V^{1/2}(2\Omega a)^{-1}|\phi|^{-5/2},$$

for

$$|\phi| \gtrsim E_H^{1/3}, \tag{15}$$

where a is the radius of the earth, Ω the angular frequency of rotation of the earth, and E_H, E_V the horizontal and vertical Ekman numbers of the ocean; τ^λ and τ^ϕ represent the westward and northward wind stresses at the sea surface and the $\pm$ sign in (14) refers to the Northern and Southern Hemispheres, respectively. From (14) and (15) it is noted that a westward surface wind stress will give rise to equatorial upwelling and an equatorward wind stress will cause upwelling along the east coastline. The boundary upwelling W_B will oppose the penetrative deepening due to wind mixing and because of the large magnitude of such upwellings, actual shallowing ($\partial h/\partial t < 0$) can occur even in the presence of strong wind stirring. The resulting decrease in MLD makes the wind-mixing terms in (12) more effective in producing a colder SST, which in turn reduces the evaporation rate [by Eq. (10)] and increases the stability of the lower atmosphere [decreases η in Eq. (7)]. As the boundary upwelling is directly coupled to the wind stress at the ocean surface, it provides a strong feedback mechanism in the coupled model through which the atmosphere and the ocean can interact.

3. Description of experimental setup

In all experiments to be described the atmosphere model is specialized into two layers with prognostic variables defined at the 750 and 250 mb levels. The lower layer overlies a constant-flux boundary layer through which moisture, heat and momentum are transferred to and from the ocean. The atmosphere is divided into three domains overlying three oceanic domains pertaining to the western Pacific (WPAC), central Pacific (CPAC) and eastern Pacific (EPAC). These oceanic domains are distinguished by 1) having

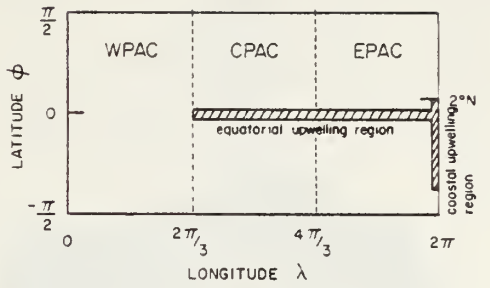

FIG. 2. Schematic diagram showing the different oceanic domains in the model. Overlying each of these domains is an atmospheric domain with the same horizontal dimensions as its oceanic counterpart.

no equatorial nor coastal upwelling in WPAC, 2) only equatorial upwelling in CPAC, and 3) both equatorial upwelling and coastal upwelling south of 2°N in EPAC (see Fig. 2). Such distinctions between different domains agree with oceanographic observations. Within each atmospheric domain the atmosphere is driven primarily by meridional gradients of radiative heating, condensation heat release, and heat and moisture fluxes from the underlying surface which are dependent on the characteristic oceanic processes operative at that domain. In the ocean mixed-layer, interfacial heat flux, wind stress from the atmosphere, meridional density gradients together with entrainment of cold water from below the seasonal thermocline contribute to the changes in the mixed-layer temperature and depth.

Values of the parameters used are the same as in LAU. The grid spacing in latitude is 4°, with centered space differences. A time-smoothed version of the leapfrog scheme is used in the time-difference scheme, with a time step of 1 h 20 min. Since the ocean variables change relatively slowly compared to the atmospheric variables, they are calculated every 12 h. The time marching therefore involves nine atmospheric time steps followed by one oceanic time step.

4. Results

Three series of experiments are designed using the coupled model with the main focus on studying the steady-state response of the coupled system to stationary forcing, seasonal variations and large perturbations.

a. Steady-state response

In this experiment the atmosphere is first allowed to evolve from rest while a steady state is reached under equinoctial conditions and a fixed SST distribution having a "warm" equator similar to the mean conditions observed over the western

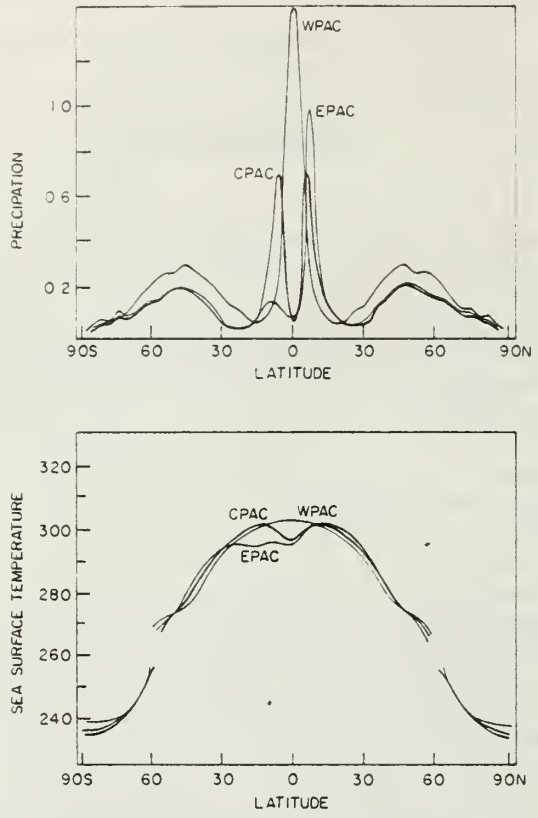

FIG. 3. Steady-state distribution of precipitation rate (cm s^{-1}) and sea surface temperature (K) for the model western Pacific (WPAC), central Pacific (CPAC) and eastern Pacific (EPAC).

Pacific (WPAC). Fig. 3 shows the steady-state distribution of rainfall rate and ocean mixed-layer temperature as a function of latitude at the end of 150 simulated days. It can be seen that in the steady-state WPAC a distinct ITCZ develops at the equator with a maximum rainfall rate measured at about 1.5 cm day^{-1} occurring over the warmest equatorial water, while a subtropical dry zone extends between 15–30° latitude. After establishing the steady-state WPAC with fixed SST, the central Pacific (CPAC) conditions (see Section 3) are developed by allowing the oceanic mixed layer to interact with the atmosphere. The presence of equatorial surface easterlies causes rapid oceanic upwelling and a shallow Ekman divergent flow to develop in the vicinity of the equator. By the end of 60 days after the atmosphere-ocean interaction sets in, the cold upwelling at the equator has increased to a magnitude close to 10^{-3} cm s^{-1}, as a result of which a SST minimum develops at the equator roughly 5°C colder than that at ±6°. Corresponding to this case, Fig. 3 also shows the double ITCZ structure straddling the equator at ±6°. Weak subsidence is observed over the equator. The situation here is very similar to that observed over the equatorial central Pacific. When coastal upwelling is included south of 2°N (EPAC), the Southern Hemisphere branch of the ITCZ shrinks rapidly and finally disappears altogether while an area of cold SST appears between 2°N and 30°S. The Northern Hemisphere branch of the ITCZ migrates northward, intensifying at the expense of its southern counterpart and eventually anchors at about 8°N. The resulting single ITCZ and its northward displacement in EPAC closely resembles the observed satellite-derived rainfall pattern (Fig. 1). For comparison, a rainfall chart (Fig. 4) over the model ocean is prepared using the steady-state values and their linear interpolations. The model depiction of the ITCZ structure is seen to be very accurate especially considering the simplicity of the model.

The results suggest that given a stationary forcing, the steady-state response of maximum ITCZ development is favored over the warmest waters. This is likely to be the case because in the approach to steady state, there is always a sufficient amount of time for the coupled systems to adjust so that the horizontal and vertical moisture fluxes, the warm ocean temperature, the large-scale circulation and the unstable stratification of the lower atmosphere can all feedback positively to produce a large response amplitude.

b. Seasonal transitions

We shall now discuss in some detail the seasonal variation of the tropical rainbelts in terms of various model parameters. In this experiment the atmosphere and ocean within each domain are allowed to evolve as the insolation follows its seasonal cycle. Our results will be based on the fourth year of the simulation, when cyclic states are observed in almost all the climatic variables.

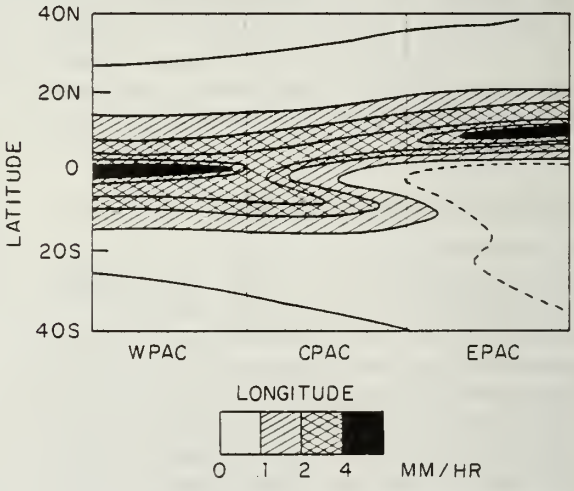

FIG. 4. Model-predicted steady-state distribution of precipitation rate over the Pacific Ocean.

84

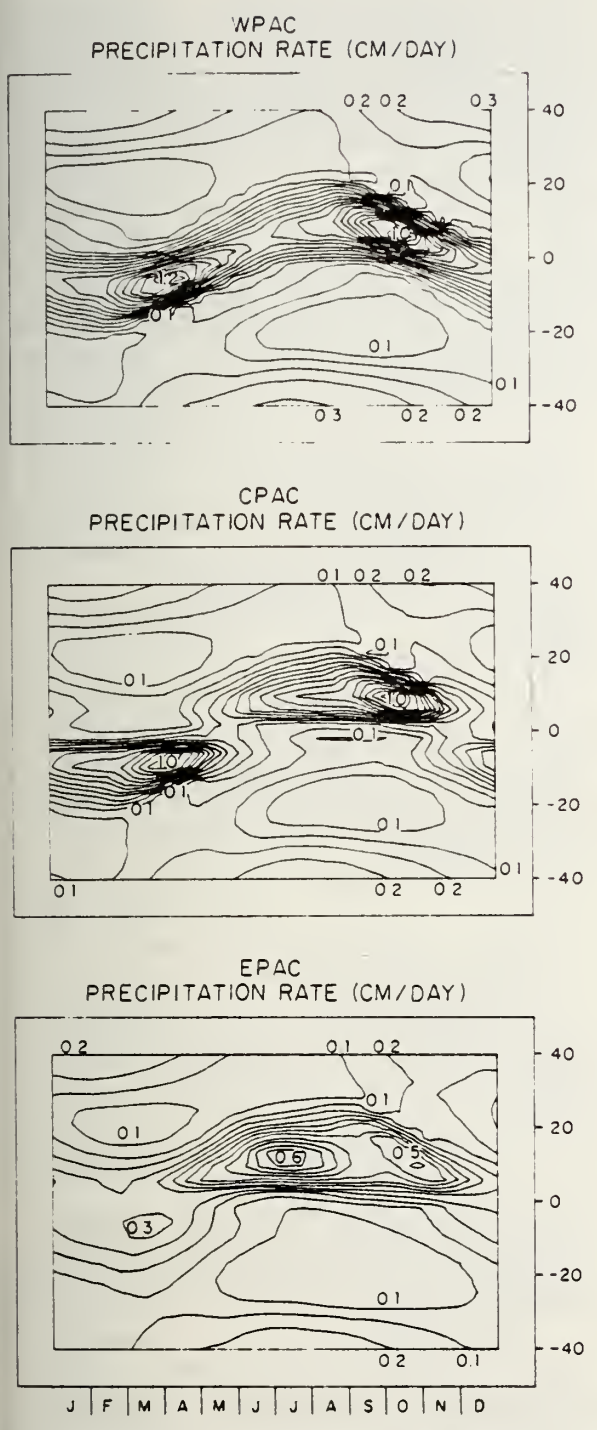

FIG. 5. Time-latitude variation of the tropical rainbelt in different domains for the fourth year of the simulated seasonal cycle.

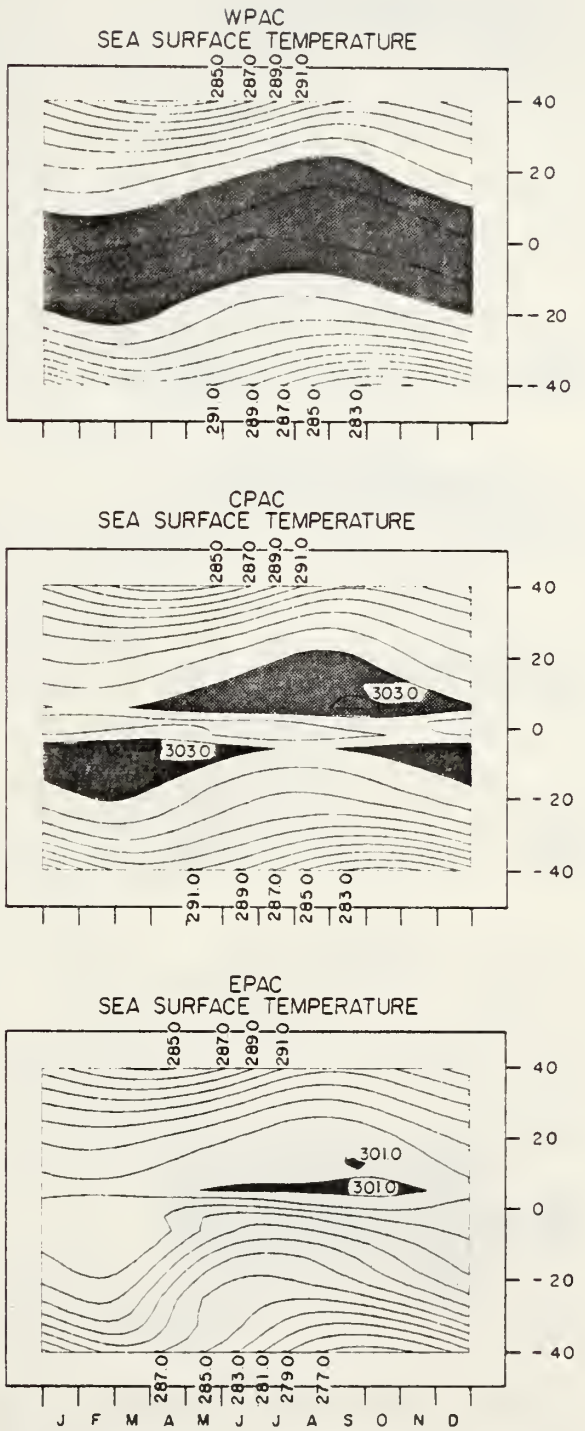

FIG. 6. As in Fig. 5 except for the sea surface temperature (K).

1) SPATIAL VARIATIONS

Fig. 5 shows the time latitude section of the rate of precipitation in the tropical rainbelt over the different domains. In WPAC, a single tropical rainbelt exists and undergoes smooth excursions between 10°S and 10°N following closely the SST variations (Fig. 6). The suppression of the ITCZ over the equatorial upwelling regions can be seen in the marked decrease in rainfall as the ITCZ crosses the equator in CPAC. A weak double ITCZ structure is

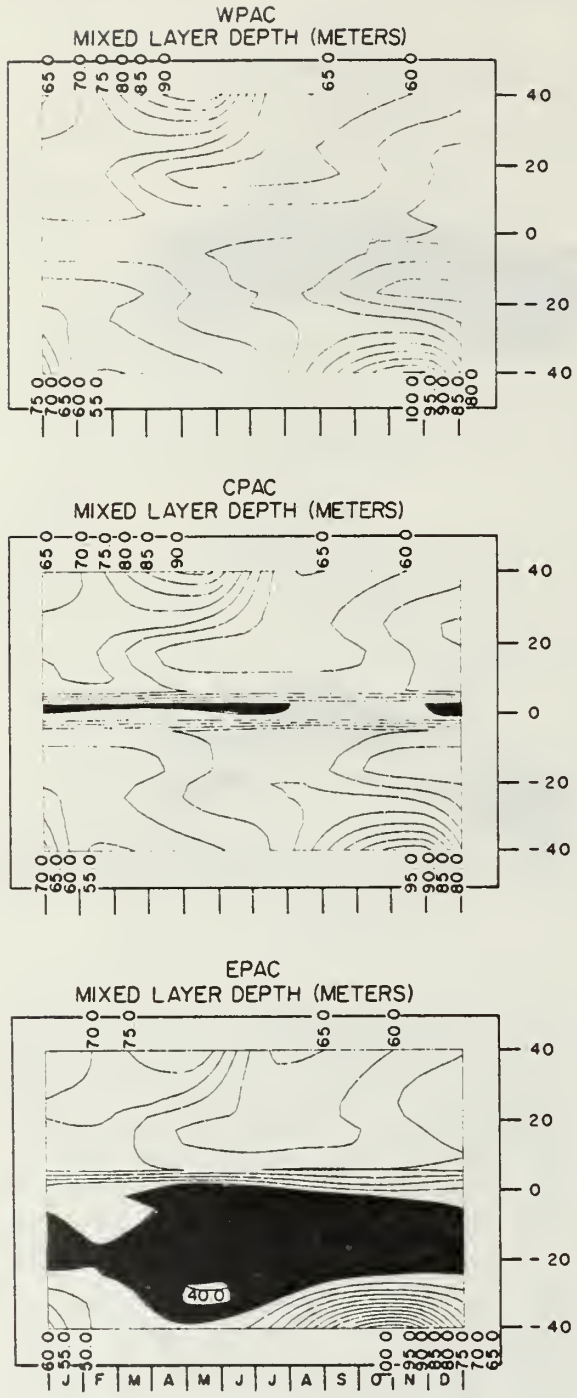

FIG. 7. As in Fig. 5 except for the mixed-layer depth (m).

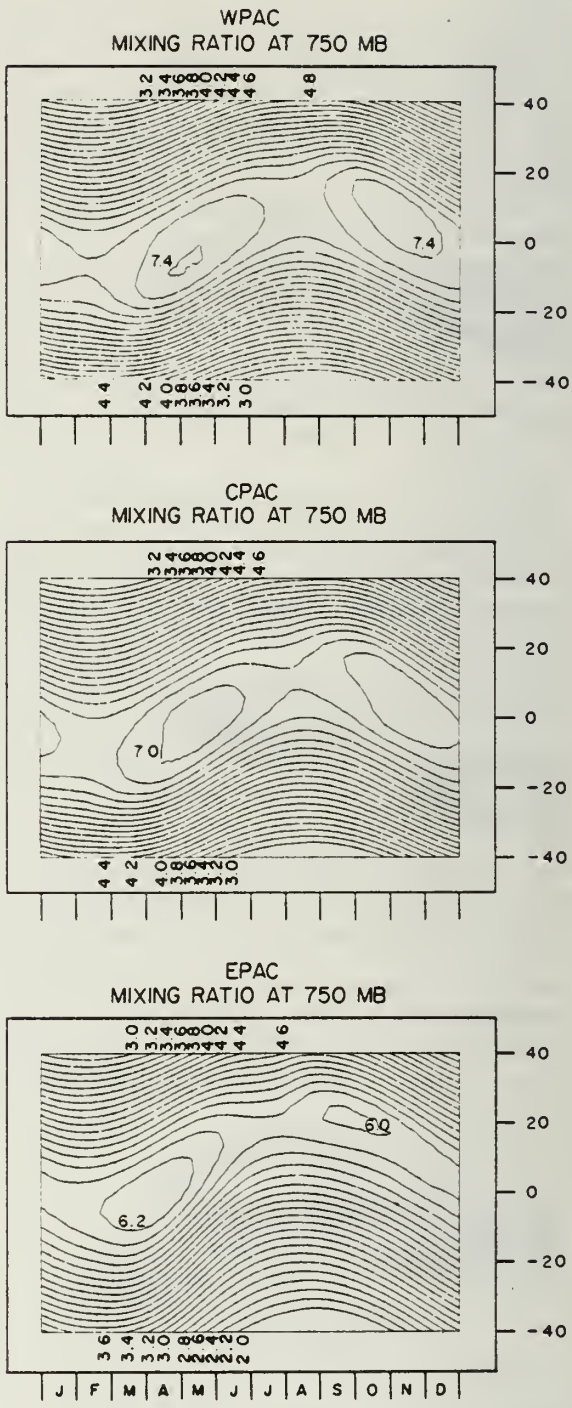

FIG. 8. As in Fig. 5 except for the mixing ratio at 750 mb (g kg^{-1}).

present in CPAC during the transition period from April to June and September to November. In both WPAC and CPAC, the northern and southern branch of the ITCZ are negatively correlated in time, signaling strong cross-equatorial influences as a result of competition between the rainbelts for moisture through low-level transport. A rather different situation occurs in EPAC where the rainbelt broadens, appearing only from June to September at about 8°N with little change in position. An arid zone extends from 30°S to 2°N throughout most of the year. The driest part of the year at these latitudes coincides with the time of the most intense coastal upwelling, as indicated by the cold SST (see Fig. 6)

and the shallow mixed-layer depth (Fig. 7). The ITCZ in EPAC appears to be much less developed than that found in WPAC and CPAC. The reduced intensity in August and September is most likely due to the increased static stability from the strong cold upwelling to the south and the reduced moisture supply from the ocean as a result of the cold SST. The latter view is further supported by the low mixing ratio at 750 mb over the cold waters in EPAC (Fig. 8). The above features of the tropical rainbelt are in excellent agreement with observations. Our results also show that even in the absence of cold equatorial SST in WPAC, the intensity of the convection tends to be weakened as the rainbelt crosses the equator. However, as the experiment indicated, there is no inherent tendency for the rainbelt to avoid the equator. The correspondence between the location of the rainbelt and the SST suggests the ITCZ is generally favored over warm SST, although its detailed structure will be affected by other factors.

2) Phase relationships

In this section, we focus on the phase relationship of the various factors affecting the tropical rainbelt development. For simplicity, we shall base our discussion in CPAC which is representative of the average conditions over the Pacific. In the time series shown in Fig. 9, we can see that in the equatorial zone, a strong semi-annual component is present in all variables shown. The spring and fall maxima coincide closely with the time when the ascending branch of the Hadley cell crosses the equator. In the tropics the annual signal becomes important with the most intense rainfall coming in mid-October at 6–10°N, at a rate of over 1 cm day^{-1}. The relative predominance of the semi-annual and annual variation in the equatorial regions and in the tropics are a direct result of variation of the solar declination with latitude and with the time of the season. Four distinct regimes in the seasonal march of rainfall amounts are demarked. They are as follows:

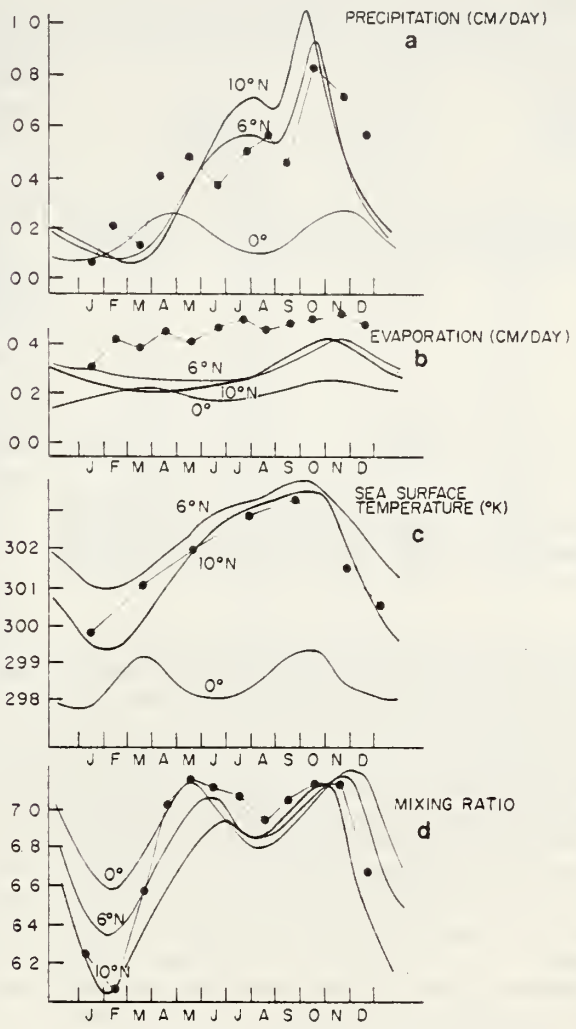

Fig. 9. CPAC time series of (a) precipitation rate, (b) evaporation, (c) SST and (d) mixing ratio at 750 mb at different latitudes for the fourth year of the simulated seasonal cycle. Observed monthly averages denoted by black dots are for the tropical central Pacific and are compiled from (a) Rao *et al.* (1976), (b) Newell *et al.* (1972), (c) Alexander and Mobley (1976) and (d) Newell *et al.* (1972).

(i) (January–April): The northern ITCZ is greatly diminished in strength because of the deficiency in moisture supply as a large amount of moisture goes into the southern ITCZ which is at its maximum development.

(ii) (May–August): During the early part of this period, low-level moisture starts to accumulate (Fig. 9d), as increased low-level convergence brings in moist air laterally and the capacity of the atmosphere to hold moisture increases with warmer air. However, at this time the moisture flux from the ocean is still weak (Fig. 9b) and the sea surfaces relatively cool (Fig. 9c). Moisture is depleted continuously from the lower atmosphere by cumulus convection in an attempt to stabilize the tropical atmosphere. The net result is the occurrence of a minimum in the low-level mixing ratio (Fig. 9d) around the end of August. This fairly strong semi-annual component of the mixing ratio in the tropics has been noted in many observations in the open ocean (Newell *et al.*, 1972).

(iii) (September–October): Strong horizontal moisture convergence, coupled with enhanced moisture flux from the warmer ocean and an increasingly unstable lapse rate, lead to a very rapid growth of the tropical rainbelt starting in late September and reaching its maximum intensity in mid-October (Fig. 10a).

(iv) (November–December): This regime is marked by diminishing insolation, rapid cooling and deepening of the oceanic mixed layer. With the

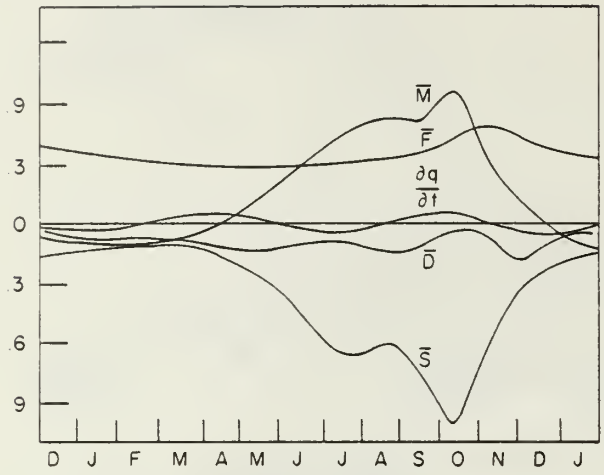

FIG. 10. Time series of the various quantities governing the moisture budget in an atmospheric column. $\bar{M}$ is the horizontal convergence, $\bar{F}$ the surface flux, $\bar{D}$ eddy fluxes including diffusion and $\bar{S}$ the sink due to precipitation. Units in 10^{-8} s^{-1}.

decrease in lateral and vertical supply of moisture, the ITCZ decays rapidly, while a large amount of moisture enters the southern ITCZ following the reverse of the cross-equatorial flow.

It is noticed from Fig. 10c at 6°N that the SST reaches its maximum value at the end of September about 4 weeks ahead of the maximum ITCZ development. The maximum evaporation from the ocean does not reach its height until about six weeks after the SST maximum. Apparently the strongest vertical moisture flux from the underlying ocean occurs not necessarily when the SST is a maximum. Such would be the case as the evaporation rate calculated by the model is dependent only on the air-sea temperature difference and the wind speed. In Figs. 9a–9d observed values of the various parameters are also shown. Except for the evaporation, the agreement with other model predicted quantities to the observed are fairly good. The discrepancies in the evaporation rate may be a result of using transfer formulas like (11) which were determined from synoptic data. Climatological application of such formulas is expected to give only approximate results.

Fig. 10 shows the time series of the various terms in the moisture prediction equation. It can be seen that a large part of the variation in the precipitation pattern is accounted for by the horizontal moisture convergence of the mean motion, $\bar{M}(\bar{q})$. The maximum precipitation lags only by about one week the maximum $\bar{M}(\bar{q})$. Fig. 10 also shows that the two major moisture sources from horizontal convergence $\bar{M}(\bar{q})$ and vertical fluxes $\bar{F}^q$ are closely balanced at all times by sinks due to precipitation and eddy fluxes $\bar{D}(\bar{q})$. Further, it is seen that during the active ITCZ period, no more than 30% of the moisture supply is derived locally from the underlying ocean. The major effect of the warm ocean surface, therefore, seems to render the lower atmosphere more unstable, and therefore more conducive to cumulus convection.

c. Perturbation responses

The experiments described in this section are designed to study the temporal and spatial response of the atmosphere-ocean system to sudden or continuous short-period changes in one or more components of the coupled system. Emphases are on the transient or low-frequency oscillations that might result. It is hoped that with these experiments, we can gain some insight into the stability and feedback mechanisms in a part of the coupled system.

1) MODEL SENSITIVITY OF THE CUMULUS PARAMETERIZATION

As the main results of this section depend strongly on the sensitivity of the model to the cumulus parameterization, we have made several test runs with the model using different values of the moisture parameters. One of the more arbitrary parameters in the parameterization is the critical relative humidity RH_c in (8), which determines the total amount of precipitable water in the model tropics. It is therefore desirable to ensure that the model is not unduly sensitive to this parameter. Fig. 11 shows the latitudinal distribution of the steady-state response in the model EPAC of various model variables for different values of RH_c (=0.25, 0.5, 0.75). Taking the standard case as $RH_c = 0.5$, a decrease to $RH_c = 0.25$ will mean approximately an increase of 20% (by 4) in the total amount of precipitable moisture. In the final steady-state, however, the increase in actual precipitation in the ITCZ is less than 10% (Fig. 11a). This illustrates that the model is capable of continuously adjusting itself to the initial increase in latent heat release by transporting heat and moisture upward, thereby depleting the available moisture from the lower atmosphere (Fig. 11b) and limiting excessive heating by increasing the stability of the tropical atmosphere (decreased η in Fig. 11c). Fig. 11d shows that for the case $RH_c = 0.25$, the MLD is shallower at the equator due to increased upwelling from increased surface easterlies, which also results in a decrease of SST at the equator by about 0.1°C (not shown). Similar changes but in the opposite direction are seen in the same parameters for the case $RH_c = 0.75$. The model is therefore fairly stable to changes of the parameter RH_c. We have also performed similar sensitivity tests with the model using different formulas for the drag coefficient C_D. Table 1 shows the latitudinal variation of the evaporation rate E_v and the condensation less

evaporation $P - E_v$ in the tropics for three different drag coefficients. In all three cases $P - E_v$ is positive between 2°N to 10°N in the core of the ITCZ and negative elsewhere in the tropics where strong subsidence prevails. It can be seen that these values do not differ by more than 10% between each case and that the relative distribution seems to be independent of the choice of the particular drag coefficient. The tests therefore demonstrate that the model is not unduly sensitive to the various parameterizations so that results described in the following sections can have meaningful physical interpretations.

2) Reference-state oscillations

Oscillations in various climatic variables in the tropical atmosphere and oceans related to air-sea interactions have been investigated extensively in many observational studies. Much of these studies revolve around the event of the El Niño. Results show that associated with the event, substantial changes are found not only in the SST but in the ITCZ, the Hadley cell, the Walker cells together with variations in oceanic upwelling, sea slope and ocean currents. Here, we again point out that since

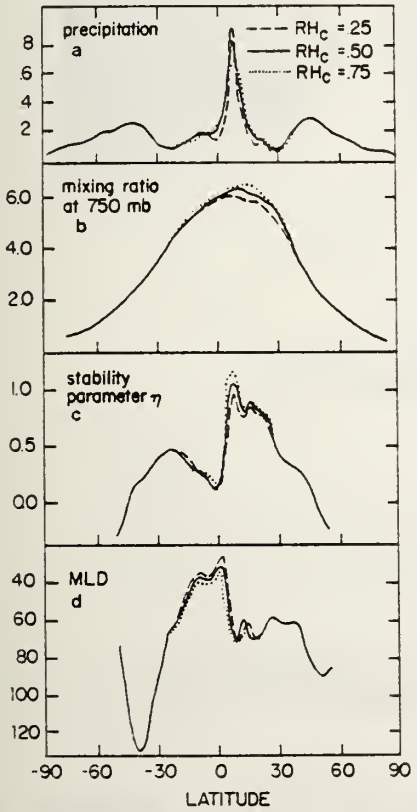

Fig. 11. Latitudinal distribution of (a) precipitation (cm day^{-1}), (b) mixing ratio at 750 mb (10^{-3} g kg^{-1}), (c) stability parameter η and (d) MLD (m) for different values of critical relative humidity RH_c.

Table 1. Latitudinal distribution of E_v and $P - E_v$ for different drag coefficients C_d. Units in cm day^{-1}.

Latitude	$C_D \times 10^3 = 1.44$ (Davidson, 1974)		$C_D \times 10^3 = 1 + 0.07\|V_s\|$ (Deacon, 1973)		$C_D \times 10^3 = 0.51\|V_s\|^{0.46}$ (Garratt, 1977)	
	E_v	$P - E_v$	E_v	$P - E_v$	E_v	$P - E_v$
30	0.22	−0.16	0.20	−0.15	0.19	−0.15
26	0.25	−0.19	0.23	−0.19	0.21	−0.18
22	0.28	−0.22	0.27	−0.21	0.27	−0.24
18	0.32	−0.25	0.31	−0.24	0.32	−0.27
14	0.33	−0.11	0.32	−0.10	0.34	−0.18
10	0.32	0.19	0.29	0.17	0.31	0.12
6	0.35	0.36	0.32	0.30	0.33	0.28
2	0.22	0.00	0.22	0.00	0.25	0.01
−2	0.17	−0.07	0.17	−0.07	0.20	−0.09
−6	0.19	−0.06	0.19	−0.06	0.22	−0.10
−10	0.20	−0.06	0.19	−0.06	0.22	−0.09
−14	0.20	−0.10	0.20	−0.10	0.22	−0.12
−18	0.22	−0.15	0.21	−0.15	0.22	−0.18
−22	0.24	−0.18	0.22	−0.18	0.21	−0.18
−26	0.23	−0.18	0.21	−0.17	0.19	−0.16
−30	0.23	−0.15	0.20	−0.14	0.21	−0.15

we are only dealing with a domain-averaged circulation, longitudinal controls like the Walker cell and the equatorial current systems cannot occur. In this section we study the response of the model EPAC to a sudden change in the moisture supply. This is achieved by introducing an amplitude factor $g(t)$ in the term involving the horizontal convergence of moisture into tropical cumulus convection:

$$F'(t) = g(t)\langle\bar{\omega}\bar{q}\rangle, \tag{16}$$

where

$$g(t) = \begin{cases} \{1 + \exp[-(t - t_0)/t]\}^{-1}, & t_1 \geq t \geq t_0 \\ 0, & t > t_1 \end{cases} \tag{17}$$

and $\tau = 20$ days, $t_1 = 140$ days and $t_0 = 3\tau$ so that $g(t) \approx 0$ at $t_0 = 0$ and $g(t) \approx 1$ at $t = t_1$. From (16) the resulting condensation due to the perturbation is given by

$$S_c' = -\eta(1 - b)g(t)\langle\bar{\omega}\bar{q}\rangle/\Delta p \tag{18}$$

and the total heating due to convection including the perturbation is

$$\bar{Q}_c = \begin{cases} -\dfrac{L}{C_p}(\bar{S}_c + S_c'), & \langle\bar{\omega}\bar{q}\rangle < 0 \\ 0, & \langle\bar{\omega}\bar{q}\rangle \geq 0. \end{cases} \tag{19}$$

The amplitude factor $g(t)$ in (17) therefore has the effect of doubling the moisture convergence in a 140-day period at the end of which the moisture convergence is suddenly relaxed back to its normal value. The model is subsequently integrated for another two years. We should point out that the imposed forcing chosen here is in the moisture con-

89

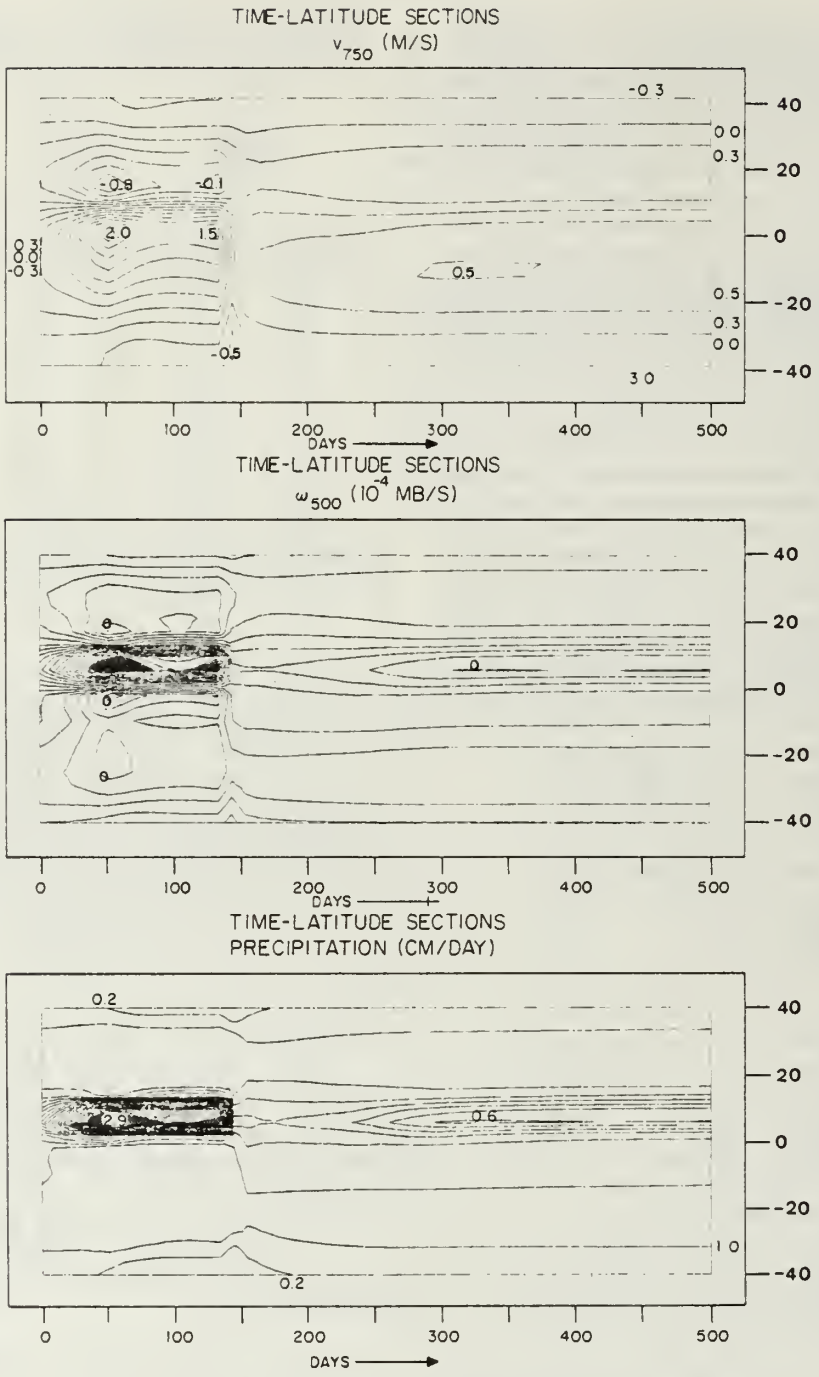

FIG. 12. Time-latitude variation for the first 500 days of the meridional and vertical winds and the associated rainfall rates in the model tropics as a result of a 140-day period of gradually increasing horizontal moisture convergence, followed by a relaxation back to normal conditions.

vergence. The choice is, however, arbitrary. We could have started the perturbation in other component or components of the system (e.g., surface wind stress, oceanic upwelling, heat transport, etc.). The goal of the experiment is, regardless of the triggering processes, to elucidate the feedback mechanisms in the model atmosphere-ocean system and its ability to adjust to or sustain a given perturbation.

(i) Winds. Fig. 12 shows the latitude-time section or the first 500 days of the meridional wind at 750 mb nd the vertical wind at 500 mb, respectively, as a esult of the increased moisture convergence. In the rst 140 days the extra energy input from the in- reased latent heat release has resulted in enhanced ow-level convergence in a narrow belt between and 10°N, with vertical motion in the center of he ITCZ reaching to over 2 cm s^{-1}. Strong, moist ow-level flows on both sides of the convergence one, in particular those of the northern tropics, rings in a large amount of moisture from the tropi- al oceans. This laterial supply of moisture, adding o the already enhanced moisture convergence, oosts the convective latent heat and precipitation within the ITCZ to an excess amount. At this stage the low-level moisture renders the lower tropical atmosphere very unstable over the warm ocean. By about 100 days, the explosive growth of the ITCZ is checked somewhat by the stabilizing effect of the cumulus convection mostly as a result of the vertical moisture transport and the cooling of the underlying ocean from strong mixing made possible by oceanic upwelling. A subtropical arid zone exists on both sides of the ITCZ, as a result of the strong compensating subsidence. Following the relaxation at 140 days, the ageostrophic components of the wind undergo vigorous adjustments for a short period, and then settle down to a quasi-steady state, evolving smoothing, as the ocean slowly recovers from its initial perturbation.

Much of the potential energy release from cumulus convection is converted into kinetic energy of the zonal flow. In the first 140 days, enhanced easterly trade winds occur in the tropics (Fig. 13) with increasing anticyclonic shear in the subtropics. As the

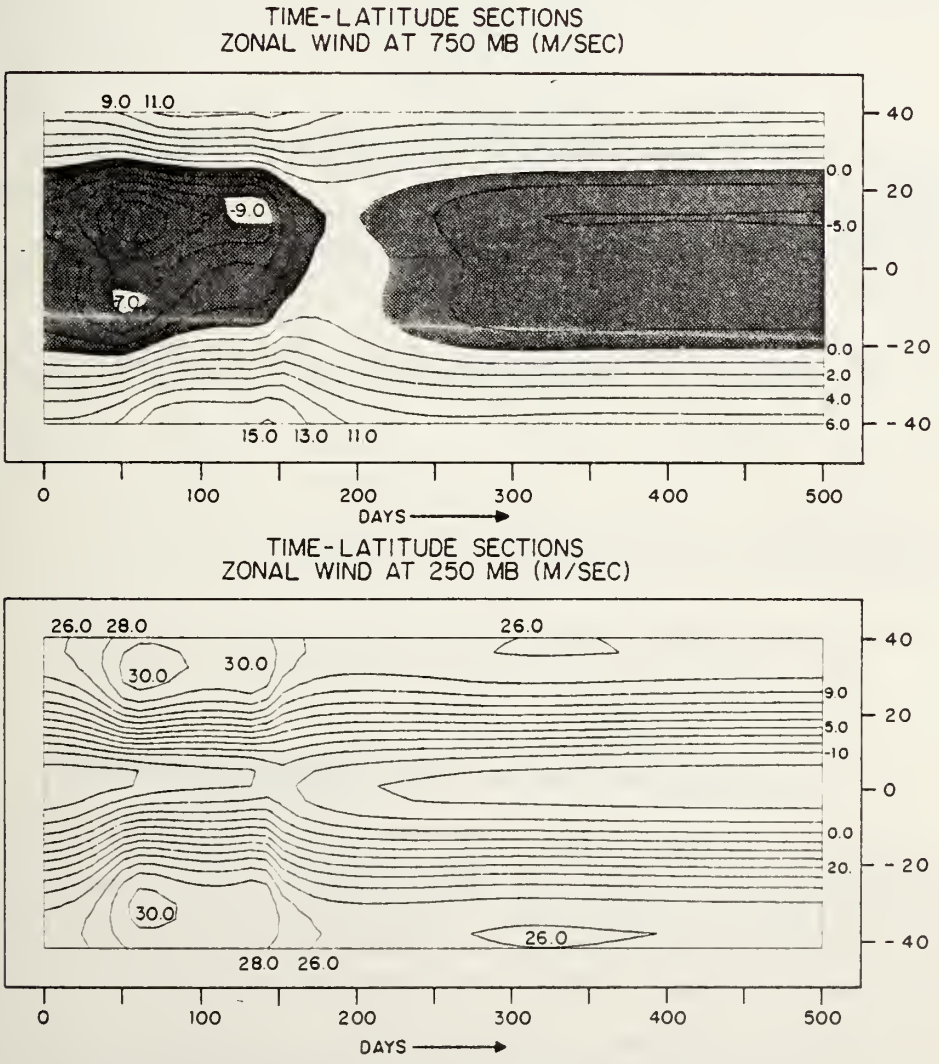

FIG. 13. As in Fig. 12 except for the zonal wind at 750 and 250 mb.

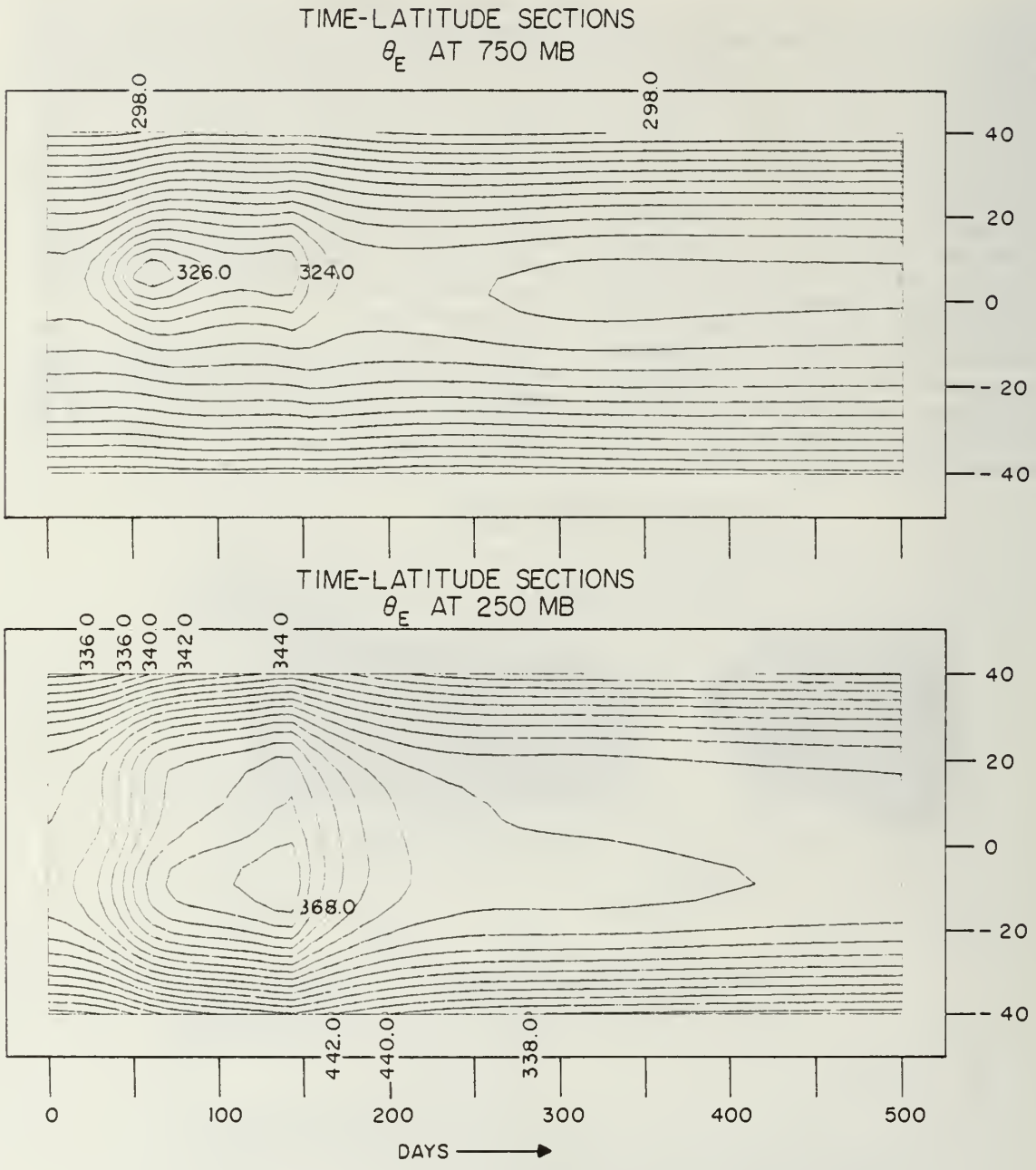

FIG. 14. As in Fig. 12 except for the equivalent potential temperature at 750 and 250 mb.

surface flow in the eastern ocean depends strongly on the surface wind stress curl, the anticyclonic wind stress causes ocean currents to flow equatorward, advecting colder water towards the warmer tropics, thus opposing the effect of the atmosphere to warm the ocean. The major part of the negative feedback in the model ocean, however, is from the enhanced coastal and equatorial wind mixing induced by the strong upwelling south of 2°N. The response of the upper level zonal wind also shows some interesting features. Upper level westerlies are seen to strengthen and isotachs concentrate toward lower latitudes during the most active ITCZ period. Westerly momentum is continuously exported from the tropics into the subtropics by the strong ageostrophic upper level outflow concentrated near the divergence region. The result is intensification and equatorward migration of the subtropical jet stream. As soon as the Hadley circulation relaxes at the end of 140 days, the upper westerly belt weakens and widens laterally. The largest response amplitude is found at subtropical latitude where the momentum flux

convergence by the mean meridional circulation is strongest, whereas the maximum conversion of zonal potential to zonal kinetic energy (not shown) is located about 2000 km upstream within the tropical convective regions.

(ii) Temperature. Thermal responses of the atmosphere are illustrated in Fig. 14 where the equivalent potential temperature (θ_E) at different levels are shown. In the first 50 days or so the lower atmosphere (750 mb) is being heated at a rate of ~1°C day^{-1}. As expected a large part of the convective heating is balanced by the adiabatic cooling induced by the strong upward motion. The net adiabatic rate is about an order of magnitude smaller than the maximum heating rate of 12°C day^{-1} due to deep moist convection. The effect of the cumulus convection to transport heat and moisture to the upper troposphere is seen in the large increase in θ_E at the 250 mb level. The maximum upper level heating is located at about 10°S coinciding with the core of the strongest subsidence in the meridional circulation. It is also noticed that, by the end of the first 150 days, the warming at the upper troposphere has spread over the tropics and subtropics. This broad latitudinal extent of heating is consistent with the fact that the large amount of available potential energy generated by cumulus convection in restricted low-latitude regions are transported to higher latitudes by the strong divergent outflow in the upper branch of the Hadley circulation.

The effect of the warm moist marine air in affecting the static stability of the lower atmosphere is best illustrated in Fig. 15, where θ_E of the surface

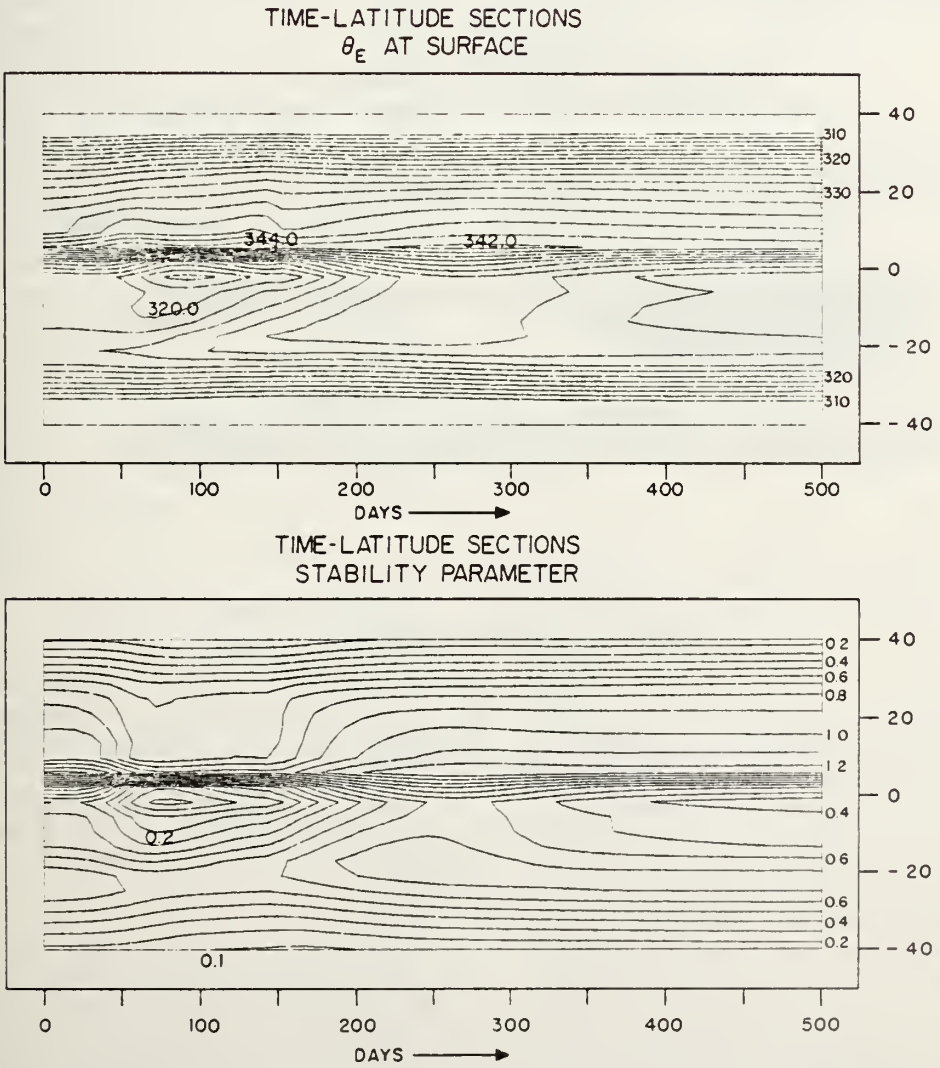

FIG. 15. Time-latitude sections of the equivalent potential temperature of the surface air and the stability parameter for the same period as in Fig. 12.

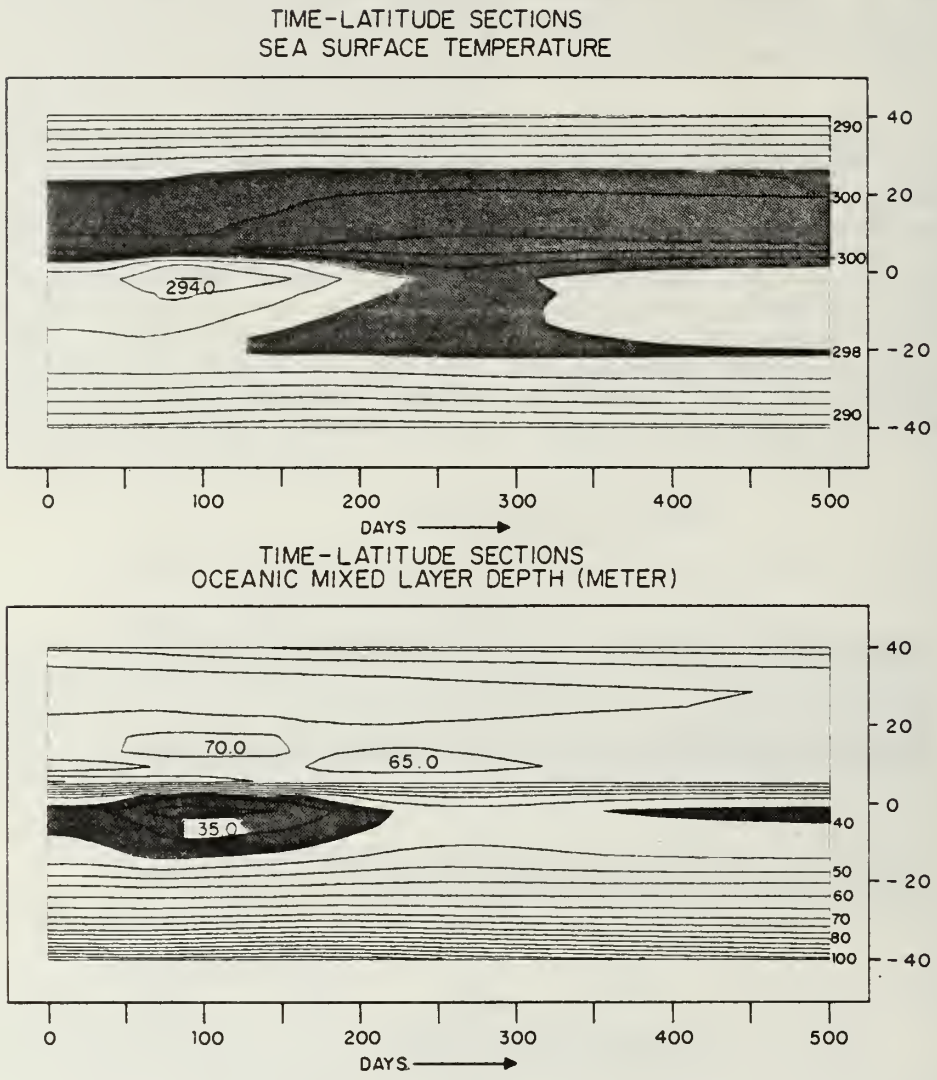

FIG. 16. Time-latitude section of the ocean mixed layer temperature and depth as a result of the perturbation, for the same period as in Fig. 12.

air and the stability parameter η are shown. During the early period of the experiment, a very strong θ_E gradient existed at the surface just north of the equator separating the warm moist air to the north with the dry, cool air over the cold upwelling ocean to the south. A large part of this steep gradient is accounted for by the variation in the low-level moisture content. The stability parameter η, which determines the entrainment rate in the cumulus convection, is positive for an unstable lapse rate in the lower troposphere [see Eq. (7)]. The larger the positive value of η, the more unstable the atmosphere. While the tropical atmosphere is most unstable during the first 50 days of the experiment, the effect of the cold upwelling to limit layer instability is seen in decreasing η as the southern ocean cools, thus providing an important negative feedback mechanism between the ITCZ strength and the SST. At 50–100 days and at 6°S to 0° the strong stabilizing effect of cold SST has resulted in a region of strong positive stability ($\eta \rightarrow 0$), which eliminates completely the existence of cumulus convection (see also Fig. 12). In contrast, the influence of warm SST has been to provide a more unstable lower atmosphere which deep moist tropical convection can easily penetrate.

(iii) SST and MLD. Much of the structure of the SST and mixed-layer depth have been alluded to in the previous discussions. The most striking feature in the oceanic response is the extent of the cold SST and shallow, mixed-layer development in the first 100 days (Fig. 16). Following closely the increasing trade winds, strong upwelling lifts the mixed layer closer to the surface, making the entrainment at the base of the mixed layer more effective

cooling the surface because a given amount of nergy input from the wind now affects a smaller epth. This effect coupled with the increased sur- ace wind causes anomalously cool water to appear etween 2°N and 20°S. In general the effect of the old underlying ocean on the atmosphere is two- old. Besides its tendency to inhibit deep moist con- ection by reducing η, it also tends to limit the mount of moisture locally available via vertical urbulent fluxes to the atmosphere. Since the verti- al moisture flux variation is small during this eriod, we are led to believe that the former effect s more prominent. The SST warming accompanied y thermocline deepening starts at about 100 days nd in a period of six-month anomalous high SST, ompared with initial values at the same latitude, as spread throughout the tropical ocean from 10°N to 20°S. It is important to note, as far as the model ocean is concerned, that it shows no high-frequency transient response to the sudden shock received by the atmosphere as the air masses undergo vigorous adjustment. Apparently, the geostrophic adjustment within the atmosphere is on a much shorter time scale than can be accommodated by the ocean. The long memory of the ocean is seen in the reappearing of a much weakened cold anomaly at about 450 days, about 12 months after the first SST minimum.

(iv) Summary. The overall picture of the interaction for the entire integration period is now summarized. In the reference state time series (Fig. 17) shown, ΔU_S, ΔV_S, ΔP and ΔT_s represent the deviations from their initial values of surface zonal wind, meridional wind, precipitation, and oceanic mixed layer temperature, respectively. All quantities have been normalized by their averaged absolute deviations over the entire tropics.

In all the latitudes shown the enhanced moisture convergence in the first 140 days has resulted in rapidly enhancing surface easterlies, intensifying Hadley cells, followed by strong oceanic upwelling and rapidly falling SST throughout the tropics. At 6–10°N the precipitation amount increases drastically as the moist convection intensifies. The intensifying ITCZ, trade winds and the Hadley circulation are opposed by the cold water upwelling. During the initial period the atmosphere goes through a major readjustment mainly in the divergent component of the wind. As a result of the adjustment, the SST overadjusts through a six-month period, to a warm anomaly within the tropics. This simulated warming is in agreement with the view that in the actual atmosphere-ocean system, the anomalous SST is only a local signal of a large-scale adjustment to circulation changes that have taken place over a wide region in the Pacific (Reiter, 1978b), although in our case the responses are strictly locally forced. By far the largest oceanic

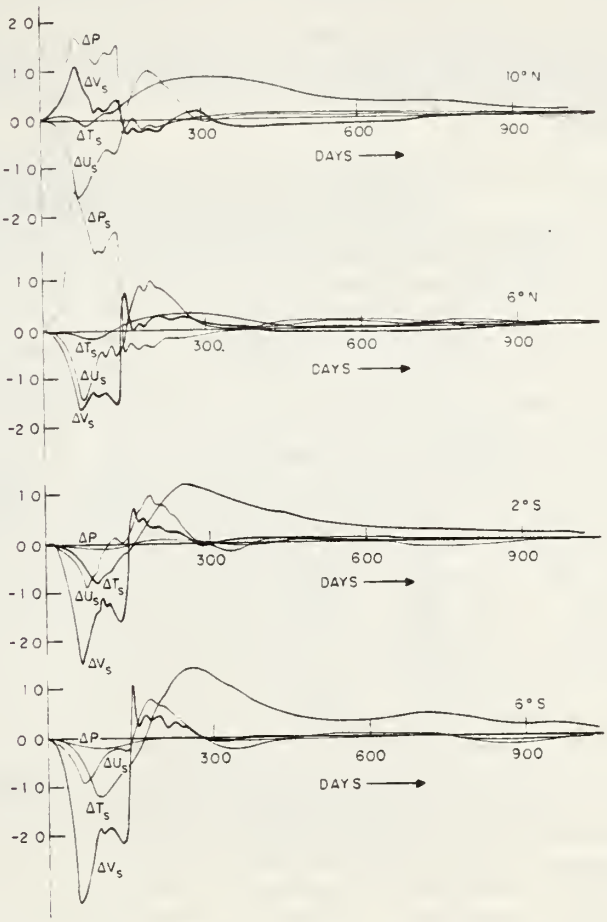

FIG. 17. Time-series of normalized anomalies of precipitation Δp_s, surface wind speed ΔV_s, ΔU_s, and sea surface temperature ΔT_s, for the entire three-year integration period at different latitudes.

response occurs over the upwelling regions of the Southern Hemisphere tropics. The largest increase in precipitation is over the warm tropical waters of the Northern Hemisphere. A time lag between the maximum surface easterlies and the coldest SST is about a month, whereas the maximum SST lags the minimum surface wind by about two months. The difference in lag time has to do with the different entrainment rates during the shallowing and deepening phases of the mixed layer. Responses subsequent to the warm SST development are strongly damped. The effect of the positive SST anomaly on the atmosphere appears to be weak, although some strengthening of the ITCZ and the meridional circulation can be detected as a result of the warm SST. It seems, therefore, that in the absence of other controls the ability of a weak positive SST anomaly to initiate a free vacillating state in the model atmosphere-ocean system is rather limited. Yet in the presence of strong atmospheric circulation changes, in this case trade wind

surges triggered by enhanced moisture convergence, the tropical ocean can be forced into an interactive role through strong readjustment processes in the atmosphere.

3) Forced oscillation

The experiment described in this section is designed to investigate the low-frequency oscillations of the coupled systems under forced conditions, based on the premise that such oscillations can arise from the "slow" integral response of the system to "fast" forcings by continuous, random, short-time-scale disturbances similar to observed weather fluctuations. As it stands now, the system of time-dependent equations we considered are inherently deterministic in that the equations will predict a unique evolution in time, approaching an asymptotic steady state for any given initial conditions, so that the model is not capable of internally generating random-type, nonperiodic variations. The inclusion of random stochastic forcings into otherwise deterministic climate models have been achieved in a number of recent studies involving climate variabilities (e.g., Frankignoul and Hasselmann, 1977; Lemke, 1978; Robock, 1978). Most of their studies, however, focus on the interpretation of the low-frequency linear responses of the "slow" (ocean) variables with no feedback on the "fast" (atmosphere) variables (Frankignoul and Hasselmann, 1977; Lemke, 1978). In our model, continuous short-period atmospheric forcings are simulated by imposing a spectrum of perturbations in the governing equations: As these perturbations are specified they are basically not truly stochastic in nature, but are chosen such that they possess the characteristics of the observed frequency spectra. As before, the perturbations are imposed on the term involving the horizontal convergence of moisture in tropical cumulus convections as in (16) and (17) but now

$$g(t) = \mathrm{Re}\Sigma G_\nu \exp[i(\nu t + \theta_\nu)], \qquad (20)$$

with $\Sigma_\nu G_\nu^2 = 1$ and the phase θ_ν arbitrary. The frequency spectrum (Fig. 20 top) ranges from periods of 1 to 9 days and is chosen such that over 80% of the variance is in the 4–5 day periods in accordance with the observed periodicities in tropical weather disturbances. From (16) the perturbation forcing is proportional to the atmospheric variables $\bar{\omega}$, $\bar{q}$, which depend also on the oceanic variables, thus providing a feedback between the "fast" and the "slow" variables.

Starting from the equilibrium state under equinoctial condition, the perturbation is imposed on the model EPAC, and the coupled system integrated for four years. An immediate effect of the imposed perturbation is the excitation of a variety of transients and short-period oscillations in the atmosphere. In the ocean variables and the surface fluxes, quasi-periodic, low-frequency changes appear, suggesting an integral response to the imposed disturbances. Time series of the specified perturbation $g(t)$ together with the resulting wind stress and surface fluxes from the tropical ocean taken every 5 days for the last 1000 days of the integration period are shown in Fig. 18. It is apparent that in addition to responses in the imposed frequency ranges a large part of the responses are in the low-frequency range (~months) of the spectrum. Also present are transients of periods ranging from 2–4 months. The fact that such oscillations are not observed in the free oscillation experiments strongly suggests that these vacillating states are a result of the excitation by the imposed continuous short-period forcings. In Fig. 19, the SST and mixed layer depth anomalies are shown. Similar low-frequency variabilities are observed as in the surface fluxes and wind stress, except in this case short-term variations (periods $\leq$ 1 month) tend to be suppressed. Close to the equator alternate warming events and cooling take place. Each of the warming events (e.g., day 500 to day 580, day 1200 to day 1300) can be traced back about two months earlier to an anomalous strengthening of the trade winds followed by rapid mixed layer cooling and then relaxation of the surface wind stress. The weakening of the upwelling during a warming period is indicated by the deepening of the mixed layer during that period. It should again be emphasized that because of the neglect of zonal exchanges, our model is strictly locally forced. The sequence of events is similar but not to be confused with the observations (e.g., by Wyrtki, 1975) regarding the origin and anomalous events associated with the El Niño.

It is interesting to look at the spectra of some atmospheric as well as oceanic variables in relation to the spectra of the forcing. Fig. 20 shows the spectra of $g(t)$, the vertical velocity (ω) at 500 mb and the SST averaged over the southern tropics (0–10°S) from time series of the 1500-day simulated period. It can be seen that while the atmospheric spectrum S_ω shows strong linear response at the forcing periods (i.e., 4–5 days), a large amount of the variance also appears at 8–20 day periods with rapidly decreasing amounts at periods over typically a month. The oceanic spectrum S_T, on the other hand, shows little response at the short periods, fairly strong variabilities at the 10–30 day periods but strongly enhanced response for periods over two months. In the spectra shown resolution at low

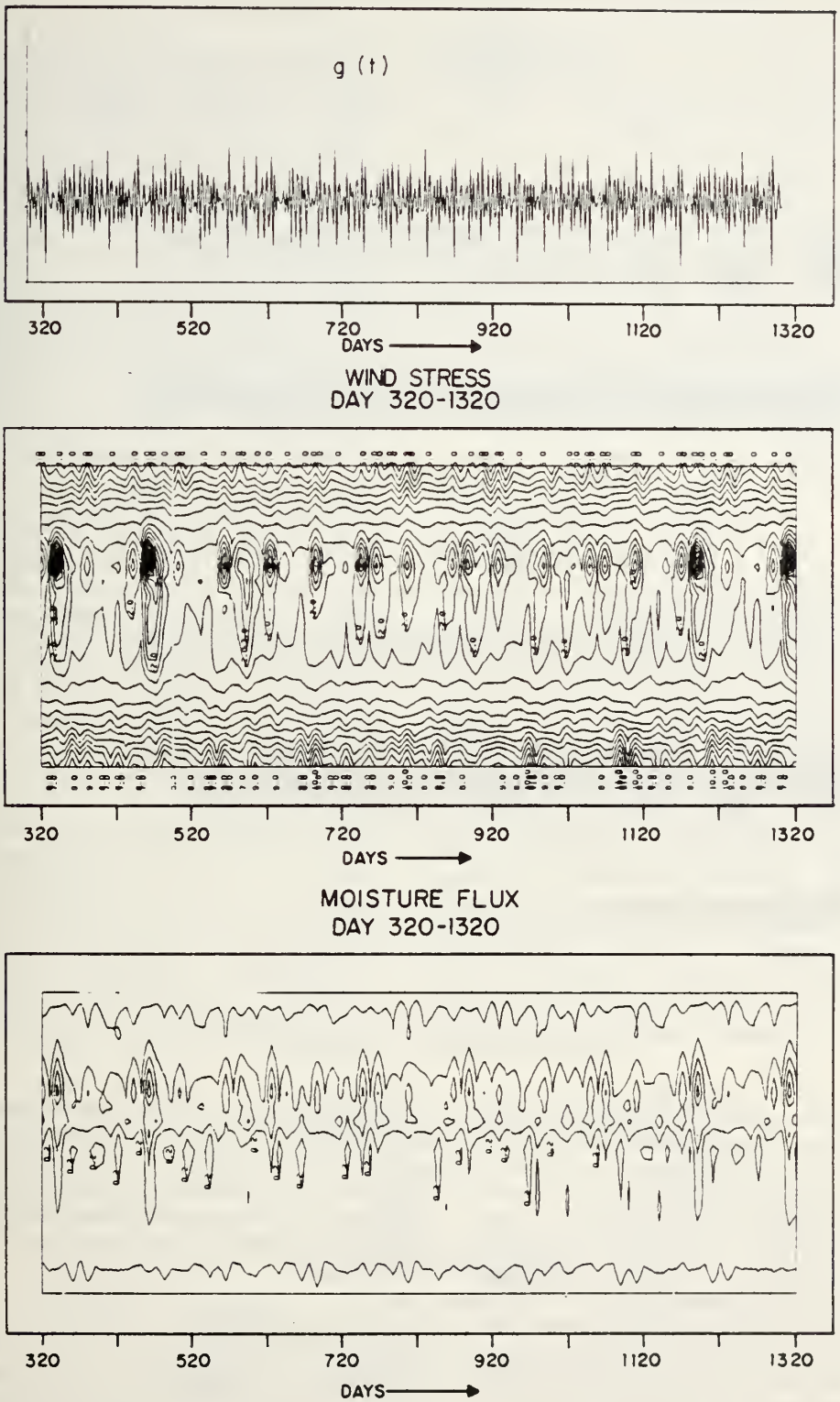

FIG. 18. Time-latitude section of the wind stress (10^{-1} N m^{-2}) and surface moisture flux (cm day^{-1}) from the ocean as a result of continuous short-period atmospheric forcings for the last 3 years of the integration period. Data taken from every 5 days in the time series.

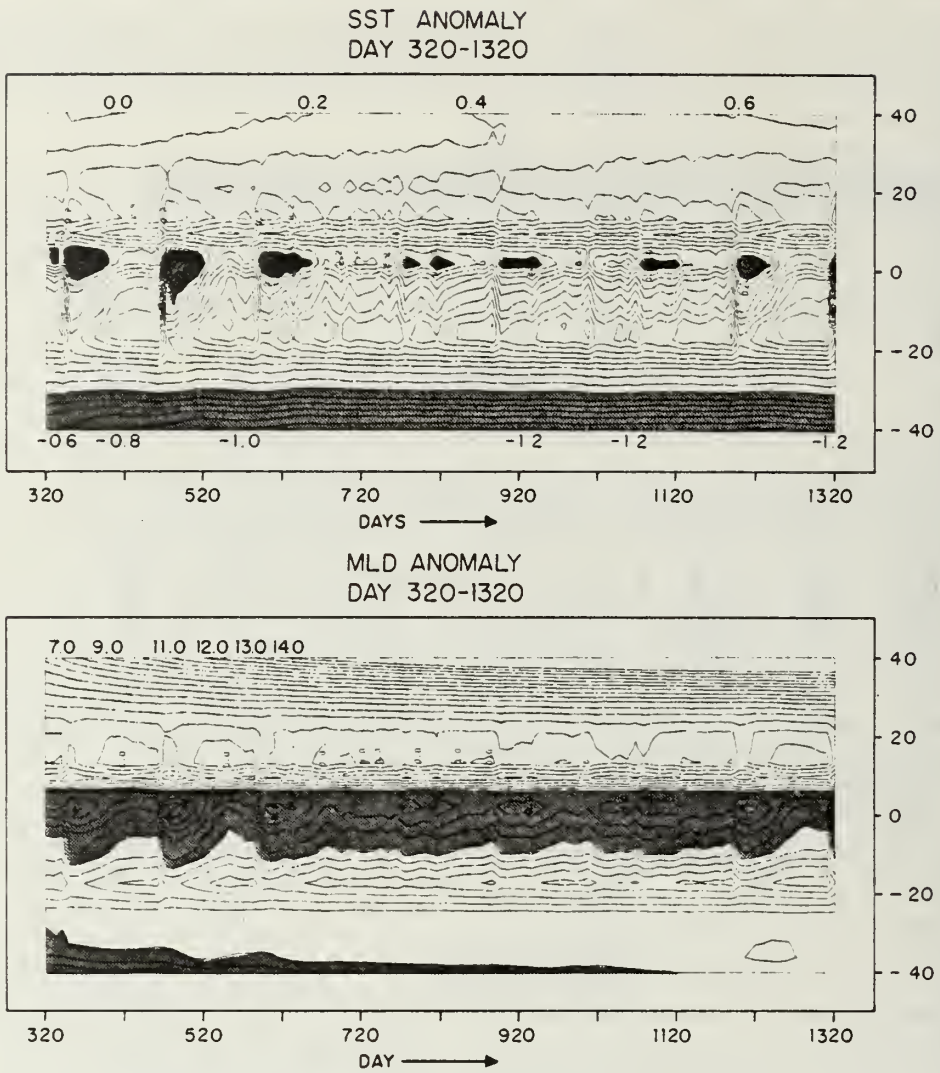

FIG. 19. As in Fig. 18 except for the sea surface temperature anomaly (K) and mixed layer depth anomaly (m).

frequencies is greatly limited by the length of the time series generated. Nevertheless, even with this limitation, there appears to be in the spectra shown a nonlinear transfer in time between the imposed forcing and the response of the coupled system. Therefore, the overall effect of the coupled atmosphere and ocean is to integrate the short-period forcings and to generate medium (10–30 days) and low-frequency (over 2 months) responses with the ocean accounting for the major part of the variance at the low-frequency end of the spectra. These separations in time scales are possibly the manifestations of a red-shifted spectral response in a multi-time-scale climate system generated by continuous, random, short-period "weather" disturbances (Hasselmann, 1976). The low-frequency climatic variabilities predicted by our model are determined mainly by the time scale of interactions involving the wind stress forcings and the entrainment processes in the oceanic mixed layer. The interactive role of the ocean is in providing a slowly (periods $\geq$ 1 month) varying component through which feedback mechanisms similar to those discussed in the last section operate.

5. Concluding remarks

Based on the results of a series of simple experiments we have demonstrated that the sea surface temperature distribution is the primary factor in determining the location and transition of the tropical rainbelt. Many features of the ITCZ, such as the absence of the rainfall minimum in the equatorial western Pacific, the existence of a double maximum

bordering the equator in the central Pacific and the northward shift in the eastern Pacific, are all closely tied to the different amount of oceanic upwelling found in these regions of the oceans. We have also shown that while the ITCZ is favored over warm waters, the period of most intense precipitation in a typical seasonal cycle does not necessarily coincide exactly with the time of the maximum SST, nor with the maximum evaporation from the ocean. More importantly, the strongest convective activities depend on the abundance of moisture supply from horizontal convergence and the static stability of the lower atmosphere. During active convective periods, the mean horizontal convergence of moisture mostly coming from the marine boundary layer and from the lower troposphere account for a major part of the total moisture in the tropical precipitation. Similar effects have been observed in heat budget studies of the tropics (e.g., Cornejo-Garrido and Stone, 1977).

The perturbation experiments indicate that in the model tropics, the primary source of kinetic energy is the conversion from eddy available potential energy generated by moist convection, and that the ocean, by virtue of its larger inertia, plays an important role in modulating large atmospheric disturbances. The self-enhancing processes between the latent heat release by cumulus convection, the moisture convergence and the Hadley cell strength are opposed by oceanic upwelling and the concomitant cooling of the mixed layer primarily through a stabilization of the lower atmosphere and a decrease of moisture supply from the tropical oceans. The major effect of the warm SST appears to be in providing an unstable atmosphere favorable for deep moist convection. The main feedback loops of the model are illustrated in Fig. 21. Further, results of the forced oscillation experiment suggest that the statistical effect of a large number of short-term atmospheric disturbances is capable of generating large-scale low-frequency variations in the coupled system. The occurrence of major anomalies in the ocean appears to be forced by anomalous atmospheric changes, with low-frequency quasi-periodicities determined by the time scale of the ocean mixed layer.

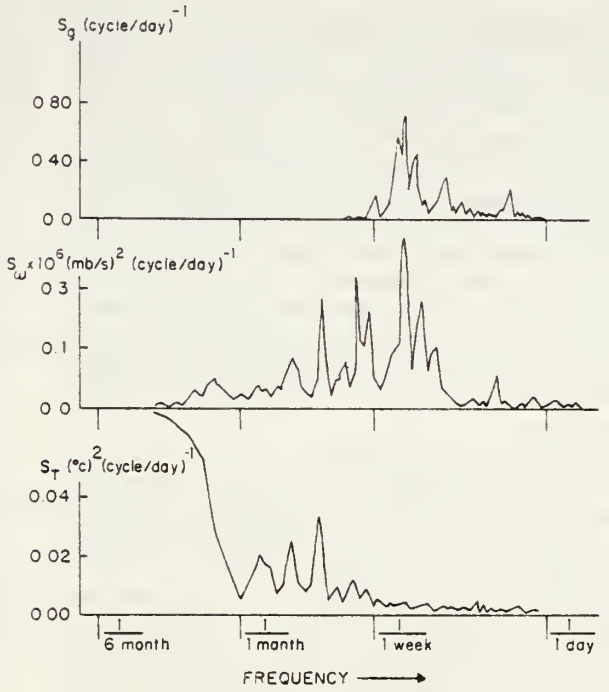

FIG. 20. Frequency spectra of the forcing function (S_q), the vertical p-velocity at 500 mb (S_ω) and the SST (S_T) averaged over the southern tropics (0–10°S) from time series of a 1500-day simulated period.

The obvious drawback of the present model is the

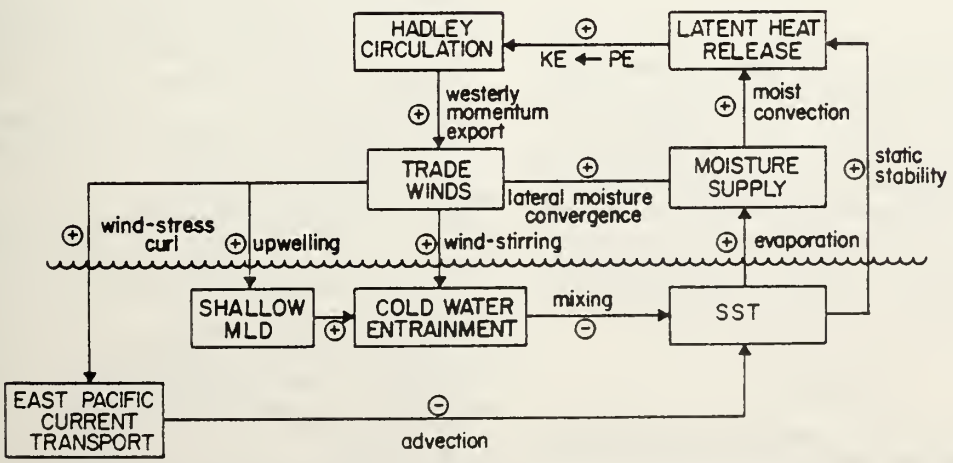

FIG. 21. Schematic diagram showing the feedback mechanisms in the model EPAC ocean-atmosphere system. Positive and negative feedbacks are denoted by + and −, respectively.

lack of longitudinal resolution, thus making the experiments highly idealized. Despite this, it is hoped that the experiments here will provide some insight into the stability and feedback mechanisms intrinsic in at least part of the system. As is generally accepted now, the primary driving force in the east-west circulation in the equatorial plane is the longitudinal distribution of convective heating (Webster, 1973; Cornejo-Garrido and Stone, 1977) and the equatorial current systems are directly related to east-west sea level changes and trade wind variations across the longitudinal span of the Pacific Ocean (Wyrtki, 1977). The details of these interactions cannot be portrayed with the present form of the model.

To add to the complexity of the interaction, the effect of continentality also seems to have profound effects on the equatorial east-west circulation. While the interannual variability of the Walker cell appears to be consistent with the eastern Pacific SST variation (Chang, 1977; Chang and Miller, 1977; Krishnamurti, 1971), Kanimutsi and Krishnamurti (1978) showed that the Walker circulation is only one part of a very strong east-west circulation mainly due to the differential monsoon heating arising from ocean-continent contrast. It therefore appears that if the SST anomaly in the eastern Pacific is correlated with the Walker circulation, it may in turn bear a relationship with the monsoon circulation over the Indian subcontinent. Therefore, the complete interaction picture of which the El Niño events are only a part seems to be far more complicated than the suggested meridional control dealt with in this paper. At present, a study using the multi-domain version of the model including explicit representation of atmosphere-ocean-land systems is being undertaken to probe further into these and other details of the interaction problem.

Acknowledgment. The author wishes to thank Professor C.-P. Chang for discussions and Professor R. L. Haney for reading the manuscript and making helpful comments. The computations of this work were done at the W. R. Church Computer Center of the Naval Postgraduate School, Monterey. This research was supported by the Climate Dynamic Research Section, National Science Foundation, under Grant ATM 77-14820. Partial support was also obtained from the Foundation Research Program of the Naval Postgraduate School.

REFERENCES

Anthes, R. A., 1977: A cumulus parameterization scheme utilizing a one-dimensional cloud model. *Mon. Wea. Rev.*, **105**, 270–286.

Alexander, R. C., and R. L. Mobley, 1976: Monthly average sea-surface temperatures and ice-pack limit on a 1° global grid. *Mon. Wea. Rev.*, **104**, 143–148.

Barnett, T. P., 1977: The principal time and space scale of the Pacific trace wind fields. *J. Atmos. Sci.*, **34**, 221–236.

Bates, J. B., 1970: Dynamics of disturbances on the intertropical convergence zone. *Quart. J. Roy. Meteor. Soc.*, **96**, 677–701.

Bjerknes, J., 1966: A possible response of the atmospheric Hadley circulation to equatorial anomalies of ocean temperature. *Tellus*, **18**, 820–829.

——, 1969: Atmospheric teleconnections from the equatorial Pacific. *Mon. Wea. Rev.*, **97**, 163–172.

——, 1972: Large-scale atmospheric response to the 1964–65 Pacific equatorial warming. *J. Phys. Oceanogr.*, **2**, 212–217.

Chang, C.-P., 1977: Viscous internal gravity waves and low frequency oscillations in the tropics. *J. Atmos. Sci.*, **34**, 901–910.

——, and C. R. Miller III, 1977: Comparison of easterly waves in the tropical Pacific during two contrasting periods of sea surface temperature anomalies. *J. Atmos. Sci.*, **34**, 615–628.

Charney, J. G., 1966: Some remaining problems in numerical weather prediction. *Advances in Numerical Weather Prediction*, The Traveller's Research Center, Inc., 61–70.

Cornejo-Garrido, A. G., and P. H. Stone, 1977: On the heat balance of the Walker circulation. *J. Atmos. Sci.*, **34**, 1155–1162.

Davidson, K. L., 1974: Observational results on the influence of stability and wind-wave coupling on momentum transfer and turbulent fluctuation over ocean waves. *Bound.-Layer Meteor.*, **6**, 305–331.

Davis, R. E., 1976: Predictabilities of sea surface temperature and sea level pressure anomalies over the North Pacific Ocean. *J. Phys. Oceangr.*, **3**, 249–266.

Deacon, E. L., 1973: Geostrophic drag coefficients. *Bound.-Layer Meteor.* **5**, 321–340.

Frankignoul, C., and K. Hasselmann, 1977: Stochastic climate models Part 2, Application to sea surface temperature anomalies and thermocline variability. *Tellus*, **29**, 289–305.

Garratt, J. R., 1977: Review of drag coefficient over oceans and continents. *Mon. Wea. Rev.*, **105**, 915–929.

Hasselmann, K., 1976: Stochastic climate models. Part 1, Theory. *Tellus*, **28**, 473–484.

Kanamitsu, M., and T. N., Krishnamurti, 1978: Northern summer tropical circulation during drought and normal rainfall months. *Mon. Wea. Rev.*, **106**, 331–347.

Kraus, E. B., 1959: The evaporation-precipitation cycle of the trades. *Tellus*, **2**, 147–158.

Krishnamurti, T. N., 1971: Tropical east-west circulations during the northern summer. *J. Atmos. Sci.*, **28**, 1342–1347.

Lau, K. M. W., 1977: A large-scale ocean atmosphere interactive model. Ph.D. thesis, Dept. Atmos. Sci., University of Washington, 220 pp.

——, 1978: Experiment with a simple ocean-atmosphere climate model—the role of the ocean in the global climate. *J. Atmos. Sci.*, **35**, 1144–1163.

Lemke, P., 1977: Stochastic climate models, Part 3, Application to zonally averaged energy model. *Tellus*, **29**, 385–392.

Manabe, S., D. G. Hahn and J. L. Holloway, 1974: The seasonal variation of the tropical circulation as simulated by a global model of the atmosphere. *J. Atmos. Sci.*, **31**, 43–72.

——, K. Bryan and M. J. Spelman, 1975: A global ocean-atmospheric climate model. Part 1, The atmospheric circulation. *J. Phys. Oceanogr.*, **5**, 3–29.

McWilliams, J. C., and P. R. Gent, 1978: A coupled air and sea model for the tropical Pacific. *J. Atmos. Sci.*, **35**, 962–989.

Newell, R. E., J. W. Kidson, D. G. Vincent and G. J. Boer, 1972: *The General Circulation of the Tropical Atmosphere*

100

and the Interaction with Extratropical Latitudes, Vol. 1. The MIT Press, 259 pp.

Ooyama, K., 1969: Numerical simulation of the life cycle of tropical cyclones. *J. Atmos. Sci.*, **26**, 3–40.

——, 1964: A dynamical model for the study of tropical cyclone development. *Geofisica Int.*, **4**, 187–198.

Pike, A. C., 1971: Intertropical convergence zone studied with an interacting atmosphere and ocean model. *Mon. Wea. Rev.*, **99**, 469–477.

Ramage, C. S., 1977: Sea surface temperature and local weather. *Mon. Wea. Rev.*, **105**, 540–544.

Rao, M. V., W. V. Abbot III and J. S. Theon, 1976: *Satellite-Derived Global Oceanic Rainfall Atlas (1973 and 1974)*. NASA Goddard Space Flight Center, Washington, DC, p. 31.

Reiter, E. R., 1978a: The interannual variability of the ocean-atmosphere system. *J. Atmos. Sci.*, **35**, 349–370.

——, 1978b: Long-term wind variability in the tropical Pacific, its possible causes and effects. *Mon. Wea. Rev.*, **106**, 324–330.

Robock, A., 1978: Internal and externally caused climate change. *J. Atmos. Sci.*, **35**, 1111–1122.

Webster, P. J., 1973: Temporal variation of low-latitude zonal circulation. *Mon. Wea. Rev.*, **101**, 803–816.

——, and K. M. W. Lau, 1977: A simple atmosphere-ocean interaction model: Basic model and a simple experiment. *J. Atmos. Sci.*, **34**, 1063–1084.

——, L. Chou and K. M. W. Lau, 1977: Mechanisms affecting the state, evolution and transition of the planetary scale monsoon. *Pure Appl. Geophys.*, **115**, 1463–1491.

Wyrtki, K., 1975: El Niño—The dynamic response of the equatorial Pacific Ocean to atmospheric forcing. *J. Phys. Oceanogr.*, **5**, 572–584.

——, 1977: Sea level changes during the 1972 El Niño. *J. Phys. Oceanogr.*, **7**, 779–787.

Reprinted from JOURNAL OF THE ATMOSPHERIC SCIENCES, Vol. 35, No. 7, July 1978
American Meteorological Society
Printed in U. S. A.

A Numerical Study of Barotropic Instability in a Zonally Varying Easterly Jet

J. B. TUPAZ,[1] R. T. WILLIAMS AND C.-P. CHANG

Department of Meteorology, Naval Postgraduate School, Monterey, CA 93940

(Manuscript received 22 December 1977, in final form 21 March 1978)

ABSTRACT

The structure and behavior of barotropically unstable and stable waves in the vicinity of a zonally varying easterly jet are studied numerically with a linearized barotropic vorticity equation on a β plane. The easterly jet is approximated by a Bickley jet with a slow zonal variation. The numerical results are also compared with a simple mechanistic analytical model using the local phase speed and growth rate concepts. In several aspects the results are grossly similar to that expected from the parallel flow theory of barotropic instability. However, in the unstable region the resultant structure of the waves causes a spatial growth rate greater than predicted by the local growth rates computed with a parallel flow model. In the stable region, the structure leads to a strong dynamic damping. When a uniform advective velocity is added to a variable mean flow, the difference between the magnitude of the growth rate of the computed waves and that implied by the parallel flow theory is somewhat reduced. However, in this case a stronger zonal asymmetry in the spatial growth rate curve with respect to the jet maximum occurs as a result of slower adjustment of the wave structure to the local stability conditions.

1. Introduction

Most theoretical studies of barotropic instability deal with basic flows that are parallel. However, often the time-average of a wind field pertaining to a particular problem shows appreciable downstream variations as a result of the forced quasi-stationary waves in the atmosphere. In such a case the stability properties and the wave behavior derived from the parallel flow theories may be subject to modification.

An example of the downstream varying, time-mean flow is the moderately strong easterly jet which develops south of the Tibetan high near 200 mb during the Northern Hemisphere summer. Westward propagating synoptic-scale disturbances have been observed in the vicinity of this jet (Krishnamurti, 1971a,b). Since the jet contains regions of large vorticity gradient where the necessary condition for barotropic instability is sometimes locally satisfied, it seems likely that the observed disturbances arise from barotropic instability of the basic flow. If this is the case, the disturbances would extract energy from the mean zonal flow and the planetary-scale waves, since the latter combine with the zonal flow to give the large vorticity gradients south of the Tibetan high. Observational evidence of such nonlinear barotropic energy conversion was provided by Kanamitsu *et al.* (1972), who showed that wavenumbers 6–8 in the wind spectrum between 15°S and 15°N receive energy from both the zonal and wavenumber 1 flow. This process was also simulated by Colton (1973) in a semi-spectral nonlinear model.

The purpose of this study is to use a numerical model to examine the effects of the downstream variation of a jet on its stability properties and the associated waves, within the context of a linear theory. We hope that such an approach can result in a better understanding of these effects. The investigation is carried out by first developing a numerical model which uses a barotropic vorticity equation in an open channel. The time-mean zonal wind is specified to be a slowly varying easterly Bickley jet and the mean meridional wind is derived in such a way that the mean flow is nondivergent. A periodic forcing is applied on the inflow (eastern) boundary to generate waves which are allowed to propagate out of the channel through the western boundary. As the waves move through the region, they grow or decay in relation to the local stability properties of the mean flow, whereas at each point the fields vary periodically. This behavior is consistent with that of the waves in a parallel mean flow. In the latter case the unstable solutions can be treated as either periodic in x (zonal direction) with an exponential envelope in t (time) or periodic in t with an exponential envelope in x. The numerical solutions obtained through long-term integration of this model are then compared with the parallel flow theory by constructing a simple mechanistic analytical model which incorporates the local stability concept of the parallel flow theory.

[1] Present affiliation: Naval Environmental Prediction Research Facility, Monterey, CA 93940.

2. Basic model

The nondivergent barotropic vorticity equation may be written

$$\frac{\partial}{\partial t}\nabla^2\psi-\frac{\partial\psi}{\partial y}\frac{\partial\nabla^2\psi}{\partial x}+\frac{\partial\psi}{\partial x}\frac{\partial\nabla^2\psi}{\partial y}+\beta\frac{\partial\psi}{\partial x}=Q-\lambda\nabla^2\psi, \quad (2.1)$$

where ψ is the streamfunction, Q represents nonbarotropic and diabatic effects, λ is a frictional coefficient and β the constant north–south gradient of Coriolis parameter computed at 10° latitude. The velocity components are

$$u=-\partial\psi/\partial y, \quad v=\partial\psi/\partial x. \quad (2.2)$$

The linearization separates the streamfunction

$$\psi(x,y,t)=\bar{\psi}(x,y)+\psi'(x,y,t), \quad (2.3)$$

where $|\psi'|\ll|\bar{\psi}|$. Substituting (2.3) into (2.1) and dropping the quadratic terms in ψ' lead to

$$\frac{\partial}{\partial t}\nabla^2\psi'-\frac{\partial\bar{\psi}}{\partial y}\frac{\partial}{\partial x}\nabla^2\psi'+\frac{\partial\bar{\psi}}{\partial x}\frac{\partial}{\partial y}\nabla^2\psi'-\frac{\partial\psi'}{\partial y}\frac{\partial}{\partial x}\nabla^2\bar{\psi}+\frac{\partial\psi'}{\partial x}\frac{\partial}{\partial y}\nabla^2\bar{\psi}+\beta\frac{\partial\psi'}{\partial x}=-\lambda\nabla^2\psi'. \quad (2.4)$$

Here it is assumed that $Q'=0$ and $\bar{Q}$ is defined in such a way that $\bar{\psi}$ is a steady-state solution of (2.1).

Eq. (2.4) is solved in a channel defined by

$$\left.\begin{aligned}-D\leqslant y\leqslant D\\ x_W\leqslant x\leqslant x_E\end{aligned}\right\}.$$

The boundary condition at the walls $y=\pm D$ is

$$\psi'=0. \quad (2.5)$$

At the inflow or eastern boundary ($x=x_E$) the conditions are

$$\psi'=A(y)\sin\omega t+B(y)\cos\omega t, \quad (2.6)$$

$$\nabla^2\psi'=-k^2\psi'+\frac{\partial^2\psi'}{\partial y^2}, \quad (2.7)$$

where ω is the frequency of the forcing. The coefficients $A(y)$ and $B(y)$ and the zonal wavenumber k will be specified later. In order for the waves to propagate smoothly out of the region, a radiation condition for both the tendency and the vorticity is used at the outflow or western boundary ($x=x_W$):

$$\frac{\partial}{\partial t}\left(\frac{\partial\psi'}{\partial t}\right)=-C_0\frac{\partial}{\partial x}\left(\frac{\partial\psi'}{\partial t}\right), \quad (2.8)$$

$$\frac{\partial}{\partial t}\nabla^2\psi'=-C_0\frac{\partial}{\partial x}\nabla^2\psi'. \quad (2.9)$$

Here C_0 is a specified constant phase velocity. The fundamental problem with most outflow boundary conditions is the reflection of incident waves from a boundary back into the interior region. This is usually disastrous for numerical models admitting dispersive waves. Pearson (1974) has shown that if C_0 is chosen judiciously, the long waves will move smoothly through the boundary. For short wavelengths, however, an area with a large coefficient of viscosity near the boundary is often required to help control the reflection problem. According to Pearson, the amount of damping is proportional to the wavenumber. Since the Euler-backward time-differencing scheme is used in our numerical model which tends to damp the short waves, a friction coefficient of $\lambda=0.15\times10^{-5}$ s^{-1} (e-folding decay time of $\sim$7.7 days) used throughout the model is sufficient for this purpose.

The basic velocity field is an easterly Bickley jet defined by

$$\bar{u}(x,y)=-\partial\bar{\psi}/\partial y=-U(x)\,\mathrm{sech}^2[y/d(x)]+U_0. \quad (2.10)$$

Here $d(x)$ is a characteristic length scale of the jet, $U(x)$ the maximum velocity due to the first term (occurs at $y=0$) and U_0 a constant velocity. The basic flow streamfunction $\bar{\psi}$ is specified to be constant at the lateral boundaries $y=\pm D$. Eq. (2.10) can be integrated to give

$$\bar{\psi}(x,y)=U(x)d(x)\{\tanh[y/d(x)]+\tanh[D/d(x)]\}-U_0(y+D)+\bar{\psi}(-D), \quad (2.11)$$

where

$$U(x)=\{[\bar{\psi}(D)+2U_0D-\bar{\psi}(-D)]/2d(x)\}\times\coth[D/d(x)]. \quad (2.12)$$

Therefore, if $d(x)$ varies slowly in x, so does the basic flow. The x variation for the characteristic length scale is given by

$$d=\left\{\begin{aligned}&850\text{ km}+350\text{ km}\{\cos[2\pi(x-\tilde{x}_0)/\tilde{L}]\}, && x\geqslant\tilde{x}_0\\ &1200\text{ km}, && x\leqslant\tilde{x}_0\end{aligned}\right\}. \quad (2.13)$$

Here $\tilde{x}_0$ is the longitude where the x variation of the cosine function starts and $\tilde{L}$ is the wavelength of this variation. Figs. 1 and 2 show the basic fields of the streamfunction $\bar{\psi}(x,y)$ and the zonal velocity $\bar{u}(x,y)$, respectively, for Experiment 1. The following parametric values are used in this experiment:

$U_0=0$ $\quad D=2000$ km

$\tilde{L}=43\,000$ km $\quad \tilde{x}_0=-21\,375$ km.

These figures show that the jet maximum is at $x=0$, $y=0$, where $\bar{u}=-30$ m s^{-1}. From this longitude the central speed slowly decreases downstream to a minimum value of -13.4 m s^{-1} at $x=-21\,375$ km. Between this longitude and the outflow boundary

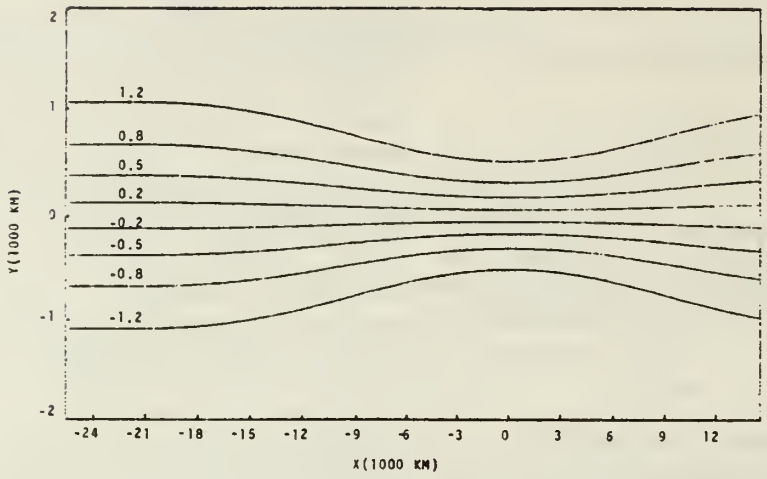

FIG. 1. Experiment 1: the $\bar{\psi}(x,y)$ field (units 10^7 m^3 s^{-1}).

($x_W = -25\,500$ km), the basic flow is parallel. Eq. (2.13) specifies that $d(x)$ varies between 500 km at $\bar{u}(x,0)_{max}$ and 1200 km at $\bar{u}(x,0)_{min}$.

3. Local stability of basic flow

The local growth rate of the variable mean flow of the numerical model is first determined by a parallel flow model in order to gain some insight on the stability characteristics of the mean flow. This model is hereafter referenced as the parallel flow model. By setting $\partial\bar{\psi}/\partial x = 0$ in (2.4) the governing equation of this model is

$$\left(\frac{\partial}{\partial t}+\bar{u}\frac{\partial}{\partial x}+\lambda\right)\nabla^2\psi'+\left(\beta-\frac{\partial^2\bar{u}}{\partial y^2}\right)\frac{\partial\psi'}{\partial x}=0, \qquad (3.1)$$

$$\bar{u}(y) = -U\,\mathrm{sech}^2(y/d)+U_0. \qquad (3.2)$$

Eq. (3.1) is solved with the initial value technique used by Williams *et al.* (1971). The equation is Fourier transformed in x and the resulting equations are integrated until the solution is growing with a constant exponential growth rate. This approach gives the growth rate, phase speed and wave structure of the most unstable meridional mode as a function of the zonal wavenumber k.

In general, (3.1) has a set of discrete normal mode solutions as well as a continuous spectrum of solutions (Case, 1960; Pedlosky, 1964; Yanai and Nitta, 1968). Only the normal mode solutions can give significant growth and the most unstable mode will dominate after a sufficient period of time.

Eq. (3.1) is solved with the same y grid as will be used in the complete numerical model. Fig. 3 shows the growth rate n corresponding to the most unstable wavelengths $L = 2\pi/k$ as a function of x from the parallel flow model. The growth rates compare closely with those computed by Kuo (1973) in his study of

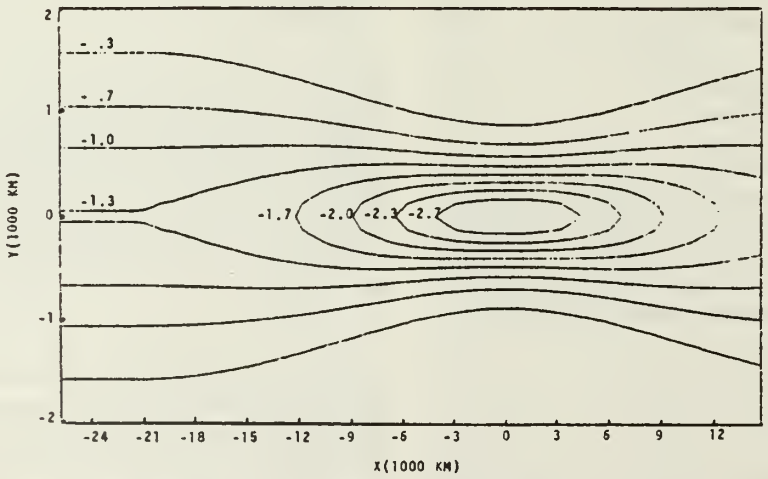

FIG. 2. Experiment 1: the $\bar{u}(x,y)$ field (units, 10 m s^{-1}).

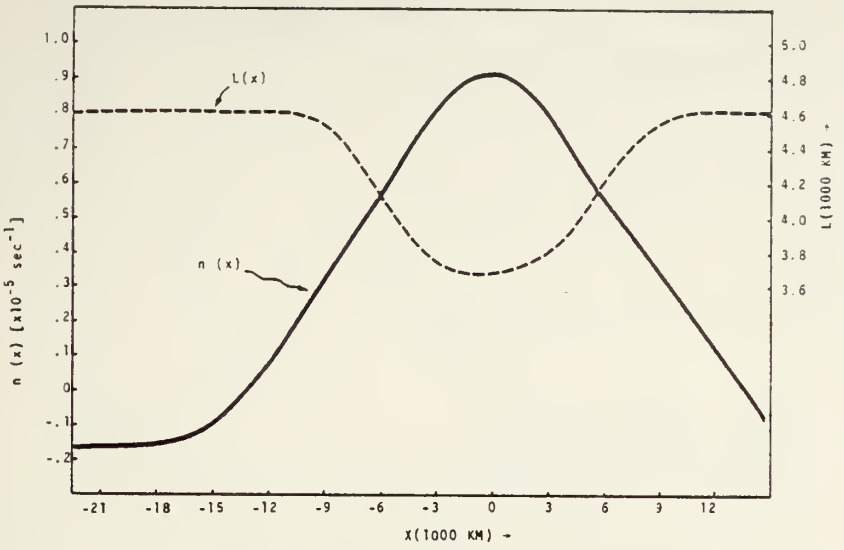

FIG. 3. The most unstable wavelength $L(x)$ and the corresponding local growth rate $n(x)$ determined from the parallel flow model.

the easterly Bickley jet. The largest growth rate occurs at $x=0$ where the jet is a maximum and its y scale is a minimum. In the outflow region for $x<-13\,500$ km the growth rate becomes negative and approaches the damping rate given by the frictional coefficient. The most unstable wavelengths range from 3650 km at $x=0$ where the jet is a maximum to 4600 km in the inflow and outflow regions. This variation follows the variation in the y scale of jet $d(x)$ which is given by (2.13).

Fig. 4 illustrates the eigensolutions of the most unstable discrete mode for two jet profiles. Since the solutions are symmetric about $y=0$, only the lower half of the y domain is shown. Both solutions show a phase tilt opposite to the shear in $\bar{u}$, which is required for barotropic growth. The maximum tilt occurs at $x=0$ where the growth rate is the largest. In Fig. 4 we see that the eigensolution amplitude is maximum at $y=0$ for $x=0$, while at $x=\pm 11\,250$ km the maximum has shifted to $y=\pm 800$ km.

4. Numerical procedure

The linearized vorticity equation (2.4) for the fully varying jet may be written

$$\nabla^2\frac{\partial\psi'}{\partial t}=-J(\bar{\psi},\nabla^2\psi')-J(\psi',\nabla^2\bar{\psi})-\beta\frac{\partial\psi'}{\partial x}-\lambda\nabla^2\psi', \quad (4.1)$$

where the Jacobian is given by

$$J(a,b)=\partial a/\partial x\,\partial b/\partial y-\partial a/\partial y\,\partial b/\partial x.$$

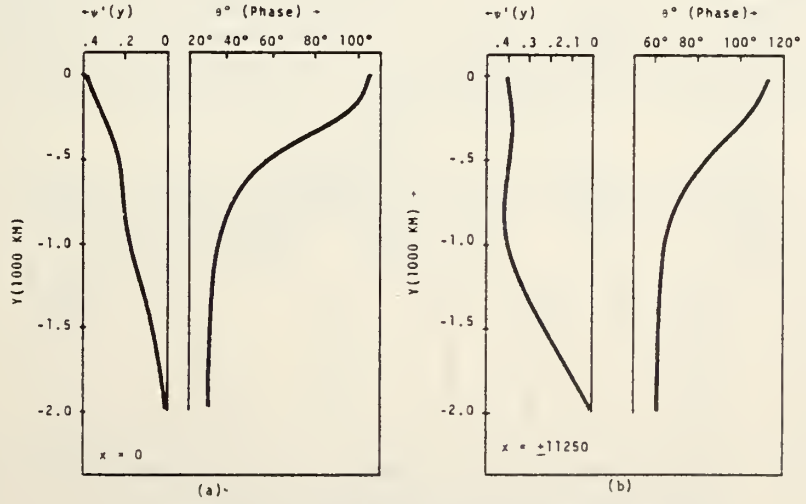

FIG. 4. Parallel flow model: wave structure of the most unstable mode for $x=0$ and $x=\pm 11\,250$ km.

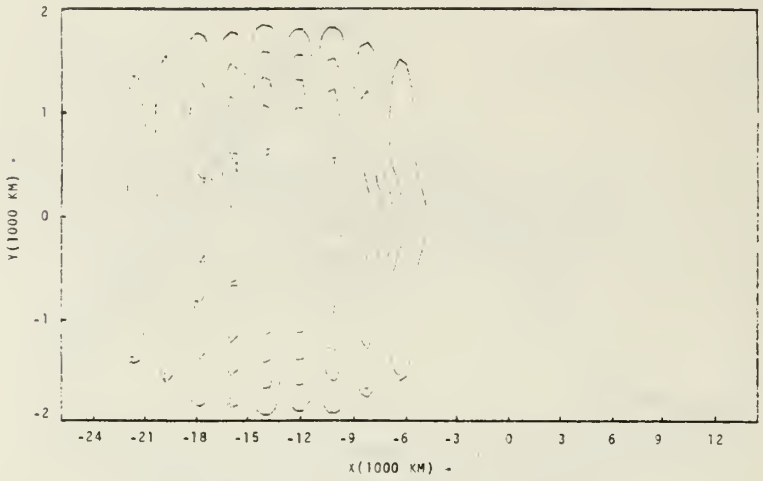

FIG. 5. Experiment 1: the ψ' field at $t=70$ days.

This equation is time-differenced with the Euler-backward procedure except that the frictional term is evaluated at the previous time step. The Jacobian terms are evaluated using the finite difference form developed by Arakawa (1966), which conserves mean enstrophy and mean kinetic energy in nonlinear calculations when the time variation is smooth. At the north–south boundaries the value of $\nabla^2\psi$ is extrapolated from the first interior points. The left-hand side of (4.1) is solved for $\partial\psi'/\partial t$ with the direct method developed by Sweet (1971).

In order to apply the inflow boundary conditions (2.6) and (2.7) we must specify the functions $A(y)$ and $B(y)$. These functions are obtained from the parallel flow model applied at the inflow point. The most unstable wavelength is used to compute k in Eq. (2.7).

The outflow conditions (2.8) and (2.9) can be applied if the phase velocity C_0 is known. It will be seen later that after a period of adjustment the entire field varies periodically with the frequency ω of the inflow fields. The phase velocity can therefore be written

$$c=-L\omega/2\pi. \tag{4.2}$$

After the numerical solution has been obtained for a trial value of C_0 then a new value may be computed from (4.2) by measuring L near the outflow boundary. It turns out that the interior solutions are not very sensitive to the value of C_0.

The forecast equation is integrated in time from an initial state of $\psi'=0$. The periodic forcing on the eastern boundary causes the interior streamfunction to grow and the integration is continued until the time variation is periodic everywhere with the forcing frequency. The integration is repeated with a different frequency until the frequency which gives the maximum ψ' amplitude is found. A possible concern of this procedure is whether modes with the "most unstable frequency" will grow in the interior and impede the search for a full periodic solution with the forcing frequency. It turns out that with careful execution this procedure proves to be successful for all the experiments performed because the finite

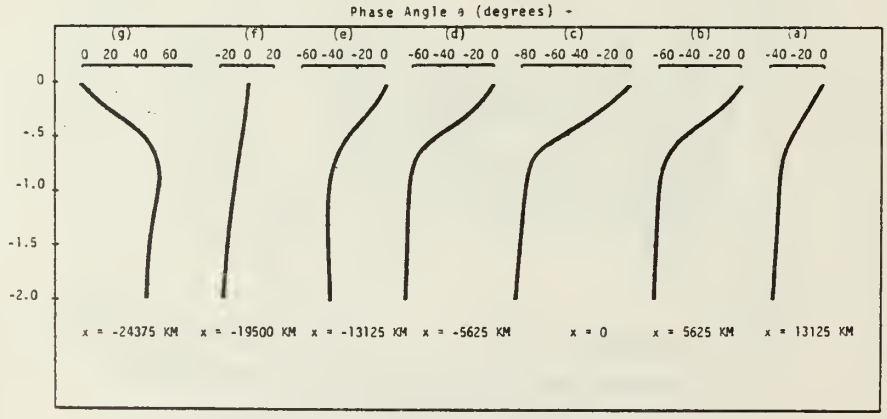

FIG. 6. Experiment 1: the phase tilt $\theta^*(x,y)$ for longitude indicated.

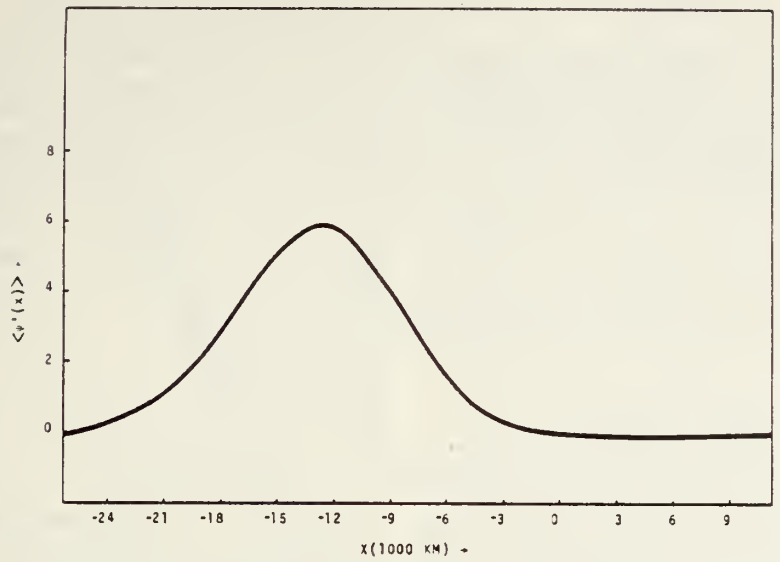

FIG. 7. Experiment 1: wave packet envelope $\langle \psi'(x) \rangle$ from the complete numerical model.

travelling distance from the inflow to outflow boundaries does not allow any noise due to truncation errors to grow to a detectable amplitude.

5. Results from Experiment 1: $U_0 = 0$

The investigation of the numerical model of the variable mean wind comprises two experiments. Experiment 1 is the principal one and will be discussed in detail in this section. In Experiment 2 a constant velocity is added to the mean flow and its results will be discussed in Section 7.

The following values are used in Experiment 1:

$$\left.\begin{aligned} &2D = 4000 \text{ km},\ x_E - x_W = 40\,125 \text{ km}, \\ &\qquad\qquad \bar{u}(0,0) = -30 \text{ m s}^{-1} \\ &U_0 = 0,\ \tilde{L} = 43\,000 \text{ km},\ \Delta x = 375 \text{ km}, \\ &\qquad\qquad \Delta y = 125 \text{ km},\ \Delta t = 1 \text{ h} \\ &C_0 = -13 \text{ m s}^{-1},\ \tilde{x} = 21\,375 \text{ km} \end{aligned}\right\}.$$

For these parameters the maximum response occurs for a forcing period of 3.25 days. The solution becomes fully periodic after 70 days. The ψ' field at $t = 70$ days is shown in Fig. 5. The maximum wave amplitude occurs at $x = -12\,750$ km and is two and four orders

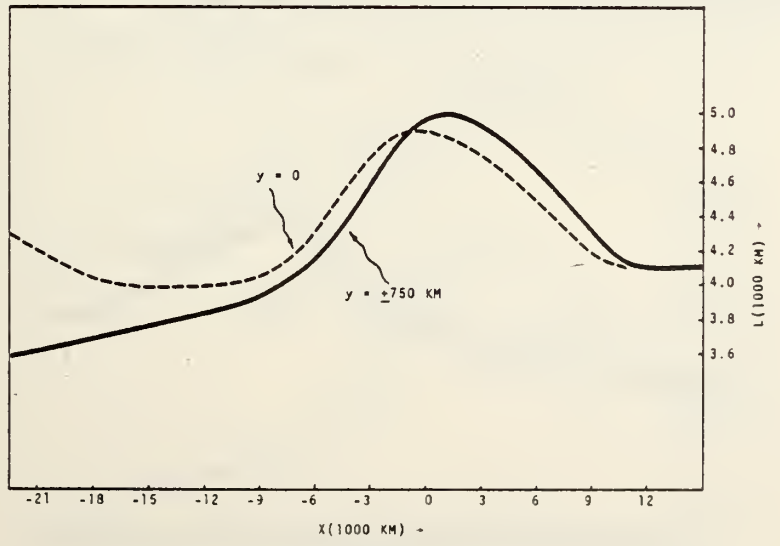

FIG. 8. Experiment 1: wavelengths $L(x)$ from the complete numerical model for $y = 0$ and $y = -750$ km.

of magnitude larger than at the jet maximum ($x=0$) and the inflow boundary ($x=14\,625$ km), respectively. The solutions show a tilt opposite to the mean wind (Fig. 2) except in the outflow region where the tilt is in the same sense as the wind shear.

In order to examine the phase tilt further, Fig. 6 shows the phase $\theta^*(x,y)$ obtained at various longitudes by observing the periodic time variation at each point for fixed x. Upstream of approximately $x=-20\,000$ km, the tilt is opposite to the mean wind shear, which is necessary for barotropic instability. The tilt near the inflow boundary is relatively weak and slowly increases westward, reaching a maximum at $x=0$ where the jet velocity is maximum. Further downstream, the tilt slowly decreases and eventually reverses near $x=-20\,000$ km. This behavior is consistent with the growth rates for the most unstable wavelengths shown in Fig. 3 computed from the parallel flow model. Near the outflow boundary, the tilt is reversed and indicates that the disturbances feed energy back to the mean flow. This is a continuous spectrum effect which is not described by the discrete modes determined in Section 3.

Fig. 7 shows the envelope of the wave packet evaluated at $y=-750$ km where the disturbance amplitude is large. This envelope $\langle\psi'(x)\rangle$ is obtained by recording the maximum and minimum ψ' values that occur at each longitude over one period after the solution becomes fully periodic. Note that the maximum amplitude occurs in the area where the local growth rate becomes zero (see Fig. 3). The smoothness of the fields in Figs. 5 and 7 indicates that the outflow boundary condition is working properly. We note in Fig. 5 that there are three maxima of ψ' in the north–south wave structure. One maximum is at $y=0$ and another on each side of the jet near $y=\pm750$ km. This distribution is consistent with the parallel flow eigensolutions shown in Fig. 4. The maximum on the wings clearly predominates. Fig. 8 shows the variation of wavelength $L(x)$ for $y=0$ and $y=\pm750$ km corresponding to the latitudes of the three observed maxima of ψ'. The disturbance wavelength is ~4100 km near the inflow boundary. The wavelength near $y=\pm750$ km is larger upstream and smaller downstream of $x=0$ than at $y=0$. At $y=\pm750$ km, the maximum wavelength of 5060 km occurs ~950 km upstream of $x=0$ and the minimum wavelength of 3600 km occurs near the outflow boundary. At $y=0$, the maximum wavelength of 4900 km occurs about 950 km downstream of $x=0$, while the minimum wavelength of 4000 km occurs near $x=-13\,500$ km with the wavelength increasing slowly further downstream to the outflow boundary. The range of the wavelength is nearly the same as that obtained for the most unstable wavelengths using the parallel flow model in Section 3, but the pattern is reversed with the longest waves near $x=0$ and the shortest in the inflow and outflow regions. Fig. 9 shows the disturbance phase speeds $c^*(x)$ for latitudes $y=0$ and $y=\pm750$ km, where

$$c^*(x)=-L(x)\omega/2\pi. \tag{5.1}$$

Since the entire domain is periodic with the forcing frequency, $c^*(x)$ has the same basic behavior as $L(x)$ [Fig. 8] for the corresponding latitudes. Namely, upstream of $x=0$ the disturbance phase velocity is faster on the wings of the jet than at $y=0$, and downstream of $x=0$ it is slower. This illustrates the tilt behavior of the waves as they move into and out of the unstable region.

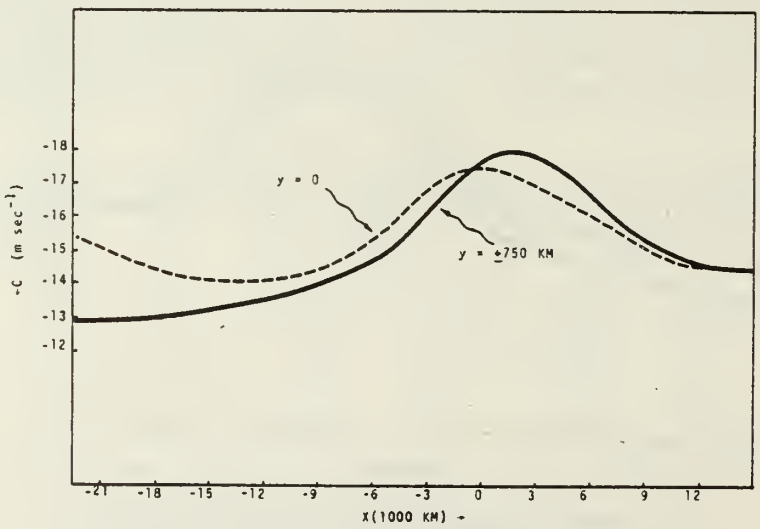

FIG. 9. Experiment 1: phase velocities $c^*(x)$ from the complete numerical model for $y=0$ and $y=-750$ km.

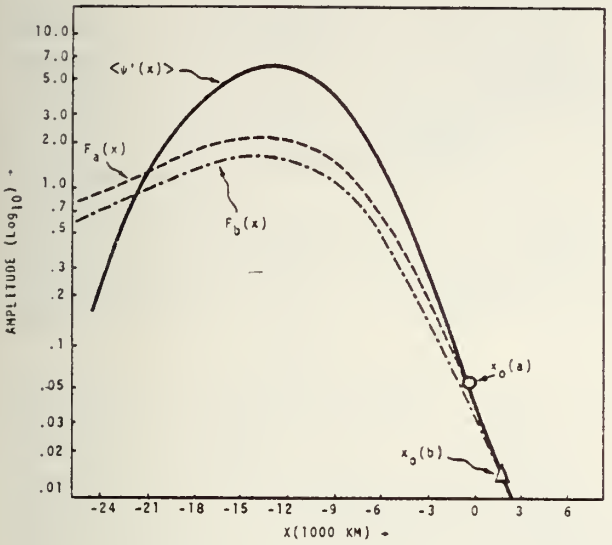

FIG. 10. Experiment 1: the wave packet envelopes. $F_a(x)$ is from the analytical model for initial point $x_0(a) = -375$ km, $F_b(x)$ is from the analytical model for initial point $x_0(b) = 1875$ km, and $\langle\psi'(x)\rangle$ is from the complete numerical model.

6. Simple mechanistic analytic model

In this section we develop a simple mechanistic analytical model which uses the locally determined parallel flow solutions. The results of this simple model can be compared with those of the complete numerical model to obtain some measure of the adjustment of the transient barotropic waves to the local stability of the variable mean wind.

The following equation allows for propagation and growth or decay:

$$\frac{\partial\psi'}{\partial t}+c(x)\frac{\partial\psi'}{\partial x}=n(x)\psi', \tag{6.1}$$

where ψ' is the disturbance streamfunction, $c(x)$ the local phase velocity and $n(x)$ the local growth rate. If c and n are independent of x, then (6.1) is exact, and should in general give a reasonable approximation to the downstream variation of ψ'.

We consider the case where ψ' has a solution of the form

$$\psi'=F(x)e^{i\omega t}, \tag{6.2}$$

where ω is a specified frequency and F the amplitude. After substituting (6.2) into (6.1), we obtain

$$i\omega F+c(x)\frac{dF}{dx}=n(x)F. \tag{6.3}$$

This equation can be integrated to give

$$F(x)=F_0\exp\left[-i\int_{x_0}^{x}\frac{\omega}{c(x)}dx\right]\exp\left[\int_{x_0}^{x}\frac{n(x)}{c(x)}dx\right]. \tag{6.4}$$

Here the amplitude of ψ' must be specified at some initial point x_0. The local wavenumber is $-\omega/c$ and the spatial growth rate is n/c. These are the real and imaginary parts of the wavenumber, if we were to write $\psi'=A\exp(ikx-i\omega t)$.

Since we are interested in the growth and decay of the wave packet, only the magnitude of (6.4),

$$|F(x)|=F_0\exp\left[\int_{x_0}^{x}\frac{n(x)}{c(x)}dx\right], \tag{6.5}$$

will be considered. Eq. (6.5) gives the exponential growth/decay behavior of a wave disturbance as it travels within its wave packet envelope. This behavior is determined by the integral effects of the local stability properties of the mean flow.

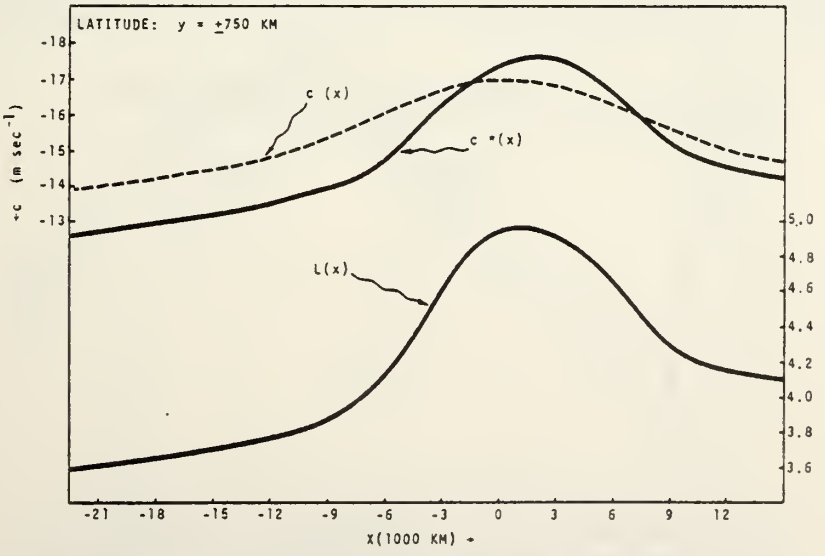

FIG. 11. Experiment 1: phase velocities $c(x)$ from parallel flow model and $c^*(x)$ from complete numerical model, and wavelength $L(x)$, for $y=\pm750$ km.

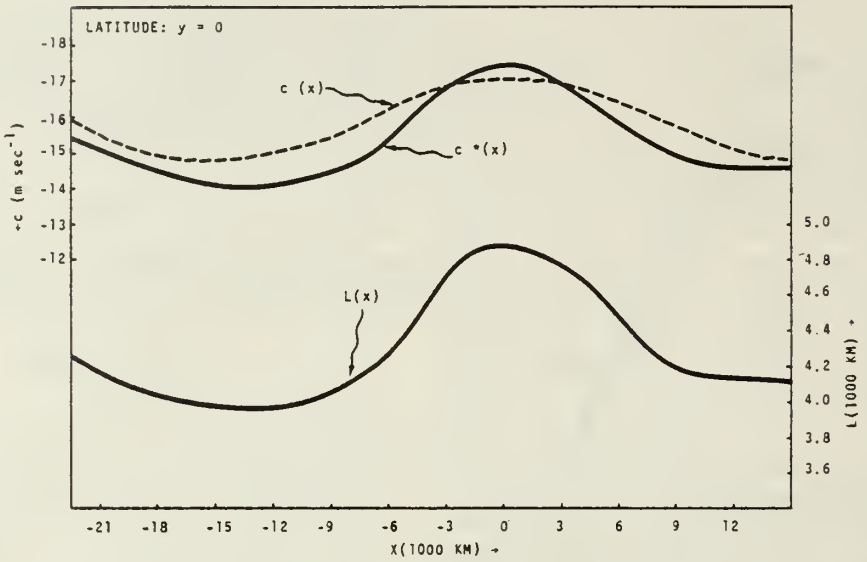

FIG. 12. As in Fig. 11 except for $y=0$.

Fig. 10 compares the envelope for $\psi'(x)$ from the complete numerical solution (Fig. 7) with the $|F(x)|$ given by (6.5) for two values of x_0. The ordinate is the logarithm of the amplitude. The analytical model uses the locally determined parallel flow growth rates (n) and phase speeds (c) based on the wavelengths measured from the complete numerical solutions. Eq. (6.5) is applied at $y=\pm 750$ km where the wavelengths are measured. The curve for $|F(x)|$ can be shifted up or down by changing x_0, but its shape does not change. In Fig. 10 all the curves have a maximum amplitude at $x=-12\,750$ km where the local growth rate is zero; however, the parallel flow model has a lower maximum growth rate and slower damping rates than the complete numerical model.

The lower portion of Fig. 11 shows the wavelength measured from the numerical solution at $y=-750$ km. In the upper portion of the diagram are the phase velocities, c from the parallel flow model and c^* from the complete numerical model for the same latitude. Here c is computed with the use of the wavelength shown. The two phase speeds have similar behavior although c^* is shifted slightly upstream and has larger variations. We also note that $c^*<c$ except for the region -1500 km$\lesssim x\lesssim 6750$ km.

Fig. 12 shows the wavelengths and phase speeds

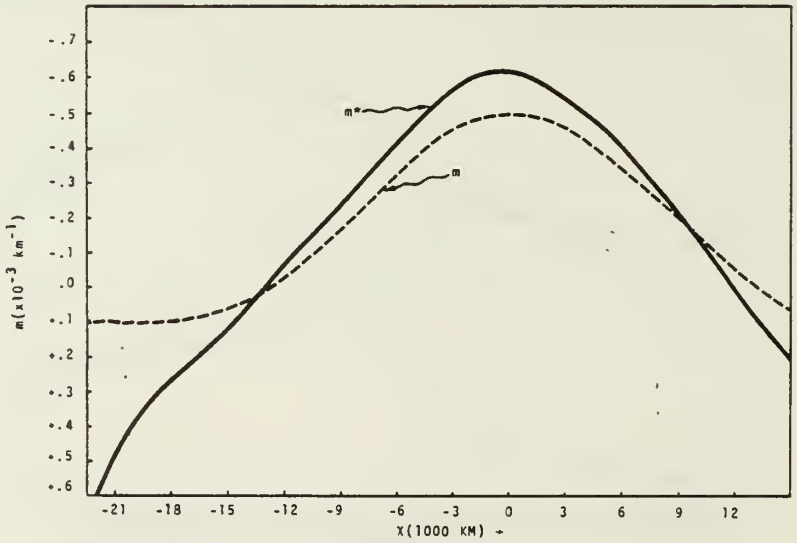

FIG. 13. Experiment 1: spatial growth rates $m(x)$ from the parallel flow model and $m^*(x)$ from the complete numerical model. When $m<0$ there is downstream growth.

for $y=0$. Again, the two phase speeds have similar behavior but at this latitude c^* is shifted slightly downstream and the difference between phase speeds is generally less than at $y=-750$ km. Here $c^*<c$ except for the region -2250 km$\lesssim x\lesssim 2250$ km. Figs. 11 and 12 indicate that both the wavelength $L(x)$ and the phase velocity $c^*(x)$ are maximum where the mean flow is strongest.

Fig. 13 contains the spatial growth rates m and m^* from the parallel flow model and from the complete numerical model, respectively. For the parallel flow model, we obtain

$$m=n/c. \tag{6.6}$$

The value of m^* is computed directly from the envelope. We note in Fig. 13 that m^* has a larger maximum than m and the maximum is shifted slightly downstream from the jet maximum. Both curves pass through 0 at $x=-12\,750$ km which is the maximum for both wave packet envelopes. However, the parallel flow solution damps at the rate given by the frictional coefficient divided by the phase speed, while m^* shows a much larger damping rate ($\sim 1\ t$ or faster). Thus a dynamic damping is indicated in the complete numerical solution. This is consistent with the wave structure in the outflow region of the complete numerical model (Fig. 3), which has a tilt in the same sense as the mean wind shear. This behavior is also indicated by the divergence of phase speed in the outflow region between $y=0$ and $y=-750$ km (see Figs. 11 and 12). Since dynamic damping is due to continuous spectrum solutions (Case, 1960), it cannot be represented by the normal mode solutions of the parallel flow theory.

In Fig. 13 the m^* curve is skewed slightly to the left with respect to m and the jet maximum. This seems to indicate that the wave structure lags spatially behind the expected value from the local stability conditions. This would give a smaller growth rate on the upwind side of the jet maximum and a larger growth rate on the downwind side, which is indicated by the asymmetry of the m^* curve with respect to the m curve in the unstable region of the mean wind. However, this is not the only effect involved because the most striking feature of Fig. 13 is the fact that the maximum value of m^* is significantly larger than the maximum value of m. We have calculated the energetics of the two models and found that the most important disturbance energy production term in the complete numerical model is proportional to

$$\int_0^{2\pi/\omega}\int_{-D}^{D} u'v'\frac{\partial \bar{u}}{\partial y}\,dy\,dt.$$

This term is the only source term for the parallel flow model, and it depends on the tilt in the disturbance field. To evaluate this term, Fig. 14 compares the tilt of the numerical model solution θ^* and that of the most unstable wavelength of the parallel flow model θ_0, at $x=0$, 3750 km and 13 125 km. It is evident that at the jet maximum the tilt from the numerical model is significantly larger than that from the parallel flow model. This is also evident but to a lesser degree at $x=3750$ km. These results are consistent with the larger growth rates for the variable jet flow. The stronger tilt is also indicated by the comparison of the c^* and c curves in the region near and slightly upstream of the jet maximum for latitudes $y=0$ and $y=-750$ km (see Figs. 11 and 12). We note that at $y=-750$ km, c^* is relatively larger than c near the jet maximum. This difference is significantly reduced and shifted slightly downstream at $y=0$. Unlike in the stable region, the effect of continuous spectrum mode must be ruled out in explaining the higher maximum growth rate of the numerical solution because near the inflow region the growth rate of the numerical solution is less than

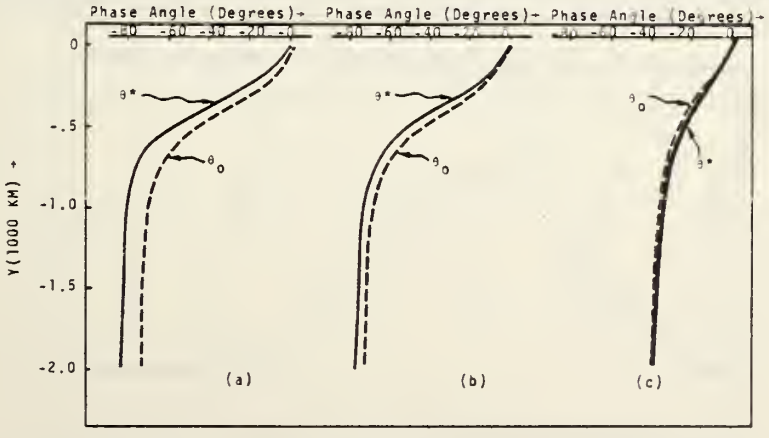

FIG. 14. Experiment 1: comparison of phase tilt of the complete numerical model θ^* and of the most unstable wavelength of the parallel flow model θ_0, for (a) $x=0$, (b) $x=3750$ km and (c) $x=13\,125$ km.

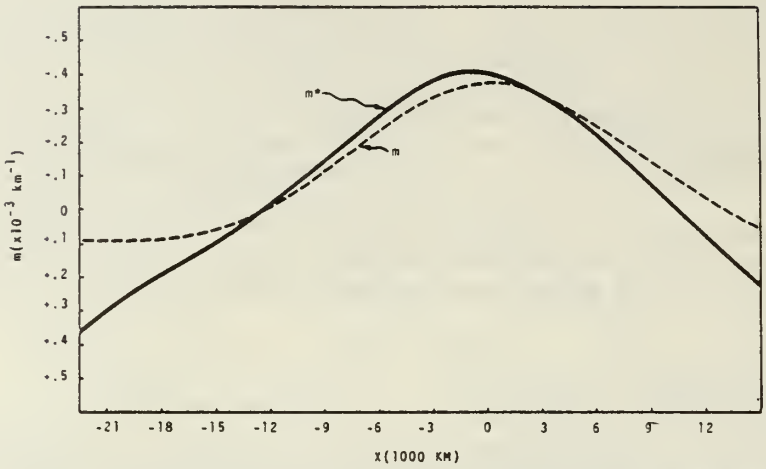

FIG. 15. Experiment 2: spatial growth rates $m(x)$ from the parallel flow model and $m^*(x)$ from the complete numerical model. When $m<0$ there is downstream growth.

that of the parallel flow solution. We also note that at the inflow region ($x=13\,125$ km), the phase tilt of the numerical solution lags slightly behind the parallel flow solution (see Fig. 14c). Apparently the downstream variation of the mean wind augments the phase tilt which gives a larger growth rate.

In comparing the parallel flow theory and the complete numerical model, a source of error could be introduced through the zonal resolution. This is because in the former the zonal variation is specified by a spectral representation, while in the latter it is resolved by finite differences. Since the wavelength appearing in the complete numerical model varies between 10 and 13.5 Δx, such resolution normally gives a good approximation to the exact solution (Haltiner, 1971). Thus this error should not be very significant. In order to confirm this we carried out an experiment in which a parallel mean flow is specified by the complete two-dimensional finite-difference model. The growth rate and phase speed calculated from the experiment agree very well with those obtained by the semi-spectral parallel flow model, the difference being only 1–2%. Hence we may conclude that the differences between the numerical solution and the local solution of the parallel flow theory are genuine and are not due to the differences in the model resolution.

7. Results from Experiment 2

In Experiment 2 a constant advective speed of $U_0=-5$ m s^{-1} is added to the mean flow, otherwise the parameters are the same as those used in Experiment 1. We hope this modification will shed some light on the adjustment process when the waves move faster downstream. The local phase speed c is now related to the Doppler-shifted phase speed $\hat{c}$ by $\hat{c}=c^*-U_0$. The maximum ψ' response in this experiment is obtained with a forcing period of 2.5 days. Since the Doppler-shifted frequency may be written

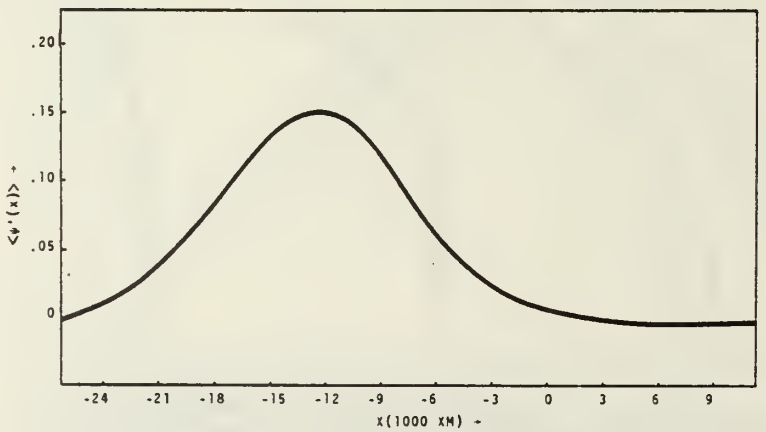

FIG. 16. Experiment 2: wave packet envelope $\langle\psi'(x)\rangle$ from the complete numerical model.

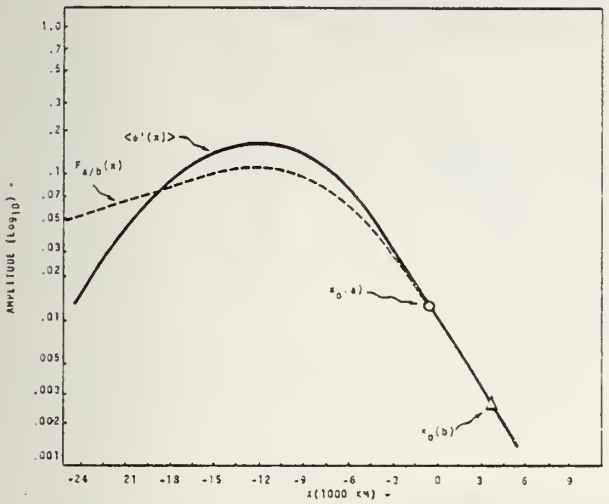

FIG. 17. Experiment 2: the wave packet envelopes. $F_a(x)$ is from the analytical model for initial point $x_0(a) = -375$ km, $F_b(x)$ is from the analytical model for initial point $x_0(b) = 3750$ km, and $\langle\psi'(x)\rangle$ is from the complete numerical model.

as $\hat{\omega} = k(c^* - U_0) = \omega - kU_0$, this shorter period actually gives approximately the same Doppler-shifted frequency as that of Experiment 1 (where the period is 3.25 days with $U_0 = 0$).

Based on the results of the simple analytical model [Eq. (6.5)], we expect that the constant advective velocity U_0 will significantly reduce the local spatial growth rate

$$m = m_I (c + U_0). \tag{7.1}$$

Fig. 15 shows the spatial growth rates from the parallel flow model (m) and from the complete numerical model (m^*). Comparing this figure with Fig. 13, the reduction in both m and m^* from those of Experiment 1 is clear. This reduction is obviously due to the advective velocity which causes the disturbances of Experiment 2 to move approximately 5 m s^{-1} faster than in Experiment 1. Thus the waves have less time to grow or damp in response to the local stability per unit distance traveled. The smaller spatial growth rate obviously affects the amplitude and spatial gradients of ψ'. Fig. 16 shows the wave packet envelope $\langle\psi'(x)\rangle$ of the complete numerical solution for Experiment 2. Fig. 17 shows this envelope along with the mechanistic model envelope $|F(x)|$ using both $x_0 = -375$ km and $x_0 = 3750$ km as the initial points (no discernible difference is noted between the use of these initial points). As expected, both envelopes are significantly smaller than those of Experiment 1. In addition, there is less variation in the wavelength (3750 km $\lesssim L \lesssim$ 4875 km) compared to Experiment 1 (see Figs. 11 and 20). This is also a result of the faster phase speed which gives the waves less time to adjust to the local mean wind.

Although the faster phase speed of the waves in Experiment 2 reduces the magnitude of growth and decay rates and therefore brings the magnitude of the spatial growth rate curve of the numerical model (m^*) closer to that of the parallel flow model (m), there is a stronger asymmetry in the m^* curve with respect to $x = 0$ in Fig. 15 compared to Experiment 1 (see Fig. 13). In addition to the occurrence of the m^* maximum slightly further downstream of $x = 0$, the cross-over points of the m^* and m curves exhibit more asymmetry in Experiment 2 than in Experiment 1. (The first cross-over point occurs at $x \approx 8500$ km and $x \approx 4000$ km for Experiments 1 and 2, respectively; while the second cross-over point for both experiments occurs at $x \approx -12\,000$ km where the spatial growth rates vanish.)

As in Experiment 1, we interpret this asymmetry as being due to the structure of the waves lagging behind the expected value from the local stability condition. The fact that this lag effect is enhanced by the faster phase speed of the waves in Experiment 2 can also be seen in Fig. 18 where the north–south phase $\theta^*(x,y)$ of the wave disturbances for both experiments are compared at several longitudes. The unstable tilt in Experiment 2 is weaker upstream and

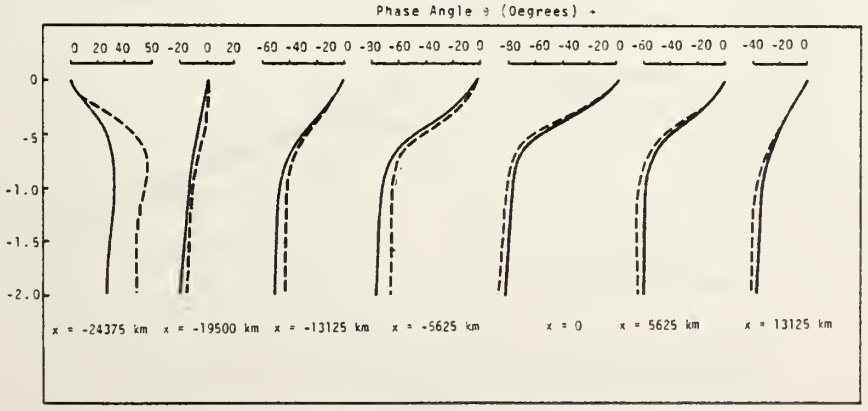

FIG. 18. Comparison of phase tilt θ^* between Experiment 1 (dashed) and Experiment 2 (solid) for longitudes indicated.

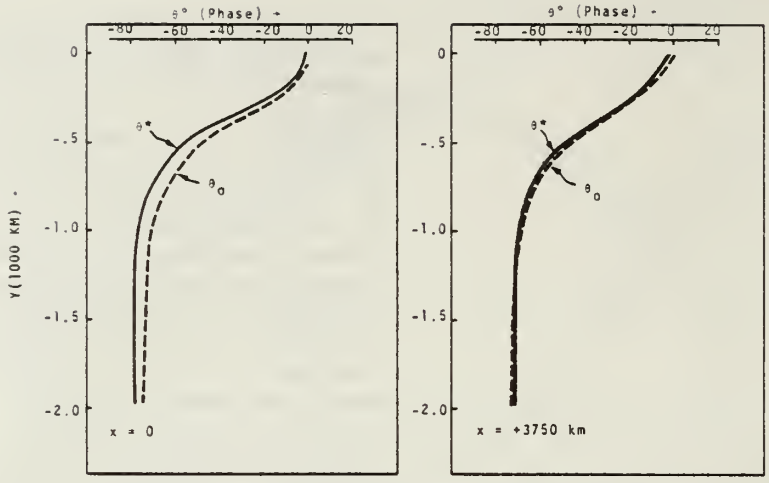

FIG. 19. Experiment 2: comparison of phase tilt of the complete numerical model θ^* and of the most unstable wavelength of the parallel flow model θ_0 for $x=0$ and $x=3750$ km.

stronger downstream of $x\approx -2000$ km, reflecting the stronger lag effect of the faster moving waves.

Fig. 19 compares the phase of the numerical model solution θ^* and that of the most unstable wavelength of the parallel flow model θ_0 for two longitudes ($x=0$ and $x=3750$ km). Comparing this figure with Fig. 14 of Experiment 1, it is obvious that the apparent augmentation of the wave tilt due to the zonal variation of the mean flow is now significantly reduced. This behavior may at least be partially explained by the lag effect caused by the advective speed U_0, which generally reduces the growth rate in the vicinity of the jet maximum.

The lower portion of Fig. 20 shows the wavelength measured from the numerical solution at $y=-750$ km. In the upper portion of the diagram are the phase velocities at $y=-750$ km, c^* from the complete numerical model and c from the parallel flow model based on the corresponding numerical solution wavelength. The two phase speeds agree very closely upstream of the jet maximum, while c^* is smaller than c downstream of this longitude. Similarily, Fig. 21 contains the wavelength and phase speeds at $y=0$. At this latitude, the two phase speeds have similar behavior throughout the length of domain with c^* being ~ 1 m s^{-1} slower than c. Fig. 22 shows the wavelength curves $[L(x)]$ for $y=0$ and $y=-750$ km. At both latitudes the maximum wavelength occurs near the jet maximum, but the wavelength (and therefore phase velocity) at $y=-750$ km is larger

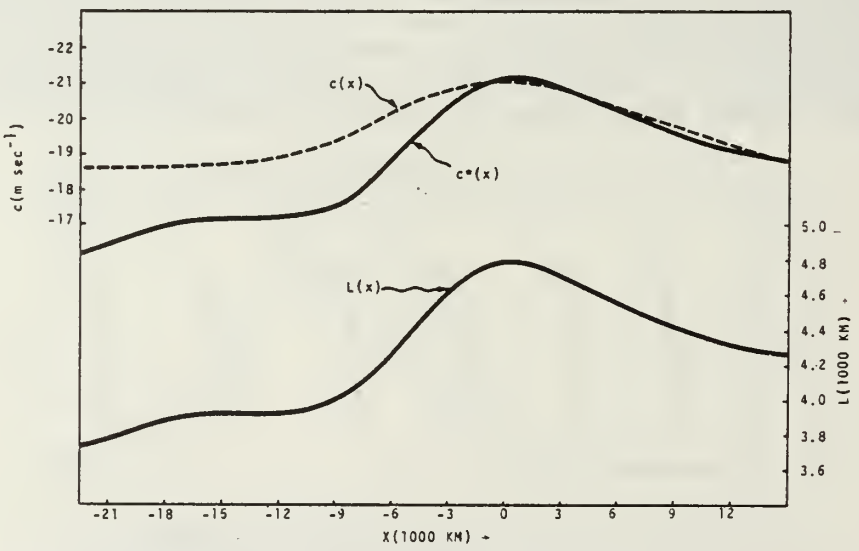

FIG. 20. Experiment 2: phase velocities $c(x)$ from parallel flow model and $c^*(x)$ from complete numerical model, and wavelength $L(x)$, for $y=\pm 750$ km.

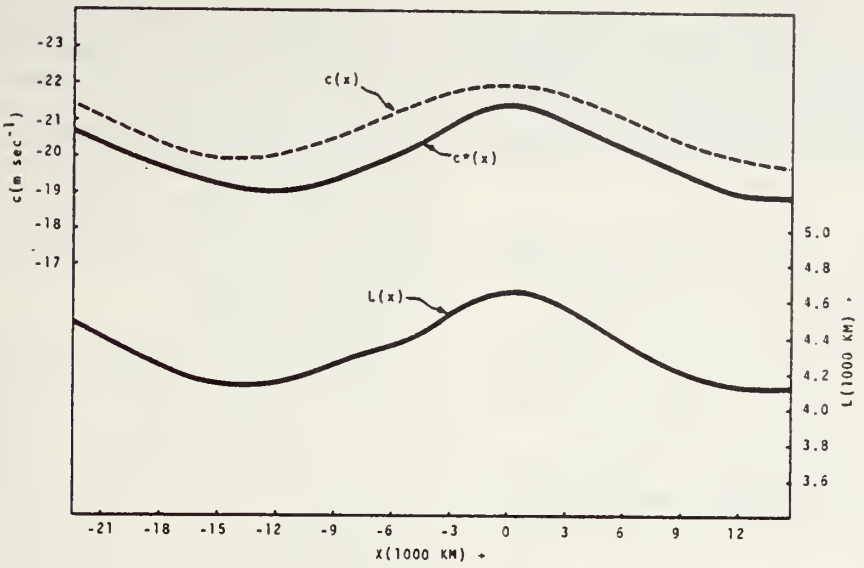

FIG. 21. As in Fig. 20 except for $y=0$.

upstream and smaller downstream of $x\approx -5000$ km. As in Experiment 1, these differences in $c^*(x)$ and $L(x)$ between the two latitudes are consistent with the observed tilt behavior of the waves.

Other than the foregoing mentioned differences, the basic behavior of the waves in Experiment 2 is similar to that of Experiment 1.

8. Summary and conclusions

In this work we studied numerically the behavior of waves moving through a barotropically unstable mean wind field which varies both in x and y. This mean wind field roughly simulates the 200 mb easterly jet south of the Tibetan high during the Northern Hemisphere summer. A rectangular domain is used to solve the vorticity equation on a beta plane with a periodic forcing on the inflow (east) boundary and a radiation condition on the outflow (west) boundary. After a certain time period of integration, the solution becomes periodic everywhere with the forcing frequency. As the waves move through the jet regime, they grow or decay spatially in response to the local stability of the mean flow, even though at each point the variation is purely harmonic. The numerical results are compared with a simple mechanistic analytical model which is developed using the local growth rate and phase velocity computed from the parallel flow theory.

Two experiments are carried out in this investigation. The parameters used are the same, except that

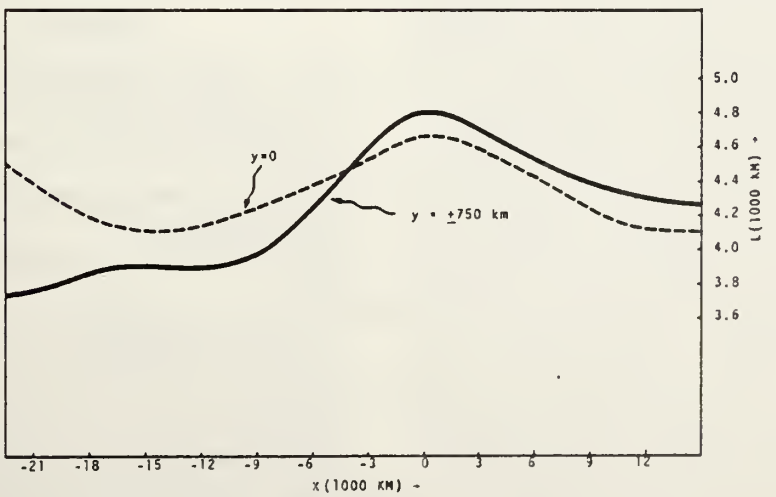

FIG. 22. Experiment 2: wavelengths $L(x)$ from the complete numerical model for $y=0$ and $y=-750$ km.

in Experiment 2 a constant advective velocity of $U_0 = -5$ m s^{-1} is added to the mean flow in order to gain a better understanding of the adjustment process of a faster moving wave chain.

The basic behavior of the waves in both experiments is similar. This includes the following:

1) The maximum amplitude of the waves occurs a considerable distance downstream from the most unstable part of the jet near the point where the local growth rate of the parallel flow theory vanishes.

2) The structure of the waves and its reversal from that of growth to that of damping occur downstream of the maximum of the wave packet envelope, in response to the local stability of the mean flow.

3) There is a zonal asymmetry in the growth rate with respect to the jet maximum resulting from the spatial lag of the wave structure as the waves propagate downstream.

4) The wavelength (and therefore phase velocity) increases slowly from the inflow boundary to a maximum value near the jet maximum, and then decreases slowly downstream reaching a minimum value near the outflow region.

5) Large spatial damping occurs in the outflow region due to the presence of the continuous spectrum modes.

A somewhat unexpected finding is that, in Experiment 1 where the mean wind vanishes toward large y, the maximum spatial growth rate in the numerical model is significantly larger than the spatial growth rate of the parallel flow model. Examination of the wave structure reveals that the unstable tilt of the waves is augmented by the downstream variation of the mean wind, thus causing an increased growth rate as compared with waves in a parallel flow. In Experiment 2 where the waves move westward faster due to the presence of a constant -5 m s^{-1} advective zonal wind, the magnitude of the spatial growth rate computed by the numerical model is closer to that given by the parallel flow theory, but the asymmetry of the numerical growth rate curve with respect to the jet maximum is enhanced. The reduction of spatial growth and decay rates is mostly due to the faster phase speed which causes the waves to have less time to grow or damp per unit distance traveled. The enhanced asymmetry is apparently due to a lag effect wherein the adjustment of the waves is delayed spatially. The latter effect is also reflected in the north–south phase structure of the waves and in the smaller variation of the wavelength as the waves propagate downstream. The augmentation of the phase tilt by the downstream variation is also significantly reduced which may at least be partially explained by the lag effect.

Recently Pedlosky (1976) used a simple analytical model to study the effect of the downstream variation of a baroclinic current. The mean flow in his model changes abruptly from a weakly unstable regime with a constant growth rate to a stable regime downstream. His model includes nonlinear effects but it does not produce strong dynamic damping due to the continuous spectrum modes. Perhaps this is because he did not include the lateral shear of the mean flow. Thus, his waves remain substantially undiminished when they propagate from a locally unstable region to a locally stable region.

Although this study employs linear equations, it is possible to estimate qualitatively the nonlinear effect of the waves on the mean flow. Since the Reynold's stress term is the dominant term in the energetics, most of the mean kinetic energy is removed by the waves on the downwind side of the jet maximum between where the wave amplitude is maximum and where the phase tilt of the waves is strongest. This implies that synoptic-scale waves may affect significantly the amplitude and phase of quasi-stationary planetary waves which combine to form the easterly jet over South Asia. These effects can be studied by including nonlinear effects in the present model. It may also be interesting to extend the present model to a three-dimensional one to study the effect of vertical shear and baroclinicity.

Acknowledgments. We wish to thank Professor F. D. Faulkner for his help in modifying the direct solver of the Poison equation. The numerical calculations were performed at the W. R. Church Computer Center of the Naval Postgraduate School. This research was supported by the Division of Atmospheric Sciences, National Science Foundation, under Grants DES 75-10719 and ATM 77-14821, and by the Naval Environmental Prediction Research Facility.

REFERENCES

Arakawa, A., 1966: Computational design for long-term numerical integrations of the equations of atmospheric motion. *J. Comput. Phys.*, **1**, 119–143.

Case, K. M., 1960: Stability of plane couette flow. *Phys. Fluids*, 3, 143–148.

Colton, D. E., 1973: Barotropic scale interactions in the tropical upper troposphere during the northern summer. *J. Atmos. Sci.*, **30**, 1287–1302.

Haltiner, G. J., 1971: *Numerical Weather Prediction.* Wiley, 317 pp.

Kanamitsu, J., T. N. Krishnamurti and C. Depradine, 1972: On scale interactions in the Tropics during northern summer. *J. Atmos. Sci.*, **29**, 698–706.

Krishnamurti, T. N., 1971a: Observational study of the upper tropospheric motion field during the Northern Hemisphere summer. *J. Appl. Meteor.*, **10**, 1066–1096.

——, 1971b: Tropical east–west circulations during the northern summer. *J. Atmos. Sci.*, **28**, 1342–1347.

Kuo, H. L., 1973: Dynamics of quasi-geostrophic flows and instability theory. *Advances in Applied Mechanics*, Vol. 13, Pergamon, 247–330.

Pearson, R. A., 1974: Consistent boundary conditions for numerical models of systems that admit dispersive waves. *J. Atmos. Sci.*, **31**, 1481–1489.

Pedlosky, J., 1964: An initial value problem in the theory of baroclinic instability. *Tellus*, **16**, 12–17.

——, 1976: Finite-amplitude baroclinic disturbances in downstream varying currents. *J. Phys. Oceanogr.*, **6**, 335–344.

Sweet, R., 1971: Subroutine POISDD. NCAR Computing Facility, Boulder, 5 pp.

Williams, R. T., T. K. Schminke and R. L. Newman, 1971: Effect of surface friction on the structure of barotropically unstable tropical disturbances. *Mon. Wea. Rev.*, **99**, 778–785.

Yanai, M., and T. Nitta, 1968: Finite-difference approximations for the barotropic instability problem. *J. Meteor. Soc. Japan*, **46**, 389–403.

Seasonal Structure of a Simple Monsoon System

PETER J. WEBSTER

CSIRO Division of Atmospheric Physics, Mordialloc, Victoria, Australia 3195

LANG C. CHOU

Department of Meteorology, Naval Postgraduate School, Monterey, CA 93940

(Manuscript received 28 June 1979, in final form 4 September 1979)

ABSTRACT

With a structure based on observational studies which indicate that the monsoon occurs on extremely large spatial scales and shows distinct seasonal character, a model is developed with the aim of discerning the basic driving mechanisms of the mean seasonal monsoon. It is argued that for the macroscale monsoon an appropriate facsimile is a zonally, symmetric, moist and primitive equation atmosphere coupled to an interactive and mobile ocean. Via experimentation with the model a hypothesis is tested which states that the character of the mean seasonal monsoon is determined by an interplay between the basic drive of the monsoon system (i.e., the differential heating between an *interactive* ocean and continental regimes) and the hydrologic cycle.

A seasonal structure of a simple monsoon system was developed and its character discussed. With full hydrology and an ocean-continent differential heating, the model displays many features of the observed mean monsoon. Comparisons between moist and dry and oceanic and ocean-continental systems indicate the importance of the various mechanisms of the monsoon circulations. For example, scale contraction is noted with the introduction of moist processes and simple arguments are introduced to explain the scale change.

It is shown that the mean summer structure of the model monsoon is made up of low-frequency variations or transients which occupy a large fraction of the variance. The manner in which the model will be used to investigate the monsoon transients is discussed.

1. Introduction

Despite severe restrictions in data coverage in the ocean areas to the south of India, the structure of the Asian monsoon has received considerable attention. So important is the determination of the basic mechanisms which drive the monsoon circulation (an importance emanating from the social-economical advantages of being able to forecast the monsoon) that it has been the subject of a number of large-scale field experiments including the International Indian Ocean Expedition (1964–65) and the Global Atmospheric Research Program's Monsoon Experiment (MONEX, 1977–79). Less effort has been made in the past with the Indonesian–North Australian and the North African monsoon systems although there is some hope that the data collected in Winter MONEX and WAMEX (West African Monsoon Experiment), both experiments having been conducted during the First GARP Global Experiment year (FGGE), will yield at least initial descriptions.

Deciphering the role of the various mechanisms which drive or influence a system is a particularly difficult task in an inherently complex structure such as the monsoon. A number of key questions emerge as critical obstacles in the path of a full description of monsoon dynamics. These are 1) the influence on the magnitude and phase of the monsoon of the heated continent, 2) the role of hydrological processes, 3) the mechanical and thermal influence of large orographic structures such as the Himalayas, and 4) the perturbation of the basic radiative forcing by variable cloud extent.

Some partial progress has been achieved in understanding the points listed above by a number of different studies although no one model has been used to investigate all questions. The simulation of the monsoon has been achieved by large-scale multidimensional general circulation models with some success (e.g., Hahn and Manabe, 1975). Such models include many important physical mechanisms, feedback processes and detailed spatial resolution which, unfortunately, render experimentation expensive and difficult, especially when processes are evolving over seasonal time scales. Normally, the logistical problems of the general circulation models are overcome by the development of simpler phenomenological models aimed modestly at elucidating one or a few basic physical mechanisms rather

0022-4928/80/020354-14$07.50

118

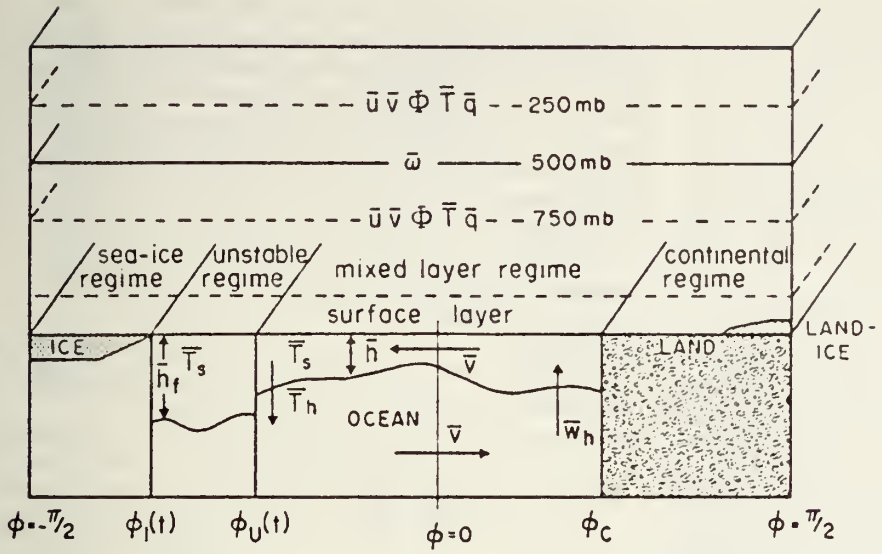

FIG. 1. Schematic representation of the interactive ocean-atmosphere model. See text for details.

ducing detailed simulations of the atmos- :ructure. For example, Webster and Lau ereafter referred to as WL) and Webster udied the influence of interactive oceans ıean seasonal and evolving seasonal flow. lel used in both studies was a dry (i.e., no ;ic cycle) version of the domain-averaged escribed in WL. They found that the magni- d phase of the monsoon circulation was directly to the lagged ocean response. ıently, the inclusion of an *interactive ocean* ısoon or climate model would seem impera- also showed that the formation of sea ice integral part of the ocean model. Without he proper phase of the latitudinal gradient ional heating could not be modeled.

mportant studies have aimed directly at the of the influence of orography on the struc- nonsoons. They are mentioned here to in- e problem involved in gleaning results from models as a means of answering the four estions listed above. Both Godbole (1973)[1] ın and Manabe (1975), the former using a symmetric model, found that orography essary for their monsoon simulations to e the observed state of the monsoon. there is apparent agreement between the lies, substantial differences occur. On one e Murakami *et al.*–Godbole study found *neglect* of hydrologic processes had little the magnitude of the model response. On the other hand, Hahn and Manabe suggested that moist processes *in conjunction with orography* were extremely important.

In order to overcome the problem of model incompatibility and to avoid the logistical constraints imposed by a general circulation model, it would appear logical to utilize one model which would allow a rational and sequential approach to the four basic questions. Such an approach is the *aggregate method* by which the physical complexity of a model is slowly increased in successive controlled experiments. This is in contrast to the general circulation model approach where there is an attempt to include as many physical features as possible. The parent model we choose is the domain-averaged model of WL and a principal aim of this paper is to develop a rational subset of the model with the purpose of attempting to understand *the role of hydrology* in the monsoon system.

2. Model formulation

The physical structure of the model is shown schematically in Fig. 1. A zonally symmetric, two-level, nonlinear primitive equation model extending from pole to pole lies over a laterally inhomogeneous lower boundary which contains ice, ocean and land areas. The ocean surface temperature and the structure of the upper ocean are determined by the simple advective mixed-layer model of WL. The model predicts the structure of the oceanic mixed layer in stable regimes and uses convective adjustment to determine the surface temperature in unstable regions where the mixed layer is undefined. The transition point between the stable and unstable regimes is computed at each iteration. The sea and land ice extents are also predicted.

[1] le's paper appears to emanate from the earlier study of *et al.* (1968). Although the latter study is a non-standard it is included in the References as it is an important ot into phenomenological monsoon studies via numeri- ques.

The continental surface temperature is determined by energy balance considerations. Vertical transports of heat, moisture and momentum are calculated using bulk atmospheric boundary-layer formulations which act as coupling mechanisms between the ocean, land and the atmosphere. The continental boundary is placed at 18°N which approximates the southern margin of the Asian land mass.

At this stage it should be pointed out that the choice of a zonally symmetric model and a particular ocean-continent geography, suggests a particular interpretation of the results. Rather than representing zonal averages, the results are more pertinent to a particular longitude belt. Such a belt would be between 60 and 100°E. Furthermore the model is developed with the aim of studying forcing and feedback processes in the tropical and subtropical region. The model thus developed will be of just that degree of sophistication to be pertinent to the tropical and subtropical latitude zones, in keeping with the aggregate philosophy.

As most of the model structure is derived from WL only certain segments of the formulation will be presented here. For greater detail, the reader is referred to WL.

a. Atmospheric model

If a zonal operator is defined such that

$$\bar{X} = \frac{1}{2\pi}\int_0^{2\pi} X d\lambda, \tag{1}$$

we can reduce a quantity X to its mean and deviation from that mean. Operating on the primitive equations in spherical coordinates, the following set emerges:

$$\frac{\partial \bar{u}}{\partial t} + \bar{G}(\bar{u}) = \bar{v}\left(f + \frac{\tan\phi}{a}\bar{u}\right) + \bar{F}_1 \tag{2}$$

$$\frac{\partial \bar{v}}{\partial t} + \bar{G}(\bar{v}) = -\frac{1}{a}\frac{\partial \bar{\Phi}}{\partial \phi} - \bar{u}\left(f + \frac{\tan\phi}{a}\bar{u}\right) + \bar{F}_2 \tag{3}$$

$$\frac{\partial \bar{T}}{\partial t} + \bar{G}(\bar{T}) = \frac{\kappa\omega\bar{T}}{p} + \bar{Q} + \bar{F}_3 \tag{4}$$

$$\frac{\partial \bar{q}}{\partial t} + \bar{G}(\bar{q}) = \bar{S} + \bar{F}_4 \tag{5}$$

$$\frac{\partial \bar{\Phi}}{\partial p} = -\frac{R\bar{T}}{p} \tag{6}$$

$$\frac{\partial \bar{\omega}}{\partial p} + \frac{1}{a\cos\phi}\frac{\partial}{\partial \phi}(\bar{v}\cos\phi) = 0 \tag{7}$$

$$\bar{G}(\bar{X}) = -\frac{1}{a\cos\phi}\frac{\partial}{\partial \phi}(\bar{X}\bar{v}\cos\phi) - \frac{\partial}{\partial p}(\overline{X\omega}). \tag{8}$$

Following usual notation, $\bar{u}$, $\bar{v}$ and $\bar{\omega}$ represent the eastward, northward and vertical zonally symmetric wind components and $\bar{T}$, $\bar{q}$ and $\bar{\Phi}$ the temperature, specific humidity and geopotential, respectively; $\bar{F}$, $\bar{S}$ and $\bar{Q}$ define the small-scale dissipative processes, the moisture and heat sources and sinks.

The atmospheric model was adapted to two layers in the vertical, the upper layer being centred at 250 mb and the lower layer at 750 mb. $\bar{u}$, $\bar{v}$, $\bar{T}$ and $\bar{q}$ appear as prognostic variables at both levels with $\bar{\omega}$ being calculated at 500 mb, the interface of the two layers.

The atmospheric model is a one-domain version of the multi-domain model of WL except that eddy effects are ignored, i.e., we have assumed

$$\bar{G}'(\bar{X}') = \frac{1}{a\cos\phi}\frac{\partial}{\partial \phi}(\bar{X}'\bar{v}'\cos\phi) + \frac{\partial}{\partial p}(\bar{X}'\bar{\omega}') = 0.$$

Such a relaxation is in keeping with the simplicity of the objectives of the study and with the emphasis on low-latitude phenomena.

In summary, Eqs. (2)–(8) form a closed prognostic zonally symmetric set in $\bar{u}$, $\bar{v}$, $\bar{T}$, $\bar{\Phi}$ and $\bar{\omega}$ provided that $\bar{Q}$, $\bar{S}$ and $\bar{F}$ are known. A knowledge of the latter factors requires the determination of the surface temperature which, in turn, relies on an interactive ocean and ice model.

b. Ocean and ice models

The ocean model is identical to that described in WL and is shown schematically in Fig. 1. Four basic variables define the ocean. These are a mixed-layer temperature $\bar{T}_s(\phi,t)$, a mixed-layer depth $\bar{h}(\phi,t)$, a deep ocean temperature $\bar{T}_{-h}(\phi,t)$ and a "thermohaline" circulation velocity $\bar{v}$ determined by the pressure gradient resulting from the latitudinal variation of the thermal structure. The system is closed by continuity and an assumption regarding the actual free ocean vertical velocity magnitude (see WL for details).

When $\bar{T}_s > \bar{T}_{-h}$, the ocean structure is determined by the advective mixed-layer model. Poleward of the latitude where $\bar{T}_s = \bar{T}_{-h}$ the ocean structure is modeled by convective adjustment which parameterizes the rapid downward mixing of the cold surface water, or equivalently, the upward heat flux from the warmer deep ocean. Ice is assumed to form when the upward heat flux cannot balance the heat loss at the surface. With continued cooling at the surface this must eventually occur as coupled with the convective adjustment is a deepening of the mixed layer which diminishes the efficiency of upward heat flux. Poleward of the latitude of freezing the thickness of ice is assumed to have a prescribed functional thickness.

...ce surface temperature of the ice surface is cal-...ed in an identical manner to that over the land ...ce except that the heat flux from below the sur-...e (T_I) is nonzero. To a first approximation, ...lux of heat flux will depend on the temperature ...ent across the ice ($\tilde{T}_s - \tilde{T}_I$), the thermal ...ductivity of ice (K_I) and the thickness of the ...h_I, i.e.,

$$F_I = \frac{K_I}{h_I}(\tilde{T}_s - \tilde{T}_I). \tag{9}$$

Hydrologic cycle

) LATENT HEAT

Two parameterizations are developed for the ...ase of latent heat by various processes. The ...t, large-scale condensation, permits the release ...en the large-scale transport of water vapor allows ...uration to occur. The heating rate of the large-...le condensation is given by

$$H_L = \frac{L}{2C_p}[(q - \tilde{q}) + |q - \tilde{q}|], \tag{10}$$

...ere the tilde denotes the appropriate saturation ...lue. Latent heat is thus released whenever $q > \tilde{q}$ ...espective of the column stability.

The second parameterization releases latent heat ...convectively unstable regions of rising motions ...ing a combination of the schemes of Ooyama ...969) and Anthes (1977). The convective heating ...e is defined by

$$H_c = \int_{p_0}^{0} \begin{cases} \eta(1 - b)\dfrac{L}{C_p}\overline{\omega' q'}\,dp, & \tilde{\omega} < 0 \\ 0, & \tilde{\omega} \geq 0. \end{cases} \tag{11}$$

...e incorporation of η and b allow effective in-...sity and moisture availability controls and ...odifies the earlier CISK (convective instability ...the second kind) models of Charney and Elias-...n (1964), for example. η and b will be discussed ...osequently.

As the present model is constrained to two ...nospheric layers, $\tilde{\omega}$ in (11) is approximated by ...(500 mb). $\tilde{q}$ is the vertically dependent moisture ...tribution. Thus $\overline{\omega' q'}$ is parameterized by the ...oduct of the vertical velocity $\tilde{\omega}$ of the model and ...e specific humidity distribution. H_c is calculated ...the integral over the two atmospheric layers plus ...e boundary layer, quantities which are calculated ...the manner described in WL.

The intensity factor η was originally defined by ...yama as the total amount of lower atmospheric ...introduced into the cloud per unit mass of air ...m the boundary layer. Consequently, $(\eta - 1)$ ...its of air are entrained from the lower layer of the ...nosphere. If H_i is the moist static energy of layer i [$=C_pT_i + gz_i + Lq_i$], it can be shown from energy balance arguments of the convective updraft that

$$\eta = 1 + \frac{H_b - H_2}{H_2 - H_1} \approx 1 + \frac{\theta_{eb} - \theta_e}{\theta_{e2} - \theta_{e1}},$$

where θ_e is the equivalent potential temperature for the boundary layer (subscript b), the lower tropospheric layer (subscript 1) and the upper tropospheric layer (subscript 2). Our designation of η as an *intensity* factor is now obvious. With continuing convection (assuming sufficient moisture availability) stabilization occurs by the relative heating of the upper troposphere. Thus, H_2 increases which simultaneously enlarges the denominator and decreases the numerator of the expression, and η is reduced. As the moist static stabilities are prognostic functions, η places an upper bound on the maximum intensity of convection. The parameterization is similar to convection in the real atmosphere in that it takes into account the larger flux of energy that is required to be injected into the column to enable the convective updraft to be maintained in an environment of increasing stability caused by the prolonged convection.

Besides the thermal state of the atmosphere, the degree of convective activity depends on the availability of moisture. To take this into account we follow Anthes (1977) and introduce a moisture control b defined such that

$$b = \begin{cases} \dfrac{1 - R}{1 - R_c}, & R > R_c \\ 1, & R \leq R_c, \end{cases}$$

where R is the layer relative humidity and R_c a critical relative humidity defined by Anthes to be 0.5. Thus if $R < R_c$, the convective heating is assumed to be zero by (11) until the column becomes sufficiently moist by advection or local evaporation.

The hydrologic scheme also contains a consistent moisture source/sink definition for (5) such that

$$\tilde{S} = C_p\left(\frac{1 - b}{b}\right)\left(\frac{H_L + H_c}{L}\right), \tag{12}$$

which allows for a realistic transport of moisture to higher levels. Precipitation is merely the integral of (12) such that

$$\tilde{P} = -\frac{1}{\rho_s g}\int_0^p \tilde{S}\,dp. \tag{13}$$

2) EVAPORATION

Bulk aerodynamical formulations are used to calculate the evaporation over the ocean surface. The evaporation is given by

$$E_0 = \rho_s|V_s|C_p(q_s - q_h), \tag{14}$$

where the subscript s denotes a surface variable

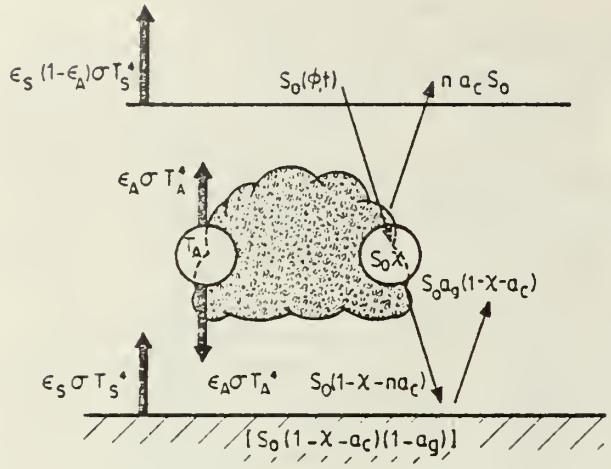

FIG. 2. Radiation model for atmosphere of cloud amount n. See text for details.

and h a variable indicative of the boundary (see WL). Over land, calculations of evaporation are identical except that the implicit assumption of an infinite evaporation source in (14) is no longer valid. The amount of evaporation will depend on the degree of wetness of the surface and the calculation of a soil moisture budget is necessary.

The method of Budyko (1974) is followed and a soil moisture W defined. If $W > W_c$, where W_c is a critical moisture content assumed to be 0.1 m, we assume that the soil is supersaturated and that the evaporation at the surface is given by (14).

If $W < W_c$, evaporation is reduced by a factor representing the moisture deficit so that

$$E = \begin{cases} E_0, & W > W_c, \quad (15a) \\ E_0 \dfrac{W}{W_c}, & W < W_c. \quad (15b) \end{cases}$$

If we define a maximum soil holding capacity W_R, we can assume that any excess moisture (i.e., $W - W_R$, if $W > W_R$) is runoff which may occur if $P > E_0$. With $W > W_R$, the rate of change of W is assumed to be zero and (15a) is invoked. If $W < W_R$, the rate of change of W is determined from the precipitation–evaporation deficit where the evaporation is calculated using (15b). In summary, the rate of change of W is given by

$$\frac{\partial W}{\partial t} = \begin{cases} 0, & W > W_R \\ P - E_0, & W < W_R. \end{cases} \quad (16)$$

d. Cloud and radiation

Recent work by Stephens and Webster (1979) indicate an extreme sensitivity of the radiative forcing of the atmosphere to the form, amount and distribution of cloud. Indeed, as an introductory example they noted the extreme longitudinal and latitudinal variability of cloud in the monsoon region and calculated the resultant variations in radiative heating. They conclude that cloud radiation-dynamic feedback calculation requires not only a detailed radiation model but also carefully construed parameterizations of the cloud production and maintenance. However, as the present model has been developed with clear and limited objectives we postpone the inclusion of fully variable clouds to a subsequent study which is assumed to be the next level of model sophistication following the philosophy of process aggregation. With the objectives in mind, we assume a constant cloud cover of 0.3 which is similar to the observed mean climatological cloud cover for the overall monsoon region.

As cloudiness is relegated to a constant value the degree of sophistication necessary to calculate the radiative forcing may be relaxed. The radiation model is an extension of Charney (1959) and matches the radiation model classification "B" of Stephens and Webster. The model structure is shown in Fig. 2 and allows for an effective atmospheric absorptivity of shortwave absorption χ and an atmospheric longwave emissivity ϵ_A. If we assume that the mean atmospheric temperature [i.e., $T_A = (T_{750} + T_{250})/2$] is equivalent to the mean radiating temperature of the atmosphere and that the radiative cooling rate Q_R of the column is equal to the net flux divergence of the column, we may write

$$Q_R = S_0(1 - na_c) - \epsilon_A(2\sigma T_A^4 - \epsilon_s\sigma T_s^4), \quad (17)$$

where ϵ_s is the surface emissivity assumed to be unity, a_c the cloud albedo (=0.6) and n the functional cloud amount (=0.3). The atmospheric emissivity and absorptivity are given values of 0.85 and 0.5 respectively. Values of the radiative parameters are consistent with those presented in Table 2 of Stephens and Webster. S_0 is the incident mean daily radiation at latitude ϕ at the top of the atmosphere so that

$$S_0 = S_{00}[(\pi/2)\sin\phi\sin\delta + \cos\phi\cos\delta]F(\sec\phi),$$

where $\delta = 23.45\sin(2\pi t/365)$, S_{00} is the equivalent solar radiation incident at the top of the atmosphere at the equator, and

$$F(\sec\phi) = [0.3 + 0.7\sec(\phi - 8)]^{-1}$$

TABLE 1. Albedo law constants.

Constant	Land	(Sea)
A_i	0.5	
B_i	0.3	
C_i	0.2	
T_i	270.0	

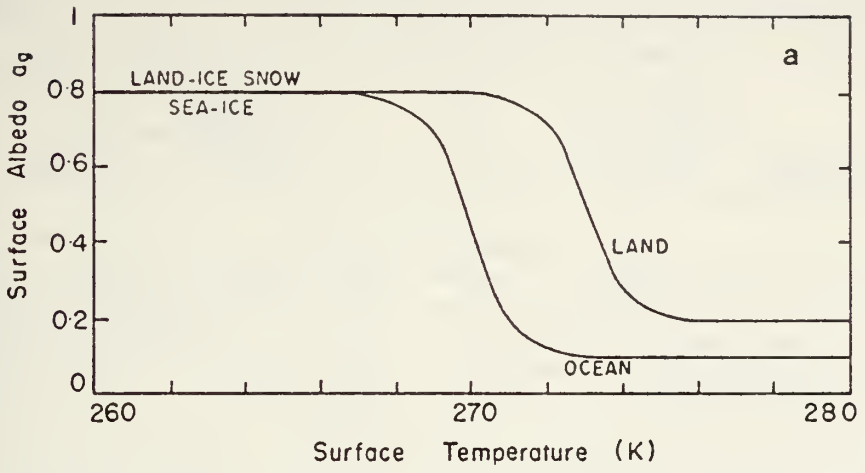

FIG. 3a. Functional dependency of albedo on surface temperature for both land and ocean surface.

where $F(\sec\phi)$ is an optical path factor and δ the solar declination angle.

The radiation model developed above differs slightly from that which is used in WL. Specifically, the longwave part of the formulation for the radiative cooling rate allows for the partial absorption of the emitted terrestrial radiation (i.e., $\epsilon_A\epsilon_S\sigma T_s^4$). With the partial opacity of the atmosphere taken into account, realistic values of atmospheric emissivities may be used (see Stephens and Webster) rather than the excessive values traditionally employed. For example, without the partial opacity (i.e., the elimination of the ϵ_A coefficient of the terrestrial longwave radiation term) values of $\epsilon_A > 1$ must be employed for balance with realistic surface temperatures (e.g., WL use $\epsilon_A = 1.02$). Thus, despite the simplification mentioned above, the radiative model provides a fair approximation to an atmosphere with constant cloud. However, in order to allow a model-produced variable cloud, the sophistication of the model must be increased—a point emphasized by Stephens and Webster.

e. Albedo formulations

As cloud and ground albedo are treated separately in the model, we deviate from WL [who used the Faegre (1972) formulation] and assume a surface albedo formulation

$$a_i = A_i + B_i \tanh C_i(T_i - T), \qquad (19)$$

where subscript i refers to the various surfaces (i.e., ocean, sea-ice, land-ice, land). The values chosen for the model are listed in Table 1. The albedo distributions shown in Fig. 3a illustrate the rapid surface albedo transition observed near the sea-ice and land-ice margins (see Budyko, 1974). To allow for the effect of ground water on the land surface albedo, an inverse dependency is introduced so that

$$a_{\text{land}} = 0.2 - 0.1\,W,$$
$$T > 273 \quad \text{and} \quad W < W_R. \qquad (20)$$

The form of a_{land} as a function of W is shown in Fig. 3b.

3. Experiments

The following initialization procedure was adopted and used in all the experiments described below. The model atmosphere was assumed to be at rest with a horizontally isothermal structure with the upper layer temperature set equal to 220 K and the lower layer to 260 K. The sea surface temperature was given by

$$T_S(\phi) = 300 - 50 \sin^2\phi \qquad (21)$$

and the continental surface temperature was set at

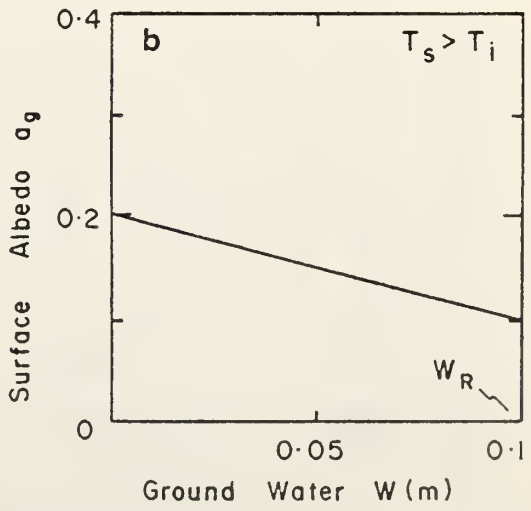

FIG. 3b. Modification of the land surface albedo by ground moisture.

TABLE 2. Properties of the various experiments.

Experiment	Label	Hydrology cycle	Geography	Integration period (years)
Dry Oceanic	DO	No	Global ocean	4
Moist Oceanic	MO	Yes	Global ocean	4
Dry Ocean–Continent	DOC	No	Continental cap ≥ 18°N	4
Moist Ocean–Continent	MOC	Yes	Continental cap ≥ 18°N	4

290 K. With an equinoctial insolation distribution maintained, the model was integrated for one year to produce an approximate steady equinoctial state which formed the initial data for all experiments. The model was then integrated for a further three years with the insolation following an annual cycle described by (18). To eliminate the effect of the transition from the initial equinoctial state to the evolving annual cycle, the mean seasonal fields were calculated from the third year of integration. Mean fields for the fourth year were quite similar but not identical.

Two sets of experiments were undertaken which involved either dry and moist conditions. In the dry case, the specific humidity was a prescribed quantity which was invariant with season, the only effect of which was in the magnitude of the atmospheric emissivity. The moist case, on the other hand, allowed the involvement of the prognostic hydrologic cycle. Each experiment was then performed for an oceanic earth and an earth containing a continental cap north of 18°N. The various experiments are summarized in Table 2.

The numerical schemes used to solve the model set

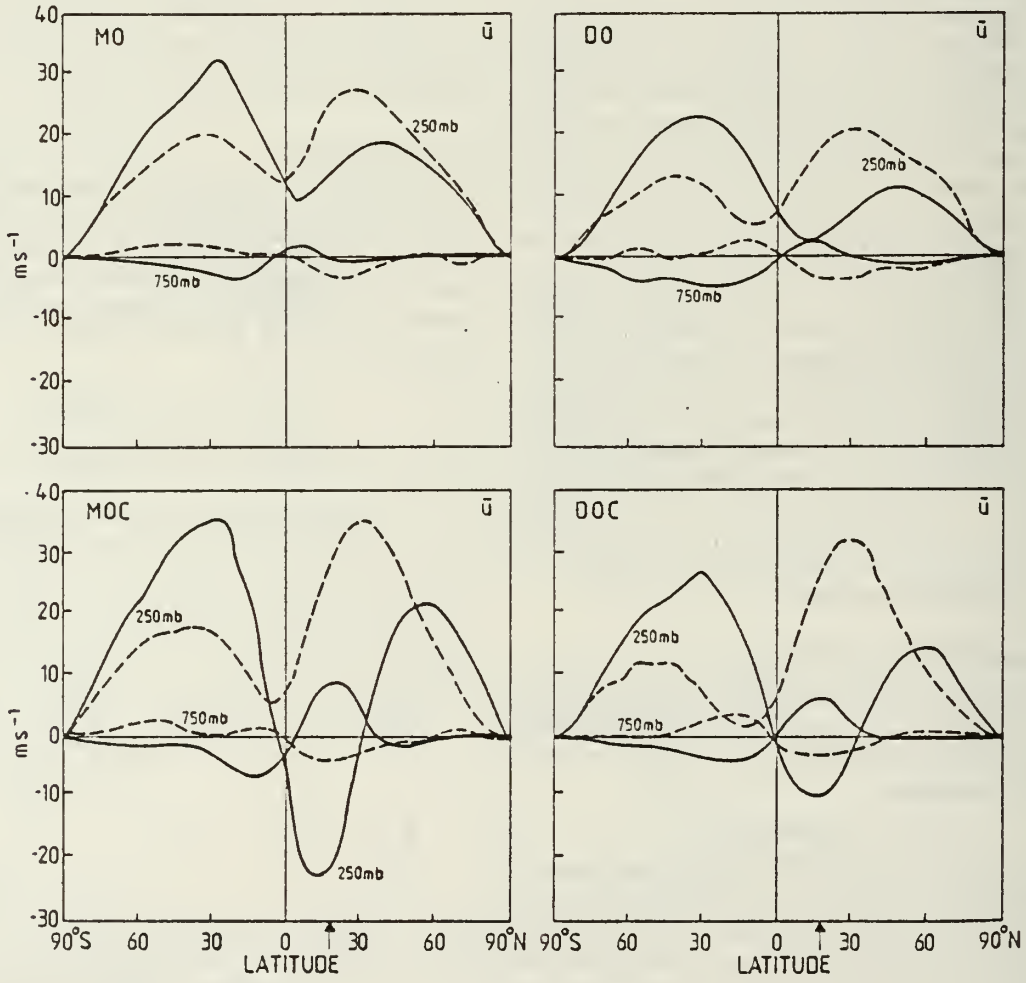

FIG. 4. Latitudinal distribution of the mean seasonal 250 and 750 mb zonal velocity component (m s^{-1}) computed for the dry ocean (DO), the moist ocean (MO), the dry ocean-continent (DOC) and the moist ocean-continent (MOC) experiments. Distributions are shown for the three month periods *following* the summer solstice (solid lines) and the winter solstice (dashed lines) of the third year of integration.

124

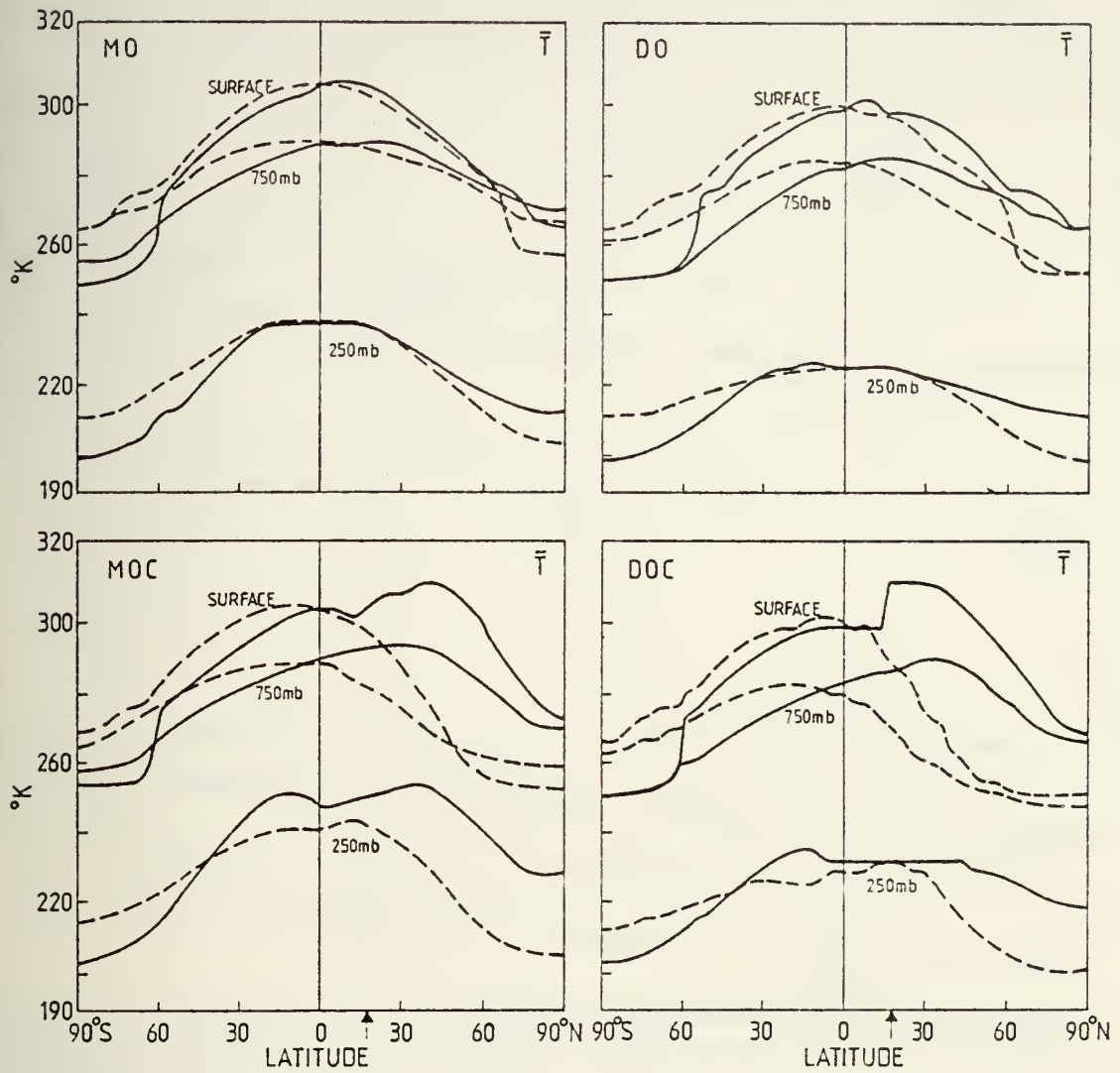

FIG. 5. As in Fig. 4 except for the mean seasonal surface, 750 and 250 mb temperature (K) fields.

are identical to those described in WL. With 80 min time steps (stable for the quasi-semi-implicit filter time-differencing scheme used) the computation time required for one simulated year of the MOC case is ~2 min on the CSIRO CDC Cyber 76.

4. Results

Figs. 4–6 show comparisons of the seasonally averaged fields of $\bar{u}$, $\bar{T}$, $\bar{\omega}$ and $\bar{v}$ for the third year of integration. Seasonal means for the fourth year were very similar. The $\bar{q}$ and $\bar{P}$ fields for the MO and MOC experiments are shown separately in Figs. 7 and 8. In each diagram the dashed curves correspond to winter season (defined as the three-month period from the winter solstice to the spring equinox) and the solid curves to the summer season (summer solstice to the autumnal equinox). As mentioned previously, the results are pertinent to the longitude belt around 80°E.

All four cases show significant individual character; the largest differences occurred between the dry and the moist experiments with the moist fields being more intense than their dry counterparts. A striking example is in the 250 mb zonal velocity field in the MOC experiment. There the equatorial easterlies are in excess of 23 m s^{-1} during the summer season compared with 9 m s^{-1} in the DOC case. Similarly, the moist vertical fields show intense narrow regions of ascending air at 10° from the equator in the MO case and over the heated continent in the MOC case, rather than the weaker and broader features of the dry experiments. Comparing the results with the observed fields presented by Webster *et al.* (1977), in particular Fig. 8, we note considerable similarity in both the magnitude and location of the mean easterly and westerly maxima.

Of all fields, only the surface temperature is stronger for the dry fields than for the moist. This is especially true over the heated continent which is

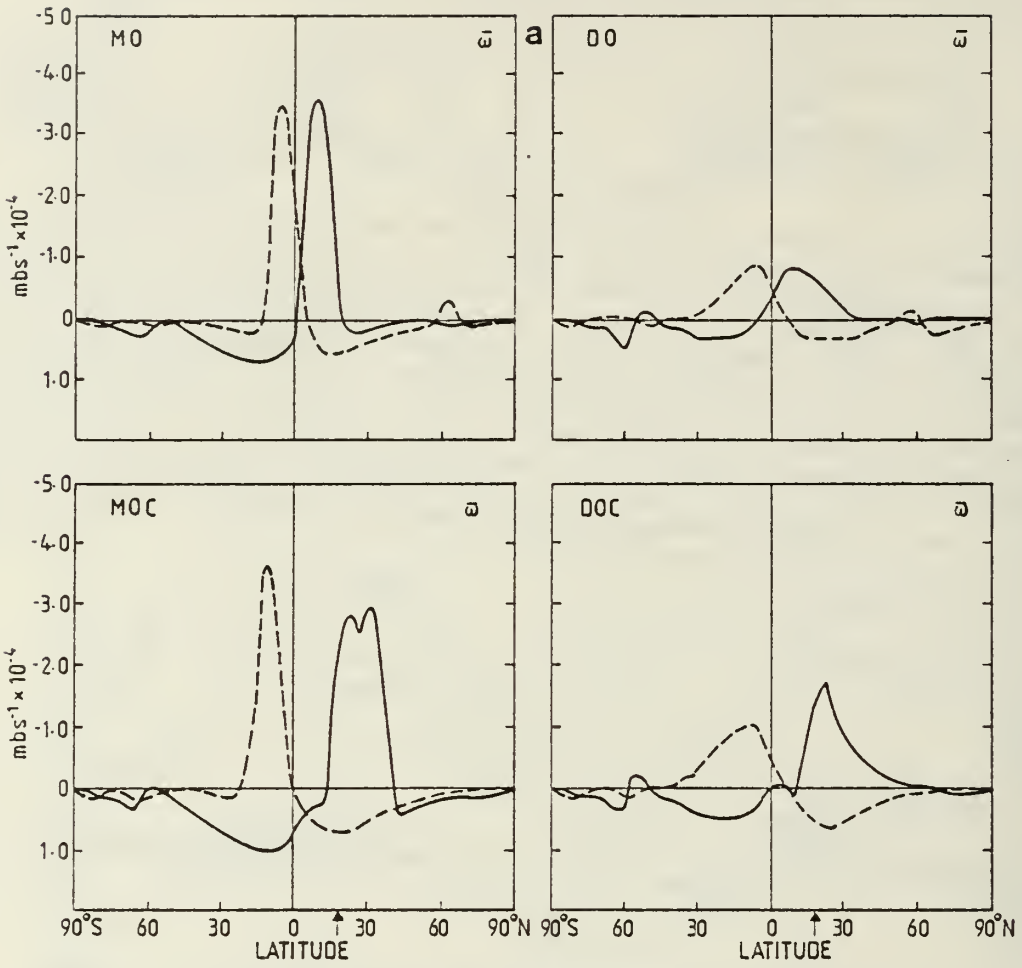

FIG. 6. As in Fig. 4 except for (a) the mean seasonal 500 mb vertical velocity (mb s^{-1}) and (b) the 750 mb meridional velocity fields (m s^{-1}).

~5 K warmer near the coastal margin. The warmer conditions can be accounted for by the absence of a hydrologic cycle and the consequent evaporational cooling from ground water accumulation. This explanation is confirmed by noting that in Fig. 5 the cooler temperatures exist only over the region of maximum precipitation shown in Fig. 8. Poleward of the precipitation peak, the continental temperature increases to near the value of the DOC experiment.

The role of moist processes is most evident in the tropospheric temperature distribution. Comparing the 250 mb temperature fields of MOC and DOC in Fig. 5 a bimodal temperature distribution may be noted about the equator. The summer maximum in the Northern Hemisphere is a result of the intense latent heating over the continental region through the entire atmospheric column and the resultant reverse temperature gradient is the cause of the strong summer easterlies to the south of the continental cap which may be seen in Fig. 4. The temperature maximum of the winter hemisphere is due to the intense subsidence (see Fig. 6) in the return leg of the meridional cell. The moist ocean case shows only a weaker version of the double upper tropospheric temperature maximum and consequently weaker (or non-existent) upper level easterlies. It should be noted that the double temperature maximum about the equator matches well the mean upper tropospheric temperatures noted by Newell *et al.* (1972) in the vicinity of the 80°E meridian. The absence of the double structure in the MO case bears a similarity to the oceanic regions of Newell *et al.*'s analyses.

Similar differences between the four experiments may also be seen in Fig. 6 which shows the vertical and meridional velocity components. For example, the moist fields are more intense and narrower than their dry counterparts as noted previously. Comparing the MOC and MO experiments, it can be seen that the winter $\bar{\omega}$ and $\bar{v}$ fields are almost identical except for a 4° poleward displacement for the MOC case. During summer the ocean-continental experi-

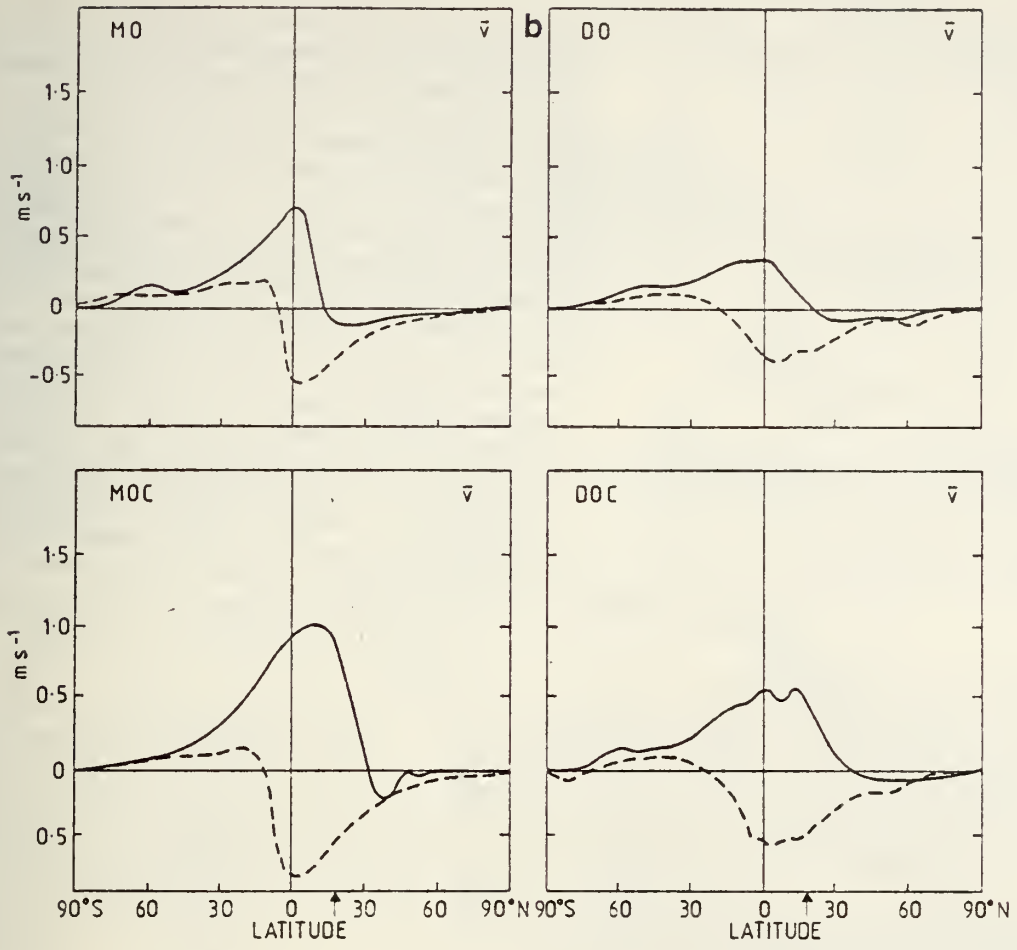

FIG. 6. (*Continued*)

ment shows a broader region of ascent over the continent, centered in the mean at ~25°N, compared to 10°N for the oceanic case. The double maximum over the continent is actually a manifestation of a substantial subseasonal variation present during the summer months. An example of the existence of the low-frequency transients may be seen in Fig. 9 which is a latitude-time plot of the 750 mb zonal velocity component.

The mean specific humidity and precipitation distributions are displayed in Figs. 7 and 8, respectively. The precipitation fields show considerable similarity to the vertical velocity fields except for the low amplitude but positive wings. Both aspects are consistent with the convective and large-scale latent heat parameterizations developed in the last section. The precipitation over land in the MOC case is considerably larger than can be accounted for solely by the vertical velocity field which, from Fig. 6, show only small differences in magnitude compared with the MO case. The reason the precipitation for the MOC case is so much greater can be seen in the considerably larger fields of specific humidity shown in Fig. 7. The difference lies in the temperature of the column in each experiment which from Fig. 5 is ~10° warmer than the MO case. Considering the simplicity of the model, the precipitation over the land area only slightly underestimates the summer precipitation in the Gangetic Plain region.

Viewed in toto the mean fields produce many interesting features, some of which bear strong resemblance to the mean fields in the vicinity of South Asia. The MO case indicates a near mirror image between the summer and winter mean vertical velocity and precipitation fields. On the other hand, the MOC case shows a strong bias in magnitude and degree of poleward penetration in the northern summer hemisphere and indicates an acute sensitivity to moisture which is particularly apparent when compared to the DOC case. That such differences occur with the inclusion of moisture is an important result as the Murakami *et al.*–Godbole study found an apparent insensitivity to the hydrologic cycle. However, by a series of experiments we have reached the contrary conclusion at least for the mean mon-

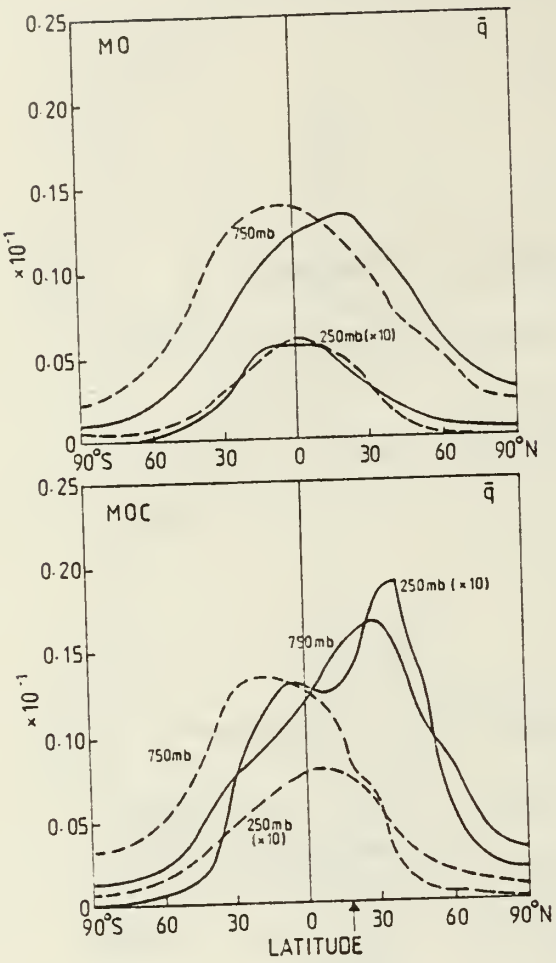

FIG. 7. As in Fig. 4 except for the latitudinal distribution of the mean seasonal specific humidity fields for the MO and MOC cases.

soon—a result which concurs with other studies of basic tropical phenomena (e.g., Charney and Elliassen, 1964; and many others).

5. Discussion

In the preceding paragraphs a number of observations were made regarding the model results and their interpretation. For completeness and in order to allow explanations to be developed of not only the mean structure of the monsoon but also, in subsequent studies, its transient state, a few of these points should be discussed.

a. Magnitude and location of the field extrema

Previously the location and magnitude of extreme mean seasonal values of some of the variables were noted. It was inferred that the mean MOC fields were complicated but recognizable combinations of the DOC and MO cases. This may be seen in the surface and tropospheric temperature distributions and the relationship to the dynamic fields. Over the ocea the temperature fields are determined by the dynan ics of the mixed layer which, in turn, depend on th deep ocean temperature and the heat balance and th wind stress at the surface of the ocean. Because a four factors are involved, a considerable lag wi maximum insolation occurs so that maximum se surface temperatures generally occur between th summer solstice and the autumnal equinox. Ov land the lag is considerably less and in the MO case, two relative surface temperatures simu taneously exist (i.e., the ocean and the continent maxima) during the summer with different phase relative to the insolation. Another complicatin factor is the moisture content in the continent region. As the surface temperature over land determined by energy balance consideration evaporative cooling (or the flux of latent heat awa from the surface) is taken into account. Co

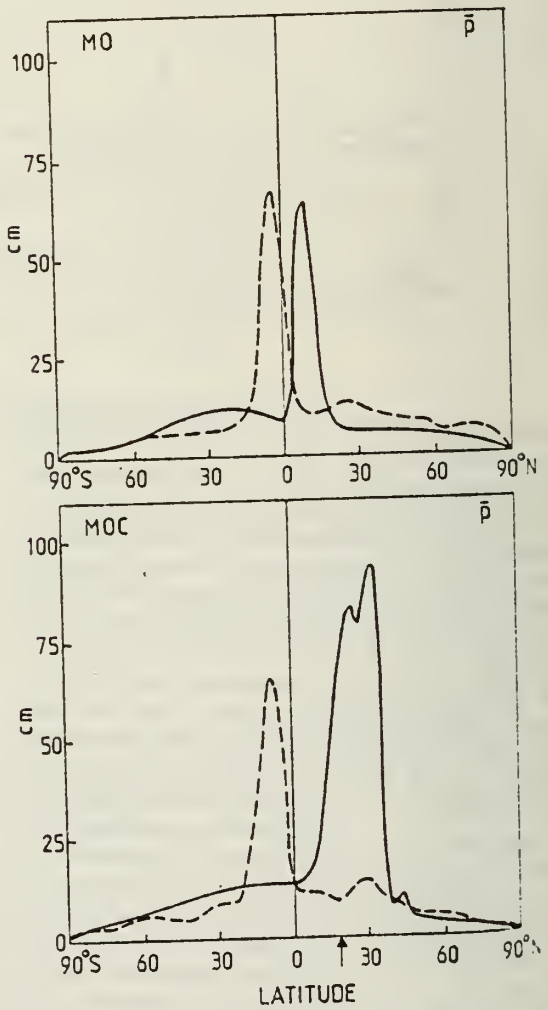

FIG. 8. As in Fig. 5 except for the latitudinal distributions of mean seasonal precipitation (cm) for the MO and MOC

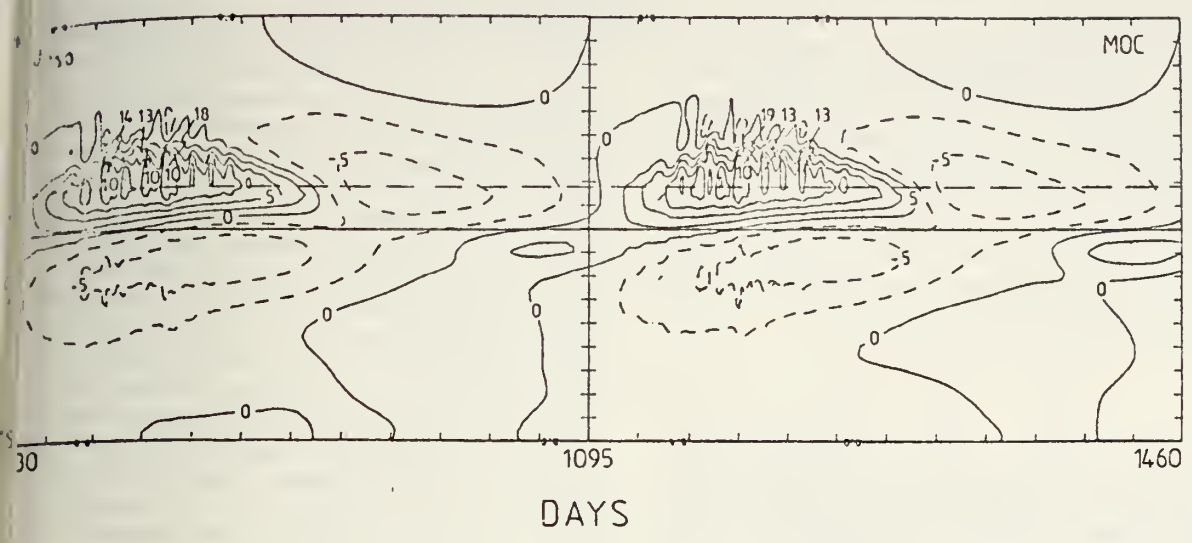

Latitude-time section of the 750 mb zonal velocity component for the third and fourth years of integration for the MOC case. Units are m s^{-1} and contour intervals 2.5 m s^{-1}.

itly, the region of maximum insolation over eed not be the region of maximum tempera- is the case in Fig. 5 for the MOC case. mechanisms which determine the rather com- d distribution of surface temperature are re- directly in the dynamic structure of the model phere. This may be seen from (4), the first thermodynamics, which may be written to pproximation as

$$\frac{\kappa \bar{T}}{P}\bar{\omega} \approx -\bar{Q}. \tag{22}$$

quation stipulates that the vertical velocity ution is almost determined by the heating ution or, alternatively, that within an atmos- column, the non-adiabatic heating is nearly etely balanced by adiabatic effects.

oth seasons of the MO case and for the winter MOC case, it can be seen by comparing Figs. 7 that maximum ascent corresponds to maxi- surface temperature. Thus from (22) we can in- t over the ocean, maximum surface tempera- pincides with maximum non-adiabatic heating. appears consistent with the boundary heat calculated by the bulk formulations where the tude of the sensible heat flux is determined pally by the surface temperature (for reason- pse rates) as is the latent heat flux over ocean s where the moisture source can be assumed ially infinite. Such correspondence also fol- o the DOC case where during summer maxi- ascent occurs over the warmest continental which, because the latent heat flux is zero, es the maximum sensible heating. Only in the case in summer over the continent does the correspondence between $\bar{\omega}$ and $\bar{T}_s$ fail. As mentioned previously in the MOC case the maximum surface temperature occurs well north of the coastal margin, the moist area close to the coast being cooled by evaporation. However, as evaporation is extremely large and correlates with a substantial latent heat flux, $\bar{Q}$ is largest to the south of the maximum surface temperature.

In summary, it appears that over the ocean maximum ascent will coincide with maximum surface temperature whereas over a moist continent it is constrained to lie equatorward of the warmest regions. In fact, in the MOC case the warmest regions correspond to substantial subsidence. It is interesting to note that it is only when moist processes are taken into account that regions of maximum surface temperature are subsident. This suggests that in the real atmosphere desert regions are strongly coupled to adjacent regions of convective activity. Indeed, Stephens and Webster (1979) allude to strong dependencies between the Bay of Bengal region and the desert regions to the west of the Arabian Sea based on energy balance considerations.

It should also be noted that in summer the simulated upper tropospheric temperature maximum in the Northern Hemisphere corresponds to the region of maximum heating. This provides an apparent equatorial slope with height between the surface and 250 mb of the maximum temperature which perhaps resembles the African or Australasian summer monsoon system rather than the summer South Asian system. According to Newell *et al.* (1972) the slope with height of maximum temperature is almost zero or perhaps poleward, indicating the influence of the heated Tibetan Plateau omitted in this study.

b. Scale contraction

By comparison of the results of the various experiments (e.g., MO with DO and MOC with DOC, especially in Fig. 8) it is obvious that hydrologic processes or the release of latent heat effects a diminishing or contracting of horizontal scales of motion. The scale reduction may be discussed using an even simpler model.

If A is the fractional ascending area of a region and $(1 - A)$ the fractional descending part, we may write from mass continuity

$$\frac{\omega_1 A}{\rho_1} + \frac{\omega_2(1 - A)}{\rho_2} = 0, \tag{23}$$

where the subscript 1 refers to the ascending part and 2 to the descending part. We note from observations that the horizontal temperature gradient is fairly small and again assume that the first law of thermodynamics scales as (22) and is appropriate for both the ascending and descending regions. Furthermore we assume that the nonadiabatic heating is given by

$$Q_i = S_i + L_i + R_i, \quad i = 1, 2, \tag{24}$$

where the right-hand side represents sensible, latent and radiative heating, respectively. To incorporate a latent heat release law we simplify (11) by assuming $L_1 = -\alpha\omega_1$ and $L_2 = 0$, where α is some function of the moisture field. L is then a measure of the interaction or feedback between the dynamics and convective heating.

Noting that $\rho_1 \approx \rho_2$ and using (22), (23) and (24) together with the latent heat parameterization, we obtain the following expression for the area of convection:

$$A = (S_2 + R_2)\left[(S_2 + R_2) - \frac{\kappa\bar{T}_2}{P} \times \left(\frac{S_1 + R_1}{\frac{\kappa\bar{T}_1}{P} - \alpha}\right)\right]^{-1}. \tag{25}$$

For the vertically averaged column $R_2 < 0$ and $|R_2| > S_2$ which must occur because in region 2 $\omega_2 > 0$ (i.e., subsidence). For no latent heating (i.e., $\alpha = 0$), $A \leq \frac{1}{2}$ for $|S_2| \approx |S_1|$ and $\bar{T}_1 \approx \bar{T}_2$. With latent heating ($\alpha > 0$), the denominator becomes larger and negative with substantial diminuation of A. Basically, Eq. (25) states that $A(\alpha = 0) > A(\alpha > 0)$ or, alternatively, that the stronger the heating in a column the larger the vertical velocity needed to provide a balancing adiabatic cooling which from mass continuity constrains A to simultaneously decrease.

c. Subseasonal transients

The seasonal mean fields were compiled from the evolving state of the model monsoon and are consequently comprised of transient features of various space and time scales. Fig. 9 shows an example of the transient nature of the monsoon in the form of a latitude-time section of the 750 mb zonal velocity component for the MOC experiment during years 3 and 4 of integration. Whereas the general features suggested by the mean seasonal fields are apparent in Fig. 9, one can also see considerable variation, especially in the northern summer over the continental region. Although not shown here, neither the DOC nor MO cases possess similar low-frequency transients. In a separate study aimed specifically at the transient structure of the monsoon (Webster and Chou, 1980), it is shown that the variations of the northern summer are coherent features of the monsoon and are associated with successive poleward propagations of the monsoon cell from the Northern Hemisphere ocean region to well north of the continental boundary. Such propagations appear to be related to the "break-active" monsoon sequence. In this study we merely point out that the MOC mean fields contain features of considerable variance which occur on substantial space scales with approximately a biweekly periodicity.

6. Concluding remarks

A simple model has been developed in order to form a base for a number of experiments aimed at the determination of the basic driving mechanisms of monsoon flow. In this first instance, the mean seasonal structure of a simplified version of the South Asian monsoon is studied. We have built on the results of earlier theoretical investigations (in particular WL) by adopting an *interactive* ocean and a continent, differentially heated by an evolving solar cycle, as the basic requirements for the monsoon model. In the spirit of process aggregation and phenomenological modeling, hydrology is added to the system and its effects gauged by careful control experimentation. Variable cloudiness and orography will be successively added to the system in later studies. The effects of eddies and laterally adjacent oceans, present in WL, were purposely omitted from the model in order to allow a tractable analysis of a very simple system.

Viewed from the confines of the simplified model, a number of conclusions have been reached regarding the role of hydrology in forming the mean seasonal structure of the monsoon. In Section 5 it was pointed out that both the location and magnitude of the various variable extrema were strong functions of hydrology. Interpretation of the model results allowed an understanding of the latitudinal variation of surface temperature, and the positioning of the mean summer easterly maximum. Simple thermodynamical arguments based on model results have allowed some insight into the scales of motion of moist processes. In fact, with hydrology, i.e., an interactive ocean and continentality, the results

the simple model show unexpected agreement ith the observed gross mean monsoon. Such agree- ent suggests that further experimentation can be pproached with confidence.

The effects of neglected processes are also ap- arent in the model results. In particular, the neglect f eddies and the lack of their influence on the mean idlatitude motions is quite noticeable and appears esponsible for somewhat weaker and less peaked esterly maxima than those observed. A better mid- titude structure was probably produced by WL ho included eddy effects. The lack of eddy trans- orts is clearly evident in the precipitation distribu- on (Fig. 8). In place of the observed midlatitude recipitation maximum, the model predicts a broad, w precipitation region through the subtropics and idlatitudes of the winter hemisphere caused prin- ipally by supersaturation resulting from large-scale onvergence. With eddies the convergence would ave occurred at higher latitudes in a considerably arrower band.

A further aim of compiling the seasonal mean fields vas to gain an understanding of the results of the Murakami *et al.*–Godbole experiments. Their basic bjective was to gauge the importance of the Hima- ayan mountains on the large-seasonal structure of he monsoon. With the orographic features included nd with a hydrologic cycle, they produced fields of onal velocity component of similar intensity and osition to those shown in Fig. 4. When the moun- ains were neglected but hydrology maintained, the magnitudes of the zonal wind fields were reduced substantially. When hydrology alone was neglected, the fields did not appear to change. Consequently, in *sharp contrast* to the results found in the current study, both Murakami *et al.* and Godbole found the hydrology cycle to be of little importance. It is difficult to state precisely why the results of the studies should differ so greatly. However, considering the correlation between vertical velocity and condensational heating which has been established by a number of studies and demonstrated here by its effect on scale and magnitude, it is difficult to conceive of a tropical system which is effectively independent of latent heating, as suggested by Murakami *et al.* and Godbole. Unfortunately, although their results support earlier hypotheses[2] regarding the importance of the Himalayas in maintaining the mean monsoon circulation, it would appear that their relegation of relative importance between hydrology and orography must be in doubt.

Within the limits defined above, the model develops its own forcing functions and feedbacks which may exist on a multitude of space and time scales. For example, through its convective parameterization relatively rapid transients may develop. At the other end of the scale the slowly evolving interactive ocean may produce time scales which are considerably longer. The mean fields presented above are integrals of all these scales over a seasonal period and define an envelope within which the component aggregates reside. Because of this multiplicity of time scales it is an insufficient test of a model to merely examine mean fields as it is also necessary to establish that the lower frequency transients are physically reasonable. Such a test of the model which will be used for further experimentation into monsoon dynamics has been undertaken by Webster and Chou (1980).

Acknowledgments. Thanks are due to Dr. G. L. Stephens and Mr. B. G. Hunt for interesting discussions relating to the phenomena studied and the form of the final manuscript. This research was sponsored in part by the National Science Foundation, under Grant ATM 78-14821A01.

[2] In particular Flohn, 1968: Contributions to a meteorology of the Tibetan Highlands. Atmos. Sci. Pap. No. 130. Colorado State University.

REFERENCES

Anthes, R. A., 1977: A cumulus parameterization scheme utilizing a one-dimensional cloud model. *Mon. Wea. Rev.*, 105, 270–286.

Budyko, M. I., 1974: *Climate and Life*, David H. Miller, Ed. *Int. Geophys. Ser.*, No. 18, Academic Press, 508 pp.

Charney, J. G., 1959: On the general circulation of the atmosphere. *The Atmosphere and the Sea in Motion*, Rockefeller Institute, 178–193.

——, and A. Eliassen, 1964: On the growth of the hurricane depression. *J. Atmos. Sci.*, 21, 68–75.

Faegre, A., 1972: An intransitive model of the earth-atmosphere system. *J. Appl. Meteor.*, 11, 4–6.

Godbole, R. V., 1973: Numerical simulation of the Indian summer monsoon. *Indian J. Meteor. Geophys.*, No. 1, 24, 1–14.

Hahn, D. G., and Manabe, S., 1975: The role of mountains in the South-Asian monsoon circulation. *J. Atmos. Sci.*, 32, 1515–1541.

Murakami, T., R. V. Godbole and R. R. Kelkar, 1968: Numerical experiment of the monsoon along 80°E longitude. Sci. Rep. No. 62, Indian Meteorological Department, Poona, 51 pp.

Newell, R. E., J. W. Kidson, D. G. Vincent and G. J. Boer, 1972: *The General Circulation of the Tropical Atmosphere and Interactions with Extratropical Latitudes*, Vol. 1. The MIT Press, 258 pp.

Ooyama, K., 1969: Numerical simulation of the life cycle of tropical cyclones. *J. Atmos. Sci.*, 26, 3–40.

Stephens, G. L., and P. J. Webster, 1979: Sensitivity of radiative forcing to variable cloud and moisture. *J. Atmos. Sci.*, 36, 1542–1556.

Webster, P. J., 1979: A model of the seasonally varying planetary scale monsoon. *Dynamics of Monsoons*, A. B. Pearce and C. D. Lighthill, Eds., Cambridge University Press.

——, and L. C. Chou, 1980: Low-frequency transitions of a simple monsoon system. *J. Atmos. Sci.*, 37, 368–382.

——, and K. M. W. Lau, 1977: A simple ocean-atmosphere climate model: Basic model and a simple experiment. *J. Atmos. Sci.*, 34, 1063–1084.

——, L. C. Chou and K. M. W. Lau, 1977: Mechanisms effecting the state evolution and transition of the planetary scale monsoon. *Pure Appl. Geophys.*, 115, 1463–1491.

Low-Frequency Transitions of a Simple Monsoon System

PETER J. WEBSTER

CSIRO Division of Atmospheric Physics, Aspendale, Victoria, Australia

LANG C. CHOU

Department of Meteorology, Naval Postgraduate School, Monterey, CA 93940

(Manuscript received 28 June 1979, in final form 4 September 1979)

ABSTRACT

Seasonal, diurnal and synoptic time scales, plus a subseasonal modulation of synoptic events, appear to dominate the temporal structure of monsoon systems. Observational studies indicate that the latter low-frequency variation modulates or groups synoptic disturbances, producing periods of intense activity (the "active" monsoon) separated by distinct lulls (the "break" monsoon). Together with the "onset" and "retreat" of the monsoon, the modulations introduce into the system time scales which are far more rapid than that which would be expected from the evolving latitudinal variation of insolation.

As observations indicate that the seasonal cycle and low-frequency transients occur in large spatial scales a model is used which appears to simulate the large-scale mean seasonal structure of the monsoon. Such a model is a zonally symmetric moist primitive equation model coupled to an interactive and mobile ocean. With such a model the hypothesis is tested that the basic character of the low-frequency subseasonal transients of the simple monsoon system are a result of feedbacks between the hydrologic cycle and the differential heating between the interactive ocean and continental regimes.

With multi-annual integrations of the joint ocean-atmosphere model, monthly and daily variations are studied with the aim of testing the hypothesis. With full hydrology and an ocean-continent contrast, the model monsoon deviates substantially from the smooth transitions noted in dry experiments. Not only do the onsets and retreats of the monsoon system accelerate but rapid, orderly transitions occur during the Northern Hemisphere summer. During such transitions, the meridional monsoon cell periodically migrates inland causing rising motion north of 30°N and subsidence near the coastal margin which is the location of mean seasonal ascent. The transition is seen to possess biweekly time scales and show some characteristics of the monsoon "break". Similar transitions occur in subsequent years of the integration and differ in timing and intensity but maintain the same basic period. Comparison of the results with those of other studies are made and further studies detailed.

1. Introduction

Four major temporal scales appear to dominate monsoon circulations. These are the seasonal, synoptic and diurnal variations plus an aperiodic subseasonal or supra-synoptic modulation. Whereas the gross features of the seasonal monsoon have been recognized at least since the time of Halley (1686), significant progress in cataloging and identifying important seasonal and subseasonal structure have been achieved by the study of a long meteorological measurement record [see Ramage (1971) for a summary] and by utilizing data sets obtained from intensive observational efforts and subsequent detailed analyses (e.g., Ramage 1971; Ramage and Raman 1972, Sadler 1975; among others). Emerging from the analyses is a picture of a generally recurring slowly varying structure on a seasonal time scale with a variety of transients existing over various space and time subscales. Fig. 1, which shows the latitude-time sections of the evolving mean monthly 200 mb wind field in the south Asia region, illustrates the slowly varying envelope of the seasonal monsoon. The transients (i.e., low-frequency transients and synoptic events) which exist within such a seasonal envelope may show great variability in both character and occurrence from case to case or year to year (Ramage, 1971). Indeed, the variation in the form and the occurrence of the transient features probably accounts for the majority of the interannual variation of the monsoon.

For convenience and simplicity, the monsoon systems are usually divided into summer and winter components.[1] Here we will concentrate on an extremely simple interpretation of the Asian summer monsoon principally because it is the system on which most work has been undertaken and for which most data exist. The general observed character of

[1] A Northern Hemisphere chronology will be used throughout the paper.

0022/4928/80/020368-15$07.75

132

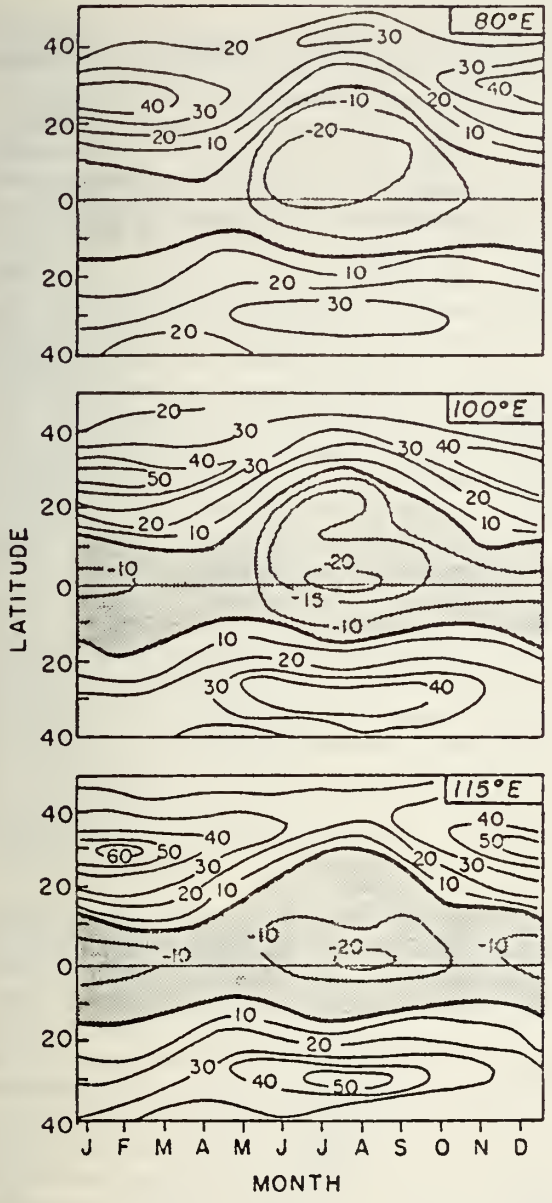

FIG. 1. Latitude-time sections of the 200 mb zonal velocity component (m s^{-1}) along the 80, 100 and 115°E meridians. Shaded area denotes easterly wind component.

the evolving summer component of the system may be summarized as follows: In late spring a vaguely defined cross-equatorial flow emerges from the Southern Hemisphere subtropics to the south of Asia and by early summer becomes both intense and steady in its southwesterly direction. The development and organization of the cross-equatorial flow coincides with the deepening of the monsoon trough over the north of India. Meanwhile, disturbed conditions are established over the Indian subcontinent, the arrival of which is often termed the monsoon "onset". Rapid modification of the upper level flow occurs and intense easterly winds in the upper troposphere ensue. Often in late summer, the disturbed pattern over India is interrupted with the cessation of precipitation over central India and an emergence of maximum precipitation to the north and south of the Indian plains. This is sometimes referred to as a monsoon "break." At such times the southern disturbed region is located nearer to its climatological spring position (i.e., just north of the equator) than to its summer position (Ramage, 1971). During autumn, with the accelerating retrogression of the latitude of maximum insolation, disturbed conditions diminish over India, the upper anticyclone weakens as do the upper easterlies and the monsoon is said to "retreat."

A number of observational studies have considered the transient nature of the monsoon. For example, Koteswaram and Rao (1963) suggest a sequence of states, explained in terms of meridional cell locations, to represent differences between active and break periods. For the active period Koteswaram and Rao suggest that two cells, a monsoon cell located from the equator to 20°N and a Hadley[2] cell lying between 20 and 40°N, possess a common ascending branch over the heated summer continent. During break situations, when precipitation is significantly diminished over central India, they propose that the ascending branch near 30°N in the active monsoon is replaced by a descending branch. Asnani (1967) embellished Koteswaram and Rao's monsoon cell by a combination double cell in order to account for the summer mean cloudiness minimum over the equator.

Recent observational studies by Krishnamurti and Bhalme (1976) and Murakami (1977) hint at strong interhemispherical coupling of the monsoon system on *subseasonal* (approximately bi-weekly) time scales. Variations appear to be communicated between the southern Indian Ocean and the precipitating regions over summer southern Asia. Although there may be some debate regarding the relative phases and lags of the variations, it is important to note that the communications appear to be accomplished by features reconcilable with the Koteswaram and Rao-Asnani descriptions of the monsoon. Most importantly, the observational studies suggest that the synoptic-scale disturbances of the monsoon flow (e.g., Bay of Bengal disturbances) occur in groups with time scales and sequences similar and consistent with the macroscale low-frequency variations, that is, they infer that the disturbances are modulated by the macroscale submonthly variations. As the disturbances are responsible for the majority of the precipita-

[2] The term "Hadley" cell is used loosely by Koteswaram and Rao as it infers a hemispheric scale and was probably chosen to distinguish the meridional circulation from their "monsoon cell" located further to the south.

tion in the summer monsoon, an understanding of the mechanisms which control or modulate their occurrence is of some importance.

In the descriptive models described above, the monsoon transitions (e.g., onset, modulation and retreat) are considered as rapid adjustments of the macroscale meridional circulation. However, the observational models do not provide mechanisms which explain the time scale of the transitions or the particular geographic location the structure occupies. Consequently, extensions of the Koteswaram and Rao-Asnani model or the testing of the Krishnamurti and Bhalme sequence must either rest on the compilation of sufficient data or on the development of theoretical and numerical models. At this stage the data base appears insufficient to sustain continued advances and perhaps we are forced to rely on models (albeit crude) to at least follow the initial leads prompted by observational studies.

In recent years, a variety of theoretical and numerical models have been developed and used for monsoon studies. Some success has been achieved in the simulation of the mean seasonal fields using general circulation models (e.g., Washington and Daggapaty, 1975; Hahn and Manabe, 1975) or simpler models (e.g., Webster, 1972, 1973; Webster and Chou, 1980, hereafter referred to as WC). Other studies have aimed at the modeling of specific phenomenology such as the role of topography on the evolving monsoon circulation (e.g., Hahn and Manabe, 1975), and the role of adjacent and interactive oceans (Webster and Lau, 1977, hereafter referred to as WL; Lau, 1978; Webster, 1979). However, studies aimed at the elucidation of subseasonal monsoon structures have received less effort. Their consideration constitutes a basic aim of this paper.

2. Hypothesis

WL tested the proposition that the interactive nature of the oceans adjacent to the Asian continent were crucial in determining the magnitude and spatial variation of the mean monsoon. Extensions of the study (Lau, 1978; Webster, 1979) showed that the phasing of the overall monsoon was a strong function of the different time lags exhibited by the oceans and land areas and the latitudinal variation of ocean response. We shall accept as a basic premise that the *addition of an interactive or specified time-varying ocean describes the lower limit of model sophistication necessary to study the longer term dynamics of the monsoon flow.*

The recent compilation of mean seasonal fields by WC indicates that at least the long-term dynamics rely critically on moist processes. By extrapolation we may suppose that moist processes are of equal importance to the evolving monsoon state.

The experiments of Lau (1978) and Webster (1979), neither of which contained a hydrology cycle, indicated only smoothly varying fields which simulated well the seasonal variability and allowed the atmospheric response to be coupled to the variable lag of the interactive ocean. However, subseasonal modulations and rapid transitions like these noted by Krishnamurti and Bhalme (1976) were not apparent. Furthermore the magnitude of various fields was less intense than those observed as were the mean fields for the dry experiments noted in WC. As precipitation and the release of latent heat appear to assume important roles in the cited observational studies, their neglect in Lau's and Webster's studies may have been critical. Consequently, we propose the hypotheses that it is *the feedbacks between hydrological processes and the basic dynamic elements of the monsoon system (i.e., the differential heating of the interactive ocean and the continent) which are responsible for rapid transitions and modulations of the system.*

To test the hypothesis we adopt the basic WL model but with the zonal symmetry assumption incorporated in WC. The assumption is consistent with a philosophy of attempting to construct the *simplest* possible model which may contain the physical ingredients necessary to produce structures described by the three observational studies. By an aggregation of physical processes, the complexity of the model is increased in steps and the hypothesis tested at each stage.

The study has the further purpose of attempting to understand the results of Hahn and Manabe (1975) from the confines of a considerably simpler system. The principal result of their study was an indication of the importance of the Himalayan Massif, a feature purposely omitted from the current study. On the other hand, the Hahn and Manabe study did not contain an interactive ocean which we stipulate as a basic physical ingredient in the monsoon system. Of course there are further differences such as the physical domain of the two models which add to the problems of comparison.

3. Experiments

The experimental format is identical to that described by WC except that it refers to evolving fields rather than seasonal means. The model was initialized as a horizontally isothermal atmosphere with an initially prescribed surface temperature. With the sun held in an equinoctial position the model was integrated for a year during which time it approached a steady state. Three experiments used the equinoctial equilibrium as initial data. These were a dry ocean-continent experiment (DOC) in which a continental cap was situated north of 18°N and an interactive and mobile ocean, a moist ocean continental experiment (MOC) which was identical to DOC except for the inclusion of hydro-

TABLE 1. Properties of the various experiments.

Experiment	Label	Hydrology cycle	Geography	Total integration period (years)	Period displayed Figs. 4–10 (years)
Moist Oceanic	MO	Yes	Global ocean	4	3, 4
Dry Ocean–Continent	DOC	No	Continental cap > 18°N	4	3, 4
Moist Ocean–Continent	MOC	Yes	Continental cap > 18°N	4	3, 4

logic processes, and a moist ocean experiment (MO) where the earth was assumed to be covered by ocean. A summary of the case abbreviations is presented in Table 1.

The rationale behind the three experiments is an effort to choose suitable cases with which to test the hypotheses posed in the last section. For example, a comparison between the DOC and MOC results provide indications of the role of the hydrologic processes. Similarly, comparing the fields of the MO and MOC experiments suggest the importance of continentality.

All experiments were run for a further three years after the generation of the initial state (i.e., in year 1). In subsequent paragraphs, the last two years of integration are discussed. The third year corresponds to the period over which the seasonal means of WC were calculated.

4. Results

a. Monthly structure

Indications of the transient state of the monsoon structure are first obtained from the evolving state of the mean monthly fields. Fig. 2 shows the variation of the upper tropospheric zonal wind field as indicated by the magnitudes and positions of the two westerly maxima (located in subtropical and middle latitudes) and the equatorial westerly minimum (or easterly maximum). Plots of the various extrema as functions of latitude are shown for both the MO (dashed curves) and MOC (solid curves) cases for the third and fourth years of integration. The numbers on each curve refer to the month of integration starting with the spring equinox of the third year.[3] Consequently, 7 and 19 refer to the two autumnal equinoxes and 1, 13 and 25 to the three spring equinoxes. The summer solstices (demarked SS) are shown on Fig. 2 for years 3 and 4. The vertical arrow on the abscissa (also on Fig. 3b) denotes the land-sea boundary at 18°N.

Considering first the MO case it can be seen that the two westerly maxima oscillate over a small range of latitude (between 25° and 30° in each hemisphere)

[3] In model nomenclature, month 1 refers to the 30-day period *following* the spring equinox. Subsequent months are defined similarly.

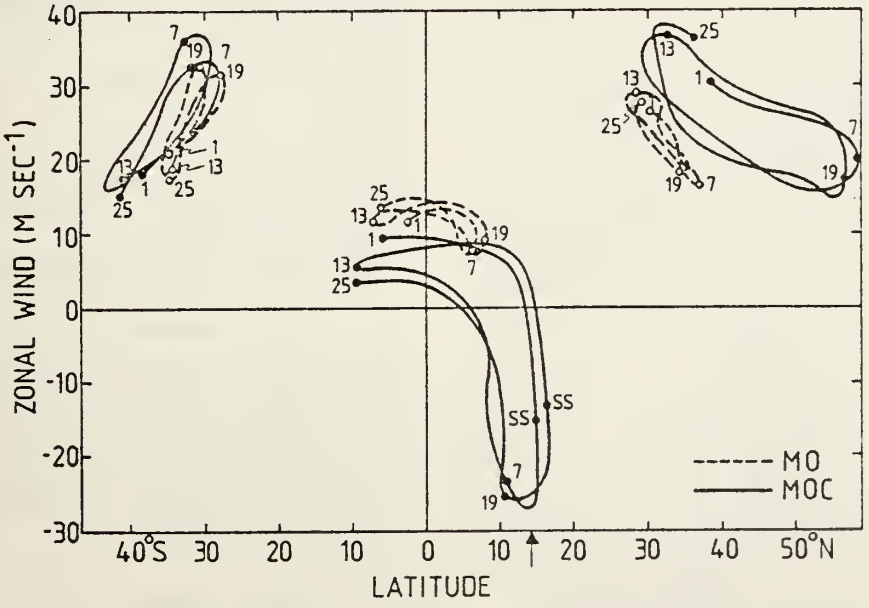

FIG. 2. Latitudinal variation of mean monthly 250 mb zonal wind component extrema during years 3 and 4 of integration. Curves connect mean monthly values of the two midlatitude westerly maxima (upper left and right) and the low-latitude westerly minimum (easterly maximum) for cases MO and MOC.

and a fairly small magnitude range. As expected, the two westerly maxima are out of phase. Maximum speeds occur near the spring equinox. The westerly minimum oscillates over a smaller amplitude range between 10°N and 10°S. Like the westerly maximum, the westerly minimum lags some months behind the solar declination.

The continental cap has a dramatic effect on the transient state of the monsoon flow. Sensible heat input during the summer is extremely large and substantial evaporation takes place over the warm continental region. The result is significant latent heat release in the atmosphere column with considerable warming in the upper troposphere. During winter, the lower boundary cools substantially, especially at higher latitudes, resulting in the enhancement of the latitudinal temperature gradient. Thus with a continental cap, the Northern Hemisphere westerly maximum now varies over a much larger latitude range and possesses a greater seasonal variability in magnitude. In summer the westerly winds are considerably further north with maxima near 50°N. The winter westerly maximas of *both* hemispheres are ~5–10 m s^{-1} stronger than in the oceanic (MO) case. The most significant effect, however, occurs in the region between the equator and the continental cap with the development of a 27 m s^{-1} easterly jet stream in the upper troposphere with rapid acceleration occurring prior to the summer solstice (i.e., during months 1, 2 and 3 and 13, 14 and 15).

In a sense, Fig. 2 may be considered sets of hysteresis curves and the space between the extrema at successive (say) spring equinoxes (i.e., points 1, 13 and 25) define a hysteresis creep which may be viewed as a measure of the deviation from an annual cyclic equilibrium. Whether or not the deviations are a result of a "natural" interannual variability or because the model has yet to achieve a state of cyclic equilibrium is difficult to resolve at this stage. On one hand, points 13 and 25 lie closer together than points 1 and 13, indicating an approach to cyclic equilibrium. However, the model does contain mechanisms which potentially may have time periods longer than one year or allow "memories" of the previous annual state. Two examples are the deep ocean temperature of the ocean model (see WC for details) and the hydrologic cycle which possesses an annual memory over the continent via the amount of stored moisture. The solution to the problem of interannual variability may be resolved by extended integrations of the model (>10 years) which are logistically feasible because of the simplicity of the model.

Figs. 3a and 3b show the variations between the monthly means of the vertical velocity profiles at 500 mb as a function of latitude for the MO and MOC cases, respectively. Rather than a linear trend of latitudinal position with time, the MO profiles oscillate about the equator some months out of phase with the solar insolation. The vertical velocity, in fact, is coupled strongly to the evolving position of the sea surface temperature maximum. The positions of the maximum ascent are similar to the climatological location of the "intertropical convergence zone" or "near-equatorial convergence zone". (In the simple model discussed here, either term may be used unambiguously as the region of maximum vertical velocity corresponds to the region of maximum convergence.) Furthermore, the intensity of the mean monthly vertical velocities which averages near -4×10^{-4} mb s^{-1} or 35 mb day^{-1} appears consistent with determinations from general circulation studies (e.g., Hahn and Manabe, 1975).

For the MOC case, the mean monthly vertical velocity profiles show rapid transitions from a Southern Hemisphere location in month 1 to over the continent in month 2 where substantial intensification occurs. The ascent over the continent is maintained until the autumnal equinox although subsequent months show some variability. The most northward extent of the ascending branch of the meridional cell occurs after the summer solstice. At that time the circulation is broad and intense and associated with substantial subsidence to the south of the continental cap and in the subtropics of the Southern Hemisphere. After the autumnal equinox, the ascent reestablishes just north of the equator similar to the oceanic convergence zone during month 7 before rapidly retreating southward.

The double maximum at the equinoctial months (1 and 7) is similar to the observed near-equatorial trough positions (see Ramage, 1971, Fig. 5.18) although the model appears to show a premature establishment of the northern trough in spring. A comparison of the winter profiles of the MO and MOC show some similarity except for a generally stronger circulation resulting from the enhanced temperature gradient—a reflection of the rapidly cooling continent.

The position of the ascending branch of the monthly mean meridional circulation is closely akin to the observed location of Koteswaram and Rao (1963) for the active monsoon (i.e., as distinct from break) over India. It is interesting to note that the agreement has occurred without mountains being included in the model which provides contrast to the findings of Hahn and Manabe (1975) although, as mentioned previously, model result comparison is difficult.

b. Transient structure

The transitions between the monthly mean vertical velocity distributions of the MOC case mask an even greater variation occurring in the submonthly structure. To illustrate this behavior latitude-time

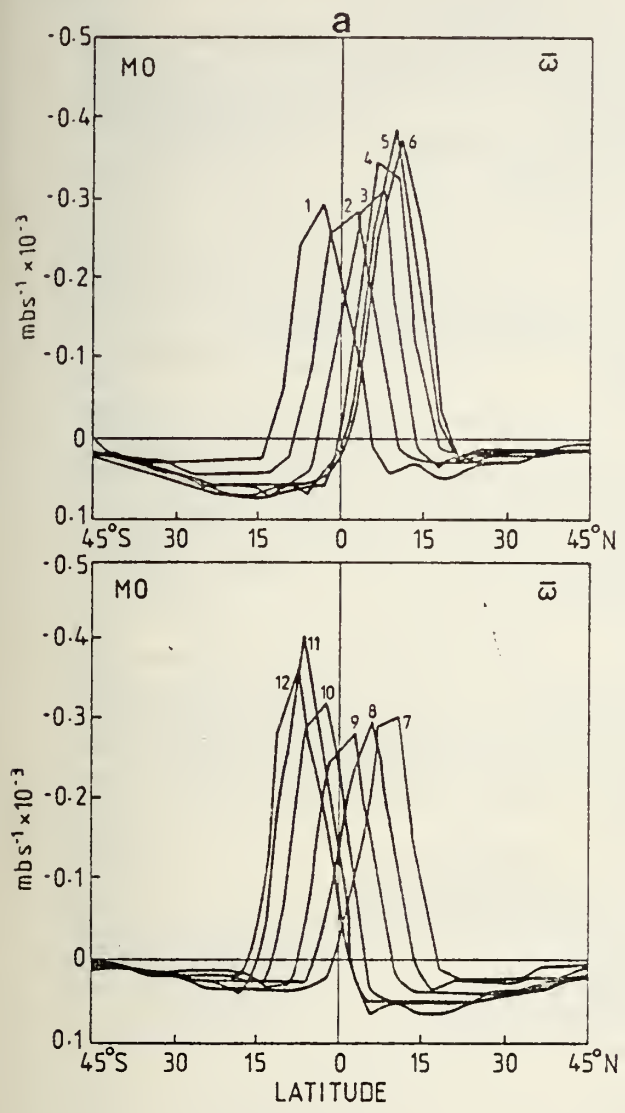

FIG. 3. Latitudinal variation of the mean monthly vertical velocity profiles for (a) MO and (b) MOC (units, mb $s^{-1} \times 10^{-3}$). Upper panel in each diagram refers to the first six months following the spring equinox of year 3 of integration. The lower panel refers to the second six months. Arrow on abscissa marks ocean-continent boundary.

sections of surface temperature, 250 mb temperature, the 250 mb zonal wind speed and the vertical velocity are shown for the MO, DOC and MOC cases in Figs. 4–7. The precipitation and specific humidity fields of cases MO and MOC are displayed in Figs. 9 and 10. Fields are shown for the 2-year period from Day 730 to Day 1460.

The surface temperature of the MO case shown in Fig. 12 has a smooth small-amplitude seasonal period with maximum temperatures near the equator[4]

[4] The version of the model used does not contain wind-driven Ekman transports capable of producing a weak relative temperature minimum along the equator. Such extensions are developed by Lau (1978).

as distinct from the MOC and DOC cases where large continental changes tend to dominate. The Southern Hemisphere temperature variation is quite similar in all experiments except that the phase of the temperature maximum in MOC slightly leads that of the MO case in the subtropics. Furthermore, the subtropics in the MOC case are cooler (~2 K) than in the MO case. Both factors stem from the interhemispheric influence of the continentality of the Northern Hemisphere. The cooler temperatures result from the increased wind stress caused by the fresher low-level winds in the Southern Hemispheres of the MOC experiment and the subsequent modification of the mixed layer. The apparent phase advance of the Southern Hemisphere surface temperature maximum is caused by an earlier start to the cooling trend, again instigated by the increased wind stress. Both factors indicate the large-scale influence of the monsoon system and, at the

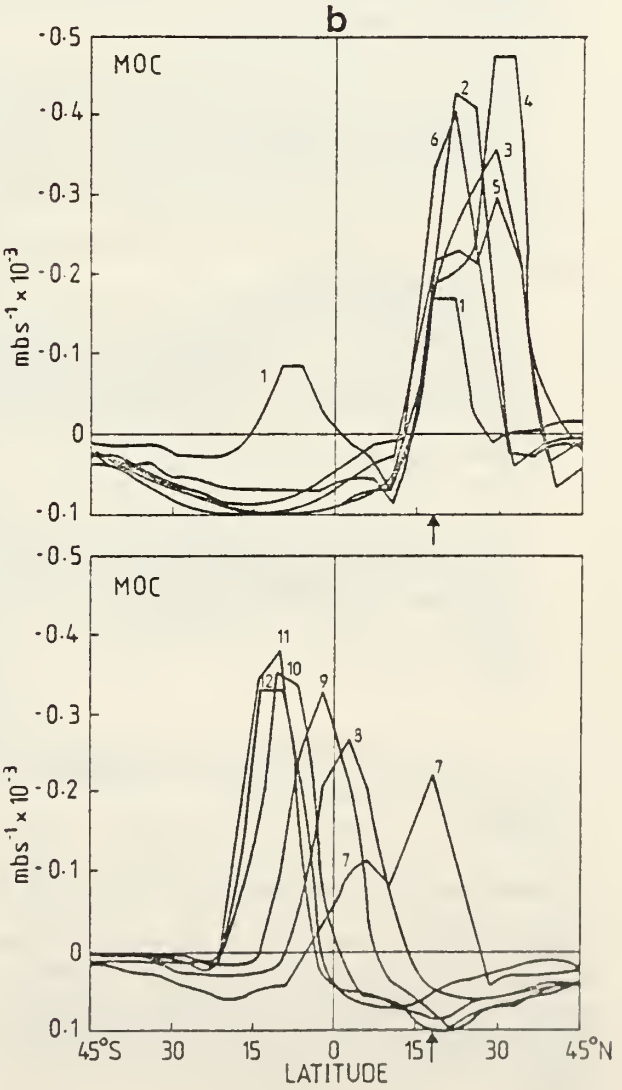

FIG. 3. (*Continued*)

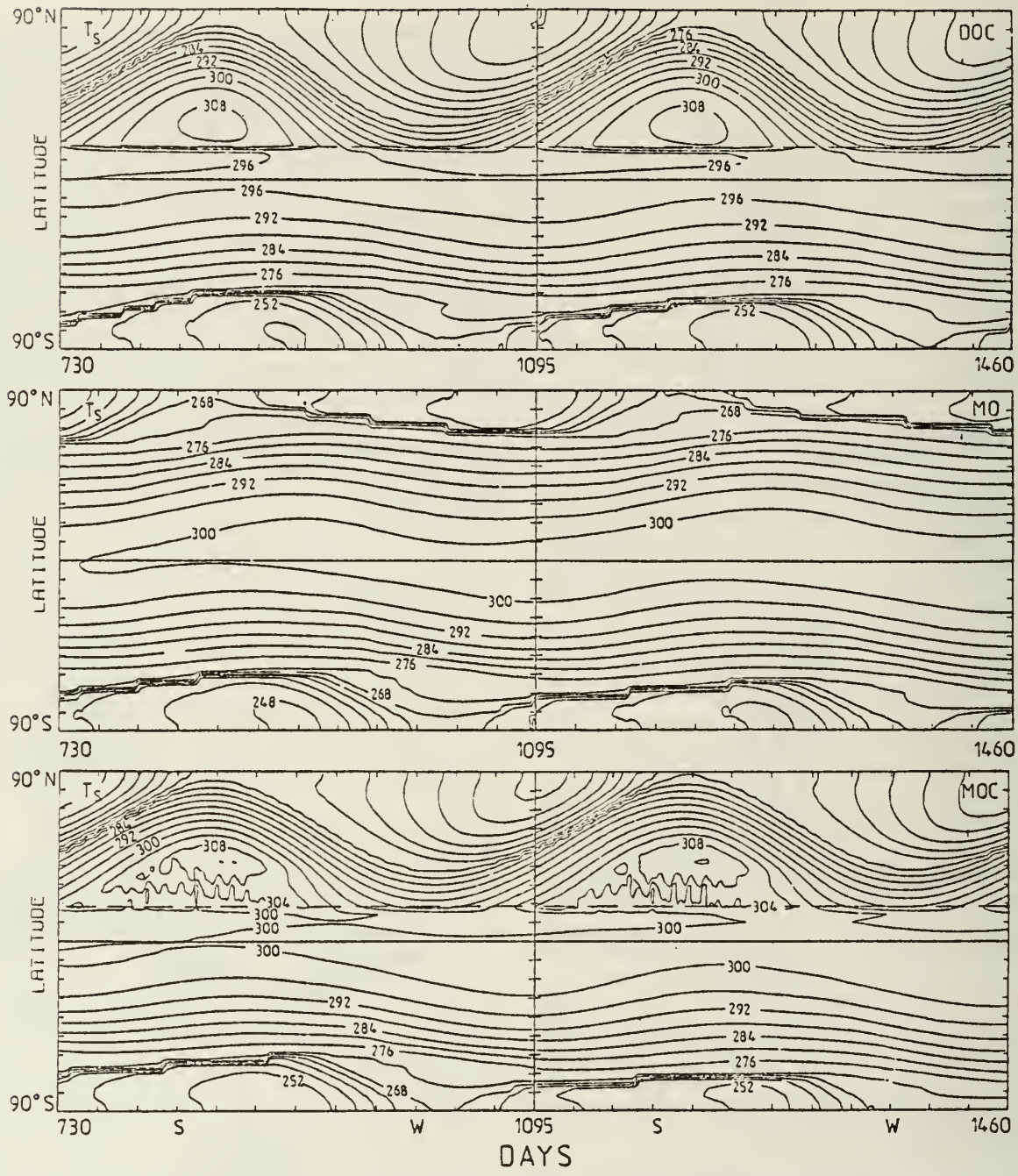

FIG. 4. Latitude-time sections of the surface temperature of cases MO, DOC and MOC for years 3 and 4 of integration. The summer and winter solstices are denoted by S and W, respectively, on the abscissa. Horizontal dashed line refers to coastal margin in the DOC and MOC cases. Solid line denotes the equator. Units are K with contour spacing 4 K.

same time, the interdependency of the ocean and the atmosphere.

Without hydrology (DOC) the maximum surface temperature appears much closer to the land-ocean margin than when hydrology is allowed. The displacement poleward of the region of maximum temperature when hydrology is included is due to the effect of groundwater accumulation and subsequent enhanced evaporation in the region of maximum precipitation. The magnitude and phase of the maxima appear little changed between the two cases.

An important feature of the MOC surface temperature structure is the rapid variation near and to the north of the continental margin of the Northern

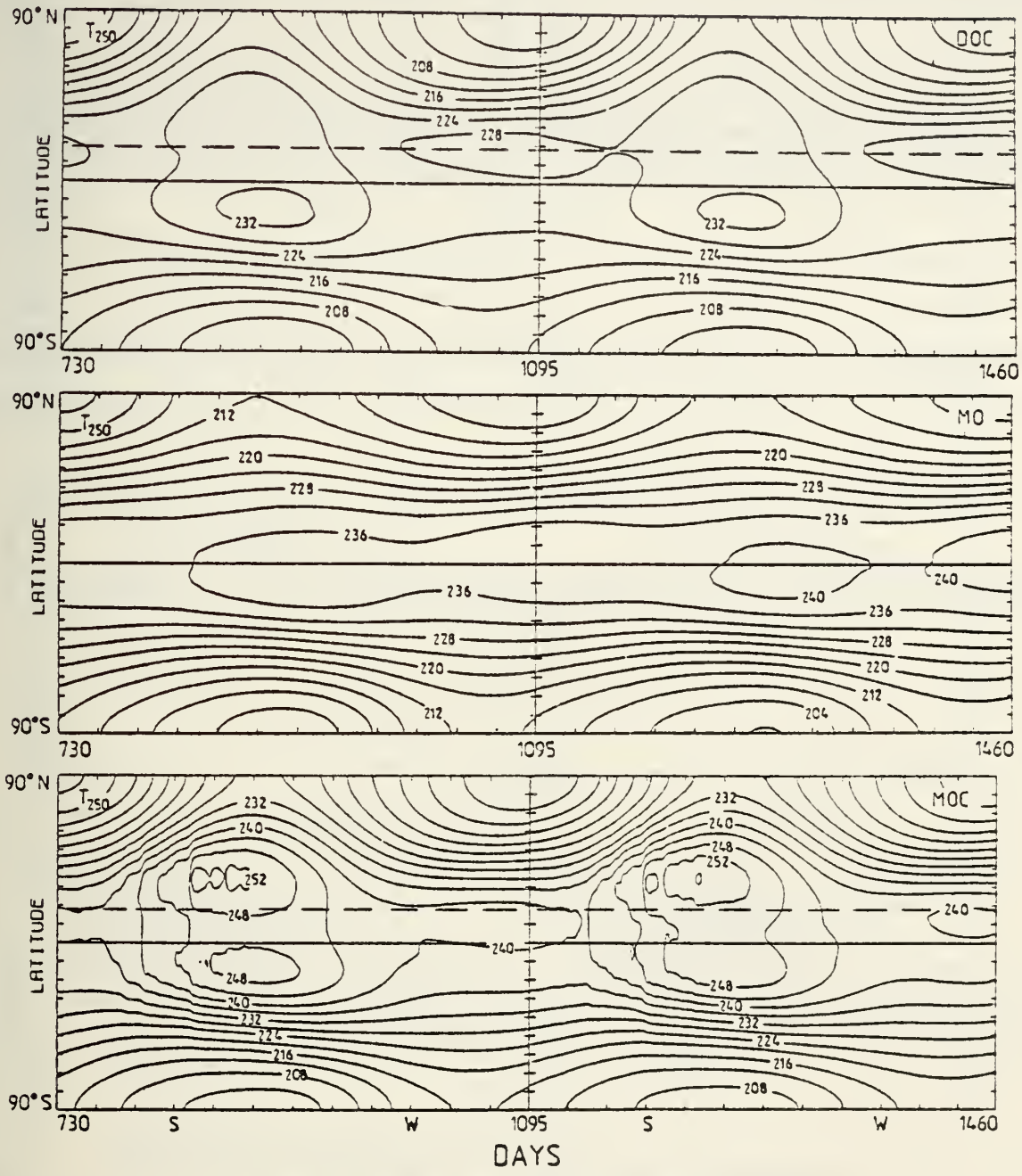

FIG. 5. As in Fig. 4 except for the 250 mb temperature field component.

Hemisphere during summer. Such variability is absent in both the MO and DOC experiments indicating that the modulations are associated with the hydrology cycle and the heated land mass. The variability has a fairly reproducible period of ~12–15 days and is reflected in an organized manner through the other variables of the model (see Figs. 5–10, especially Fig. 8).

The surface temperature for year 4 shows similar broad-scale features to year 3. Only the details of the summer modulations are different. Whereas the period of the modulation appears reproducible from year to year, its basic structure is different in detail which is perhaps indicative of the interaction of highly nonlinear processes existing within the model.

The effect of hydrology and continentality is best seen in the plots of the upper troposphere temperature (Fig. 5) and the 250 mb zonal wind (Fig. 6). With oceans and hydrology (MO), the upper

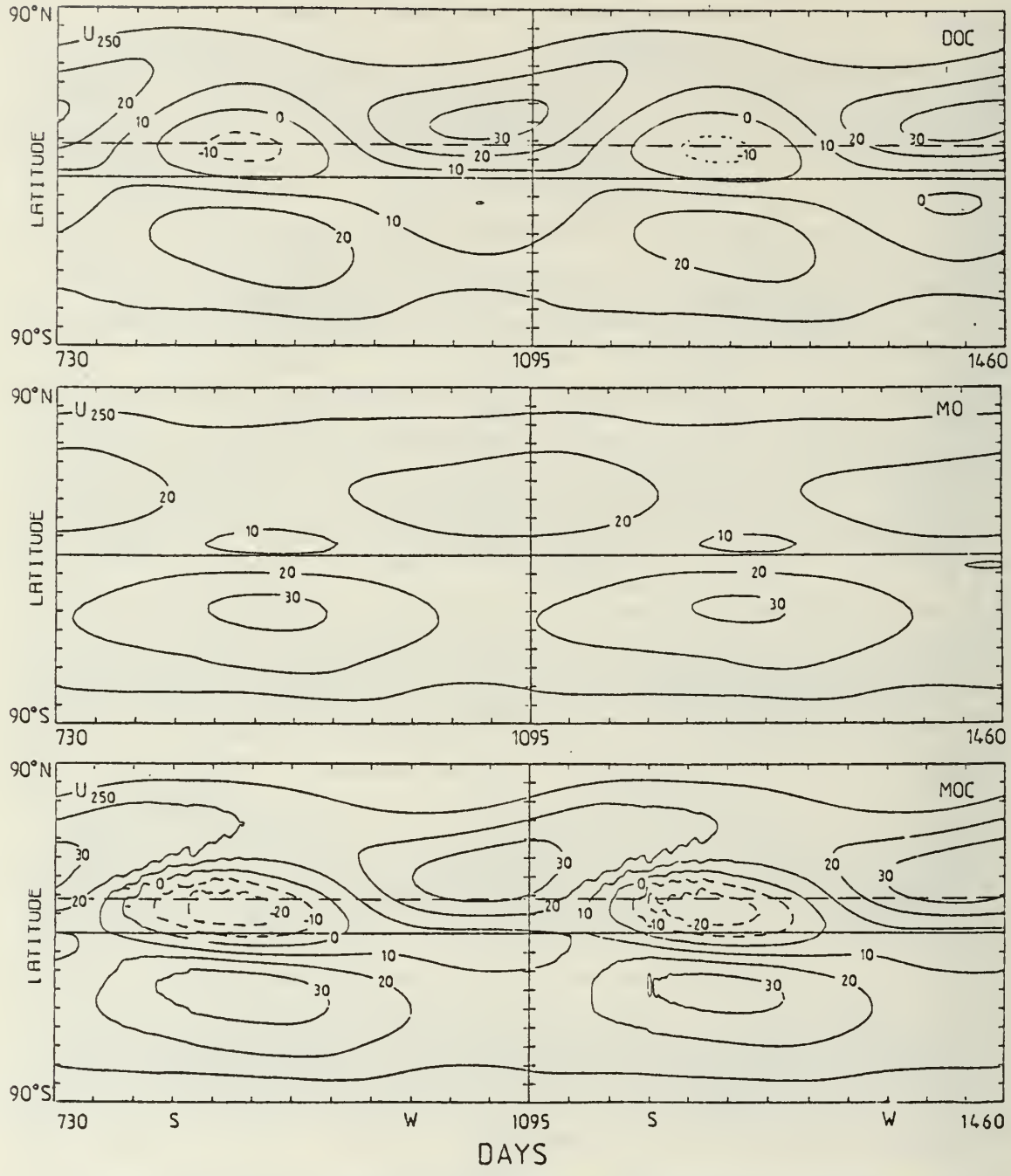

FIG. 6. As in Fig. 4 except for the 250 mb zonal wind component. Dashed lines denote easterlies. Units are m s^{-1} and contour spacing every 10 m s^{-1}.

tropospheric temperatures show an even seasonal variation, symmetric about the equator. With a continental cap but no hydrology (DOC) asymmetries are introduced into the structure with warmest regions coincident with maximum subsidence to the south of the equator in late summer. A secondary maximum occurs over the continent and corresponds to enhanced sensible heating. With both hydrology and continentality (MOC) the magnitude of the two maxima are increased substantially due to the increase in latent heating over the land and the increased subsidence in the winter hemisphere. It is interesting to note that the regions of maximum temperature in the MOC case are to the north of the strong ascent and correspond to significant subsidence in contrast to the DOC case. This agrees with the vertical velocity distribution over real deserts and suggests that desert regions

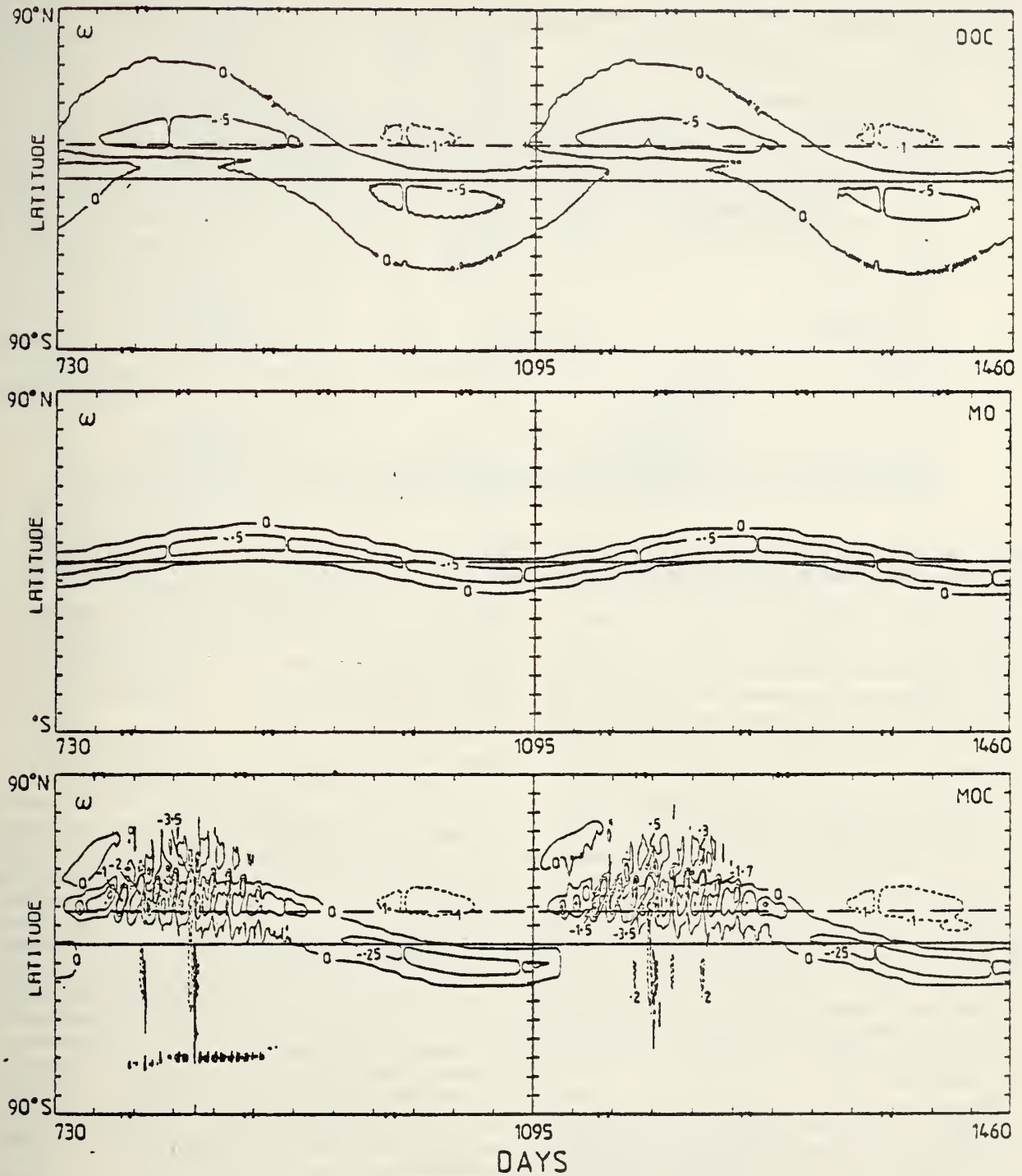

FIG. 7. As in Fig. 4 except for the 500 mb vertical velocity component (10^{-4} mb s^{-1}).

cannot be considered as isolated regions but are dynamically coupled to intensive moist-convective regions. A connection between the desert regions to the west of the Arabian Sea and the Bay of Bengal during summer was hinted at by Stephens and Webster (1979).

A most important effect occurs in the modification of the near-equatorial temperature gradient. In the MO case, the latent heating being relatively weak and fairly close to the equator, the low-latitude temperature gradient is rather flat. Consequently, the upper tropospheric winds (Fig. 5) show

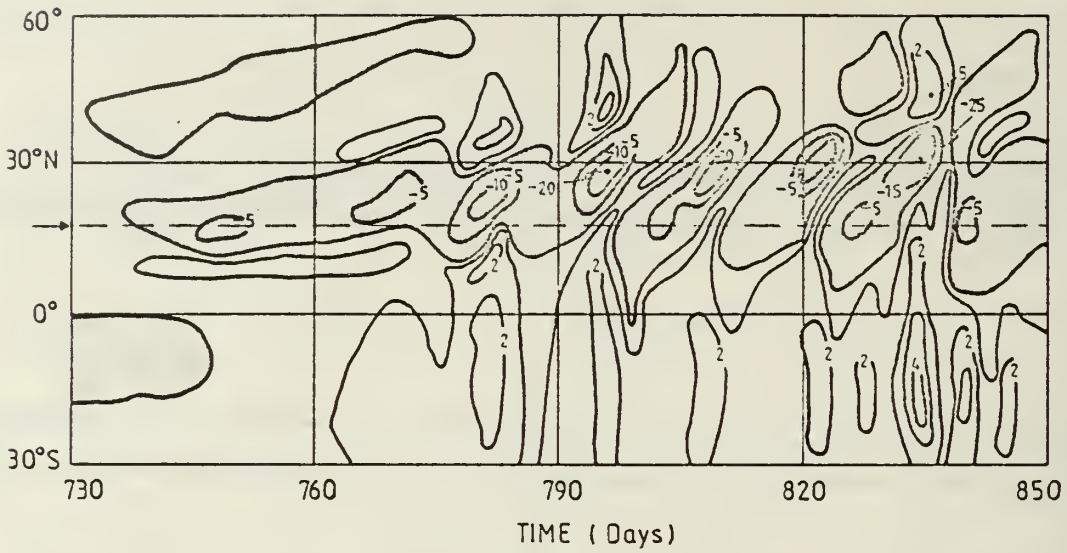

FIG. 8. Detail of the MOC ω field (500 mb) shown in Fig. 7 from day 730 to day 850 between 30°S and 60°N. Units are mb $s^{-1} \times 10^{-4}$. Shaded area denotes ascent.

only a relative westerly minimum. The double temperature maximum of the DOC case results in a reversed temperature gradient at low latitudes producing a weak easterly jet stream in summer to the south of the continental margin. The reverse is emphasized in the MOC experiment by the convective heating and a considerably stronger easterly jet stream is produced. Comparing Fig. 5 with the observed distribution of Fig. 1 shows the magnitude and phase of the seasonal variation of the zonal winds.

The low-frequency transients noted in Fig. 4 are also apparent in the upper troposphere temperature and zonal velocity fields shown in Figs. 5 and 6 for the MOC case. Such vertical consistency between the various variables is to be expected as in the convectively unstable regions the hydrologic cycle accomplishes a rapid and vigorous link between the lower and upper troposphere. Because of the absence of the modulations in either the MO or DOC experiments it is clear that the driving mechanisms result from interactions between the hydrologic cycle and continentality, the latter emphasized by the interactive ocean.

The vertical velocity fields are shown in Fig. 7 and keenly indicate the effects of hydrology and continentality. As expected from the monthly variation of the vertical velocity for the moist ocean, the maximum ascending motion is contained to near the equator in a narrow band which appears in phase with the maximum sea surface temperature. The dry ocean-continent experiment possesses a much more varied vertical velocity field. Fairly rapid latitude changes of the maximum occur in early summer coupled with the rapid heating of the continent (see Fig. 4) followed by a slower transition to the Southern Hemisphere during winter. The most striking differences between the MOC and DOC cases is the intensity of the vertical circulation produced by the release of latent heat and the variability of the circulation during the summer period. Furthermore, the "onset" and "retreat" of the monsoon appear more sudden in the MOC case than the gradual transition or slow meander which occurred in the DOC case.

To illustrate the subseasonal structure apparent in the MOC vertical velocity field during summer and to present a simpler picture, a detail of Fig. 7 is shown in Fig. 8. Plotted for only 120 days and commencing at the spring equinox of year 3 of integration, the diagram shows the evolving vertical velocity field between 30°S and 60°N. In the period immediately following the spring equinox, the maximum rising motion is to the south of the equator. Near Day 740, three weak vertical velocity maxima occur with the emergence of ascent near the coastal margin and near 40°N. With increasing insolation and the consequent rapid heating of the continent the rising motion increases at the expense of the Southern Hemisphere circulation. Further intensified by the increased flux of moisture from the ocean, the continental region of ascent finally quenches the southern maxima by increased subsidence.

The most interesting episodes occur even later in summer when period intensification of the circulation occurs. From Day 780 onward, the meridional circulation, as indicated by the vertical velocity distribution, shows periods of intensification some 12–15 days apart. While intensifying the meridional cell appears to propagate poleward from the coastal margin, reaching a maximum intensity usually between 15–20 mb s^{-1} (i.e., ~150 mb day^{-1} or 20

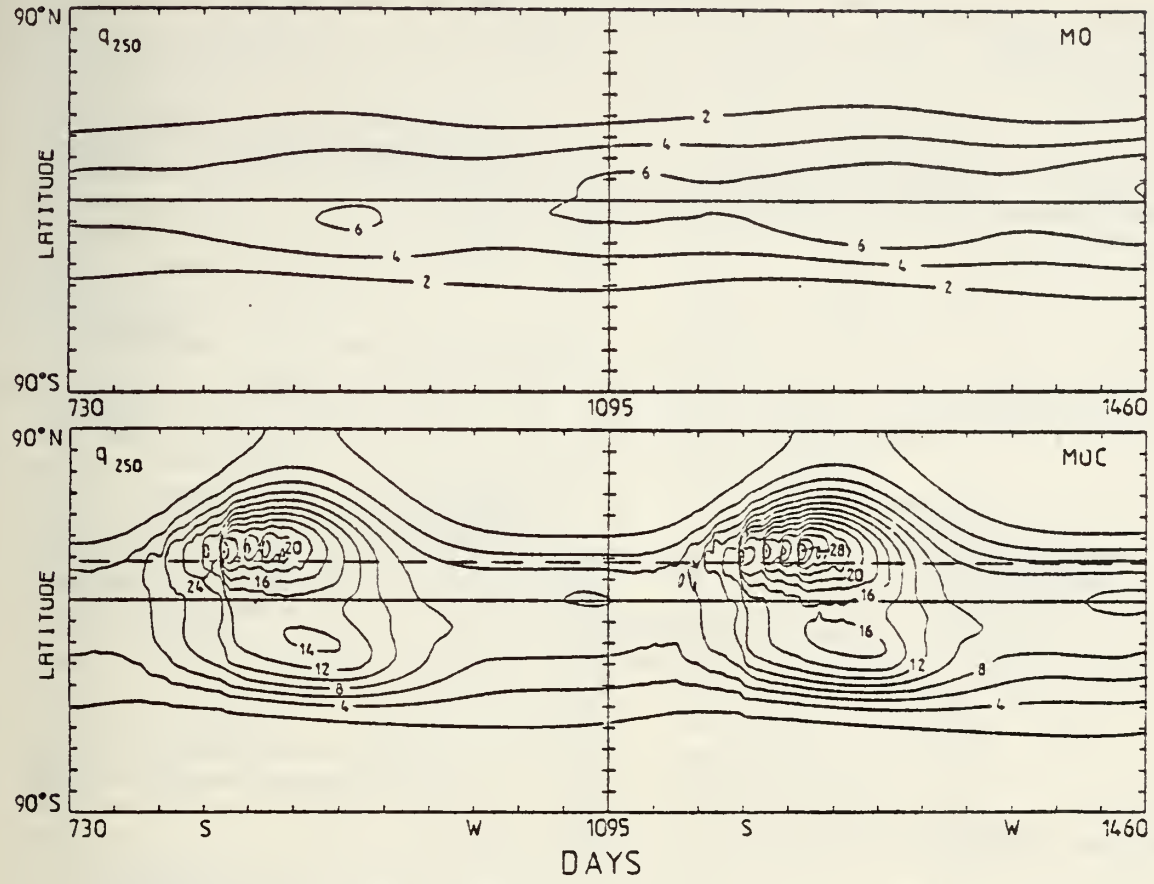

FIG. 9. as in Fig. 4 except for the 250 mb specific humidity fields. A scale factor of 10^4 has been applied.

cm s^{-1}) with considerable subsidence to the north and south. Rapid decay ensues, accompanied by the formation of a second cell. In turn the second cell intensifies, moves poleward and becomes the dominant circulation.

Such a sequence is repeated perhaps five or six times per simulated summer. In the next year (year 4) a similar periodicity of events occurred although with different timing, detailed position and intensity. The mechanisms which are responsible for the variations are related to a complex interaction between the hydrology cycle over the heated land mass and the effect of the ocean to the south. A detailed description of the mechanisms will be presented in a companion paper. It suffices here to note that the variations of Figs. 7 and 8 are coherent features of the model monsoons and are reproducible, at least in form, from one year to the next and possess many characteristics of the variation noted by Krishnamurti and Bhalme (1976) and Murakami (1977).[5]

The 250 mb moisture fields are shown in Fig. 9 for the MO and MOC cases. Following from the strong temperature dependency of specific humidity, some similarity exists between the form of the q fields and the temperature at 250 mb shown in Fig. 4 including the submonthly variability. The variations follow from the efficient upward transport of moisture by the convective processes described in WC. As the convective processes strongly correlate with the vertical velocity distribution and hence the release of latent heat, regions of maximum temperature and maximum specific humidity will correlate on the time scale of the submonthly variation (cf. Figs. 4 and 9).

Fig. 10 shows the precipitation fields for the MO and MOC cases. Except for the regions where the moisture has converged in the upper troposphere, the precipitation fields follow the vertical velocity

[5] We have recently become aware of a detailed observational circulation study by Sikka and Gadgil ("On the maximum cloud zone and the ITCZ over Indian longitudes during the Southwest Monsoon", Report 79 FM7, Indian Institute of Science, Bangalore, India May 1979) aimed specifically at low-frequency transients of the southwest monsoon. Sikka and Gadgil emphasize the establishment of the continental precipitation following breaks by ". . . northward moving epochs of the oceanic ITCZ. . . ." Similar time scales are indicated.

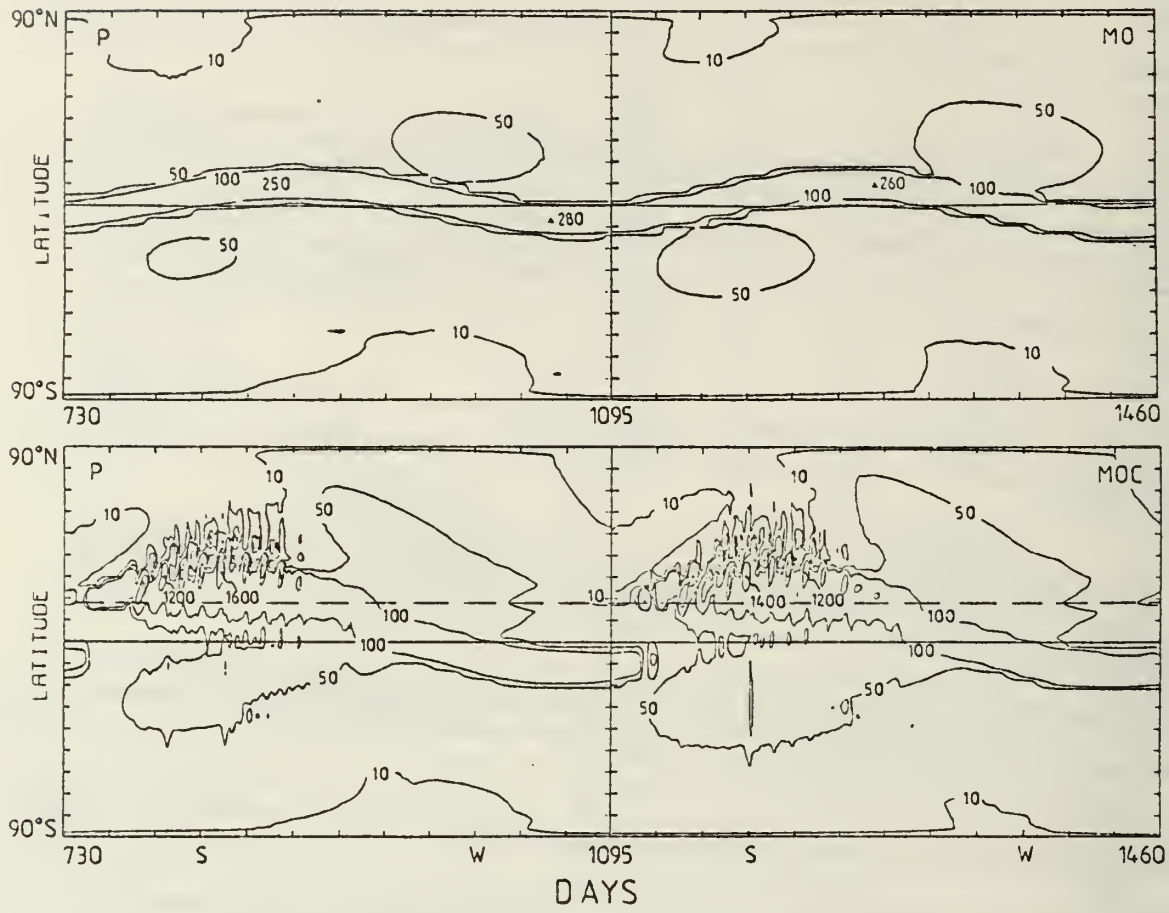

FIG. 10. Same as in Fig. 4 but for the precipitation rate fields. Units are cm day^{-1} and contours are drawn for precipitation rates of 10, 50, 100, 500 and 1000 cm year^{-1}.

as might be expected from the convective parameterization schemes. The light precipitation in the subsident subtropical regions of the winter hemisphere is probably an artifact of the neglect of eddies within the model. Without eddy transport, moisture tends to converge in regions of maximum meridional cell subsidence. Eddies, on the other hand, may move moisture most efficiently further poleward and possibly cause a second precipitation maximum. Even so, precipitation within the tropical regions follows observations quite well. For example, the MOC case estimates total annual precipitation between 22 and 31°N to be ~130 cm which is similar to the rainfall on the Gangetic Plains.

5. Concluding remarks

A hypothesis which postulated that low-frequency sub-seasonal modulations or transients may result from the interaction of hydrological processes and the basic dynamic elements of a monsoon was tested. The minimal components of a monsoon system were derived by WL to include an interactive ocean to the south of an "Asian" continental cap. The tool chosen to test the hypothesis was a relatively simple ocean-atmosphere interaction model which was compiled to allow a tractable analysis. The aim of the analysis was the identification and relegation of the various driving mechanisms of the monsoon. The study was prompted by a number of observational studies, most notably Krishnamurti and Bhalme (1976) and M. Murakami (1977), who noted large-scale and low-frequency modulations of the monsoon system.

The evolution of the mean monthly structure (Figs. 2 and 3) for the MO and MOC cases indicate, by comparison, the interactive nature of the hydrologic cycle and the basic drive of the monsoon system. For example, in the MO experiment (Fig. 3a) the strong interaction between the ocean and the atmosphere is indicated by three-month phase lag behind the solar heating of the vertical velocity variation, thus following closely the sea surface temperature variation. The lag is reminiscent of the behavior of the near-equatorial troughs or intertropical convergence zones of the western

Pacific Ocean and underlines the importance of local moisture availability or evaporation from a warm ocean surface. With greater surface heating coupled with the availability of moisture from the wet continental region, considerable variability is added to the system (Fig. 3b). During the winter, the system maintains the same phase lag as the oceanic case. However, during spring the ascending motion rapidly advances its northward propagation to become in phase with solar insolation over the continental region. The result is an extremely rapid "onset" and a somewhat retarded "retreat."

The interplay of the heated land mass and the hydrology cycle appears most pronounced in the latitude-time sections shown in Figs. 3–10. Only the cases which possess both a hydrology cycle and an ocean-continent contrast appear capable of temporal variations which are of a time scale less than seasonal. Fig. 8 is particularly pertinent and shows two major transition types which apparently depend on the interplay. These are the rapid "onset" of the monsoon in late spring and the variability of the established monsoon itself. The latter variation shows a coherent transition between periods of strong ascent and subsidence as the ascending branch of the Hadley cell propagates northwards. Although the details of the mechanisms which cause the monsoon modulation warrant a separate study and consequently will be reported in a companion paper, it should be noted that the periods of intermittent activity and the lulls in between occur as low-frequency transients similar to those reported by Krishnamurti and Bhalme (1976) and Murakami (1977). In a simple sense, the modulations appear to be similar to the active-break cycle of Koteswaram and Rao (1963); the active period corresponding to vertical motion just to the north of the coastal margin and the break period following the propagation of the cell northward when strong subsidence exists near the coastal margin. Despite the similarity it would probably be excessive to speculate that the model utilized in this study contains all the physical ingredients of what must be a very complicated system. On the other hand, what is apparent is that some of the basic mechanisms which contribute to the large-scale modulation of the monsoon system must be included in the model. A vital test would be the extension of the model to allow longitudinal variability in the manner of WL.

It is interesting (although difficult) to compare the results of this study with the careful experiments of Hahn and Manabe (1975). Granted that the model, even with its interactive ocean, is significantly simpler than that of Hahn and Manabe, the time scales of transitions of the monsoon system appear to be consistent with their experiments which *included* mountains. This is a surprising result as Hahn and Manabe found that without orography, the transitions of the monsoon system were significantly slower, especially the onset of the monsoon. It should be noted that the fields presented in the last section were somewhat weaker than those found by Hahn and Manabe and whether this is due to the neglect of eddies or omission of the Himalayas is difficult to determine at this stage. Perhaps the most important result of the study is the indication that the monsoon system possesses low-frequency transients without the modification of the latent and sensible heating which would be introduced by orography. Nor is this supposition without some observational support as both the West African and the North Australian monsoon systems, both substantially removed from substantial orographic features, are characterized by low-frequency modulation.

It should be emphasized that clouds were held constant in the experiment so that a potentially strong feedback mechanism was omitted. It is difficult to know what modification the effects of an evolving cloud field would have had on the fields displayed in Figs. 4–10. However, as cloudiness appears as an important modifier of the local radiation budget its effect on the monsoon system would probably be significant. Thus the incorporation of cloud into the model is the next logical step. To include cloud variability a more sophisticated radiation model [such as that developed by Stephens and Webster (1979)] is necessary, plus consistent parameterization of cloud formation, maintenance and decay. At the same time, the findings of Hahn and Manabe insist that orography be included in the system. Consequently, the present paper should be considered as just one part of an ongoing research programme aimed at investigating monsoon dynamics using the "aggregate" philosophy. An ultimate aim is the establishment of a multi-domain version of the WL domain-averaged model so constructed as to produce a useful tool for the study of the total monsoon system and the interaction of the Asian, Australasian and African components.

Acknowledgments. Thanks are due to Dr. G. L. Stephens and Mr. B. G. Hunt for interesting discussions and suggestions regarding the final manuscript.

REFERENCES

Asnani, G. C., 1967: Meridional circulation in the summer monsoon in South-east Asia. *Nature*, 214, 73–74.

Hahn, D. G., and Manabe, S. 1975: The role of mountains in the South-Asian monsoon circulation. *J. Atmos. Sci.*, 32, 1515–1541.

Halley, E., 1686: An historical account of the trade winds and monsoons observable in the seas between and near the tropics with an attempt to assign a physical cause of the said winds. *Phil. Trans. Roy. Soc. London*, 16, 153–168.

Koteswaram, P., and N. S. B. Rao, 1963: The structure of the Asian summer monsoon. *Aust. Meteor. Mag.*, 42, 35–36.

Krishnamurti, T. S., and H. H. Bhalme, 1976: Oscillation of a monsoon system, Part 1: Observational aspects. *J. Atmos. Sci.*, 33, 1937–1954.

Lau, Ka Ming W., 1978: Experiment with a simple ocean-atmosphere climate model: The role of the ocean in the global climate. *J. Atmos. Sci.*, 35, 1144–1163.

Murakami, M., 1977: Spectrum analysis relevant to Indian monsoon. *Pure Appl. Geophys.*, 115, 1149–1166.

Ramage, C., 1971: *Monsoon Meteorology*. Academic Press, 296 pp.

——, and C. V. R. Raman, 1972: *Meteorological Atlas of the International Indian Ocean Expedition*, Vol. 2. National Science Foundation, Washington D.C. [Superintendent of Documents, Washington, DC, Stock No. 3800-00124].

Sadler, J. C., 1975: The upper tropospheric circulation over the global tropics. Rep. UHMET 75-05, Department of Meteorology, University of Honolulu, 35 pp.

Stephens, G. L., and P. J. Webster, 1979: Sensitivity of radiative forcing to variable cloud and moisture. *J. Atmos. Sci.*, 36, 1542–1556.

Washington, W. M., and S. M. Daggapaty, 1975: Numerical simulation with the NCAR general circulation model of the mean conditions during the Asian-African summer monsoon. *Mon. Wea. Rev.*, 103, 105–114.

Webster, P. J., 1972: Response of the tropical atmosphere to local steady forcing. *Mon. Wea. Rev.*, 100, 518–541.

——, 1973: Temporal variation of the low-latitude zonal circulation. *Mon. Wea. Rev.*, 101, 803–816.

——, 1979: A model of the seasonally varying planetary scale monsoon. *Dynamics of Monsoons*, R. Pearce and J. Lighthill, Eds., Cambridge University Press, (in press).

——, and K. M. W. Lau, 1977: A simple ocean-atmosphere climate model: Basic model and a simple experiment. *J. Atmos. Sci.*, 34, 1063–1084.

——, and L.. C. Chou, 1980: Seasonal structure of a simple monsoon structure. *J. Atmos. Sci.*, 37, 354–367.

Tropical Upper-Tropospheric Extended Clouds: Inferences from Winter MONEX

PETER J. WEBSTER AND GRAEME L. STEPHENS

CSIRO Division of Atmospheric Physics, Aspendale, Victoria, Australia.

(Manuscript received 5 March 1979, in final form 7 April 1980)

ABSTRACT

The most common cloud species observed during the Winter Monsoon Experiment (WMONEX) was thick (optically black) middle and upper tropospheric extended cloud. Data from the Geostationary Meteorological Satellite (GMS) showed the extended cloud to occupy half the near-equatorial South China Sea and Indonesia on some days with tops in the vicinity of the 200 mb level. Detailed observations from the WMONEX composite observing array indicated that the clouds extended up to 750 km from the convective source regions, possessed bases in the vicinity of the freezing level and lay above a generally suppressed and subsident lower troposphere. The observation of widespread precipitation from the extended cloud and the encountering of ice particles during the cloud penetrations suggest that the extended clouds are active in a diabatic heating sense.

Calculations using a radiative transfer model and cloud and atmospheric states derived from WMONEX data indicate substantial net heating at the base of the cloud ($\sim$20 K day^{-1}) and cooling at the top (-5 to -15 K day^{-1}), resulting in a heating rate differential between the base and top of the cloud of up to 35 K day^{-1}. Net heating or cooling occurs depending upon the diurnal cycle. It is conjectured that the effect of the radiative heating is to destabilize the cloud layer. As the magnitude of the radiative *heating* at the base of the cloud is at least within a factor of 2 of estimates of the *cooling* at the cloud base due to melting for moderate disturbances and relatively greater for weak disturbances or in locations well removed from the convective source in any disturbance, it is argued that radiative effects cannot be ignored in the calculation of the total diabatic heating fields in tropical cloud systems.

1. Introduction

The realization that there exist unique phenomena in the low latitudes and that such phenomena exert a profound influence on processes at higher latitudes has substantially increased interest in the meteorology of the tropical regions during the last two decades. During this period, a number of key problems associated with basic modeling have received considerable emphasis. The most notable is the consideration of convective processes and the general problem of scale interaction between subgrid-scale processes and those of larger scale. So important are the convective transports in the tropics that most effort appears to have focussed on their parameterization. In most parameterizations the cloud, or cluster of clouds, is treated as a one-dimensional entity and the transports related to the larger scale (prognostic) fields. The parameterizations consider diabatic processes but lend emphasis to latent heat release usually at the expense of other heating fields such as radiation. Further, the residual effects of the cloud clusters (middle and upper tropospheric extended clouds[1]) are generally ignored, even though the area they cover is perhaps an order of magnitude larger than the convective region itself. Possibly the principal reason for this neglect has been that such cloud decks have been assumed passive from a diabatic heating viewpoint.

Contrary evidence has emerged from the GARP Atlantic Tropical Experiment (GATE) and even earlier from the Line Islands Experiment. Extended middle and upper level cloud decks were found to be *strongly active* as both a radiative and latent heating source. For example, Albretcht and Cox (1975) and Cox and Griffith (1979) showed explicitly that upper level extended clouds interact strongly with and are instrumental in determining the local radiative field. That strong variations in radiative heating occur in both longitude and latitude was discussed in the theoretical study of Stephens and Webster (1979). They also showed that middle and upper cloud substantially influenced the character of the net radiative flux divergence in a manner which keenly depended on the cloud type and

[1] We use here the term middle and upper level extended cloud to avoid confusion with the proper term "stratus" or the more restrictive term "anvil." The former has come to refer commonly to low-level cloud whereas the latter refers to the outgrowth of convection in the vicinity of the convective source. As we will refer later to middle and upper level cloud removed hundreds of kilometers from the source region, we choose a more general term.

0022-4928/80/071521-21$09.25

height, as well as the latitude of the cloud deck. The potential for strong radiative-convective-dynamic coupling was hinted at by Stephens and Wilson (1980) who illustrated distinct sensitivity of convective parameterizations to the radiative heating profiles chosen. In summary, a large number of studies point toward substantial variations in both the magnitude and scale of the radiative heating function. Rather than the weak and fairly constant heating profile suggested by Dopplick (1972), the picture which has emerged is of a strong function varying rapidly in space with magnitudes in disturbed regions which are similar to the heating rates traditionally ascribed to latent heating functions. Radiative properties which refer particularly to extended clouds in the WMONEX region will be discussed in Section 4.

If the radiative arguments are sound, observations made during the Winter Monsoon Experiment (WMONEX) would suggest an important role for upper and middle tropospheric extended clouds in determining the radiative budget of the equatorial region. For long periods of December 1978 (Phase 1 of WMONEX) in the South China Sea–Indonesian region thick (optically black) altostratus and cirrostratus appeared as the predominant cloud species and extended hundreds of kilometers from convective source regions. Sources of the extended cloud could usually be traced to either synoptic-scale disturbances or to the considerable diurnal activity associated with the large islands of Indonesia. Regions of precipitation from the extended cloud decks were commonly observed.

Earlier field experiments in the western Pacific found considerable variability in the structure of disturbances and associated cloud fields (Malkus and Riehl, 1964). Of particular interest were the vast regions of upper level extended cloud, areas of which were observed to precipitate. Whereas it was generally assumed such cloud originated from convective debris, the observation of precipitation in the generally subsident and divergent "exterior" portion of the disturbance was surprising. Acknowledging this observation, the "Tropical Whole Sky Code" was developed to allow a detailed cataloging of the tropical atmosphere and substantial precipitation from the ". . . upper sheet . . ." is taken into account in classifications 13–16 (Malkus and Riehl, 1964) as typical of the disturbed tropical atmosphere.

Beyond the Malkus and Riehl study and the occasional reference in early observational, operationally oriented reports or manuals, the existence of stratiform precipitation in the tropics received scant attention in the literature. With the Line Islands Experiment and GATE a number of pertinent studies emerged. Most notable are those of Zipser (1977) and Houze (1977) who noted considerable anvil precipitation in propagating squall lines. Houze estimated that 40% of the total precipitation of the disturbance emanated from the anvil. Later work (Leary and Houze, 1979) suggested a complicated substructure of heating and cooling in the vertical relating to hydrometeor phase changes within the anvil. They suggested that substantial cooling due to *melting* at the base of the anvil accounted for cooling rates of the order of 1–7 K h^{-1} and cooling due to evaporation of water droplets *below* the anvil to be of the order of 0.2–6 K h^{-1} which cumulatively resulted in subsidence in the lower troposphere. As there was precipitation, a net heating was assumed in the main body of the anvil resulting in mean ascent. Horizontal inflow from the convective source near the melting layer satisfied the mass continuity constraints. *In all studies, including a numerical simulation by Brown (1979), radiative effects are not considered or are ignored.*

As the GATE studies of Zipser (1977), Leary and Houze (1979), and Houze (1977) are perhaps the best-documented tropical disturbance case studies, they will serve as useful base references for the present investigation. As such it is important to question whether or not the GATE disturbances are comparable with the WMONEX disturbances. Some differences in space and time scales seem apparent. The GATE squall lines were propagating phenomena with lifetimes of hours and horizontal scales [defined by the radar determined precipitation zone (Leary and Houze, 1979)] were between 100 and 200 km. In comparison, the WMONEX disturbances appeared to possess lifetimes of days and to possess horizontal scales (defined by the extent of the cloud canopy from satellite observation) in excess of 600 km from the convective centers. The systems are similar in that they possessed convective source regions and extensive middle and upper cloud systems which resembled nimbostratus. Detailed comparisons between the disturbances of the two regions must really await the analysis of the WMONEX radar data as it is radar which has formed the basics of the GATE analyses.

In summary, a number of questions arise:

1) What is the source of the extended middle and upper level cloud? Are the decks merely upper tropospheric debris from cloud clusters or are the middle level extended cloud systems developed independently of the cumulonimbus cloud?

2) What are the maintenance mechanisms of the extended cloud systems at distances well away from the convective source regions? Are the space and time (longevity) scales determined merely by the amount of cloud debris pumped into the middle and upper levels or are other processes involved in perpetuating and maintaining the extended cloud decks?

3) What is the distribution of total diabatic heat

ing associated with the cloud decks away from the convective sources and what is its influence on the state of the tropical atmosphere? Is the concept of strong radiative effects in the outflow region of convective systems compatible with the latent heating fields described by other workers?

The study has one further purpose. In the theoretical study of Stephens and Webster (1979), the potential climatic importance of extended cloud decks was discussed. The present paper may be thought of as one part of an ongoing study into the role of clouds in structures where dynamic and diabatic time scales are similar. Both climatic and low-latitude structures fall within this range.

In the following paragraphs, the WMONEX period will be referred to extensively. Whereas there are significant weaknesses in the data set for a study aimed at elucidating dynamic-cloud interactions, it does stand at the present time as a unique low-latitude ensemble. Even so, it would be foolish to suppose that the set is indicative of all low latitude regions; the South Asian-Indonesian region is unique from a meteorological viewpoint. Consequently, the paper should be considered as a discussion of tentative results and inferences from a pilot study aimed at establishing connections (if any) between the theory of Stephens and Webster (1979) and the reality of observed processes. Generalizations must await the establishment of a grander scheme; probably the completion of a cloud climatology based on remote sensing.

In the next section spatial scales of the upper level cloud will be identified as they existed during the entire period of WMONEX.

2. Cloud scales

From a radiative viewpoint, the depth, height and horizontal extent of the various cloud species are extremely important. Such information is critical in order to determine the three-dimensional distribution of the radiative state of the atmosphere and, consequently, the structure of the diabatic heating. In this section we will use the GMS (the Japanese Geostationary Meteorological Satellite which operates over 0°N, 140°E)[2] to establish the horizontal extent, the height of the cloud and to some extent its time scale. The data period corresponds to Phase 1 of WMONEX (i.e., December 1978).

The five-day mean cloud distributions for the area 90°E–170°W and 20°N–20°S are shown on Figs. 1a–1c. The upper panel of each diagram shows the *total* cloud in tenths and the lower panel the *upper* cloud. High cloud is defined as clouds which are cooler than the climatological ambient 400 mb temperature as sensed by the GMS. Regions of total cloud > 60% are stippled as are the upper level region where coverage exceeds 40%.

The total cloud fields show four major regimes. There are the equatorial maxima, the Northern Hemisphere maxima near 20°N and the two subtropical minima. The equatorial maximum extends across the domain and shows a bifurcation in the Central Pacific: the southern fork being associated with the South Pacific cloud band (Streten, 1973; Webster and Curtin, 1974). The bifurcation is also evident in the upper cloud amounts, most of which appear to be restricted to the equatorial region. In general, in the low latitudes total and upper level clouds possess strong positive correlation.

In the region of the WMONEX, the cloudiness distributions may be divided into two main categories. The first category occurs with the maximum cloudiness (total and upper) being concentrated in the near-equatorial Southern Hemisphere. Such periods were the 2–6 December, 22–26 December and 27–31 December 1978. Periods 12–16 and 17–21 December showed cloud maxima in the near equatorial Northern Hemisphere. The period 7–11 December possessed maxima in both hemispheres. Certain areas maintained maximum concentration of upper level clouds for successive 5-day periods. For example, the Java Sea region maintained upper level cloud coverage through three 5-day mean periods (e.g., 2–16 December) at > 60%. Similar persistence was observed along the near equatorial trough, especially in the region of the Southern Hemisphere Central Pacific cloud band and also northwest of Borneo in the South China Sea region during most periods.

Fig. 2 provides an indication of the cloud-top height of the distributions shown in the previous diagram (data obtained from JMSMR). Isopleths of the corresponding cloud top pressures are drawn for the three periods 2–06, 12–16 and 17–21 December 1979. Two major domains are apparent. In the equatorial regions, cloud top pressures are generally less than 200 mb, whereas further away from the equator cloud distributions rarely appear to penetrate the 700 mb level.

In summary, satellite data indicate that in the region of GMS coverage, middle-level extended cloud was a common and abundant species. Persistence of large coverage of the cloud in certain regions suggests that the cloud species are long-lived or are associated with persistent low latitude processes or phenomena. However despite some indications of the properties of low-latitude cloud cover the satellite observing platform cannot provide the *base level* of the extended clouds. All that is known is their geographic distribution and cloud-top height and that the clouds were optically black.

[2] In particular, data from the Monthly Report of the Meteorological Satellite Center, Tokyo, Japan, obtainable from Japanese Meteorology Service, Tokyo, Japan (referred to as JMSMR).

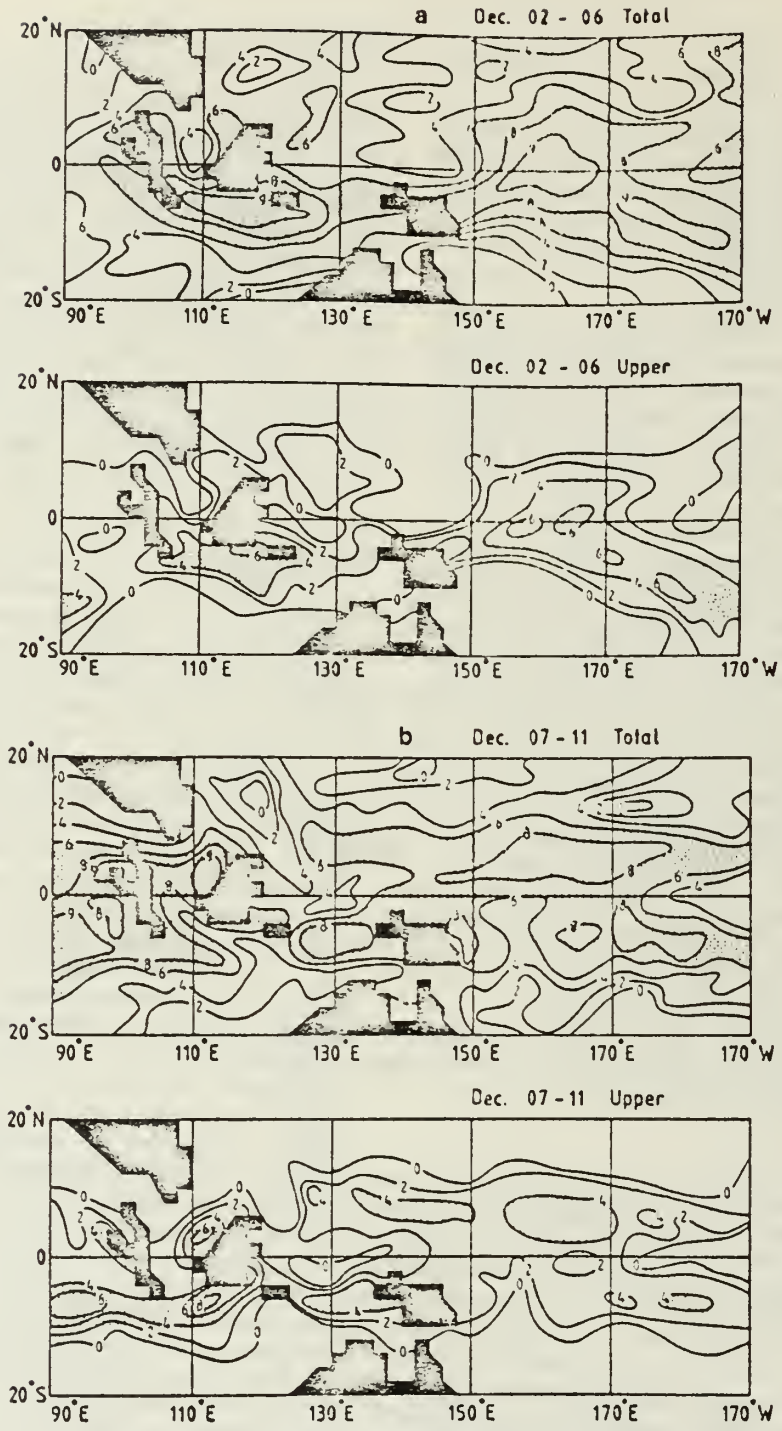

FIG. 1. Five-day average cloudiness distributions for total (upper panel) and upper (lower panel) cloud. Shaded areas denote > 0.6 total cloudiness or 0.4 upper cloudiness. Periods are (a) 2–6 December (b) 7–11 December (c) 12–16 December (d) 17–21 December (e) 22–26 December and (f) 27–31 December 1978 (units: tenths of cloud).

3. Observations

a. The WMONEX composite observing network

The composite observing array for Phase I of WMONEX (i.e., December 1978) contained five major components. These were an enhanced ob serving conventional network (both rawin and pibal), a number of special rawinradiosonde sta tions, a digitalized weather radar system, three research ships, and three dedicated research air

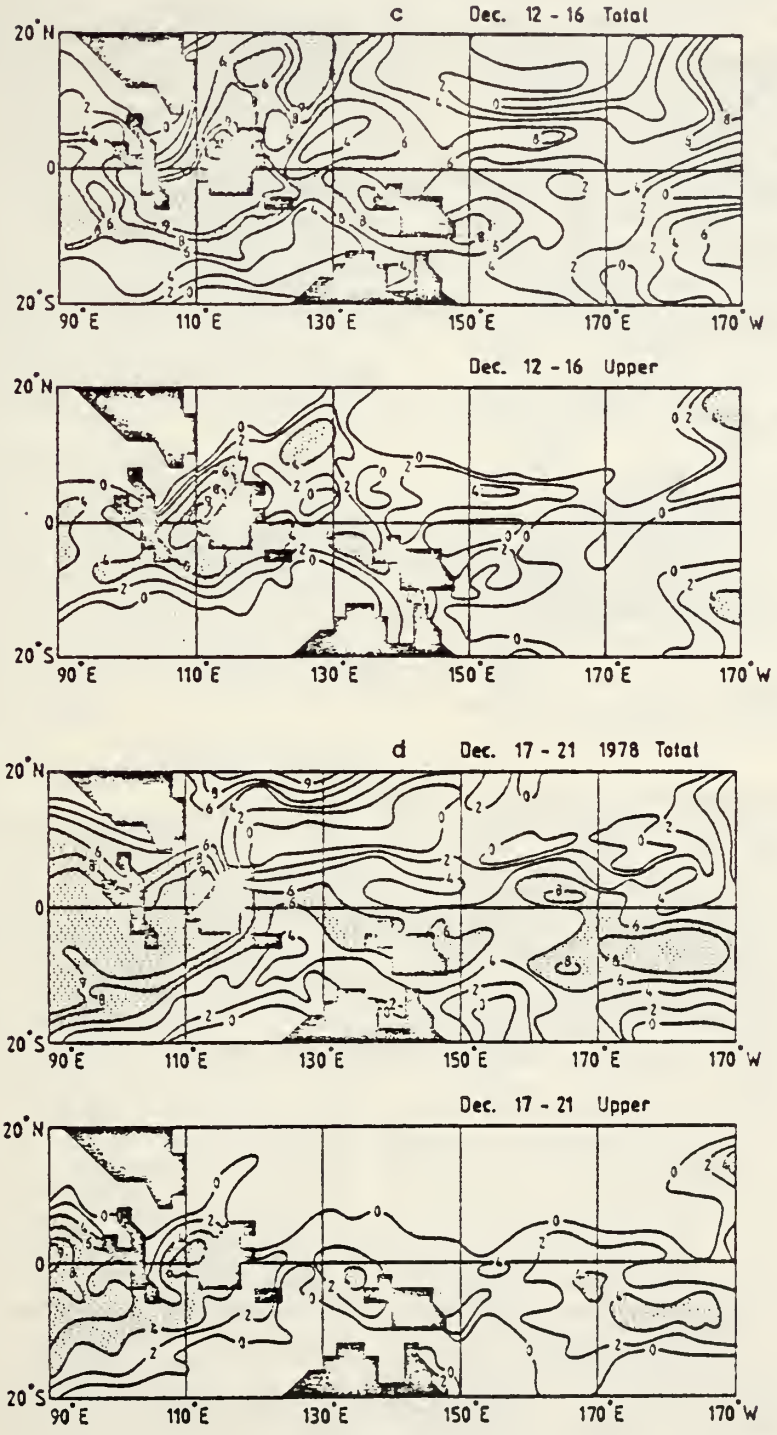

FIG. 1. (*Continued*)

craft. Of particular pertinence to this study are the two aircraft[3] which operated in the South China Sea out of Kuala Lumpur, Malaysia; the USA NOAA P-3 and the USA NCAR Electra, and the three USSR research ships located at 4°N, 111°E, 7°N, 111°E and 7°N, 109°E. Whenever possible, the two aircraft operated in the vicinity of the digital weather radar located at Bintulu, Sarawak. In addition, the GMS provided a periodic coverage of infrared and visible radiation fields as well as providing derived cloud vector winds.

[3] A third low-level aircraft provided by the Royal Hong Kong Observatory operated in the vicinity of Hong Kong.

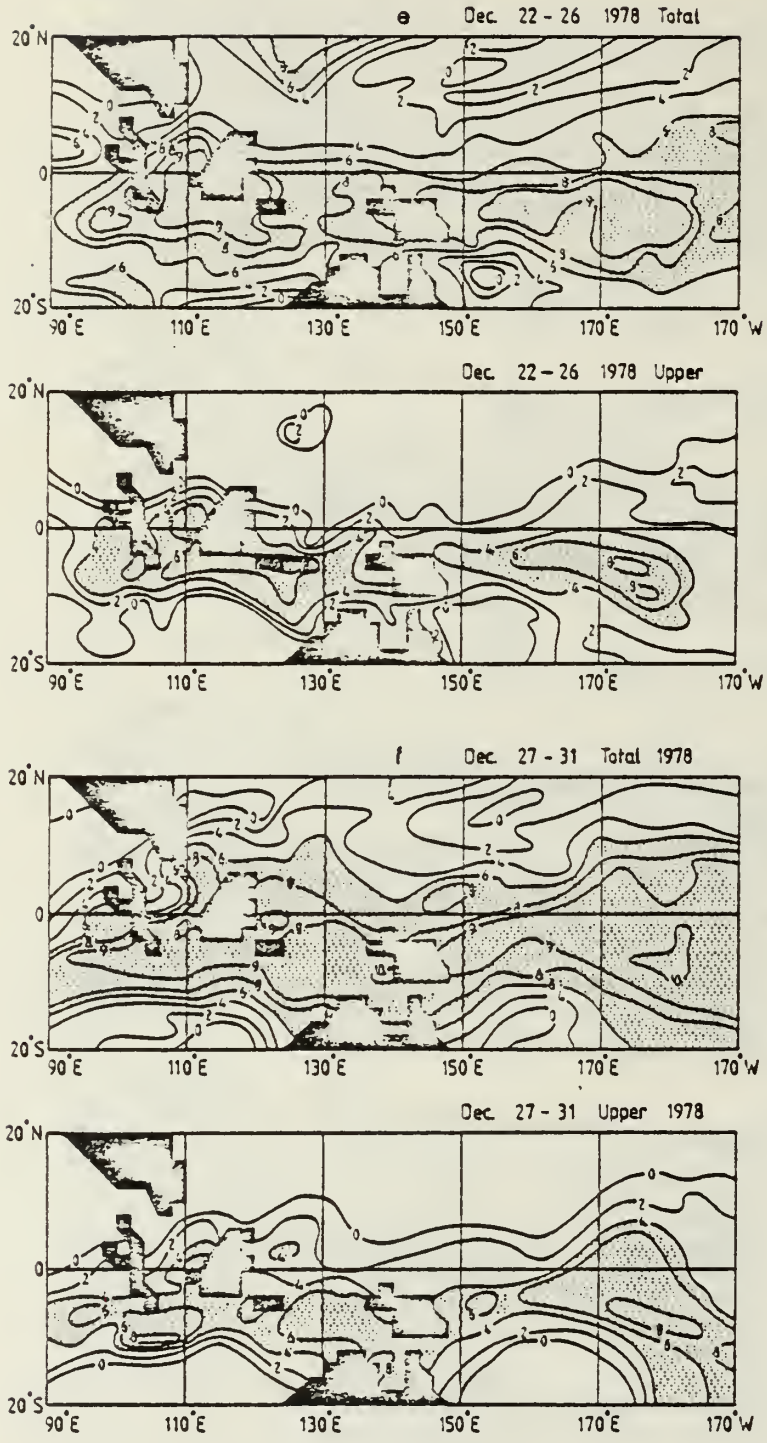

FIG. 1. (*Continued*)

For the purposes cited in the first section, a combination of the USSR radiosonde data, the aircraft data and the GMS photometry appears sufficient. The USSR ships provided observations every 6 h on a routine basis but every 3 h during a declared "intensive period." Consequently, the three ships provided a potential of excellent thermodynamic and dynamic coverage of the state of the South China Sea, immediately to the north of Kalimantan (Borneo). On the other hand, the GMS provided a wider overview of the region which, together with the land-based observations, allows the relationship between the USSR ship triangle and the ambient large-scale flow to be established. The

most important utility of the GMS is the provision of an effective radiating temperature structure of radiating surfaces from which estimates of the cloud-top heights of (optically thick) clouds can be determined. Thus the GMS is capable of determining *the extent, duration and top height* of the cloud. However, it provides no information regarding the thickness of the cloud or the height of its bottom. Fortunately, the structure of the lower part of the middle and upper tropospheric extended cloud decks were often obtainable from the research aircraft. Although neither the P3 nor the Electra carried dedicated radiation equipment, they operated (in the dropsonde mode) in the 500–400 mb range.

In summary, a combination of ship, aircraft and satellite data collected during WMONEX appears capable of providing an estimate of the four-dimensional structure of the extended clouds together with the evolving thermodynamic and dynamic structure of the atmosphere. However, as the aircraft were often deployed in other modes (e.g., low-level boundary layer missions as distinct from dropsonde flights) estimates of cloud base were only available on certain days.

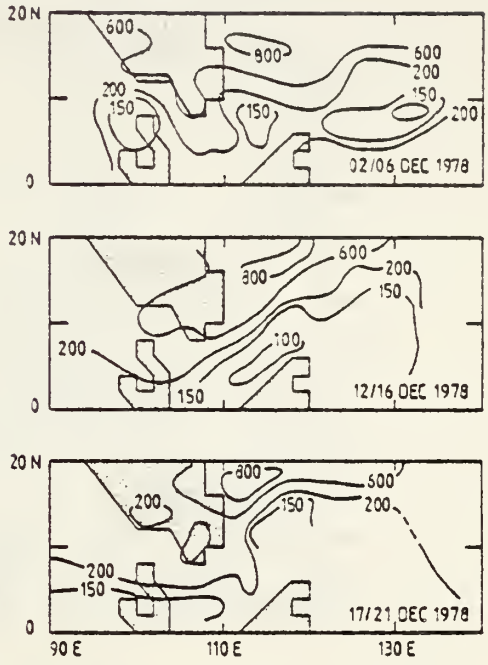

FIG. 2. Isopleths of cloud-top heights for the periods 2–6, 12–16 and 17–21 December 1978 (units: mb).

b. Structure during Phase I of WMONEX

A summary of the mean cloud structure during Phase I of WMONEX was presented in Fig. 1. The cloud distributions will now be related to the corresponding atmospheric structure using the serial atmospheric soundings from the USSR ships. For a detailed summary of the atmospheric state during WMONEX the reader is referred to the quick-look data set; in particular Sadler (1979).[4]

In a loose classification based on the location of the near-equatorial trough(s) to the west of 130°E, WMONEX may be divided into three major periods: 1–14 December, 15–22 December and 23–31 December. During the first period the equatorial trough resided for the most part in the Southern Hemisphere to the south of the main observing network in the South China Sea. Consequently, the disturbed regions were mostly to the south of Kalimantan in the Java Sea region. Although the 5-day periods of Fig. 1 do not precisely correspond to the first period (i.e., 1–14 December) the locus of the belt of extended upper level cloud may be seen to lie roughly along 5–10°S. Over the South China Sea, the area of upper level cloud northwest of Sarawak and Sabah appears more associated with dense "blow-off" from the diurnal towering cumulus over the heated land regions rather than organized disturbances. The surface and gradient level flows showed a general northeasterly stream with unimpeded cross-equatorial flow. During the second major period of WMONEX (15–22 December) the South China Sea was in its maximum disturbed state during Phase I. The trough appeared north of Sarawak and Sabah with the surface flow generally offshore in the lower levels depending on the location of the disturbances. The final period (23–31 December) was similar to the first with the trough and disturbed region to the south of the equator. In summary, data from the WMONEX indicated an association between the fields of middle and upper level extended cloud and the disturbed regions of the WMONEX region. Extensive (and persistent) cloud decks also appeared upwind (i.e., relative to the middle-level wind structure) of the towering cumulus attached to the large island land masses[5] during undisturbed periods.

Moisture fields are shown in Fig. 3a. Time cross sections of daily mean relative humidity have been constructed for the three USSR ships for Phase I of WMONEX. During the first and last periods described above the region of maximum humidity is confined to the boundary layer with drier conditions aloft. Conversely, the middle period is characterized by a bimodal moisture distribution with a relatively dry lower tropospheric slab between 550 and 800 mb separated from a moist mid-troposphere by a large

[4] Sadler, J. C., 1979: Synoptic scale quick-look for Winter MONEX: December 1979. Department of Meteorology Tech. Rep. UHMET 79/02, Dept. of Meteorology, University of Hawaii, 3 pp.

[5] Similar features were observed during the Bay of Bengal experiment of Summer MONEX (July 1978). During periods of severe large-scale suppression GOES imagery indicated considerable cloudiness emanating from Burma. Aircraft penetrations identified the cloud as thick altostratus with characteristics similar to those noted above.

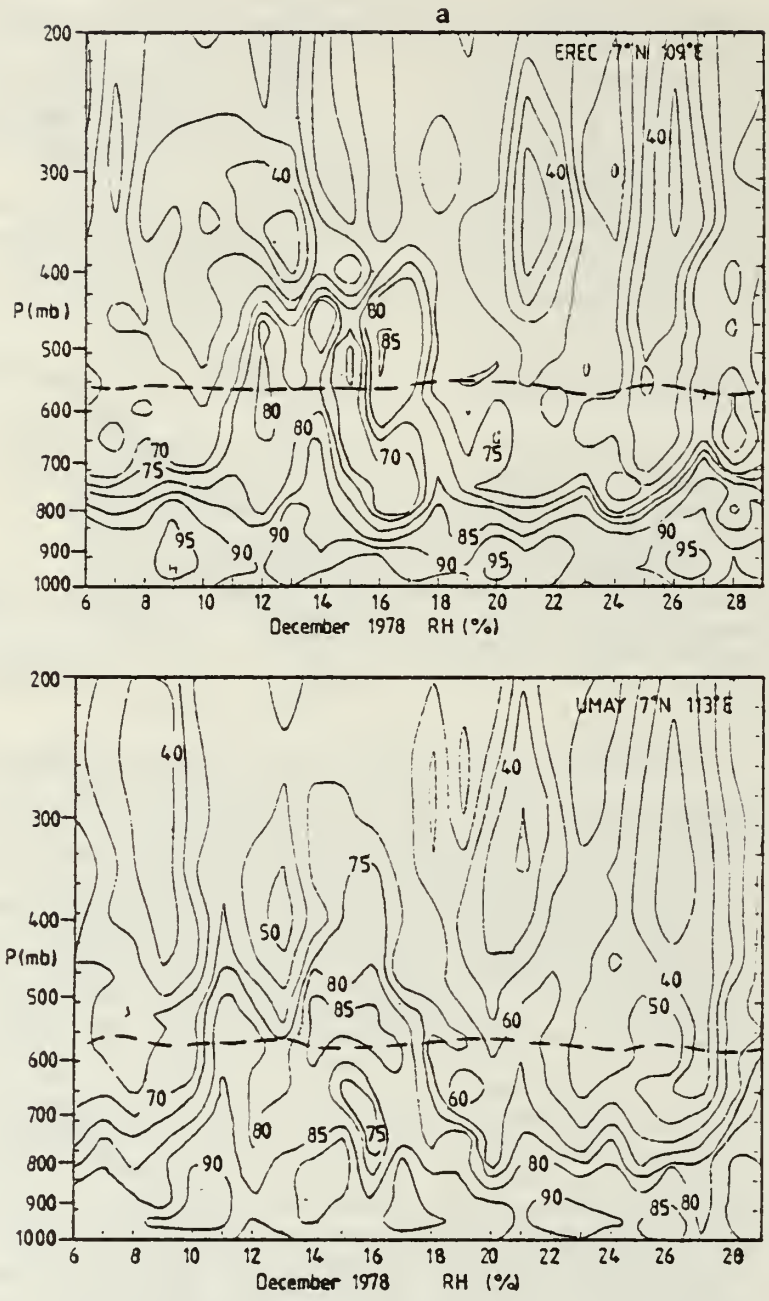

FIG. 3. (a) Time sections of relative humidity against pressure height for the three USSR ships located in the South China Sea during Phase I of WMONEX between 6–31 December 1978. The 0°C isopleth is shown as a dashed line. (b) As in Fig. 3a except for equivalent potential temperature (units: K).

humidity gradient near 550 mb. These features were common to all three ship locations. The humidity gradient was in the vicinity of the freezing level which is denoted by a dashed line in all three sections.

Companion θ_E sections are shown in Fig. 3b. The mid-tropospheric minimum (which generally characterizes tropical θ_E sections) appears in the vicinity of 600 mb for the undisturbed periods and closer to 800 mb for the disturbed periods. Values in the mid-troposphere are considerably larger during the disturbed period which with the smaller θ_E in the lower troposphere is consistent with the moisture distribution already discussed.

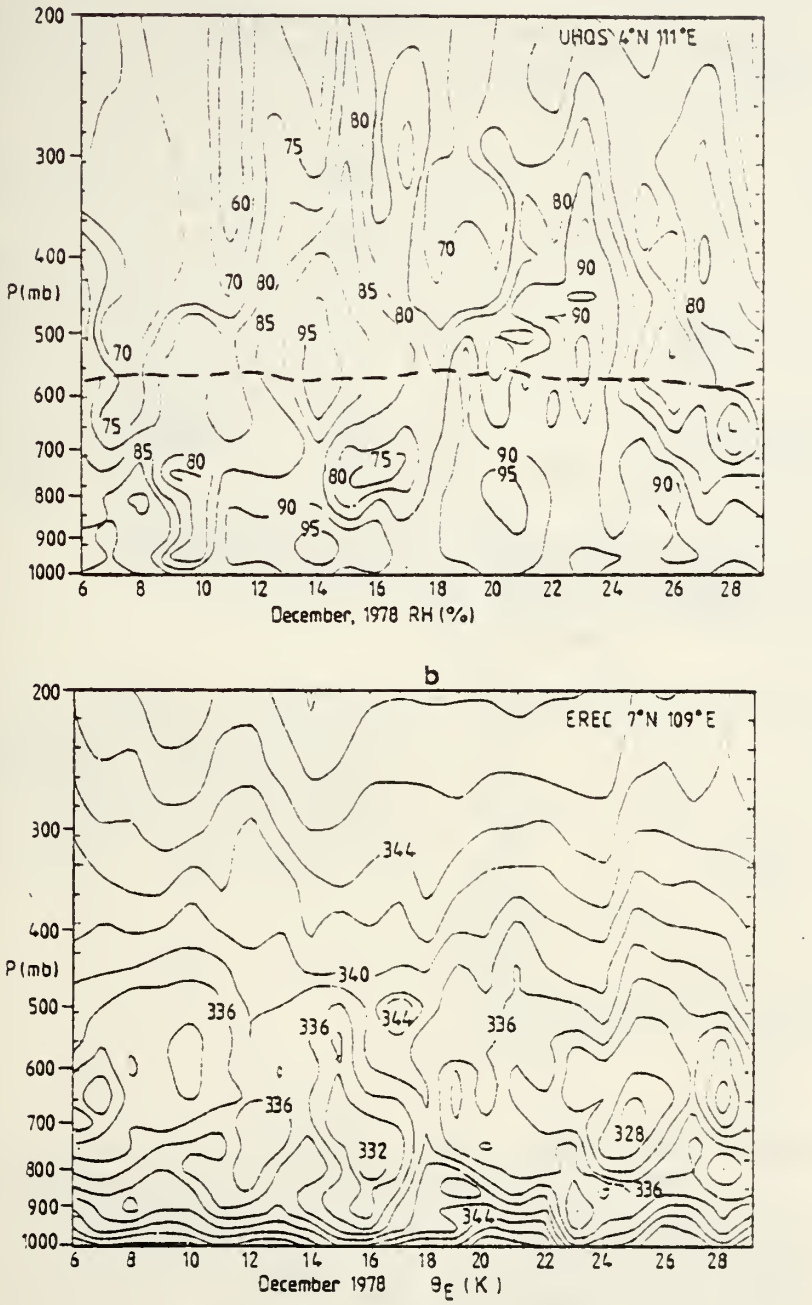

FIG. 3. (*Continued*)

Mean temperature and dewpoint profiles averaged over the USSR ship array are shown in Fig. 4a. The periods 7–9 December and 15–17 December 1978 are used to represent the first (undisturbed) and second (disturbed) periods, respectively. The dewpoint fields stress the nature of the undisturbed and disturbed periods: a dry middle and upper troposphere during the first period and a moist middle troposphere during the second above a relatively sharp moisture gradient. Interestingly, the temperatures in the boundary layer are slightly warmer in the mean (~1°C) during the first period although the temperature profiles are almost identical in the middle troposphere. Beyond this only the moisture structure is significantly different.

The corresponding equivalent potential temperature profiles are shown in Fig. 4b. Calculated for the same periods, the θ_E profile for the disturbed period shows a 5 K excess in the middle troposphere with slightly lower values in the lower

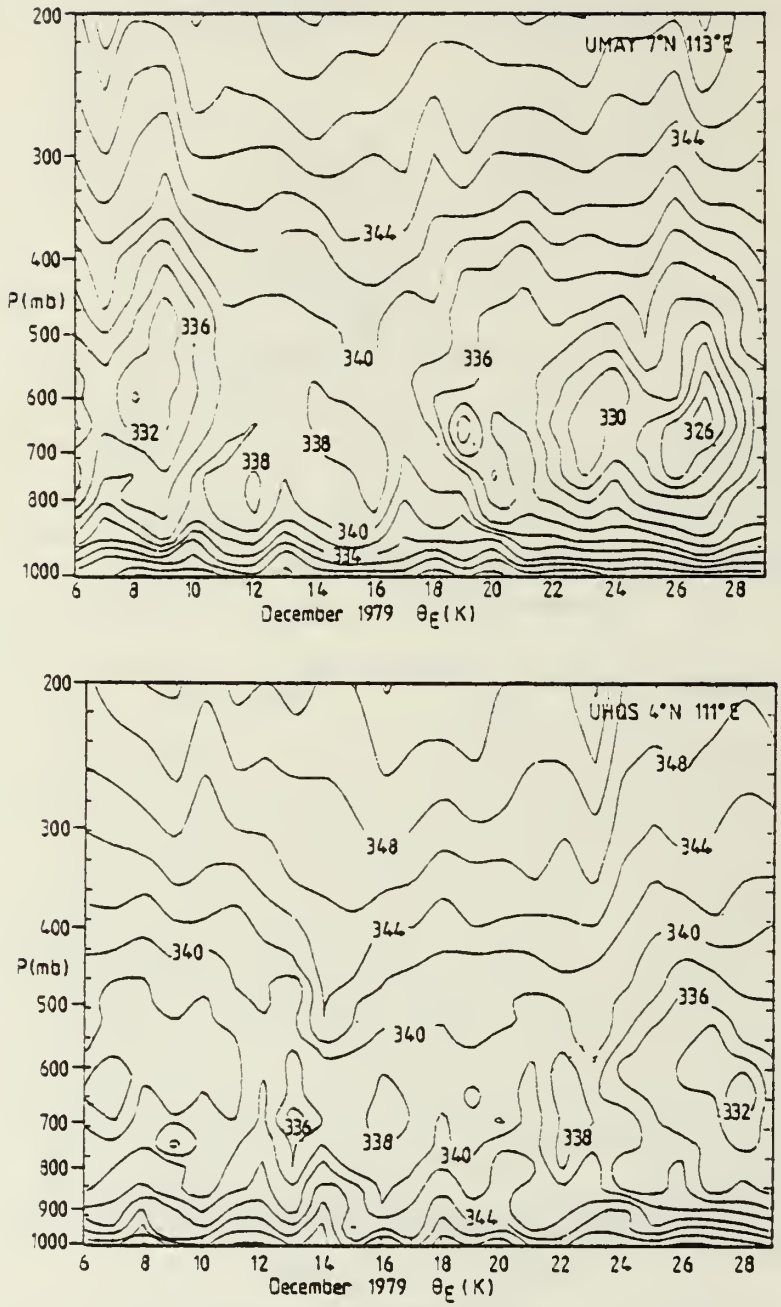

FIG. 3. (*Continued*)

troposphere. The θ_E profiles are consistent with temperature and humidity distributions of Fig. 4a. It is interesting to note that the θ_E profiles differ greatly from those obtained in the *convective* areas of tropical disturbances. Plotted with the mean WMONEX data in Fig. 4b are the convective and suppressed θ_E profiles obtained from the 1957 and 1963 research cruises of the *Crawford* to the east of Barbados in August.[6] The suppressed curve possesses a considerably lower mid-tropospheric

[6] Based on data summarized by N. Laseur, M. Garstang and C. Aspiden, 1967: Equivalent potential temperature as a measure of the structure of the tropical atmosphere. Final Report. U.S. Army ERDL, No. 67-10, 44 pp.

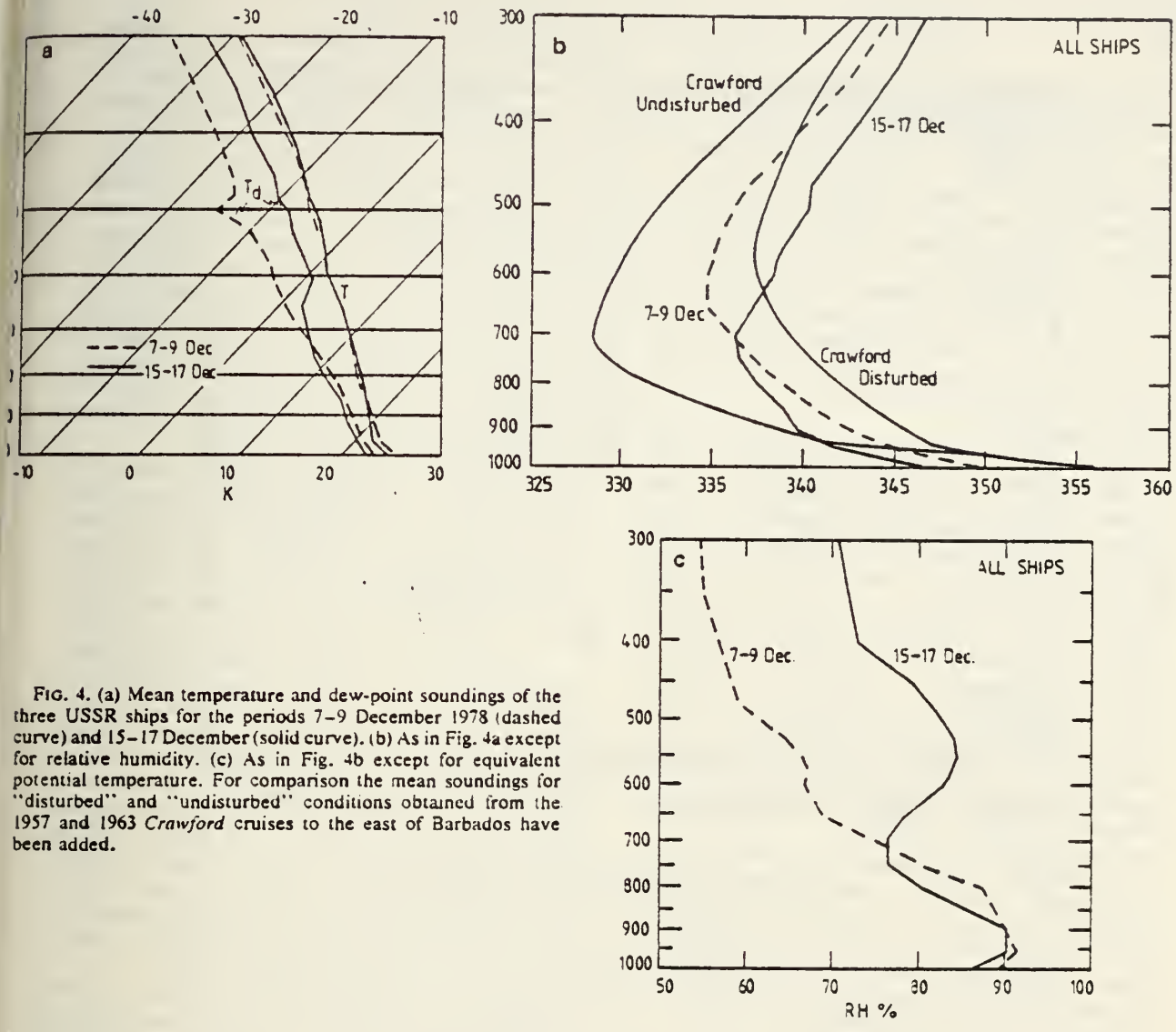

FIG. 4. (a) Mean temperature and dew-point soundings of the three USSR ships for the periods 7–9 December 1978 (dashed curve) and 15–17 December (solid curve). (b) As in Fig. 4a except for relative humidity. (c) As in Fig. 4b except for equivalent potential temperature. For comparison the mean soundings for "disturbed" and "undisturbed" conditions obtained from the 1957 and 1963 *Crawford* cruises to the east of Barbados have been added.

minimum than for either period during WMONEX. In fact, the WMONEX first-period curve appears to match the *Crawford* convective profile quite well. What is most evident is the extremely high values of the WMONEX disturbed curve in the middle and upper troposphere compared to the convective curve and the considerably lower values in the lower troposphere. The implication is that the soundings of the three USSR ships during the period from 15–17 December 1978 were not in the convective region of the disturbance *but were in the outflow region dominated by the middle tropospheric extended cloud*.

Fig. 4c shows the mean relative humidity sections for the two periods. The bimodal moisture distribution is particularly evident in the 15–17 December mean profiles.

c. *Case study—17 December 1978*

As emphasized earlier, middle and upper tropospheric extended clouds appeared as the most common species in the main observational region of WMONEX during the second period (i.e., 15–22 December 1978) when the locus of disturbances temporarily established itself in the Northern Hemisphere. During this period the cloud was densest off the Sabah and Sarawak coasts and generally extended north and west of the disturbed region for hundreds of kilometers.

A characteristic day of the period was 17 December which corresponded to the second day of a 2-day "vortex mission"[7] which employed the two principal research aircraft operating at maximum altitude in the dropsonde mode. The aircraft flightpaths complemented the USSR ship array and operated (at least during part of the mission) in the vicinity of the Bintulu radar. Other missions were planned and implemented during WMONEX during active periods with extensive middle decks (e.g., the Java Sea mission of 6 December) but they did not have the advantage of being supported by the WMONEX composite observing network in the South China Sea.

Figs. 5a and 5b show the visible (portion of the full disc picture) and infrared (section of the Mercator section)[8] GMS data for 0600 GMT 17 December. Three principal areas of bright upper level cloud may be discerned. For the present purposes the most important area is that occupying the South China Sea. A second area exists over the Java Sea which is typical of the cloud extent in that region during the first weeks of WMONEX (see Figs. 1a and b). A third area is evident west of Sumatra and is associated with a propagating disturbance which formed to the west of the island. Overall, the middle and upper level extended cloud is so extensive that it occupied over 50% of the area bounded by 105°E, 115°E, 7.5°N and 5°S, i.e., an area in excess of 6×10^5 km^2.

To provide an indication of the height of the cloud deck, isopleths of cloud top pressure (mb) are drawn on Fig. 5b. The data obtained from the GMS shows the cloud deck to the northeast of Borneo to be above 200 mb. Unfortunately, data was not available for the Java Sea region but comparisons using the grey calibration scales indicates similar cloud-top temperatures.

Fig. 6a shows the aircraft tracks and cloud fields observed from the aircraft. Times (local) at which the aircraft reached certain points along the tracks are marked. Preliminary dropsonde data (kt) for the 950 mb level are plotted for both the P3 and Electra (dashed and solid lines, respectively) along their flight paths. The USSR ship winds are also superimposed. A weak vortex is discernible at 950 mb in the vicinity of 7°N, 114°E as noted by Greenfield and Krishnamurti (1979) in their analysis. Two major cloud structures were identified from the aircraft. These were the extensive upper and middle-level cloud shield discussed earlier (denoted by light stippling) and the regions of active convection (shaded) which corresponds to either P3 radar echoes or aircraft penetrations. Hatched areas denote regions of precipitation observed to emerge from the base of the middle-tropospheric extended cloud deck or encounters by the aircraft during penetration of ice particles or supercooled water droplets.[9] Note that only those regions of precipitation well removed from the active convection are shown. In fact, in all cases of observed stratiform precipitation the lower troposphere possessed little or no cumulus activity except for scattered stratocumulus. In summary the regions of extensive precipitating middle and upper level extended decks possessed indications of complete suppression, a point previously noted in Fig. 4a.

The base of the extended cloud, away from the regions of convection, appeared to be in the vicinity of the freezing level. The estimates obtained from the aircraft flight-level information were substantiated by the USSR ship data seen in Fig. 3. Fig. 6b shows a composite of the dew-point depression ($T - T_d$) obtained from the research aircraft flight-level information, dropsonde data, USSR ship rawinsondes and the convection upper air sounding network. Two major regimes are evident. The first, which is representative of the majority of the tropical atmosphere away from the cloudy regions of Fig. 5, shows a dew-point depression in excess of 10°C. The second regime, which mirrors almost exactly the extent of the cloud shield noted in Fig. 6a, indicates near saturation in the vicinity of the 500–600 mb levels. Most importantly, Fig. 6b indicates that the base of the extended cloud deck extends at least 700 km from the major convective region with a thickness of some 300 mb.

The flight level and 500 mb winds are indicated on Fig. 6c; the data source and precise level being identifiable from the legend. The flow emerges from Borneo in a generally east-southeasterly direction turning to southwesterly around the ridge extending across the South China Sea. Most importantly, the middle and upper level cloud shield extends downwind from the convective source regions and is thus consistent with the larger scale flow.

Fig. 7 indicates the character of the subcloud layer below the extended clouds. Shown are a sample of the dropsonde profiles obtained from the research aircraft during the mission. Profiles A and B (which refer to points marked on Fig. 6a) indicate the characteristics of the vertical distribu-

[7] Greenfield and Krishnamurti, (1979) present a short summary of the various WMONEX missions and the data available from them. They present circulation charts for 17 December 1978 at 950, 850 and 700 mb using the dropsonde data as examples of the aircraft data.

[8] A common area is outlined on the full disc and mercator projections to facilitate comparison.

[9] Specific identification of the ice crystal form and size distribution must await analysis of the cloud physics experiment. Tentative inflight identification was graupel. Supercooled water droplets were associated with icing and easier to identify.

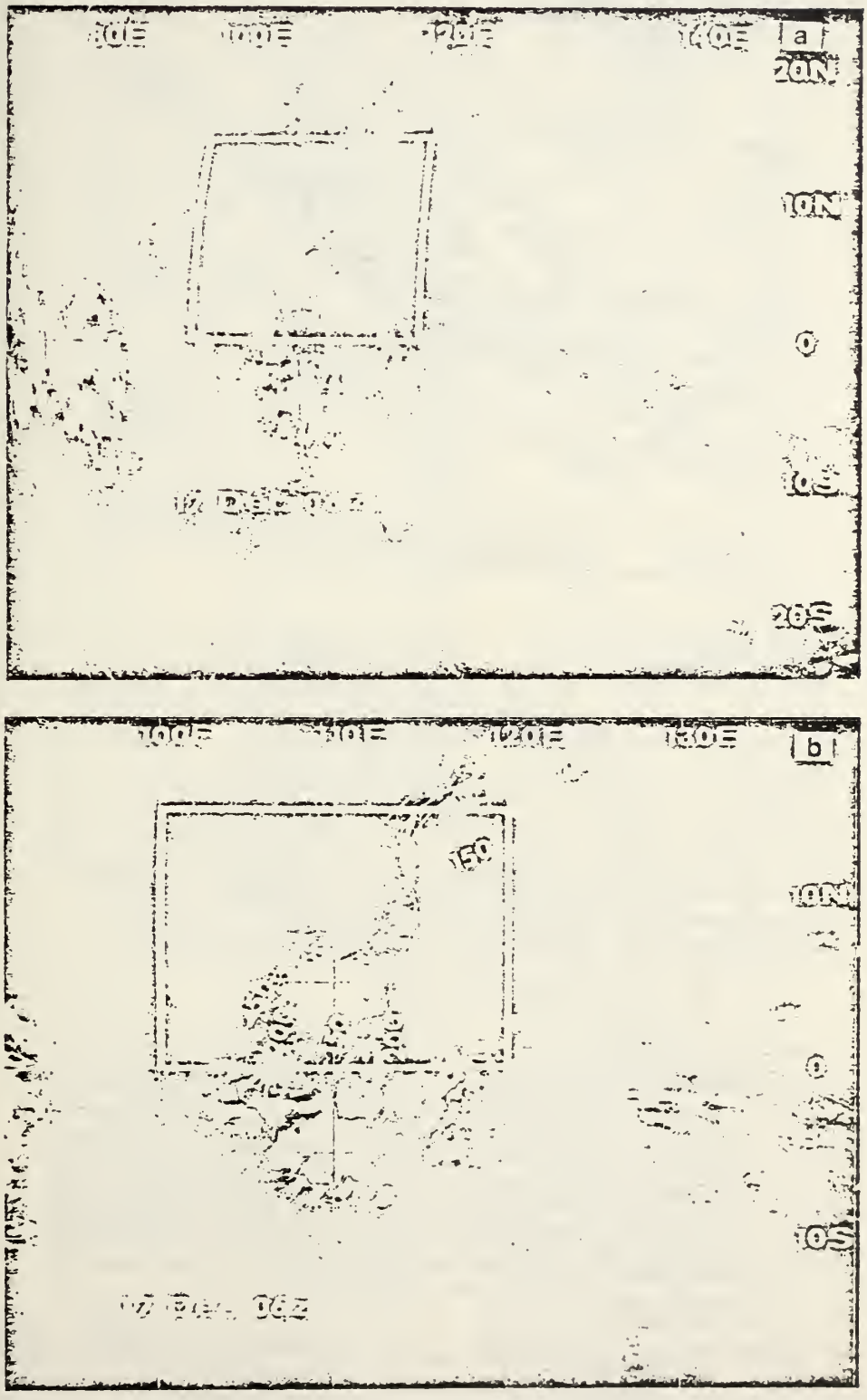

FIG. 5. (a) Visible GMS 1 imagery for 0600 GMT, 17 December 1978, from full disc image. (b) Infrared GMS 1 imagery for 0600 GMT, 17 December 1978, from Mercator projection image. Common area with Figs. 5a and 6 is bordered in white. Isopleths of cloud-top height are superimposed.

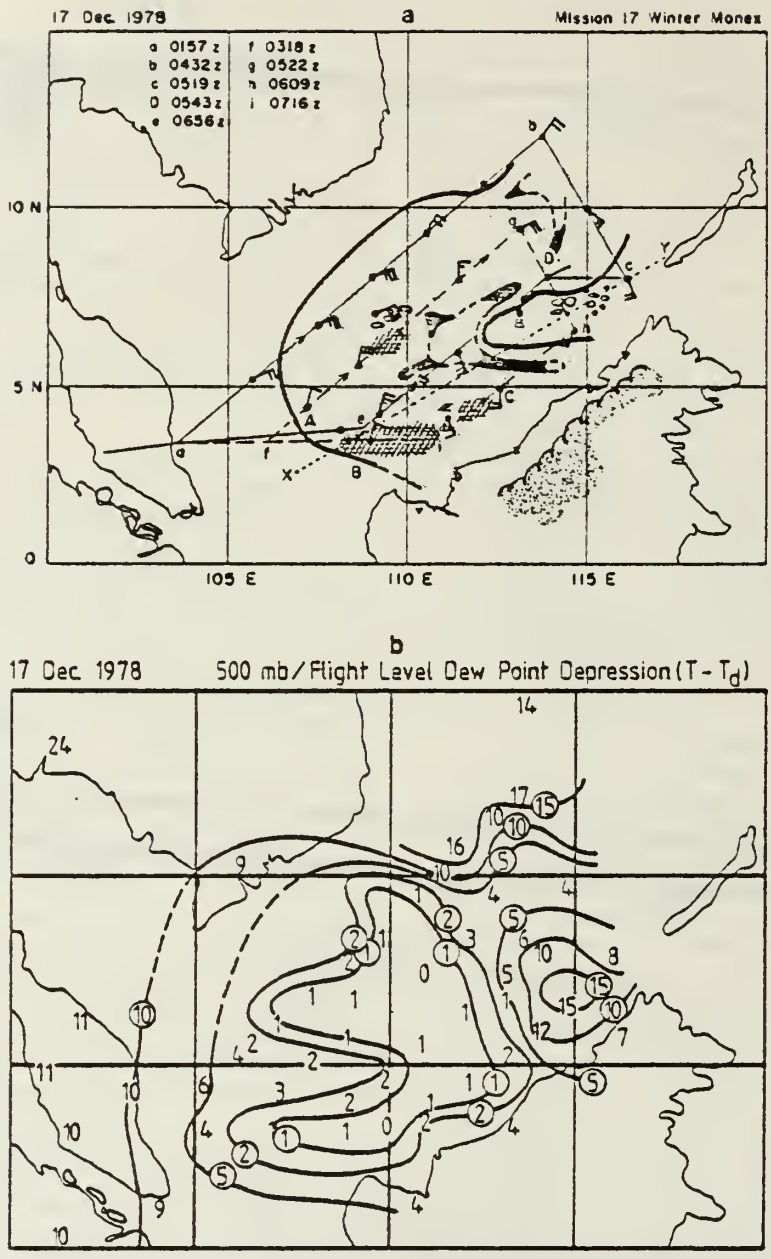

FIG. 6. (a) Flight-level visual record of mission 17 of the Winter Monsoon Experiment, 17 December 1978. Flight paths are shown as thin solid lines (NOAA P3) and thin dashed lines (NCAR Electra). 950 mb Electra and P3 dropsonde winds and surface observations are shown in conventional format. Light shading shows upper level cloud area. Dark shading denotes convective regions. Hatched area indicates observed extended cloud precipitation or graupel. Letters A–D refer to location of dropsondes shown in Fig. 7. (b) Distribution of dewpoint depression of mission 17. Data base includes regular radiosonde data, USSR ship data and the P3 and Electra flight-level record. (c) Composite middle tropospheric wind data. Data base is as in Fig. 6b and analysis refers to 500 mb.

tions of T and T_d beneath the extended decks. Both A and B indicate an extremely moist upper and middle troposphere and a dry lower troposphere above a shallow, moist boundary layer lying below a weak inversion. It should be noted that A and B show strong similarity to the USSR ship data noted in Figs. 3 and 4a. Such structures are consistent with the suppressed lower troposphere noted earlier.

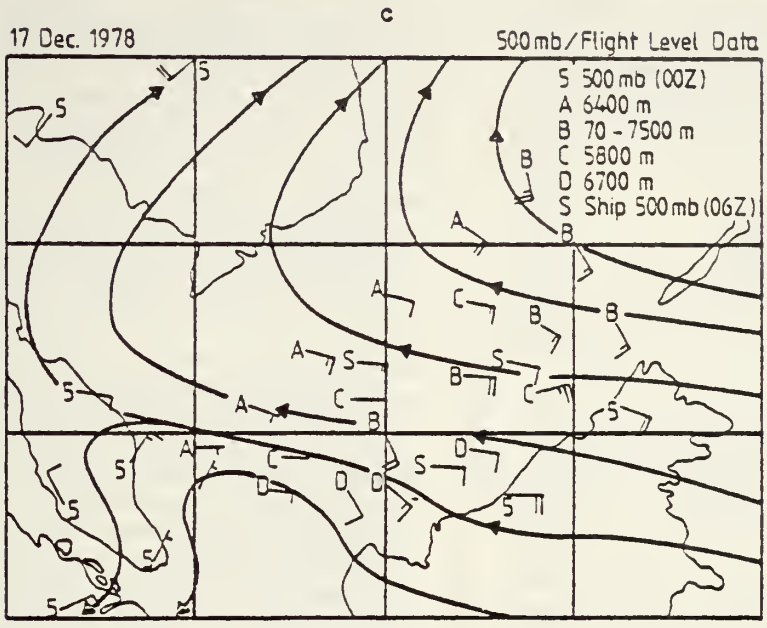

FIG. 6. (*Continued*)

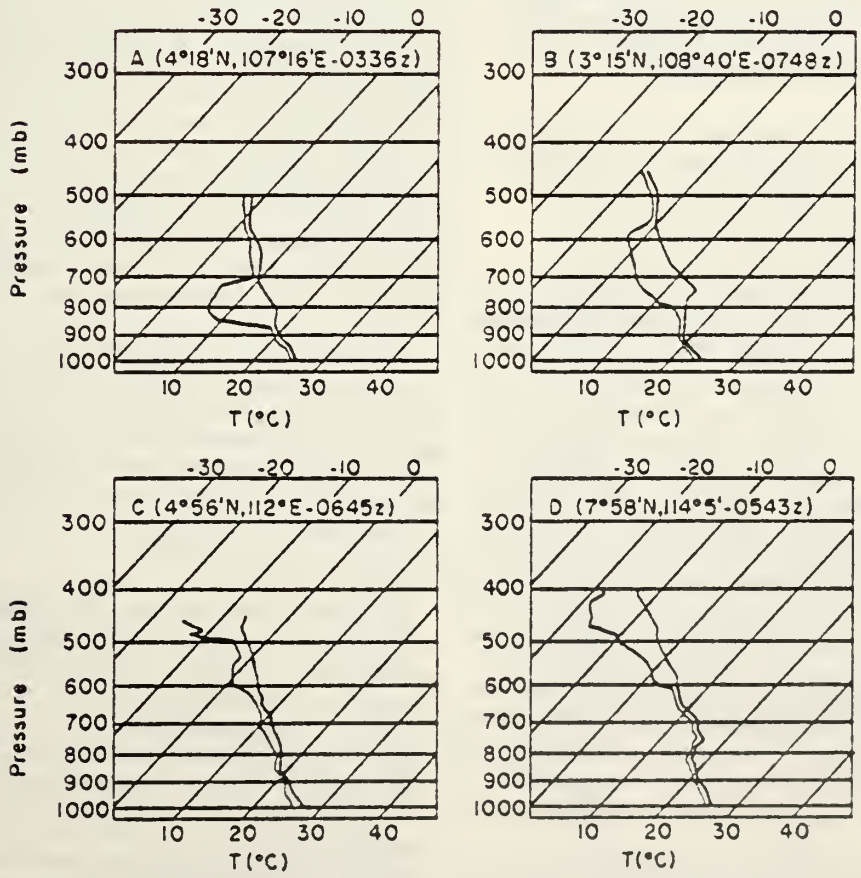

FIG. 7. Dropsonde temperature and dew-point profiles for 17 December 1978. Letters refer to locations marked on Fig. 6a.

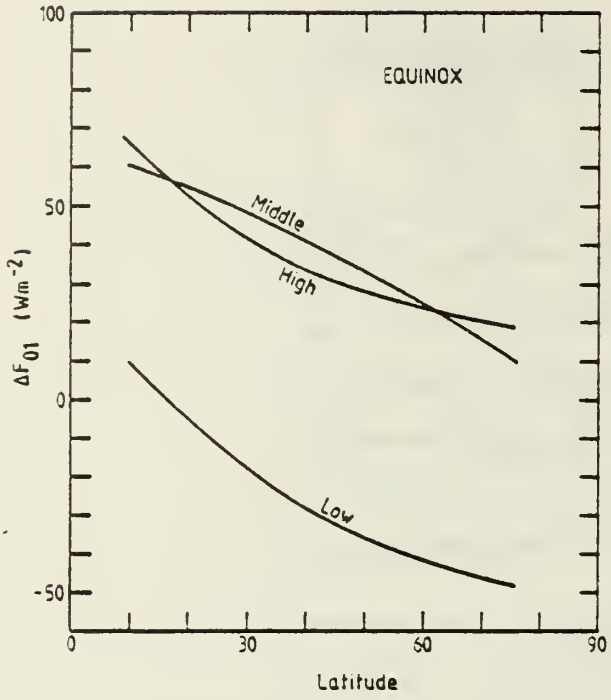

FIG. 8. Variation of net radiative flux is an atmospheric column between totally covered and clear skies as a function of latitude for three cloud species. Calculations from the static radiative transfer model of Stephens and Webster (1979).

Shown for contrast, the profiles C and D indicate conditions nearer to the regions of penetrative convection noted in Fig. 6a.

4. Radiative properties

An indication of the potential importance of the middle and upper level extended clouds, viewed from a radiative perspective, may be gained from Fig. 8.[10] Shown is the variation of the *difference* of the net radiative flux of the atmospheric column between totally covered and clear skies of low, middle and high clouds plotted as a function of latitude. Two points are apparent. First, the magnitude of the differential net radiative flux for the middle and high cloud is considerably greater than that for low cloud. Second, the magnitude of the net radiative flux is a maximum in low latitudes. Most importantly, the net radiative difference between clear and totally covered sky of (say) 10°N is of the same magnitude as the corresponding latitudinal gradient of net flux divergence. In fact, from Fig. 1, an extremely strong gradient in radiative flux divergence would be expected in the vicinity of the edge of the equatorial upper level cloud band.

[10] Calculations were made using the radiative transfer model developed by Stephens and Webster (1979). The properties of the three species are listed in their Table 1.

With the cloud and atmospheric structure obtained from WMONEX it is possible to calculate the radiative heating profiles in the vertical for various cloud structures. To obtain the profiles we use the relatively sophisticated multiple-scattering radiative transfer model (Model A) of Stephens (1978) which calculates both long- and shortwave fluxes through a cloudy atmosphere. The atmosphere is composed of 50 mb slabs extending from the surface to 100 mb and the basic atmospheric state was chosen to match the mean South China Sea conditions (see Fig. 4). The cloud portion was assumed to be in the ice phase and the thickness determined from the satellite-derived cloud-top height. The cloud bases were chosen to match those observed by the research aircraft. The particle size distribution of the crystal cloud employed in the calculations was taken from the measurements of Cox and Griffith (1977).

Figs. 9a and 9b show the vertical distribution of the infrared heating rate (solid curve), the shortwave heating rate (dashed, and calculated using daily average insolation) and the total radiative heating rate for two clouds (shaded area) occupying the 600–200 mb slab, which matches the observations, and the 350–200 mb slab calculated for comparison. In each case, the effect of the cloud deck is dramatic in both the long- and shortwave regions. The shortwave radiative heating is due to the effective absorption of solar radiation by both cloud material and water vapor. The infrared heating at the base of the cloud underlines the effectiveness of an upper deck to absorb the ingoing longwave radiation emanating from lower, warmer regions, i.e., both systems are optically black. The longwave structure in the upper portion of the cloud represents the distinct cooling to space.

The *total* effect of the radiative heating is to produce substantial heating in the lower part of the deck (~20 K day^{-1}) with cooling at the top (~ −15 K day^{-1}). Such a result is in sharp contrast to the mean tropical heating rates of Dopplick (i.e., weak net cooling throughout the atmospheric column irrespective of cloudiness) but in agreement with Albrecht and Cox (1975) and Cox and Griffith (1979).

Integrating the heating with height shows for both cases a net *heating* throughout the slab and, incidentally, through the entire depth of the atmosphere. Considerable diurnal variation is also implied. During nighttime, the shortwave contribution is absent and the total heating curve matches the longwave curve. Integrating once again with height, the total heating shows *small net cooling* both throughout the column and in the cloud. Such radiative heating or cooling would constitute *part* of the total diabatic heating function which would

include the Leary and Houze functions of evaporation and melting cooling at and below the base of the cloud deck.

5. Extensions and conclusions

a. Summary

Using data obtained from both the conventional and special observing platforms of the WMONEX, a number of general statements may be made regarding the cloud structure. These are summarized as follows:

1) The predominant cloud species during December 1978 in the Indonesian and South China Sea region was extended upper and middle troposphere cloud layers or shields. Within 10° of the equator there existed a strong positive correlation between total cloud and high cloud. The high cloudiness values which lasted through the 5-day average periods indicated substantial persistence of coverage.

2) The majority of the middle and upper level cloud appeared to be associated either with disturbances along the equatorial trough(s) or with the diurnal thunderstorms which appear as recurring features over the large islands of Southeast Asia and Indonesia. The upper level cloud shields often extended laterally to 1000 km from identifiable convective source regions.

3) GMS data indicated cloud-top heights above the 200 mb surface. Research aircraft data indicated bases in the vicinity of the 500–550 mb levels (or near the −5 to 0°C isotherms). Dropsonde data indicated warm and dry conditions below the cloud deck above a moist boundary layer surmounted by a weak inversion. On all occasions there was little or no evidence of convective activity in the low troposphere below the extended cloud away from the convective source regions. Radiosonde data from the USSR ship triangle corroborated the research aircraft observations as well as providing limits on cloud longevity and spatial extent.

4) In the disturbed situation from 15–17 December 1978, large upper and middle level cloud decks were constant features over the USSR ship array, indicating a disturbance longevity substantially greater than the well-documented GATE disturbances.

5) Precipitation was observed to fall from the base of the upper and middle level extended cloud system in locations well removed from the convective source region. The cloud systems

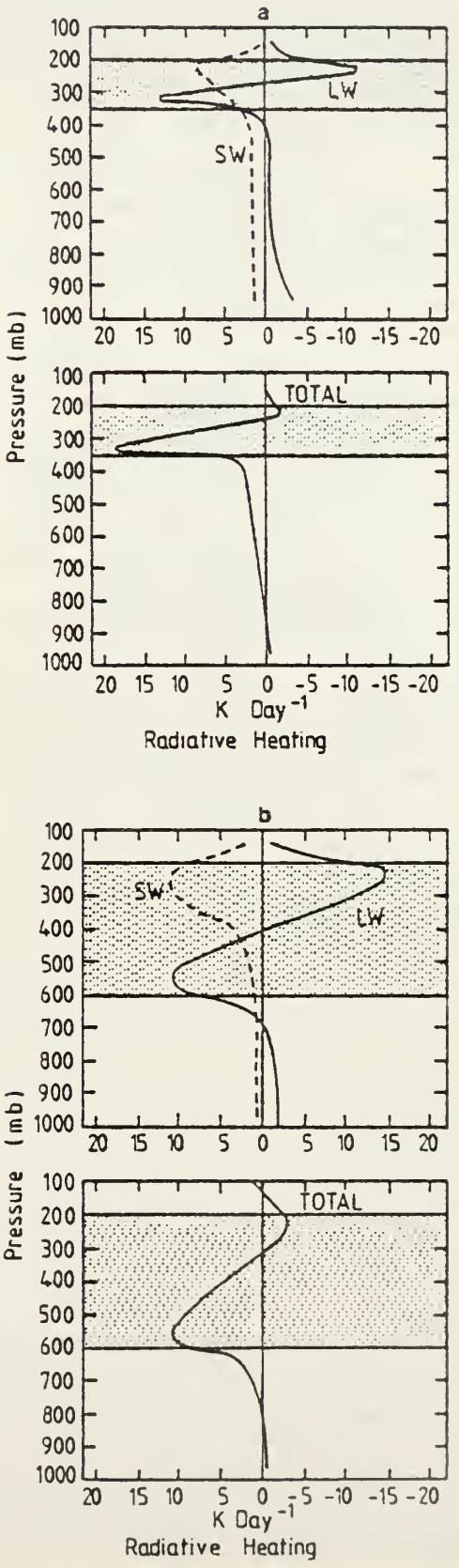

FIG. 9. Vertical distribution of radiative heating in the visible (dashed) and infrared (solid) relative to a cloud slab (a) between 200 and 350 mb and (b) between 200 and 550 mb.

were observed to have the form of nimbostratus decks. Cloud-base penetrations by the research aircraft indicated supercooled water droplets and (probably) graupel. Precipitables were observed on scales which varied from tens to hundreds of kilometers.

Using the data collected from the WMONEX which defined the atmospheric and cloud structure transfer models, developed in earlier papers, a number of inferences could be made regarding the interaction of extended clouds and the radiative field. These were as follows:

1) Dense optically black middle and upper level cloud impart a significant perturbation on the net radiative flux of the atmospheric column. Because of the areal extent and persistence of the extended clouds they probably form the major perturbation to the near-equatorial radiation balance.

2) Substantial horizontal gradients in the net radiative flux of the atmospheric column may be expected between the equatorial trough region and the clearer regions to the north and south.

3) Optically black middle and upper tropospheric cloud decks appear as major perturbers of the vertical radiative heating profile. In sharp contrast to the Dopplick (1963) profile, radiative transfer calculations indicate substantial heating at the base of the cloud deck and a larger cooling to space at the top of the cloud. A heating rate differential of nearly 30°C day^{-1} was estimated. A large diurnal variation in net radiation was shown to exist which would be caused by the diurnal variation of absorption of incoming short wave radiation in the upper portion of the cloud.

b. Processes and mechanisms

Ideally, at this stage, one would hope to describe a physical process or a chain of processes which would aid in understanding the phenomena noted above. However, prior to undertaking a considerable modeling effort (see below) we are forced to test the observations against earlier results of both a theoretical and observational nature in an attempt to trace either consistency or inconsistency in the logic. With this methodology we will discuss the three questions raised in the Introduction.

1) Source of the extended cloud

There appeared abundant evidence during WMONEX of the extended cloud being associated with large-scale convection. In all cases of extensive shield cloud either a circulation feature or convective event associated with the diurnal heating of the islands was evident. Overall there appeared to be no evidence of synoptic scale uplift with which one may often associate midlatitude decks.

2) Cloud maintenance; longevity and extent

If extended clouds are at least initially cumulonimbus debris, a knowledge of particle fall speed, evaporation rate, vertical motion and total horizontal wind speed would yield an estimate of the horizontal extent of the cloud system. That is, if we hypothesize that there is no diabatic heating within the anvil the estimate of extent reduces to knowing the fall time from ejection to evaporation. The following estimates are based on the *conservative* assumptions that the environment of the source region is *non-subsident* with a zero vertical velocity component, possesses a relative humidity of 75% (see Fig. 3) and that the emitted particles are ice crystals which originate in the source region near 350 mb. Using the terminal velocity estimates of Heymsfield (1972) for the slab 350–550 mb and taking into account the evaporation of the ice near the melting zone, horizontal cloud deck extents were calculated to be from 150 km for 0.5 mm bullets to 200 km for 0.5 mm plates if a horizontal wind speed of 12.5 m s^{-1} was assumed throughout the slab. That is, in the *absence of external heating* (i.e., utilizing a "quiescent debris" model), the horizontal extent of the cloud decks would be < 200 km.

The quiescent debris model utilizing conservative assumptions aimed at *maximizing* the cloud horizontal extent, underestimates the real extent by a factor of three or four. Thus either the basic premise of the model is incorrect or an approximation ill-founded. In any event, a mechanism is required to increase the suspension time of the cloud ice-particles by a considerable amount. In fact, if the size distribution of the particulates was correct, then a net upward vertical velocity of $\sim$0.30 m s^{-1} (i.e., the difference between the fall speed necessary to produce the required suspension and the ice-particle terminal velocity) either as a mean uplift or as a rectified effect of smaller scale processes would be required to produce an extended cloud of observed proportions.

3) Diabatic heating

In order to account for the longevity of the cloud debris diabatic heating must be invoked. Two forms are applicable; latent and radiative heating.

The latent heating is associated with phase changes within and below the cloud deck. As noted earlier for the GATE systems (Leary and Houze, 1979) melting produced cooling at the base of between 1 and 7 K h^{-1} while evaporation provided cooling of 0.2–6 K h^{-1} below the cloud deck. Five case averages were 3.6 and 2.2 K h^{-1}, respectively. The estimates refer to rather intense systems exhibiting anvil precipitation of between

1 and 10 mm h^{-1} within 100 km of the convective region. Such systems are probably much more intense than the WMONEX disturbances. Besides the question of anvil scale discussed earlier, it seems that the extended cloud precipitation observed during WMONEX was considerably weaker than noted in the GATE system. However, the GATE systems of Leary and Houze are probably the best-documented systems and at least allow the role of radiation to be assessed in conditions of *intense* convection and anvil precipitation.

The radiative function results from cloud-radiative feedbacks. The form of the function is summarized in Fig. 9 and shows many of the characteristics observed by Albrecht and Cox (1975) and Cox and Griffith (1979).

An important aspect of the total diabatic heating function is that it is a composite of functions of different signs. Latent effects tend to cool the lower part of the cloud (melting) and the subcloud layer (evaporation) and to heat the interior of the cloud. Conversely, the radiative processes tend to warm the lower part of the cloud (absorption of upcoming infrared radiation) and to cool the top (cooling to space, which is emphasized at nighttime due to the absence of solar radiation). Consequently, *latent heating effects tend to stabilize the thermal structure of the cloud, whereas radiative processes tend to destabilize the thermal structure*. The important factor lies in the relative magnitude of the two component functions. Radiative processes will tend to remain constant for the same cloud structure; the magnitudes depend primarily on the cloud thickness (i.e., its optical blackness) and the cloud-base height. On the other hand, the magnitude of the latent effects are strong functions of the intensity of anvil precipitation which, in turn, depends on the intensity of the disturbance, the stage of its lifecycle and the distance of the atmospheric column from the convective source.

With these criteria in mind, it would appear that radiative processes will possess a varied importance depending on the disturbance in question or the particular location within the disturbance or its outflow region. For an extremely vigorous disturbance such as Leary and Houze's case 1, which exhibited anvil precipitation of 8–9 mm h^{-1}, radiative processes will almost certainly be of secondary importance in the total diabatic heat balance of the column. For disturbances 2 and 4 (precipitation rates of 0.3 and 2.3 mm h^{-1}, respectively) radiative heating at the base of the cloud tends to approach magnitudes which are similar to that of the latent heating due to melting. This is shown schematically in Fig. 10 where profiles of the two diabatic heating rates are drawn. For the average Leary-Houze disturbance the magnitude of the

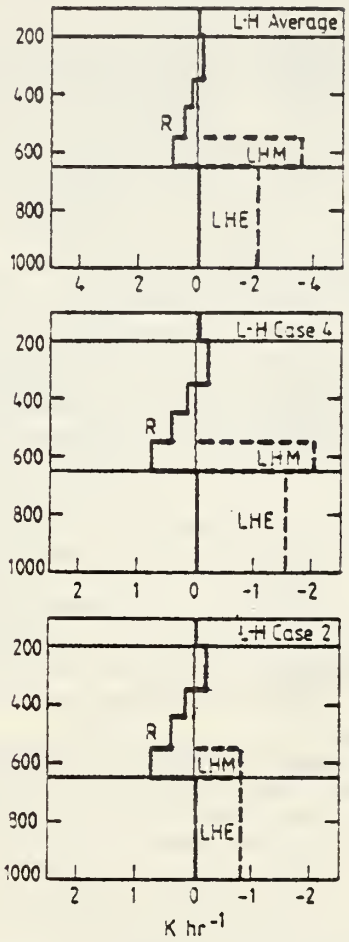

FIG. 10. Schematic comparison of diabatic heating rates for the average disturbance of Leary and Houze (1979) (upper) and their cases 4 (middle) and 2 (lower panel). R refers to radiative heating, LHM to cooling due to melting and LHE to cooling due to evaporation. Cloud slab extends from 200–650 mb. Note scale change between upper and lower two panels. Units are K h^{-1}.

radiative heating is only 11% of the total cooling for melting and evaporation. For case 4 it accounts for 17%, whereas for the weakest example of the set, case 2, the magnitude has risen to 33%. Thus with decreasing intensities the effect of radiative processes gain in importance.

The apparently smaller precipitation rates of the WMONEX disturbances, observed in discrete regions well away from the convective source region (see Fig. 7), are perhaps less intense than Leary and Houze's disturbance 2. Unfortunately, the WMONEX estimates depend on visual observations of the precipitation and quantitative assessments must await analyses and publication of the research aircraft and land-based radar data. However, extrapolation of the analysis of Fig. 10 to weaker disturbances with smaller outflow region precipitation allow some indication of the role

radiative processes play in the disturbances observed during WMONEX. Considering the limiting case when precipitation processes are absent from the extended cloud, radiational heating at the base of the cloud must become the dominant diabatic heating form and destabilization preponderate. The preferred scale of convective overturning resulting from the destabilization would be of the scale of the extended cloud thickness itself (i.e., ~7–10 km) which would produce regions of precipitation from the anvil. The undulations which were observed to occur well below the mean base height of the deck in the region of precipitation are consistent with the formation of melting regions of the aggregated crystals below the freezing level. That such crystals occur is substantiated by the research aircraft observation of graupel in passages through the precipitating zones. A similar latent heat format to that of Leary and Houze, but substantially smaller in magnitude, follows with cooling below the cloud deck caused by evaporation of the precipitation. There was some evidence of evaporation during WMONEX with the light precipitation falling from the undulations of the cloud deck in the form of virga.

Besides providing a potential for precipitation formation of the extended cloud at great distances away from the convective source, it should be noted that the radiative effects themselves constitute a *net* warming of the cloud deck during the day which would partially maintain the cloud system via lifting. Such heating is in addition to the latent heating from within the cloud.

Whether or not the extended cloud breaks into *visible* cellular structure following the initiation of the stabilizing convection within the extended cloud depends on the ability of the residual ice crystals to withstand sublimation within the enhanced subsidence between the precipitation regions during their descent to cloud base. Furthermore, it is not possible at this stage to understand why precipitation was observed to occur over a large variety of scales (see Fig. 6) when the initial convection would possess a preferred scale.

The solution of these problems may be connected with the reemergence of the latent heating (or cooling) within and below the cloud after the advent of precipitation. However, further speculation should await the development of appropriate models or the diagnosis of more specialized data than was used in this study.

c. *Concluding remarks*

A varying degree of importance has been suggested for radiative processes in the near-equatorial regions. Calculations suggest that from a purely radiative viewpoint, the existence of vast decks of middle and upper extended clouds (see Fig. 1) must have a large influence on the radiative balance of the tropical atmosphere. The role of radiation in the maintenance of features close to the convective source appeared to depend on the strength of the disturbance itself. In systems with vigorously precipitating anvils latent effects clearly dominate. However, with smaller precipitation it appears that radiative effects must be carefully taken into account in the calculation of the total diabatic heating field. Less direct observations were available for extended clouds at great distances from the convective source but it was speculated (with the aid of extrapolation of the results pertaining to more vigorous disturbances) that radiative effects had become increasingly important. Such influences appear consistent with WMONEX observations of discrete regions of extended cloud precipitation.

Beyond further analysis of data, the development of models offers a potentially fruitful area of investigation. Using numerical techniques Brown (1979) tested the hypotheses that evaporative cooling of anvil rainfall explains the downdrafts observed below tropical systems. Brown's model was able to produce many of the features of such systems, although he neglected both radiative processes and cooling due to melting. However, we have noted that these two effects tend to cancel for the weakest of the Leary and Houze cases (case 2) which possesses rainfall most similar to that simulated by Brown (i.e., 0.5–1.0 mm h^{-1} compared to 0.3 mm h^{-1}). We have also noted that this need not be the case and that radiative effects may be of either major or minor importance. Consequently, a series of numerical studies is being undertaken using a model which includes a relatively sophisticated radiative model similar to that of Stephens and Webster (1979) thus catering to the radiation feedback processes discussed above. The primary aim is to develop a systematic estimate of the total diabatic heating field through the life cycles of convective systems and to obtain quantitative estimates of the broader question: the role of radiative processes in the tropical atmosphere over synoptic and climatological time scales.

Acknowledgments. The authors would like to thank Professors R. S. and J. S. Simpson, Professor R. A. Houze and Drs. C. M. R. Platt and E. J. Zipser for many helpful discussions during the course of this study. Thanks are also due to P. R. Brenton and P. A. Watterson for their help in analyzing data. This research was sponsored in part by the National Science Foundation under Grant ATM 78-14821A01.

REFERENCES

Albrecht, B., and S. K. Cox, 1975: The large-scale response of the tropical atmosphere to cloud modulated infrared heating. *J. Atmos. Sci.*, 32, 16–24.

Brown, J. M., 1979: Mesoscale unsaturated downdrafts driven by rainfall evaporation. A numerical study. *J. Atmos. Sci.*, 36, 313–338.

Cox, S. K., and K. T. Griffith, 1979: Estimates of radiative divergence during Phase III of the GARP Atlantic Tropical Experiment: Part II. Analysis of the Phase III results. *J. Atmos. Sci.*, 36, 586–601.

Dopplick, T. G., 1972: Radiative heating of the global atmosphere. *J. Atmos. Sci.*, 29, 1278–1294.

Greenfield, R. S., and T. N. Krishnamurti, 1979: The Winter Monsoon Experiment—report of December 1978 field phase. *Bull. Amer. Meteor. Soc.*, 60, 439–445.

Heymsfield, A. J., 1972: Ice crystal terminal velocities. *J. Atmos. Sci.*, 29, 1348–1357.

Houze, R. A., Jr., 1977: Structure and dynamics of a tropical squall-line system. *Mon. Wea. Rev.*, 105, 1540–1567.

Leary, C. A., and R. A. Houze, Jr., 1979: Melting and evaporation of hydrometeors in precipitation from anvil clouds of deep tropical convection. *J. Atmos. Sci.*, 36, 669–679.

Malkus, J. S., and H. Riehl, 1964: *Cloud Structure and Distribution over the Tropical Pacific Ocean*. University of California Press, Berkeley and Los Angeles, 229 pp.

Streten, N. A., 1973: Some characteristics of satellite observed bands of persistent cloudiness over the Southern Hemisphere. *Mon. Wea. Rev.*, 101, 486–495.

Stephens, G. L., 1978: Radiative properties of extended water clouds, Part I. *J. Atmos. Sci.*, 35, 2111–2122.

——, and P. J. Webster, 1979: Sensitivity of radiative forcing to variable cloud and moisture. *J. Atmos. Sci.*, 36, 1542–1556.

——, and K. J. Wilson, 1980: The response of a deep cumulus convection model to changes in radiative heating. *J. Atmos. Sci.*, 37, 421–434.

Webster, P. J., and D. Curtin, 1974: Interpretations of the EOLE Experiment II: Spatial variation of transient and stationary modes. *J. Atmos. Sci.*, 32, 1848–1863.

Zipser, E. J., 1977: Mesoscale and convective scale downdrafts as distinct components of squall-line circulation. *Mon. Wea. Rev.*, 105, 1568–1589.

Initial Distribution List

		No. Copies
1.	Defense Technical Information Center Cameron Station Alexandria, Virginia 22314	2
2.	Library, Code 0142 Naval Postgraduate School Monterey, California 93940	2
3.	Research Administration, Code 012A Naval Postgraduate School Monterey, California 93940	1
4.	National Science Foundation Division of Grants and Contracts Post-Award Projects Branch Washington, D.C. 20550	2
5.	Dr. Richard Greenfield Division of Atmospheric Sciences National Science Foundation Washington, D.C. 20550	1
6.	Dr. Jay S. Fein Global Atmospheric Research Program National Science Foundation Washington, D.C. 20550	1
7.	Dr. Pam Stevens Global Atmospheric Research Program National Science Foundation Washington, D.C. 20550	1
8.	Dr. Alan Holt Division of International Programs National Science Foundation Washington, D.C. 20550	1
9.	Dr. Maurice Edwards U.S.- Taiwan Cooperative Science Program Division of International Programs National Science Foundation Washington, D.C. 20550	1
10.	Professor C.-P. Chang, Code 63Cp Department of Meteorology Naval Postgraduate School Monterey, California 93940	17
11.	Professor R. T. Williams, Code 63Wu Department of Meteorology Naval Postgraduate School Monterey, California 93940	2

12. Professor R. J. Renard, Code 63Rd — 1
Department of Meteorology
Naval Postgraduate School
Monterey, California 93940

13. Professor R. L. Elsberry, Code 63Es — 1
Department of Meteorology
Naval Postgraduate School
Monterey, California 93940

14. Dr. William M. Tolles, Code 012 — 1
Dean of Research
Naval Postgraduate School
Monterey, California 93940